Author:
Scott, D A

Title:
Utilising de novo-designed -helical peptides as a modular cytoscaffold for primary neurons and sensor for small-molecules

Redacted thesis cover sheet

Chapter 6 of this Thesis has been redacted in this version of the text, as agreed by the author and supervisors (Prof. Dek Woolfson and Prof. Jeremy Henley) and approved by the graduate director of Life Sciences, Prof. Harry Mellor. This redacted material contains commercially sensitive data and methods that are of interest to The University of Bristol and one of its spinout companies, Rosa Biotech. The University may want to patent this information in the future and, therefore, permission has been granted for this section to be redacted for 12 months from the date of the award (25/03/2020).

Utilising *de novo*-designed α-helical peptides as a modular cytoscaffold for primary neurons and sensor for small-molecules

David Arne Scott

A dissertation submitted to the University of Bristol in accordance with the requirements for award of the degree of Doctor of Philosophy in the Faculty of Life Sciences.

School of Biochemistry, September 2019.

Word count: 41,322

Author’s Declaration

I declare that the work in this dissertation was carried out in accordance with the requirements of the University's Regulations and Code of Practice for Research Degree Programmes and that it has not been submitted for any other academic award. Except where indicated by specific reference in the text, the work is the candidate's own work. Work done in collaboration with, or with the assistance of, others, is indicated as such. Any views expressed in the dissertation are those of the author.

SIGNED: ..... DATE:.....

For Emily,

without whom I would have done very little.

Abstract

Our ever-increasing understanding of how proteins fold has allowed the design of completely new peptides and proteins from first principles. So-called *de novo* protein design opens opportunities for the generation of novel biomaterials with easily tuneable properties. For instance, there are now several examples of *de novo* designed self-assembling peptide systems that form hydrogels for *in vitro* cell culture and tissue engineering. However, owing to the relative infancy of these systems, they have not been as well explored as similar scaffolds derived from natural sources or synthetic polymers. Studies often do not exploit the biggest asset of such designed systems – an ability to tune scaffold properties through a fundamental understanding of its makeup.

This thesis presents work to tune the chemical and physical properties of one such self-assembling peptide hydrogel; hydrogelating self-assembling fibres (hSAFs). This scaffold consists of two *de novo* designed α-helical peptides that form a heterodimeric coiled coil and subsequently fibrous structures. I demonstrate that this scaffold can support the growth of primary neurons and that, by modifying the sequence of the underlying peptides, I can generate scaffolds with varying viscoelastic properties. In addition, I show that both peptides and proteins can be incorporated into the scaffold, in a spatially controllable manner. Primary neuronal responses to these scaffolds are assessed to demonstrate the applicability of hSAFs as a modular and tuneable scaffold for neurons.

Another area in which *de novo* protein design might be utilised is the construction of novel biosensors. Recently, the Woolfson group demonstrated the differential binding of lipophillic small molecules to *de novo* designed α-helical peptide assemblies with solvent accessible pores. Here, I use an array of these peptides to differentiate between different fatty acids.

These studies go some way to realising the potential of protein design to deliver novel biomaterials with real-world applications.

Acknowledgements

First and foremost, I would like to thank Dek and Jeremy, both for their excellent supervision over the last 4 years and for cooking up such an open ended and challenging project for me to sink my teeth into. They have allowed me to pursue any and all avenues I desired during a project encompassing peptide synthesis, neurobiology, materials science, microbiology, microfluidics, photolithography and biosensing. I have encountered very few students whose PhD has allowed them to work within quite so many different and disparate fields – I am indebted to Dek and Jeremy for allowing me to do so. Aside from this, they have been extremely supportive of my personal endeavours during the last four years, for which I am grateful.

The work presented here has been highly collaborative and I am grateful to all past and present members of the Woolfson and Henley groups for their contributions and guidance when required. Specific thanks go to Alex Wasmuth for her work redesigning hSAFs to form stiffer gels, and to Nazia Mehrban, Kieran Hudson and Edgardo Abelardo for their previous contributions to the development of hSAFs. I am also grateful to Alex Fletcher-Jones, Caroline Binda and Rachel Milligan for their help with dissections, Suko and Dan Rocca, who have given me advice regarding neuronal cell culture, and Matt Hockley, for his guidance regarding microfluidics. With regard to the work designing an α helical peptide biosensor for small-molecule detection, a lot of credit and thanks go to Will Dawson, Guto Rhys, Chris Wood, Jordan Fletcher and Kathryn Shelley for their sizeable contributions to the presented work. Thank you also to Will for proofreading various sections of this thesis and providing advice along the way.

I have been lucky to be involved in the process of spinning out a company from The University of Bristol. This has been an exciting experience and I am grateful to Dek and Andy Boyce for involving me in the process where possible and appropriate. Also, a thank you to James Field and everyone else at LabGenius, with whom I spent 3-months during my studies. Additional thanks are to Sam Southern and all others involved in the SW-Bio DTP programme, the other members of my cohort, particularly Katy, Travis, Alex, Clara and Emily, with whom I have shared and enjoyed the PhD experience, and also to the British tax payers that have allowed me to conduct this work and provided me with the training required to pursue my future endeavours.

Finally, I would have done very little without the substantial support of my family. Particularly my wife, Emily, who has put up with my early starts and late returns for the past 4 years, and stuck with me through every aspect of academic life since completing my GCSEs. She has also blessed me with a beautiful daughter, Lola, who has been an excellent motivator through the final months of my studies. Lastly, thank you to my parents, who have supported me financially throughout my studies and encouraged me to always push a little harder.

Abbreviations

αHB	α-helical barrel
APS	Ammonium persulfate
Alloc	Allyloxycarbonyl
AU	Absorbance units
BDNF	Brain derived neurotrophic factor
BSA	Bovine serum albumin
CD	Circular dichroism
CuAAC	Cu^{2+}-catalysed azide-alkyne cycloaddition
DAPI	4',6-Diamidino-2-phenylindole
DCM	Dichloromethane
dH_2O	Deionised water
DIC	N,N'-Diisopropylcarbodiimide
DIPEA	Diisopropylethylamine
DIV	Days *in vitro*
DMF	Dimethylformamide
DMSO	Dimethyl sulfoxide
DNA	Deoxyribonucleic acid
DPH	Diphenylhexatriene
ECM	Extracellular matrix
EDTA	Ethylenediaminetetraacetic acid
FDA	Food and Drug Administration
FGF	Fibroblast growth factor
Fmoc	Fluorenylmethyloxycarbonyl
GFAP	Glial fibrillary acidic protein
GFP	Green fluorescent protein

GuHCl	Guanidinium hydrochloride
HATU	Hexafluorophosphate azabenzotriazole tetramethyl uranium
HBS	HEPES buffered saline
HisTag	Hexahistidine tag
HOBt	6-chloro-2-hydroxybenzotriazole
HPLC	High performance liquid chromatography
hSAFs	Hydrogelating self-assembling fibres
IGF1	Insulin-like growth factor 1
rIGF1	Recombinant IGF1
IVR	*In vitro* refolding
K_D	Dissociation constant
LB	Lysogeny broth
mal	Maleimide
MALDI-TOF-MS	Matrix-assisted laser desorption/ionisation time of flight mass spectrometry
MAP2	Microtubule associated protein 2
MEM	Medium essential medium
MOPS	3-(N-morpholino)propanesulfonic acid
MRE	Molar residual ellipticity
NaAsc	Sodium ascorbate
norb	Norbornene
NSC	Neural stem cell
dNTP	deoxynucleotide triphosphate
PAGE	Polyacrylamide gel electrophoresis
PBS	Phosphate buffered saline
PCN	Primary cortical neuron
PCA	Principal component analysis
PCR	Polymerase chain reaction
PDB	Protein data bank
PDMS	Polydimethylsiloxane
PEG	Polyethylene glycol
PEG_{2SH}	2,2-(ethylenedioxy)diethanethiol
PFA	Paraformaldehyde
PHN	Primary hippocampal neuron

PMSF	Phenylmethylsulfonyl fluoride
PN	Primary neuron
SAFs	Self-assembling fibres
SC-GFP	SpyCatcher-GFP
SC-GFP-IGF1	SpyCatcher-GFP-insulin-like growth factor 1
pSC-GFP-IGF1	Periplasmic tagged SC-GFP-IGF1
SDS	Sodium dodecyl sulfate
SEC	Size exclusion chromatography
SEM	Scanning electron microscopy
$shSAF_{W1,4}s$	Shifted hydrogelating self-assembling fibres
SPPS	Solid phase peptide synthesis
SPR	Surface plasmon resonance
SVM	Support-vector machine
TAMRA	5(6)-Carboxytetramethylrhodamine
TCEP	Tris(2-carboxyethyl)phosphine
TECC	Thiol-ene click chemistry
TEM	Transmission electron microscopy
TEMED	Tetramethylethylenediamine
TE-MTCC	Thiol-ene, maleimide-thiol click chemistry
TFA	Trifluoroacetic acid
TIPS	Triiosopropylsilane
Tm	Melting temperature
VEGF	Vascular endothelial growth factor

Amino acids

Alanine (Ala, A), Arginine (Arg, R), Asparagine (Asn, N), Aspartic acid (Asp, D), Cysteine (Cys, C), Glutamic acid (Glu, E), Glutamine (Gln, Q), Glycine (Gly, G), Histidine (His, H), Isoleucine (Ile, I), Leucine (Leu, L), Lysine (Lys, K), Methionine (Met, M), Phenylalanine (Phe, F), Proline (Pro, P), Serine (Ser, S), Threonine (Thr, T), Tryptophan (Trp, W), Tyrosine (Tyr, Y), Valine (Val, V).

Unnatural amino acids

Azidonorleucine (Kz), propargylglycine (pG), Alloc-Lysine (Kal).

Fatty acids

Butyric acid (But), hexanoic acid (Hex), octanoic acid (Oct), decanoic acid (Dec), dodecanoic acid (Dod), myristic acid (Myr), palmitic acid (Pal), stearic acid (Ste), oleic acid (Ole), palmitoleic acid (Pol), nervonic acid (Ner), linoleic acid (Lin), arachidonic acid (Ara).

Contents

List of Figures

List of Tables

Chapter 1

Introduction

1.1 *De novo* designed self-assembling peptides

De novo design of α-helical coiled coils

Natural proteins form an astonishing number of intricate and complex 3-dimensional shapes using only the information provided in their primary amino-acid sequences. While these tertiary and quaternary structures are diverse, proteins generally consist of well-defined secondary structural elements. The most common of these are the α helix and β strand. Our understanding of how these elements fold has enabled the rational and computational design of completely new peptide and protein structures from first principles (1, 2). Over the last few decades, so-called *de novo* protein design has yielded completely novel protein folds and assemblies, not seen in nature (1).

Nonetheless, the *de novo* design of peptides and proteins that fold to predefined structures determined by the designer is non-trivial (1). Its success relies on a firm understanding of the structural motif that one wishes to create (2). The α-helical coiled coil is one of the most abundant structural motifs in nature, with a very well-defined relationship between sequence and structure (2). Thus, the coiled coil has been one of the most fruitful targets for *de novo* protein design (3-6).

Coiled coils consist of two or more amphipathic α-helices that wrap around each other about a central hydrophobic core. Dimeric assemblies are common in nature (2). Here, hydrophobic (*h*) and polar (*p*) amino acids are spaced in a heptad repeat pattern of *hpphppp*. These repeats are named *abcdefg* (2). As

there are 3.6 residues per turn in an α helix, polar residues project out and away from the dimer interface, while hydrophobic residues project in, towards the central axis (Figure 1.1.1).

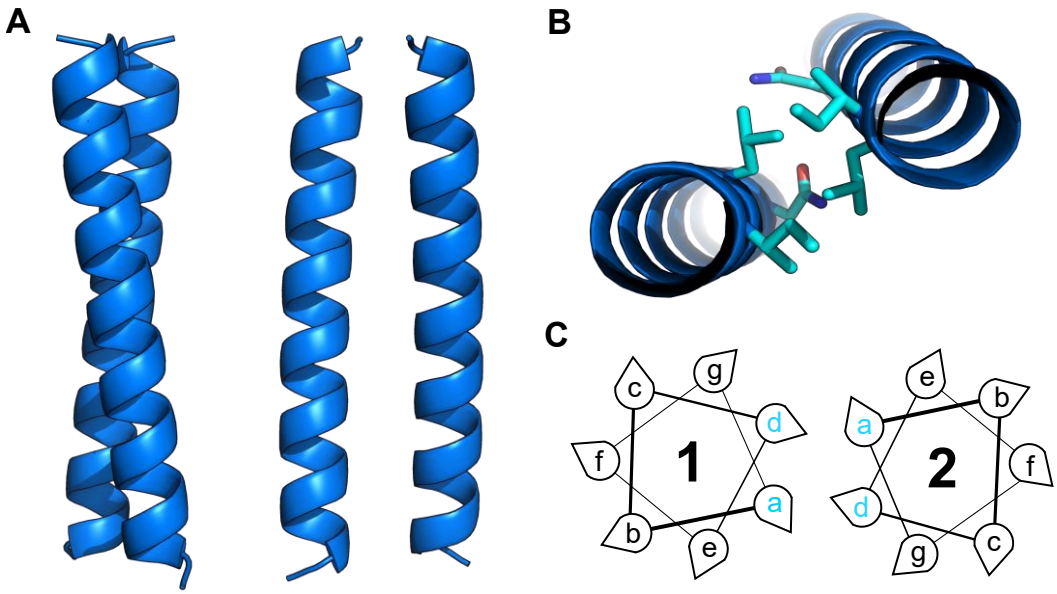

Figure 1.1.1: Dimeric coiled-coil structure. **A:** Crystal structure of CC-Di, a parallel homodimeric coiled coil designed by the Woolfson group (PDB code = 4DZM) (3). **B:** Cut through of a section of each helix, with *a* and *d* residues in the core highlighted (cyan). This shows a classic dimer interface: Ile at *a* and Leu at *d*. An Asn at *a* in a single heptad helps to specify dimer assembly. **C:** Helical wheel diagram showing the arrangement of polar (black) and hydrophobic (cyan) residues around each helix.

Examples of completely *de novo* designed homo and heterodimeric coiled coils are now relatively common (3, 7-9). Peptides that form trimeric and tetrameric coiled coils have also been designed (3, 4, 6), as well as pentamers, hexamers, heptamers and octamers (5, 6, 10, 11), which are extremely rare in natural protein structures. Thus, *de novo* design has allowed the creation of a range of coiled-coil assemblies that form predefined structures with astonishing precision (Figure 1.1.2). These novel peptides and proteins are beginning to be used as tools for applications away from the field of protein design. These include: scaffolds for tissue engineering and cell culture (12); artificial catalysts (13); receptors for ligand binding (14); protein-protein interaction domains within cells (15, 16); and capsid-like assemblies for drug delivery (17). The Woolfson group has been particularly instrumental in both the design and application of coiled-coil peptides.

In addition, non-coiled coil *de novo* designed peptide and protein assemblies are being similarly widely applied (18-20). These include computationally designed repeat proteins (21, 22), miniproteins (23), all

α (21), all β (19, 24) and mixed α/β proteins (25) (Figure 1.1.2). These designs are being used: as in-cell switchable systems for directing cellular processes (20); for virus-like particle assembly (26, 27); for the generation of novel fluorescent proteins (19); as catalysts (18); and as membrane proteins (28, 29). Therefore, the potential of protein design to create tools with real-world applications is beginning to be realised.

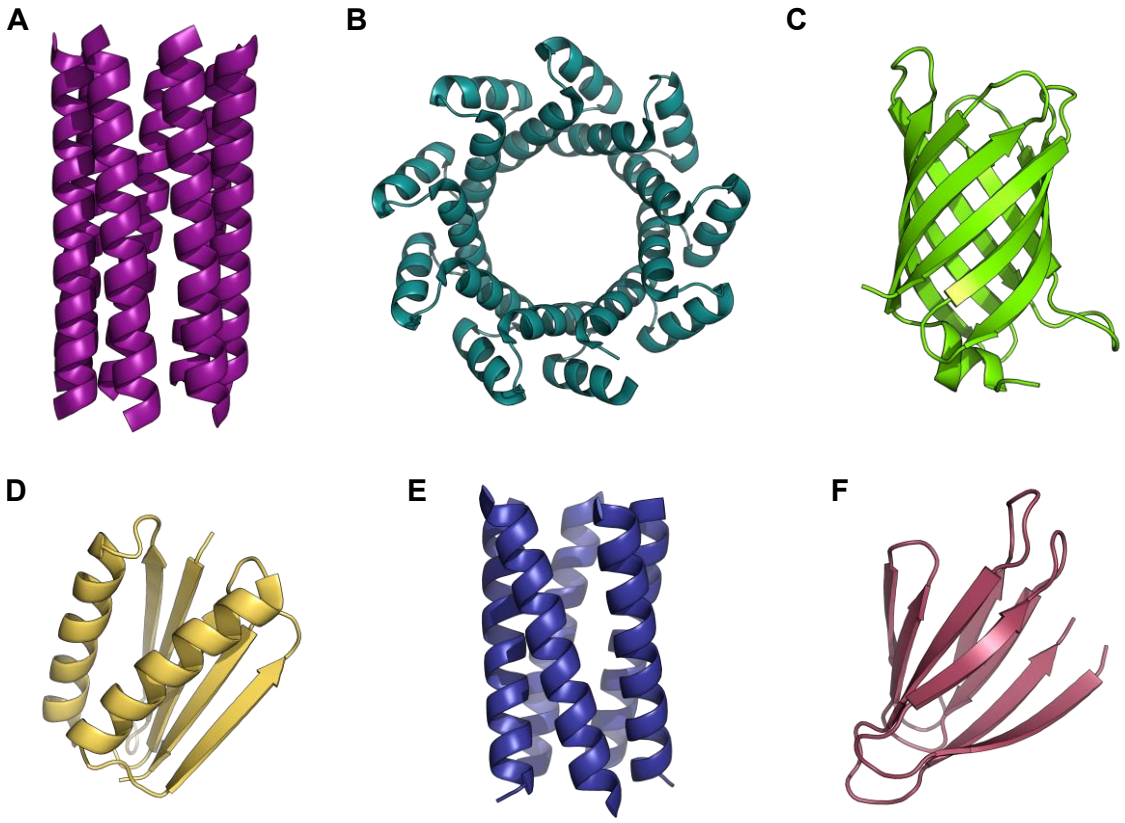

Figure 1.1.2: Examples of *de novo* designed peptides and proteins. **A:** CC-Hept, a heptameric coiled coil designed by the Woolfson group (PDB code = 4PNA) (5). **B:** An all-α toroid tandem repeat protein designed by the Baker group (PDB code = 4YXZ) (21). **C:** A β-barrel protein designed by the Baker group that binds the small-molecule DFHBI, resulting in green fluorescence (PDB code = 6D0T) (19). **D:** Top7, a 93-residue α/β protein designed by the Baker group (PDB code = 1QYS) (25). **E:** A pentameric transmembrane coiled-coil peptide designed by the DeGrado group (PDB code = 6MQ2) (30). **F:** An all-β jellyroll structure designed by the Baker group (PDB code = 6E5C) (24).

Self-assembly of higher order peptide structures

Nature uses the self-assembly of proteins into larger structures for a range of purposes, including: actin and tubulin oligomerisation in the cytoskeleton (31); collagen fibrillization in the extracellular matrix (ECM) (32); and viral capsid formation (33). Similarly, *de novo* design has yielded peptides and proteins

that self-assemble into larger structures. Among the most common of these are fibres (34, 35), nanotubes (36-38), cages (17, 39) and 2D arrays (40). For the rest of this section, I will focus on fibre and nanotube-forming peptides, as these are the most relevant to this work.

In 2000, Pandya et al. reported the design of a pair of α-helical peptides that self-assemble into 30 – 70 nm diameter fibrous structures, named self-assembling fibres (SAFs) (34) (Figure 1.1.3A). The two peptides (SAF-p1 and SAF-p2) form a heterodimeric coiled coil with an off-set interface, inferred by oppositely charged polar residues (Lys or Glu) at the *g* and *e* positions. This leads to patches of opposite charge along each of the four heptad α helices, such that heptads 3 and 4 of SAF-p1 pair with heptads 1 and 2 of SAF-p2, and *vice versa* (34, 41). Asn residues at *a* in the fourth and second heptad of SAF-p1 and SAF-p2, respectively, hydrogen bond. This helps to direct parallel heterodimers, rather than antiparallel homodimers (34). Assembly in this way leads to dimers with sticky ends for further heterodimers to associate. This drives the longitudinal self-assembly of dimers into fibres. Complementary charged residues at *b*, *c* and *f* are proposed to promote fibre-fibre interactions and lateral assembly of fibres into thick fibrils (42, 43).

Another example of coiled-coil peptide fibre self-assembly is the pentameric peptide fibres reported by Potekhin et al. (44). Here, assembly is proposed to proceed through the staggered helical arrangement of a single peptide in a pentameric arrangement, though the authors provided little structural information to support this. Coiled coils have also been designed to form nanotubes, which differ from fibres in that they contain a core region not occupied by peptide. The group of Conticello have modified the designed heptameric coiled coil, GCN4-pAA, so that it forms nanotubes (37). Here, the acetyl and amine caps (typically incorporated into peptides to increase stability) are removed from the peptide termini and oppositely charged residues are incorporated in the *N* and *C* terminal heptads. This leads to complementary electrostatic interactions between the *N* and *C* termini of GCN4-pAA and results in end-to-end self-assembly of the peptides into nanotubes (37). Inspired by this work, the Woolfson group have redesigned their discrete tetrameric, pentameric, hexameric and heptameric peptides to self-assemble into nanotubes (36) (Figure 1.1.3C). Like Conticello, they have achieved this by removing the acetyl and amine caps from the peptide termini, resulting in nanotubes with various morphologies.

In addition, Egelman et al. have redesigned two previously described coiled-coil peptides (45) to form large cylindrical assemblies (38).

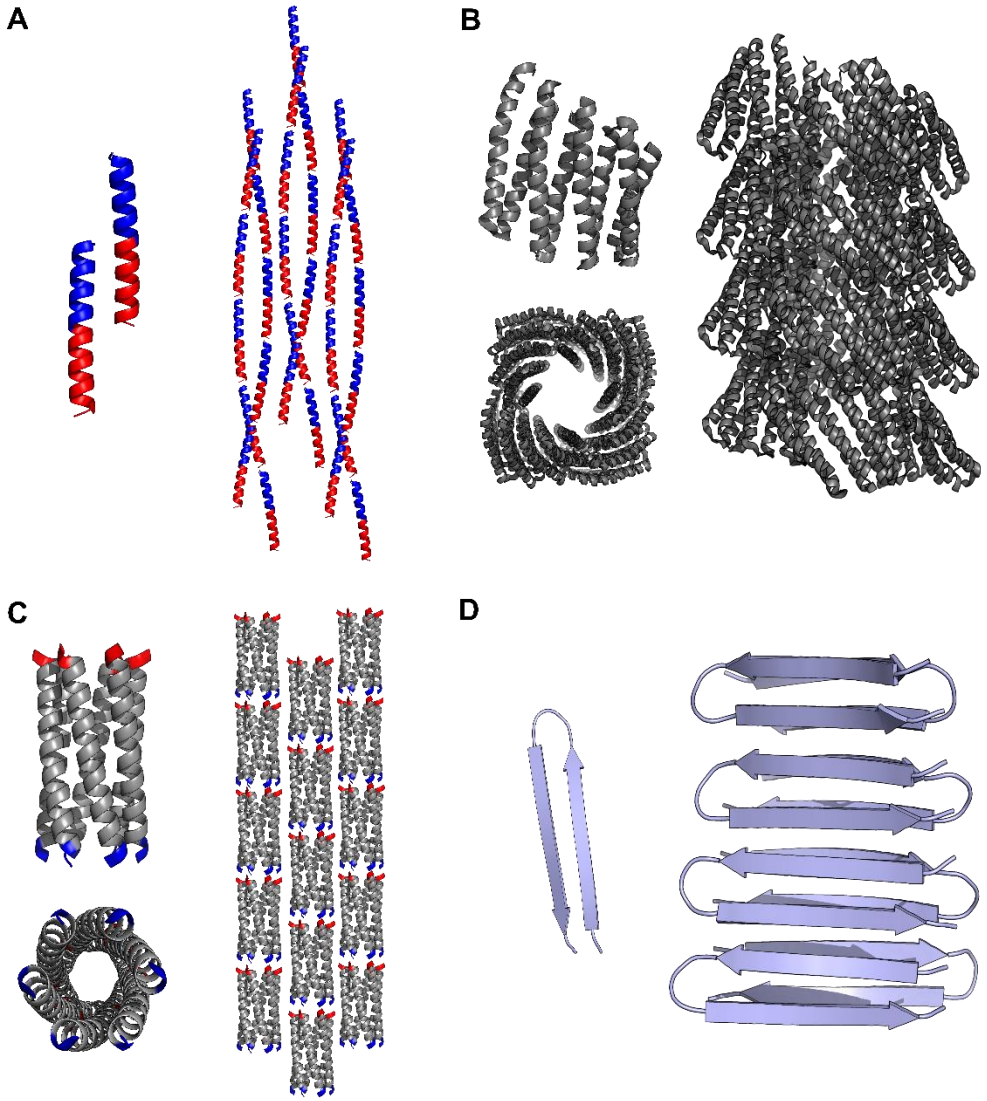

Figure 1.1.3: Examples of *de novo* designed self-assembling peptide systems. **A:** The SAFs designed by the Woolfson group. SAF-p1 and SAF-p2 form a heterodimeric coiled coil with oppositely charged sticky ends that drive fibre assembly (34). **B:** The Baker group DHF38 repeat protein and the cryo electron microscopy structure of a section of the nanotubes it forms (35) (PDB code = 6e9y). **C:** The nanotubes formed by uncapped CC-Hex (PDB code = 3R46), a hexameric coiled coil designed by the Woolfson group (36). **D:** Crystal structure of the MAX1 peptide designed by the Schneider group, accompanied by the crystal structure of a section of the fibres resulting from peptide self-assembly (46) (PDB code = 2n1e).

Coiled coils are by no means the only peptide motifs used for fibre self-assembly. Shen et al. have used *de novo* designed α-helical repeat proteins with computationally designed interfaces to generate fibres of varied diameter (35) (Figure 1.1.3B). In addition, many peptides have been designed that form

amyloid-like fibrils and nanotubes. Kaltofen et al. have described computationally designed amyloidogenic βαβ peptides (47), while the Schneider group rationally designed amyloid-forming peptides termed MAX (48) (Figure 1.1.3D). Amyloid-like structures have also been formed from a large number of short aromatic peptide sequences (49, 50). While some of these cannot strictly be regarded as 'designed' – owing to their extremely short sequences – their simplicity demonstrates the propensity of peptides to self-assemble.

Another class of self-assembling peptide are amphiphilic peptides. These typically consist of a hydrophillic head group – comprising polar amino acids – and a hydrophobic tail – comprising either hydrophobic amino acids or an alkyl chain. The Zhang group have designed surfactant-like peptides A_6D, V_6D, A_6D_2 and L_6D_2 that form nanotubes (51), while Stupp's group have reported the formation of fibrils with controllable geometry from tetrameric peptides with alkyl tails (52, 53). Alternatively, amphiphilic peptides can be designed by alternating polar and hydrophobic residues, yielding peptides that form β-structure (48, 54). For example, the Hartgerink group have designed multidomain peptides consisting of charged terminal residues separated by an amphiphilic region, comprising alternating hydrophobic and hydrophilic amino acids (55). These peptides form β-strand assemblies and fibrous structures. Other notable examples are the aforementioned MAX peptides designed by Schneider and colleagues (48) and the RAD_{16} and EAK_{16} peptides designed by Zhang's group (56), both of which are covered in more detail in Chapter 1.3.

Many of these self-assembling fibrous and nanotube systems have been used as novel biomaterials for a range of purposes. Among the most common are cytoscaffolds for tissue engineering and cell culture, with which Chapters 1 – 5 of this thesis are concerned.

1.2: Biomaterials for cell culture and tissue engineering

The extracellular matrix (ECM)

The ECM is a gel-like mix of proteins, proteoglycans and polysaccharides that surrounds cells, maintaining tissue structure, supporting cell growth, and directing cell signalling (57) (Figure 1.2.1).

Generally speaking, it can be thought of as containing three principle components: structural molecules, which maintain tissue structure and support inhabiting cells; adhesion molecules, which form a physical link between the ECM and encapsulated cells; and other signalling molecules, such as growth factors, of which there are many with myriad purposes in different tissues (57). Structural molecules include fibrous proteins, such as collagens, as well as polysaccharides like hyaluronic acid (HA) (57). Common adhesion molecules include laminin and fibronectin (58). These contact transmembrane receptors at the cell surface, known as integrins, triggering downstream signalling cascades that direct cytoskeletal remodelling and changes in cellular morphology, motility and growth (59). Additional signalling molecules are often associated with the ECM. For example, many growth factors are physically bound to heparan sulphate proteoglycans, which are thought to act as a sink to concentrate these signalling molecules at particular locations (60-62).

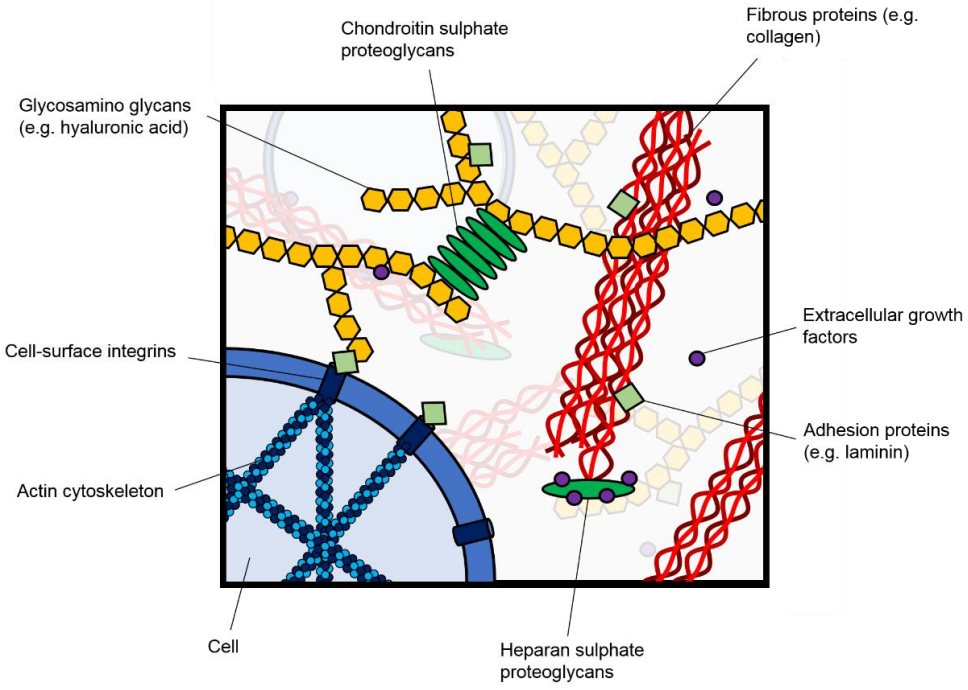

Figure 1.2.1: Schematic diagram showing the primary molecular components of the ECM and their interactions.

ECM molecular makeup and gross architecture varies between tissue types

The molecular makeup of the ECM varies significantly between tissue types – and in some cases disease states – leading to gross differences in tissue properties (63). For example, skeletal muscle is highly organised and contains a high level of fibrous proteins, such as collagens I-III and elastin (64). In

contrast, brain tissue has a low content of fibrous protein and instead contains high levels of HA (65). These molecular differences result in large differences in overall tissue properties: muscle tissue is relatively rigid, with a high tensile strength, while brain tissue is relatively soft (63).

The elasticity of a particular tissue is measured by its elastic modulus, which is a measure of the resistance to deformation (or stiffness) of a material (measured in Pascals (Pa)) (63, 66). Bone, for example, is rigid and very resistant to deformation. Therefore, it possesses a much higher elastic modulus than muscle tissue, which in turn has an elastic modulus greater than brain tissue (Figure 1.2.2) (63, 66, 67).

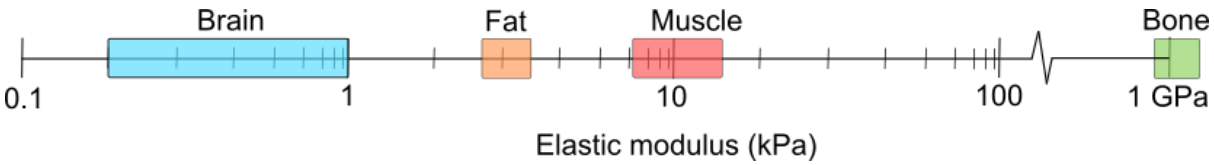

Figure 1.2.2: Diagram showing how elastic modulus varies between tissue types (66, 68).

Neural tissue – encompassing both the central nervous system (CNS) and neural tracts of the peripheral nervous system – is some of the softest tissue in the mammalian body. It is generally considered to range in elastic modulus from 0.1 – 1 kPa (69-71). The principle structural components of brain tissue are glycosaminoglycans (GAGs), of which HA is the most abundant (65). HA is composed of repeating disaccharide units of N-acetylglucosamine and N-glucoronic acid that can reach up to 25,000 repeating units in length (72). HA binds many ECM-constituent proteoglycans (72, 73), such as heparan sulphate proteoglycans, which bind to growth factors containing heparan binding motifs (*e.g.* basic fibroblast growth factor (bFGF) and the hedgehog proteins) (60, 62). This facilitates binding of these proteins to their receptors and establishes growth factor gradients required for tissue patterning (60). Finally, chondroitin sulphate proteoglycans are a further family of brain-constituent proteoglycans that cross-link the ECM structure and contribute to the overall elasticity of brain tissue (74, 75).

Hydrogels can be used to model the ECM *in vitro*

Given the relative complexity of the ECM, its interaction with cells and variation between tissue types, it is surprising that most *in vitro* cell culture is performed in a monolayer culture on plastic or glass. These inert, 2-dimensional and rigid environments do not reflect the ECM *in vivo* (76). Certain cell

types behave completely differently in monolayer culture. The classic example is chondrocytes, which dedifferentiate and divide aberrantly when cultured on plastic or glass (77). Therefore, efforts have been made to design materials that more accurately model the ECM. Hydrogels are self-supporting, porous, gel-like materials that have a high water content. This allows solutes to pass freely through their 3D structure. These properties are analogous to the ECM and make hydrogels ideally suited for supporting cell growth *in vitro* (78). In the seminal study by Benya and Shaffer, chondrocytes regained their differentiated phenotype when cultured in an agarose gel (77). Many mammalian cells (*e.g.* neurons, adipocytes, cancer cell lines and muscle cells) have now been shown to behave aberrantly in 2D compared with 3D (*i.e.* within hydrogels) culture (78-80).

The number of different hydrogels used as cytoscaffolds for cell culture is vast. However, generally these materials can be separated into those composed of naturally occurring ECM components, and those that are synthetic (80). These each have their own advantages and disadvantages that will be outlined in the following sections.

Naturally occurring ECM mimics

Initial efforts to mimic the ECM *in vitro* utilised gels formed from whole-ECM extracts. For example, tumour basement membrane was isolated from Engelbreth-Holm-Swarm (EHS) tumour cells and shown to support cell growth (81). Owing to their ease of production and compatibility with diverse cell types, these extracts are now marketed as *in vitro* cell culture tools (*e.g.* Matrigel™) and widely used by the scientific community (82-86).

More commonly, specific ECM components are isolated that form hydrogels *in vitro*. Contributing 25% of the dry mammalian protein mass, collagen is the most abundant of the ECM constituents (31). Collagen fibres consist of three polyproline type II helices that wrap around each other, forming a rope-like structure with high tensile strength (87) (Figure 1.2.3C). Collagen can be relatively easily extracted from various tissue types and organisms and, therefore, numerous studies have utilised collagen gels for culturing various cell types (88, 89). The abundance of collagen *in vivo* also make it an ideal vehicle for cell transplantation and collagen-based materials have been widely utilised for tissue engineering purposes (90). Collagen-based materials are FDA-approved for wound healing applications (91).

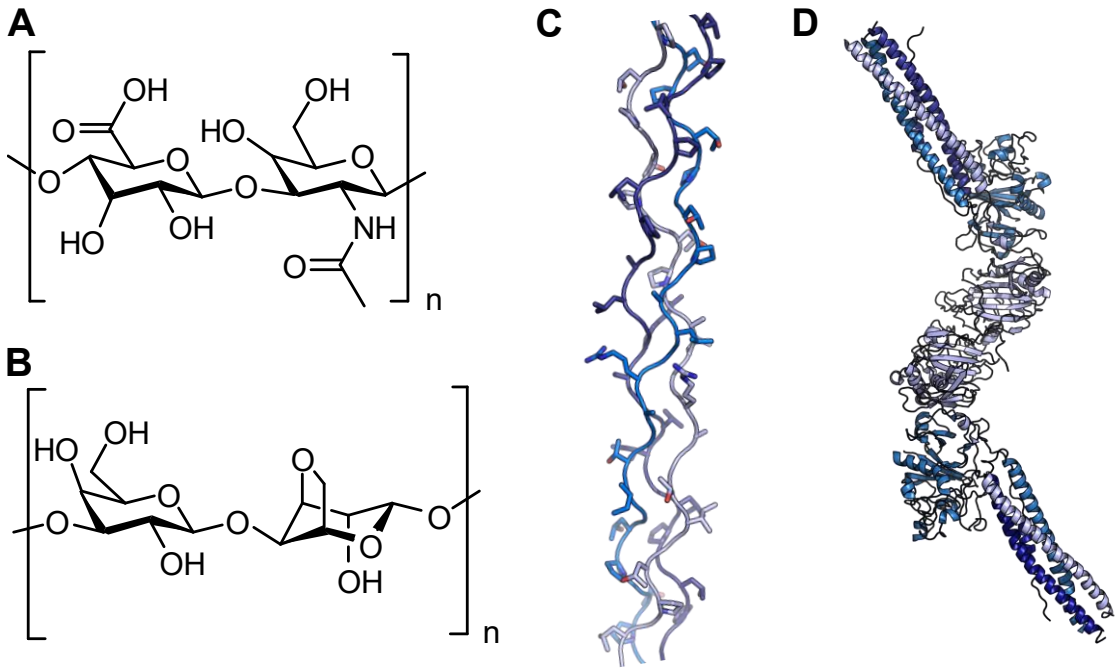

Figure 1.2.3: Examples of naturally occurring ECM components used for cytoscaffold generation. **A:** The N-acetylglucosamine, N-glucoronic acid repeating unit of HA. **B:** The D-galactose, 3,6-anhydro-L-galactopyranose repeating unit of agarose. **C:** Crystal structure of the collagen triple helix (92) (PDB code = 1BKV). **D:** Crystal structure of a fibrin dimeric unit (93) (PDB code = 1N73).

HA has also served as an attractive building block with which to form cytoscaffolds. Unlike collagen, HA polymers typically require additional cross-linking for gelation (94). This provides the user with greater control over the gelling process. Variants of HA have been synthesised, incorporating different chemical groups into the disaccharide unit (95-97). In doing this, the mechanism of cross-linking can be controlled and additional chemical groups can be introduced to tune the growth of encapsulated cells (95, 96, 98, 99). Other notable examples of naturally occurring ECM-mimicking materials include fibrin (Figure 1.3.3D), agarose (Figure 1.3.3B) and alginate (77, 100-103).

Utilising natural ECM components for cytoscaffold formation has distinct advantages. These systems most closely mimic the ECM *in vivo* and often contain naturally occurring growth factors and adhesion molecules that provide support to cultured cells (76). These natural ECM components often gel without the addition of gelling agents or further engineering (76). However, there are disadvantages to using these natural systems. First, the makeup of these gels is inherently complex and can suffer from batch-to-batch variation (76). For example, basement membrane extracts contain numerous ECM components, the relative concentrations of which are difficult to determine and vary between

preparations (85). Second, components of these gels are often difficult to modify in order to tune gel elastic modulus or introduce additional chemical ligands (91) (certain natural polysaccharides, such as HA, are notable exceptions to this). Third, the presence of extracellular growth factors and other ECM components cannot be easily manipulated (91). Synthetic alternatives have been investigated to overcome these disadvantages.

Synthetic polymer ECM-mimicking materials

The principle advantage of using synthetic ECM-mimicking hydrogels is the ability to construct the material from the bottom-up. The user has control over the starting material, mechanism of gelation, and can tune the mechanical and chemical properties with relative ease (91). Therefore, a range of synthetic materials have been used for cytoscaffold generation. The two primary groups are synthetic polymer and self-assembling peptide hydrogels.

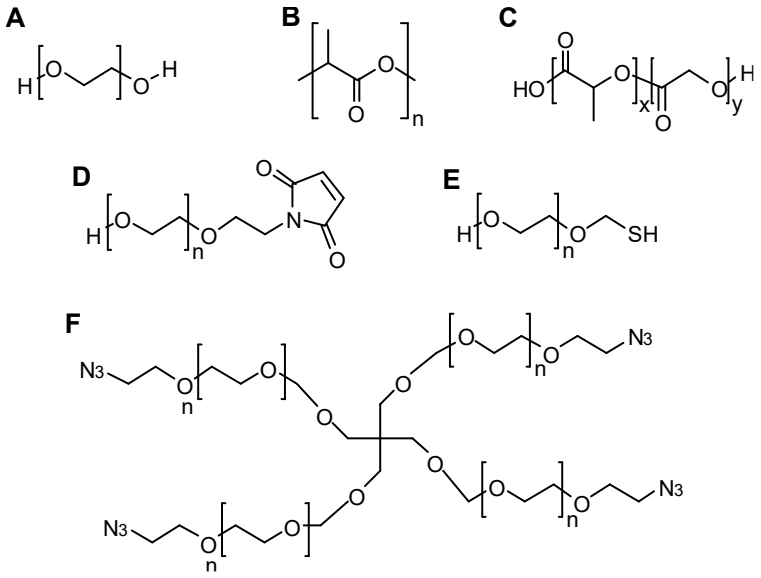

Figure 1.2.4: Common synthetic polymer building blocks used for cytoscaffold generation: Polyethylene glycol **(A)**, polylactic acid **(B)**, poly(lactic-co-glycolic acid) **(C)**, PEG-maleimide **(D)**, PEG-thiol **(E)** and 4-arm PEG-azide **(F)**.

Synthetic polymers consist of repeating units of synthetic monomeric building blocks, of which polyethylene glycol (PEG), polyacrylamide, polylactic acid (PLA), poly(lactic-co-glycolic acid) (PLGA) and poly-N-isopropylacrylamide (PNIPAAm) are some of the most common (104) (Figure 1.2.4). Generally, these are crosslinked to trigger the gelling process (80, 104). As they lack cell-recognising motifs (105), these polymers provide the perfect starting material upon which to build

a cell-supporting scaffold from the bottom-up. In addition, they are highly modifiable and a range of different polymer types – functionalised with various chemical groups – are commercially available (Figure 1.3.4). As such, synthetic polymers have been extensively utilised as cytoscaffolds for a range of cell types (106-111) and some are FDA approved as scaffolds for tissue engineering (104). Composite gels incorporating both synthetic polymer and natural ECM constituents have also been developed (112, 113). These provide the user with an additional level of control and combine the benefits of working with synthetic and natural systems.

1.3 Biomaterials from self-assembling peptides and proteins

Peptides and proteins possess properties that make them ideally suited to biomaterial generation. First, chemical additives are often not required for the self-assembly process to occur. Second, the biological nature of the molecules involved means that self-assembling structures can be formed within cells for particular applications (114). Third, the inherent variety of the amino acid building blocks (20 natural and many more unnatural residues) means that a variety of structures can be formed with unique properties. Finally, peptide self-assembly is largely driven by relatively weak non-covalent interactions – hydrogen bonds, hydrophobic contacts, salt bridges and van der Waals forces – meaning these systems have the potential to be reversible and dynamic (115). Thus, self-assembling peptides and proteins have been exploited for biomaterial generation.

Biomaterials from engineered natural proteins

Natural and engineered self-assembling proteins have been used to generate novel biomaterials. *E coli* secrete the 13 kDa protein CsgA, which self-assembles into amyloid fibres known as curli pili. These form a key component of *E. coli* biofilms (116). CsgA has been used as a building block for the formation of tuneable biomaterials (116). As it is bacterially expressed, CsgA has been engineered to incorporate various peptide tags to tune fibre assembly and incorporate proteins into the structure (117, 118).

Y. pestis produce the ~15 kDa immunoglobulin-like fold protein capsular antigen fraction 1 (Caf1), which self-assembles into fibres through non-covalent interactions (119). These fibres form a hydrogel that surrounds the bacterium and protects it from phagocytosis by host immune cells (120). Caf1 can be bacterially expressed and so is amenable to engineering. Roque et al. have engineered Caf1 fibres to allow crosslinking with PEG, leading to hydrogel formation (121) (Figure 1.3.1A). The group incorporated bioactive peptide ligands into the Caf1 protein, allowing these hydrogels to be used for mammalian cell culture (121, 122). In addition, by varying the protein concentration and using different PEG crosslinkers, the elastic modulus of these gels can be varied between ~10 – 2300 Pa, rendering them suitable for a range of cell types (123).

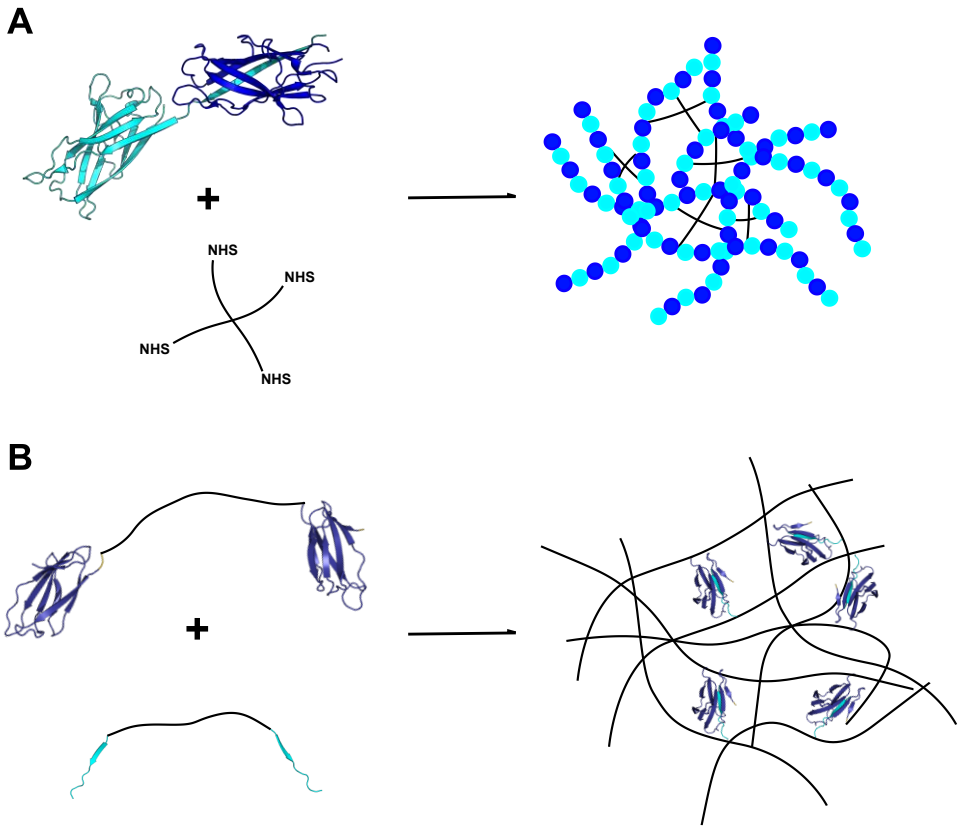

Figure 1.3.1: Engineered self-assembling protein systems. **A:** Crystal structure of the Caf1 dimer (blue, cyan) that forms a fibrous scaffold (blue and cyan dots). This scaffold can be stabilised with a 4-arm PEG-NHS crosslinker to form a scaffold (PDB code = 1P5U (124)) Adapted from (121, 123). **B:** SpyTag- and SpyCatcher-containing fusion proteins form a self-supporting hydrogel *via* the covalent interaction between SpyTag and SpyCatcher. Adapted from (125) (PDB code = 4MLI).

Other groups have utilised proteins that do not normally form fibres as the basis for novel biomaterials (125, 126). For example, hydrogels have been based on the SpyTag-SpyCatcher system reported by

Howarth and colleagues (125, 127) (Figure 1.3.1B). Sun et al. have expressed SpyTag and SpyCatcher (a peptide and protein that form a covalent complex *via* an isopeptide bond) modules in *E. coli* that form a hydrogel with an elastic modulus of ~300 Pa when mixed (125). Owing to the bacterial expression of these modules, bioactive peptides and proteins can be incorporated to promote mammalian cell growth (125).

Biomaterials from designed peptides

As eluded to in Section 1.1, our ability to design peptides with predefined structures has led to the design of novel materials from *de novo* designed peptides (Table 1.3.1). Two of the first examples of fully synthetic self-assembling peptide hydrogels are the RAD_{16} and EAK_{16} peptides designed by Zhang and co-workers (54, 56). These peptides consist of alternating hydrophobic and polar amino acids that form β-strand assemblies in aqueous solution. Upon the addition of monovalent cations present in most buffers and cell culture medium, these fibres form a self-supporting hydrogel. These matrices support the attachment of a variety of cell types (54, 56) and are now marketed commercially, as Puramatrix, for cell culture purposes.

Name	**Sequence**	**α/β**	**Ref.**
RAD_{16}	RARADADA RARADADA	β	(56)
EAK_{16}	AEAEAKAK AEAEAKAK	β	(56)
MAX1	VKVKVKVKV^{D}PPTKVKVKVKV	β	(48)
-	K_2(TL)$_6K_2$	β	(128)
-	Fmoc-FF	β	(129)
-	KYF	β	(130)
-	$K_{160}V_{40}$	-	(131)
-	(15C alk)-CCCCGGGS(Ph)RGD	-	(132)
hSAF-p1	KIAALKA KIAALKA EIAALEW ENAALEA	α	(12)

Table 1.3.1: Examples of hydrogel-forming designed peptides. 15C alk indicates a 15-carbon alkyl chain.

A similar approach has been taken by Schneider and co-workers to design the MAX peptides. These contain alternating Lys and Val residues that also form β-structured assemblies in solution (48, 133). Alterations to the peptide sequence (yielding MAX1 – 8) allow the elastic modulus of MAX peptide gels to be tuned (133). These gels support the growth of mammalian cells (133).

Peptide amphiphiles are also used to generate hydrogels. For example, Nowak et al. have synthesised various peptide sequences containing long stretches of polar (Lys or Glu) followed by hydrophobic (Leu or Val) residues (131). These form soft gels (1 – 200 Pa) with either β-sheet or α-helical structure, depending on the sequence. Peptides with alkyl tails, designed by Stupp and co-workers, also form hydrogels (132). Recently, the group have described the co-assembly of these peptides with DNA to form intricate twisted ribbon structures and scaffolds that support astrocyte growth (134). Similarly, the self-assembling amphiphilic peptides designed by the Hartgerink group can be either covalently or non-covalently crosslinked to form hydrogels (135). The group have demonstrated that stem cell proliferation is promoted on gels comprised of certain amphiphilic sequences (*e.g.* $K_2(SL)_6K_2$GRGDS), but not others (*e.g.* $K_2(TL)_6K_2$GRGDS) (128).

A great deal of attention has been given to shorter peptide sequences that self-assemble, often into amyloid-like fibrils. These consist of two or three amino acids, often with the addition of an *N*-terminal protecting group, such as a fluorenylmethyloxycarbonyl (Fmoc) (49, 50, 129, 130, 136). For example, the Xu group have designed a series of Fmoc-dipeptides (e.g. Fmoc-^{D}Ala-^{D}Ala and Fmoc-Gly-Gly) that form gels at different peptide concentrations, pH values and in response to the addition of vancomycin (137). These sequences have distinct advantages compared to longer peptides like RAD_{16} with regard to synthesis. However, the mechanism by which they self-assemble is often difficult to determine and identifying which sequences will form hydrogels is largely serendipitous. The Ulijn group have described a combination of computational and experimental approaches to address these issues and used these to predict optimum tripeptide sequences for self-assembly and hydrogel formation (130).

These gels have been utilised for cell culture. Zhou et al. combined Fmoc-FF and Fmoc-RGD to form a gel that promoted human adult dermal fibroblast growth (138). Similarly, the Ulijn group demonstrated differential chondrocyte responses to different hydrophobic Fmoc-dipeptide sequences

(129). Chronopoulou et al. have demonstrated that microglial cell growth and proliferation is promoted by encapsulation within an Fmoc-FFF gel (139). While the number of different sequence permutations are vast (49, 50, 129, 137-139), it should be noted that – in relation to cell culture – such gels are not typically taken past the early stages of initial characterisation and demonstrating cell growth.

Hydrogelating self-assembling fibres (hSAFs)

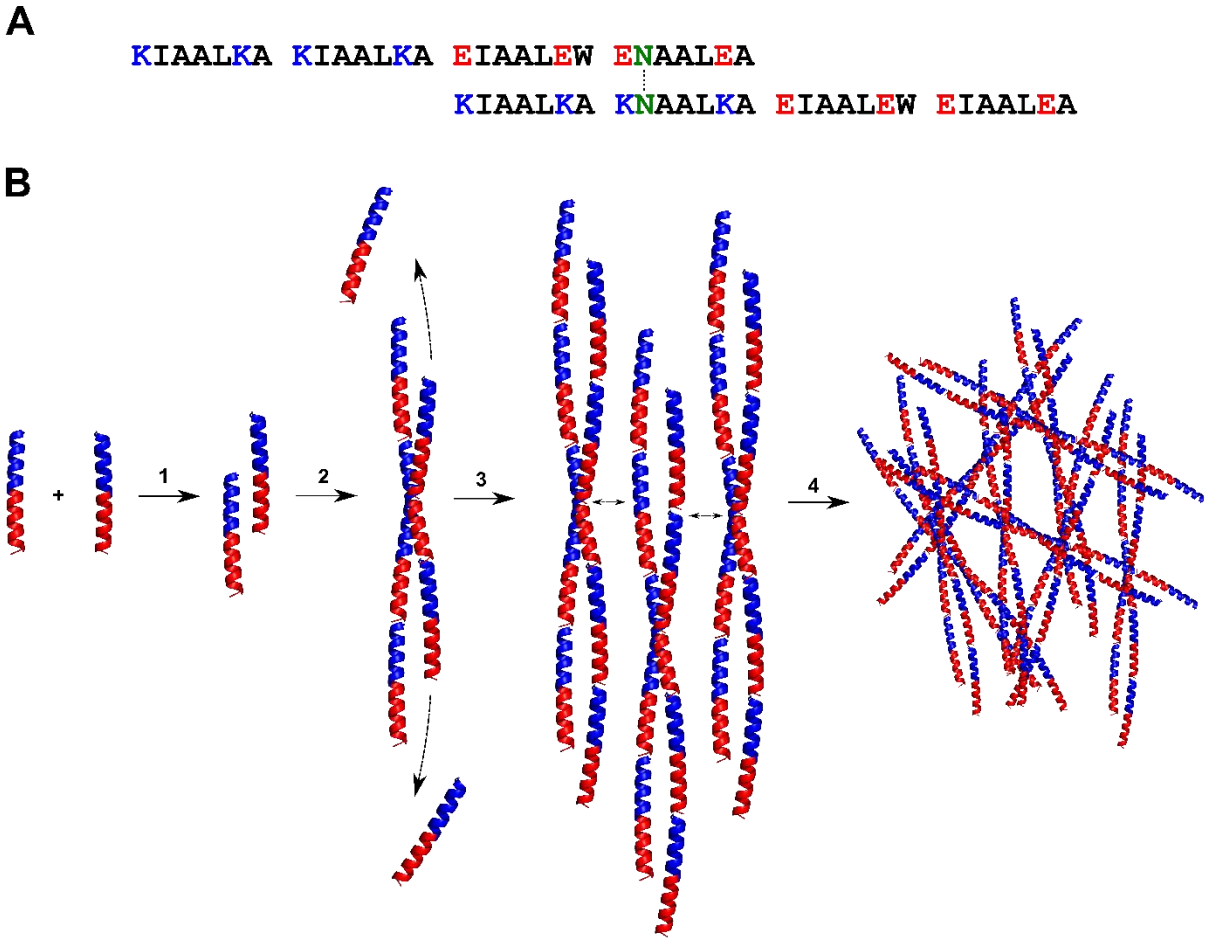

Figure 1.3.2: hSAF self-assembly. **A:** hSAF peptide sequences showing offset heterodimer assembly, directed by salt bridges between oppositely charged Glu and Lys residues, and a hydrogen bond (dotted line) between Asn residues. **B:** Schematic diagram of hSAF gel assembly. **1:** Heterodimeric peptide self-assembly. **2:** Longitudinal assembly of dimers into fibres *via* the recruitment of further peptides. **3:** Lateral assembly of fibres into thicker fibrils. **4:** Entangling of fibrils to form an interconnected network. Adapted from (12, 34).

The SAF system (described in Section 1.1) developed by the Woolfson group has been redesigned to form hydrogels (Figure 1.3.2). Here, the sticky end longitudinal assembly principle of the SAFs is retained, but the charged residues at the *b*, *c* and *f* positions are replaced with Ala. This weakens interactions between fibres and designs towards the formation of a fibrous network, rather than the thick

crystalline fibres of the SAFs. This new system is termed hydrogelating self-assembling fibres (hSAFs) and the new peptides are named hSAF-p1 and hSAF-p2.

These peptides give rise to narrower (~13±5 nm diameter) fibrils and the formation of a hydrogel with an elastic modulus of ~1 kPa, around the upper reported limit for brain tissue (Figure 1.2.2) (12, 140). Gel formation occurs in minutes under ambient conditions in MOPS buffer (pH 7.4). hSAFs support the growth of PC12 cells (a neuron-like neuroblastoma cell line) (12) and NSCs (141).

Dexter et al. have also formed hydrogels from 3-heptad designed coiled-coil peptides that form fibrils (142). These gels have an elastic modulus of ~200 Pa and support the growth of NIH-3T3 fibroblast cells. The group hypothesise that these sequences form pentameric assemblies, however, they are unable to confirm this (142). This system remains considerably less developed than hSAFs.

1.4 Tuning scaffold properties for specific applications

In recent years, further complexity has been introduced into synthetic (and some natural polymer) cytoscaffolds. These modifications are generally made with the aim of promoting cell attachment and growth on the scaffold, tailoring the gel to a specific cell type, or directing cell behaviour in a way that models a particular system or process. The ability to make such user-defined modifications is arguably the principle advantage of working with these minimal systems.

Our ability to modify cytoscaffolds with increasing ease is due, in part, to the development of click chemistry. This refers to a number of chemical reactions that proceed under ambient conditions – without the need for excessive changes in temperature and pH – in aqueous solution (143). Key examples include Cu^{2+}-catalysed azide-alkyne cycloaddition (CuAAC) (144), strain-promoted azide-alkyne cyloaddition (SPAAC) (145), thiol-ene (146) and maleimide-thiol reaction (147) (Figure 1.4.1). Owing to their versatility and compatibility with biological systems (143), many of the examples outlined in this section utilise click chemistries to tune cytoscaffold properties.

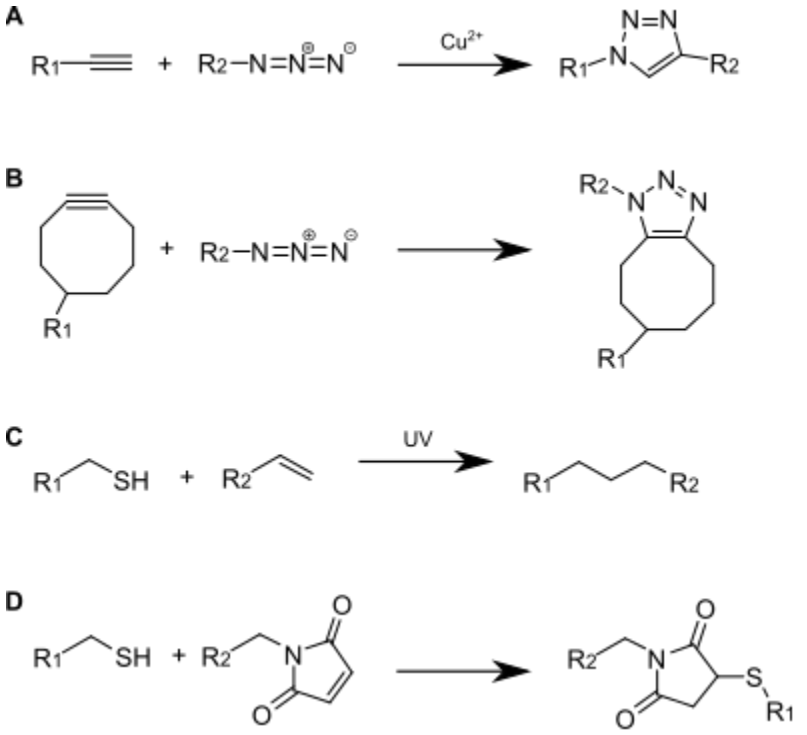

Figure 1.4.1: Common click chemistries used for modifying biomaterials. **A:** Cu^{2+}-catalysed azide-alkyne cycloaddition (CuAAC). **B:** Strain-promoted azide-alkyne cycloaddition (SPAAC). **C:** The photo-activated thiol-ene reaction. **D:** Maleimide-thiol reaction.

Chemical modification with cell adhesion peptides

The most common scaffold modification is the introduction of adhesive ligands that promote cell attachment. Several bioactive amino-acid sequences have been identified in ECM-resident adhesion proteins that are typically incorporated into cytoscaffolds (148). These shorter peptides are easier to synthesise compared to their full-length protein counterparts. The most common of these, RGDS, is an abundant motif found in both fibronectin and laminin that binds various cell surface integrins (148). This results in the activation of downstream integrin-related signalling pathways that are linked to cell migration, differentiation, proliferation and spreading (149). Other sequences include IKVAV and YIGSR, both derived from laminin (150). These peptides have been incorporated into synthetic scaffolds to promote cell attachment, proliferation, differentiation and direct cell growth (107, 125, 132, 140, 151-158).

Adhesion peptides are introduced *via* a range of chemical modification strategies, including: Click chemistries (97, 140, 159), affinity peptide interaction (160), and direct incorporation into the

scaffolding molecule (125, 132, 157). The level of peptide incorporation into the scaffold is often under the user's control, allowing cell responses to differing adhesion peptide concentrations to be investigated (97, 140, 161).

By replacing the *N*-terminal Lys of hSAF-p1 with the unnatural amino acid azidonorleucine, Mehrban et al. have incorporated an alkyne-modified RGDS into hSAFs *via* CuAAC (140). This peptide promoted PC12 cell and neural stem cell (NSC) adhesion and proliferation on hSAFs (140, 141). Furthermore, when exposed to an interface between undecorated and RGDS-decorated gel, NSCs migrated towards areas of RGDS (141).

Tuning gel elastic modulus

Modifications to hydrogel elastic modulus allow materials to be formed that mimic different tissue types and, thus, allow specific cell niches to be modelled. The elastic moduli of both peptide and polymer gels have been modified extensively. The most common strategy is to alter the concentration of peptide, polymer or crosslinking agent during gelation (102, 108, 154, 162). Gels with a lower concentration of these components are generally softer – owing to fewer interactions between neighbouring fibres – than those with a higher concentration (102, 108, 154, 162).

As self-assembling peptide hydrogels are normally held together through non-covalent interactions between side chains, their elastic modulus can also be altered through changes to the peptide sequence. For example, by mutating a single Lys residue to Glu in MAX1, Haines-Butterick et al. have increased the elastic modulus of the gel from ~40 Pa to >100 Pa (133). Anderson et al. have altered the peptidic head group of peptide amphiphiles to generate gels between 1 – 150 Pa (163). Similarly, the Hartgerink group have investigated how changing the sequences of their amphiphilic peptides alters the elastic modulus of the resulting hydrogel (135). By varying both the peptide sequence and constituents of the buffer (Salt and Mg^{2+}), the group formed hydrogels ranging from 10 – 6100 kPa (135).

There are also studies where scaffold stiffness and adhesion peptide content are varied independently of one another (97, 154, 159). DeForest et al. have varied the elastic modulus of PEG hydrogels between 1 – 6 kPa by altering the concentration of azide crosslinker included in the scaffold (159). The group

can then vary the exposure of the gel to UV light, which is required for introduction of RGDS *via* the thiol-ene reaction. Hogrebe et al. have independently varied the stiffness (0.5 – 3 kPa) and adhesive capacity of KFE-repeat peptides through altering the peptide concentration and percentage inclusion of RGDS in the sequence, respectively (154).

Incorporating growth factors

Growth factors are extracellular signalling proteins that perform diverse functions, including influencing cell growth, differentiation, proliferation and migration (164-171). In addition, growth factors direct tissue maintenance and protect cells from damage and disease (168, 172, 173). Common growth factors that carry out these functions in the nervous system (collectively known as neurotrophic factors) include: the neurotrophins (brain derived neurotrophic factor (BDNF) (164, 174), nerve growth factor (NGF) and neurotrophin 1-4) (175), insulin-like growth factors (IGFs) (176-180), fibroblast growth factors (FGFs) (181), vascular endothelial growth factor (VEGF) (171), ciliary neurotrophic factor (CNTF) (165) and sonic hedgehog (shh) (170) (Figure 1.4.2).

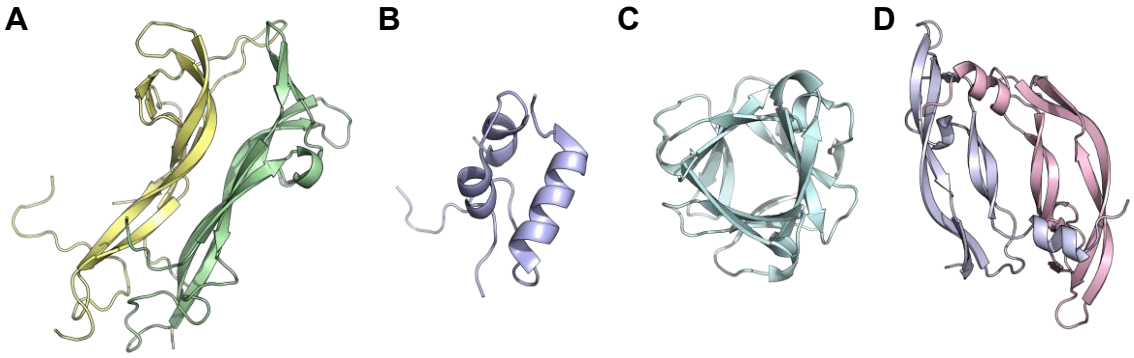

Figure 1.4.2: Examples of common extracellular growth factors that have been incorporated into ECM mimics: BDNF (PDB code: 1B8M) **(A)**, IGF1 (PDB code: 1IMX) **(B)**, bFGF (PDB code: 1BFB) **(C)** and VEGF PDB code: 2VPF) **(D)**.

Hydrogels have been either covalently modified with, or used to passively encapsulate, full-length neurotrophic factors to promote the growth of neurons and other cell types (182, 183). For example, Yamaguchi et al. have passively incorporated VEGF into PEG hydrogels to promote the proliferation of porcine aortic endothelial cells (184). Wylie et al. reported two different affinity tag-based methods to independently covalently modify agarose gels with CNTF and shh (185). The group use a photolabile chemical group to allow spatiotemporal patterning of the gel with the two growth factors. Parker et al.

use Src-homology 3 (SH3) domain binding peptides, covalently attached to a HA-methylcellulose composite gel, to incorporate an SH3-IGF1 fusion protein into the scaffold (186). In this system, IGF1 is shown to promote retinal pigment epithelium cell viability.

Passive encapsulation of growth factors is another common strategy. This enables slow release of the growth factor into the cell culture medium over time, thus, lengthening the exposure time of encapsulated cells (183). However, this strategy does not allow spatial patterning of the gel with the protein. Bruggeman et al. have modified BDNF and GDNF with the polysaccharide chitosan to promote electrostatic interactions between the growth factors and an Fmoc-DDIKVAV peptide hydrogel (187). This allowed the growth factors to be released from the gel over longer periods. Similarly, Galler et al. have non-covalently incorporated heparin into an amphiphilic peptide gel, allowing FGF-2 and transforming growth factor β (TGF-β) to be incorporated *via* heparin binding (188). Dental pulp cell proliferation was promoted by slow release of these growth factors from the gel.

Spatially patterning hydrogels to direct cell behaviour

In vivo, precise arrangements of extracellular growth cues and structural ECM components lead to chemical and physical patterns that shape cell growth and result in correct tissue formation (189-191). In the context of neural tissue, these patterns direct axonal outgrowth, cell migration, neurogenesis and differentiation during nervous system development and in adult tissues (192-194). Therefore, cellular patterning in this way is essential for correct formation of the nervous system.

Soft lithography, microcontact printing and microfluidics have been used to recreate these patterns in synthetic and natural polymer hydrogels (97, 185, 195-199). In addition, through 3D bioprinting, researchers have had success in building tissue-like architectures of defined shape and size (200-202). These techniques allow tissue mimics to be formed with increased complexity. For example, Armstrong et al. have printed 3D organ-like shapes using an alginate-F127 hybrid gel loaded with mesenchymal stem cells (MSCs). A number of groups utilise light-activatable chemical reactions to pattern hydrogels by photolithography (97, 161, 185, 203, 204). In this way, DeForest and Anseth have formed physical channels modified with RGDS in a PEG hydrogel (205). NIH-3T3 cell migration to, and preferential growth in, these channels is observed. Finally, Liu et al. have designed a microfluidic gradient

generating device that they use to pattern a PEG hydrogel with a concentration gradient of RGDS (197). When MSCs are seeded onto the patterned gel, cell density increases with RGDS concentration.

1.5 Biomaterials for neuronal cell culture

Brain and peripheral nerve tissue are some of the softest and most plastic in the mammalian body (67). Therefore, the neuronal niche is arguably the most disparate from traditional 2D cell culture environments on rigid surfaces (67). Consequently, there are now many examples of self-assembling peptide (206-209), synthetic polymer (109, 210) and naturally derived (96, 101, 103, 211, 212) hydrogels that are used for neuronal cell culture and tissue engineering. As this thesis is primarily concerned with the *in vitro* modelling of brain tissue, the following section does not outline materials used for neuronal tissue engineering. These are reviewed extensively elsewhere (213).

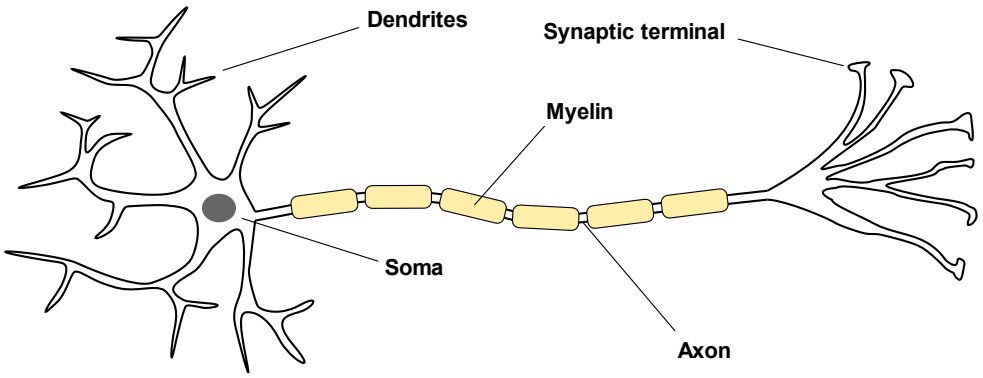

Figure 1.5.1: Schematic diagram of a typical neuron showing the key structural features. The cell receives electrical input from other cells through the dendrites, propagates this signal down the axon and to other cells *via* the synaptic terminals. Neuronal processes or neurites refer to both dendrites and axons that extend out from the cell body. These terms are used interchangeably throughout this thesis.

Self-assembling peptide gels for neuronal cell culture

Much of the published literature regarding self-assembling peptide neuronal scaffolds focuses on neuron-like cells and stem cells. As already stated, hSAFs promote the proliferation and differentiation of PC12 cells and NSCs that both send out processes in an RGDS-facilitated manner (140, 141). Similarly, $RADA_{16}$ gels promote NSC differentiation into neurons and process (see Figure 1.5.1) formation after the addition of RGDS, IKVAV or other neuroprotective peptides (208, 214). In all these

studies, it should be noted that neurites appear relatively underdeveloped. In contrast, the group of Stupp have cultured NSCs on amphiphilic peptide gels, incorporating IKVAV into the polar head group (215). The group demonstrate that NSC differentiation to neurons (confirmed by staining with the neuron-specific marker β-III-tubulin or MAP2 in all these studies) is accompanied by the formation of long neurites.

Studies showing that self-assembling peptide gels support the growth of primary neuronal cultures, *i.e.*, mature nerve cells isolated from primary tissue, are less common. This is largely due to the difficulty in culturing primary neurons (PNs) relative to neural progenitors and neuron-like cell lines (216). The first demonstrations of PN culture on a self-assembling peptide gel have been made by Zhang's group, where extensive neurite and synapse formation are observed on unmodified $RADA_{16}$-II (a variant of the original $RADA_{16}$ peptide) gels (206). More recently, Martin et al. have demonstrated that primary hippocampal neurons (PHNs) can be cultured on short tetrapeptide gels (Fmoc-FFKK and Fmoc-FKFK) (136). In addition, Sur et al. have shown that PHNs can be cultured on peptide amphiphile hydrogels (209). In both of these examples, fluorescence imaging using synaptic markers demonstrate that cells produce extensive neurite networks and synapses, indicators of neuronal maturation (136, 209).

Modifying cytoscaffolds to direct neuronal growth

Just as cell culture materials have been modified to tune the growth of other cell types, neuronal cytoscaffolds have been modified to promote and direct neuronal growth. For example, neurons behave differently on hydrogels of differing stiffness. The Stupp group have shown that neuronal maturation, neurite length and cell density increase on softer (7.3 kPa) compared to stiffer (22.9 kPa) gels (209). This study also demonstrates that, while neural tissue is typically reported to range from 0.1-1 kPa (69-71), neurons are robust to stiffer environments and their growth likely depends on other factors. Similarly, groups have demonstrated that NSCs preferentially differentiate to neurons on softer gels (217). Neurotrophic factors have been incorporated into cytoscaffolds to promote neuronal growth. For example, the Schneider group have passively encapsulated NGF and BDNF into their MAX8 peptide gel (218). These proteins are released gradually into the culture medium over a period of days, in a tuneable manner. MAX8 gels incorporating growth factors promote PC12 cell differentiation (218).

Directing neurite outgrowth by hydrogel micropatterning is one of the principle areas of interest for neuronal biomaterials. In this way, researchers aim to model the process of axonal guidance *in vitro* (219), and direct axonal regrowth *in vivo* (220-222). Hynd et al. have microcontact printed tracks of biotinylated laminin and fibronectin onto streptavidin-modified polyacrylamide gels, along which PHN processes preferentially grow (223) (Figure 1.5.2). Similarly, Luo and Shoichet have directed neurite outgrowth through RGDS-modified channels in a photopatterned agarose gel (224). The Anseth group take a different approach. By photopatterning a PEG gel crosslinked with a photolabile linker, patterns of varying elastic modulus are formed, and neurites preferentially grow along channels of softer gel (210). In addition, the Shoichet group have patterned synthetic polymer gels with immobilised gradients of NGF and NT-3, along which dorsal root ganglion neurons (DRGs) grow (225). Others have shown that neurites can be directed on scaffolds containing aligned fibres (226, 227). Taken together, these studies demonstrate that neurite outgrowth can be directed through changes in gel elastic modulus, adhesive ligand and growth factor concentration, and fibre morphology. Some of these methods have been applied to synthetic polymer gels and used to direct axonal regrowth in animal models of spinal cord injury (221, 222, 228).

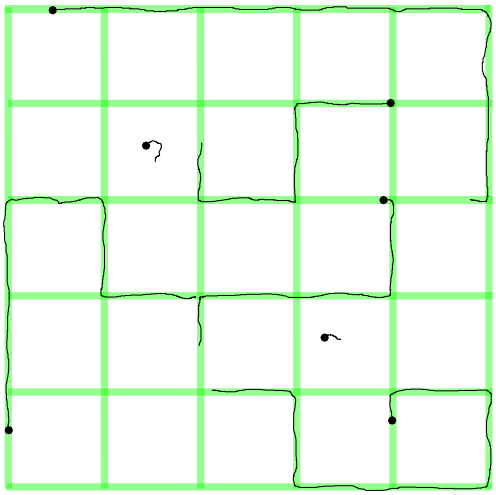

Figure 1.5.2: Schematic diagram of the patterned polyacrylamide gels and axonal responses reported by Hynd et al. Neuronal processes (black) grow preferentially along tracks of fibronectin and laminin (green) (223).

1.6 The scope of this thesis

While there are now many examples of self-assembling peptide hydrogels – some of which are of *de novo* design – synthetic and natural polymer gels are still more commonly used by the wider cell biology and tissue engineering communities. Consequently, *de novo* designed peptide gels remain considerably less developed than these other gel types. Aside from a few notable exceptions (218, 226), these systems are typically shown to support cell growth, allow the introduction of adhesive peptides, and form soft gels with a narrow range of accessible elastic moduli. Efforts to covalently incorporate growth factors, drastically alter the elastic modulus, or spatially pattern gels with growth cues, have almost entirely been performed with synthetic and natural polymer gels.

Introducing these changes into self-assembling peptide systems would likely promote the growth of cells on the scaffold, allow scaffolds to be tailored to support specific cell types, and allow complex cellular behaviours (e.g. axonal guidance) to be modelled *in vitro*. In addition, it should be noted that the more developed *de novo* designed hydrogel systems use peptides that form β structure – the α helix remains relatively underutilised for cytoscaffold generation. Therefore, the huge potential of designed peptide hydrogels as modular platforms upon which to build bespoke environments for cell culture, has only been partly realised.

In the subsequent four chapters, I seek to address this through the development of the *de novo* designed peptide hydrogel, hSAFs, as a modular and tuneable scaffold for PN culture. Chapter 6 of this thesis is concerned with using higher-order coiled-coil oligomers (known as α-helical barrels) for the development of a novel biosensor for small-molecule detection. This work is distinct from the rest of this thesis and, therefore, the relevant literature is reviewed at the start of Chapter 6. Both studies go some way to realising the potential of protein design to create tools for real-world applications in cell culture and biotechnology.

Chapter 2

Materials and Methods

Unless otherwise stated, all materials were obtained from Sigma Aldrich (UK).

2.1 Peptide synthesis and characterisation

Solid Phase Peptide synthesis (SPPS)

All peptides were synthesised on a 0.1 mmol scale by solid phase peptide synthesis (SPPS) on a CEM "Liberty Blue" microwave-assisted peptide synthesiser (CEM, USA) using fluorenylmethyloxycarbonyl (Fmoc) chemistry. Each amino acid coupling cycle consisted of the following steps: removal of the Fmoc protecting group (on the resin or amino acid) by addition of 20% morpholine in dimethylformamide (DMF); washes with DMF; addition of 5 equivalents Fmoc-amino acid, 1 M DIC and 0.5 M 6-chloro-2-hydroxybenzotriazole (Cl-HOBt) in DMF; and further DMF washes. Peptides containing an Asp residue were deprotected using 20% morpholine with 5% formic acid in DMF. The resins used are listed in Table 2.1.1.

Resin	**Peptide**
H-Ala-HMBP-ChemMatrix (PCAS BioMatrix, Canada)	hSAF peptides
Fmoc-Glu(ODmab)-Wang resin (Merck Millipore, Germany)	$shSAF_{W1,4}$ peptides
Rink Amide-ChemMatrix (Merck Millipore, Germany)	All other peptides

Table 2.1.1: Resins used for SPPS of peptides described in this thesis.

After any manual coupling steps or *N*-terminal acetylation were performed (see below), all peptides were washed three times with DMF, then dichloromethane (DCM). Peptides were cleaved from the resin by addition of 90% trifluoroacetic acid (TFA), 5% triiosopropylsilane (TIPS) and 5% H_2O and mixing for 3 hours at room temperature. Peptides were filtered, the TFA removed by evaporation, and the peptide precipitated by addition of chilled diethyl ether. Peptides were centrifuged at 1620 x g for 10 minutes and the resulting pellet was dissolved in 50% (v/v) acetonitrile (in H_2O), frozen in liquid nitrogen and lyophilised overnight. The dry peptides were stored at -20^{o}C until required.

Manual peptide couplings

Where required, unnatural amino acids and other functional groups were coupled to the *N*-terminal amine of peptides synthesised by SPPS.

Azidonorleucine coupling

2 equivalents N-Fmoc-L-azidonorleucine (Figure 2.1.1, Chiralix, Netherlands), 1.9 equivalents hexafluorophosphate azabenzotriazole tetramethyl uranium (HATU) and 4.5 equivalents diisopropylethylamine (DIPEA) were added to hSAF-p1 peptide (synthesised without the *N*-terminal Lys), on-resin, and mixed at room temperature for 3 hours. The Fmoc group was removed by addition of 20% (v/v) morpholine in DMF and mixing for 1 hour at room temperature.

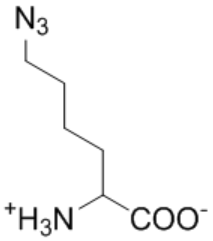

Figure 2.1.1: Azidonorleucine.

Propargylglycine coupling

2 equivalents N-Fmoc-L-propargylglycine (Figure 2.1.2, Merck Millipore, Germany), 1.9 equivalents HATU and 4.5 equivalents DIPEA were added to the peptide (either RGDS, IKVAV or SpyTag, all synthesised without the *N*-terminal Gly), on-resin, and mixed at room temperature for 3 hours. The

Fmoc group was removed by addition of 20% (v/v) morpholine in DMF and mixing for 1 hour at room temperature.

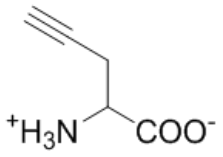

Figure 2.1.2: Propargylglycine.

Alloc-lysine coupling

2 equivalents N-Fmoc-L-Lys(Alloc)-OH (Figure 2.1.3, AGTC Bioproducts, UK), 1.9 equivalents HATU and 4.5 equivalents DIPEA were added to hSAF-p1 (synthesised without the *N*-terminal Lys), on-resin, and mixed at room temperature for 3 hours. The Fmoc group was removed by addition of 20% (v/v) morpholine in DMF and mixing for 1 hour at room temperature.

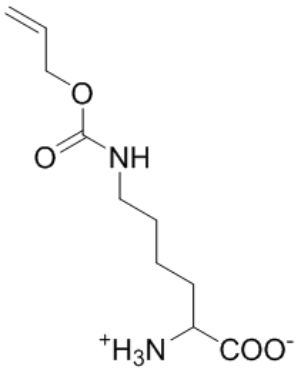

Figure 2.1.3: Alloc-lysine.

Maleimidopropionic acid coupling

2 equivalents *N*-maleimidopropionic acid (Figure 2.1.4, Alfa Aeser, USA), 1,9 equivalents HATU and 4.5 equivalents DIPEA were added to the peptide (either RGDS or SpyTag), on-resin, and mixed for 3 hours at room temperature.

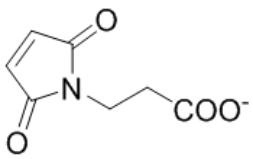

Figure 2.1.4: Maleimidopropionic acid.

5(6)-Carboxytetramethylrhodamine coupling

5 equivalents 5(6)-Carboxytetramethylrhodamine (TAMRA, Figure 2.1.5, Merck Millipore, Germany), 4.5 equivalents HATU and 7.5 equivalents DIPEA were added to CC-Hept, on resin, and mixed for 3 hours at room temperature. To prevent the further coupling of additional TAMRA molecules, 20% (v/v) morpholine in DMF was added and the reaction mixed for a further 1 hour at room temperature.

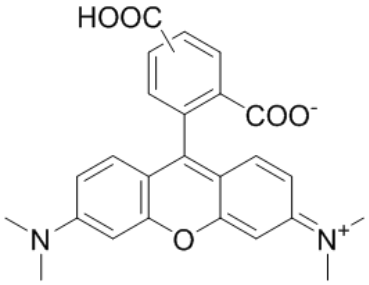

Figure 2.1.5: 5(6)-Carboxytetramethylrhodamine.

Peptide N-terminal acetylation

α-helical barrel peptides were *N*-terminally acetylated, following SPPS. 30 µl acetic anhydride and 100 µl DIPEA, in 10 ml DMF, were added to the peptide, on resin, and mixed for 30 minutes at room temperature.

High-performance liquid chromatography (HPLC)

Peptide	**HPLC gradient (% acetonitrile)**
hSAF peptides	30-50
$shSAF_{W1,4}$ peptides	30-50
SpyTag peptides	10-60
RGDS peptides	5-40
IKVAV peptides	10-50
CC-Tri	40-100
CC-Hex2	40-100
TAMRA-CC-Hept	40-100

Table 2.1.2: HPLC gradients used for purification of peptides described in this thesis.

10 mg crude peptide was dissolved in water-acetonitrile and purified by reverse-phase HPLC (Jasco UK) on a Luna C18 column (5µm, 100 Å, 4.6 mm x 150 mm ID), using an appropriate water-acetonitrile gradient (Table 2.1.3) and 0.1% TFA over 40 minutes.

Purified peptides were determined to be >95% pure by analytical HPLC (Jasco, UK) using a Phenomenex Prodigy ODS-3 column (5 µm, 4.6 x 100 mm) and an appropriate gradient (Table 2.1.2), over 25 minutes.

Matrix-assisted laser desorption/ionisation-time of flight mass spectroscopy (MALDI-TOF MS)

Peptide sample solution was added to α-cyano-4-hydroxycinnamic acid matrix solution (10 mg α-cyano-4-hydroxycinnamic acid dissolved in 1 ml 50% (v/v) acetonitrile) at a 1:1 ratio, on a mass spectrometry sample plate, mixed and left to dry. Mass spectra were recorded using Applied Biosystems 4700 Proteomics MALDI-TOF Analyzer and positive ion spectra were obtained at 25 kV accelerating voltage.

2.2 hSAF scaffold formation and characterisation

Peptide concentration determination

Peptide concentrations were determined by UV absorbance using a NanoDrop 2000 spectrophotometer (Thermo Fisher Scientific, Loughborough, UK). All peptides contained either a single Trp or Tyr residue (except for CC-Tri, which contained one of each) and, therefore, concentrations were determined using the reported extinction coefficients of these amino acids: ε280(Trp) = 5690 $mol^{-1}cm^{-1}$ and ε280(Tyr) = 1280 $mol^{-1}cm^{-1}$.

Peptide concentration was determined using the Beer-lambert equation:

$$c = \frac{A}{\varepsilon l}$$

c = concentration, A = absorbance at 280 nm, ε = extinction coefficient, l = pathlength

hSAF scaffold formation

2 mM hSAF-p1, -p1KAz, -p1KAlloc or p1Cys was mixed with 2 mM hSAF-p2 at 4 ºC in 20 mM MOPS buffer (3-N-morpholino-propanesulfonic acid, 5 mM sodium acetate, 1 mM EDTA), pH 7.4. Typically, for cell studies, 15 µl each peptide was mixed in wells of a 96-well plate to give gels with a final volume of 30 µl. The peptides were briefly mixed and incubated on ice for 30 minutes. Gels were then incubated at 4 ºC overnight and subsequently stored under dH_2O until required.

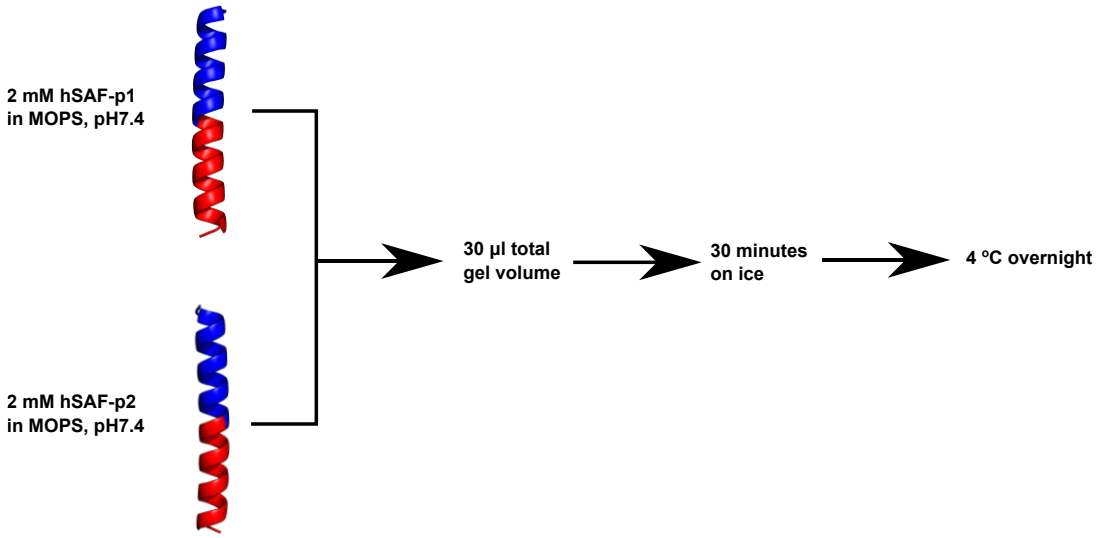

Figure 2.2.1: Schematic showing the protocol for hSAF gel formation.

For investigations of gel stiffness, 6 different gels were formed by mixing the pairs of peptides outlined in Table 2.2.1, following the protocol outlined above. hSAFs required for cell studies were prepared under sterile conditions.

Gel type	p1 peptide and concentration	p2 peptide and concentration
0.5 mM hSAF	1 mM hSAF-p1	1 mM hSAF-p2
1.0 mM hSAF	2 mM hSAF-p1	2 mM hSAF-p2
1.5 mM hSAF	3 mM hSAF-p1	3 mM hSAF-p2
0.5 mM $shSAF_{W1,4}$	1 mM $shSAF_{W1,4}$-p1	1 mM $shSAF_{W1,4}$-p2
1.0 mM $shSAF_{W1,4}$	2 mM $shSAF_{W1,4}$-p1	2 mM $shSAF_{W1,4}$-p2
1.5 mM $shSAF_{W1,4}$	3 mM $shSAF_{W1,4}$-p1	3 mM $shSAF_{W1,4}$-p2

Table 2.2.1: hSAF and $shSAF_{W1,4}$ concentrations used for the formation of gels of varying stiffness.

Circular dichroism (CD) spectroscopy

For analysis of individual peptides, 100 μM peptide samples were prepared in 20 mM MOPS buffer at pH 7.4. For fibre analysis, p1 and p2 peptides were similarly prepared and mixed in equal volumes before incubating for 1 hour at room temperature to form fibres. For analysis of Cu^{2+}-catalysed azide-alkyne cycloaddition (CuAAC)-decorated hSAFs, p1KAz:p2 fibres were incubated with 100 μM alk-RGDS, alk-IKVAV or alk-SpyTag, 400 μM $CuSO_4$ and 400 μM sodium ascorbate (NaAsc) for a further 1 hour at room temperature. For analysis of thiol-ene-decorated hSAFs, p1KAlloc:p2 fibres were incubated with 500 μM 2,2-(ethylenedioxy)diethanethiol (PEG_{2SH}) and irradiated with UVB light (9W, Philips Fluo Compact bulb, 10 mm above gel) for between 0 – 3 minutes. For analysis of maleimide attachment, PEG-decorated fibres were then subsequently incubated with mal-SpyTag for 1 hour at room temperature.

CD measurements were taken in a 1 mm Hellma quartz cuvette at 20 °C or 37 °C, using a JASCO J-810 or J-815 spectropolarimeter fitted with a Peltier temperature controller (Jasco, UK). Spectra were recorded from 190 nm to 260 nm, with a 50 nm/min^{-1} scan rate, 1 nm interval, 1 nm bandwidth and 1 second response times over 8 accumulations. Baseline readings were subtracted from the recorded ellipticities in millidegrees. These were then converted to molar residual ellipticities (MRE, millidegrees cm^{-2} $dmol^{-1}$ res^{-1}). Thermal denaturation curves were acquired by measuring the 222 nm signal at 5 – 95 °C. The temperature was increased at a rate of 40 °C/hour.

Transmission electron microscopy (TEM)

For analysis of individual peptides, 100 μM peptide samples were prepared in 20 mM MOPS buffer at pH 7.4. For analysing mixtures, peptides were similarly prepared, combined in equal volumes and mixed briefly, before incubating at room temperature for 1 hour. For studying peptide attachment by CuAAC, 100 μM alk-peptide, 400 μM $CuSO_4$ and 400 μM NaAsc were added to 100 μM p1Kaz:p2 hSAFs and incubated for 1 hour at room temperature. For analysis of thiol-ene-modified hSAFs, 100 μM p1KAlloc:p2 hSAFs were incubated with 500 μM PEG_{2SH} and irradiated with UVB light (9W, Philips Fluo Compact bulb, 10 mm above gel) for 3 minutes. For analysis of mal-peptide attachment,

200 μM mal-peptide was incubated with these PEG-decorated p1KAlloc:p2 hSAFs for 1 hour at room temperature.

6 μl each sample was then pipetted onto a 400-mesh carbon-coated copper grid and stained with 6 μl 1% (w/v) uranyl acetate solution. Samples were left to dry overnight and imaged on a JEM 1200 EX MKI (JEOL, UK) microscope at 120 kV on a MegaViewII digital camera (Olympus Soft Imaging Systems GmbH, Germany).

Scanning electron microscopy (SEM)

hSAF and $shSAF_{W1,4}$ gel samples were prepared as outlined above in MOPS, pH 7.4. Samples were fixed in 2.5% (v/v) glutaraldehyde for 1 hour at 4 ^{o}C. They were then incubated for 10 minutes each in 20%, 30%, 50%, 70%, 90% and 100% (v/v) ethanol. The dehydrated gels were then dried by exchange of ethanol with liquid CO_2 and subsequent evaporation of the CO_2 at 1070 psi, 31^{o}C (Galaxy S+, RS Biotech, Eppendorf Limited, UK).

Samples were gold-coated using a K575X sputter coater (Emitech, Quorum Technologies, UK). Images were collected using a Quanta 400 scanning electron microscope (FEI, Netherlands) and analysed using ImageJ.

Rheology

Owing to the availability of equipment, the rheological studies outlined in this thesis were performed using two different instruments. Studies performed by Alex Wasmuth outlined in Chapter 1.3 were performed using a Bohlin CVO rheometer (Malvern Panalytical, Malvern, UK). All other studies were performed by me using a Kinexus DSR rheometer (Malvern Panalytical, UK).

In both cases, viscoelasticity of scaffolds was determined by oscillatory frequency sweep measurements using a conical plate (CP 4^{o}/20 mm) with 0.5% strain and frequencies from 0.01 – 10 rad/sec. Peptides were mixed *in situ* at 4 ^{o}C, the geometry lowered into position, and samples incubated for 30 minutes. The temperature of the bed was then increased to 20 or 37 ^{o}C and samples were incubated for a further 1 hour. Measurements were then taken to determine storage (G') and loss (G'') moduli.

For analysis of protein- and thiol-ene-decorated scaffolds, gels were first formed *in situ* and incubated at 4 °C for 30 minutes. After increasing the plate temperature to 37 °C, a reaction mix was dispensed onto the gel and incubated for 1 hour. This mix was wicked off using filter paper before the geometry was lowered and measurements taken.

2.3 hSAF scaffold modification

Decorating scaffolds *via* Cu^{2+}-catalysed azide-alkyne cycloaddition (CuAAC)

hSAFs required for cell studies were modified under sterile conditions.

alk-peptide concentrations were determined by UV absorbance (ε280(Tyr) = 1280 $mol^{-1}cm^{-1}$) using a NanoDrop 2000 spectrophotometer (Thermo Fisher Scientific, UK). Peptides were prepared at 2 mM in 20 mM MOPS buffer, pH 7.4. One gel volume (typically 30 µl) of alk-peptide was added to each hSAF gel, followed by 4 mM $CuSO_4$ and 4 mM NaAsc. The reaction was mixed gently before incubating at room temperature for 6 hours.

The reaction mix was removed from the gel and excess Cu^{2+} removed by incubating six times with two gel volumes 10 mM EDTA, for 30 minutes each. Gels were then similarly incubated a further six times with PBS and either analysed or incubated under cell culture media overnight.

Decorating scaffolds *via* thiol-ene and thiol-maleimide click chemistry

hSAFs required for cell studies were modified under sterile conditions. The below is the method used for the GFP photopatterning studies outlined in Chapter 5.3. All experiments outlined in Chapter 5.2 used different light sources, irradiation times and conditions that are detailed in the text.

p1KAlloc:p2 hSAFs were incubated under one gel volume of a reaction mix containing 5 mM PEG_{2SH}, 0.1% (w/v) Irgacure 2959 in 20 mM MOPS, pH 7.4, for 30 minutes. Gels were then irradiated with UVB light (9W, Philips Fluo Compact bulb), placed <1 mm above the plate, for 2 minutes, unless otherwise stated. Gels were incubated three times with two gel volumes PBS for 30 minutes.

2 mM maleimide-peptide was prepared in 20 mM MOPS, pH 7.4. Two gel volumes of peptide was added to p1KAlloc:p2-PEG_{SH} hSAF and incubated for 15 hours at room temperature. Gels were then washed three times with PBS for 30 minutes each, and either analysed or incubated under cell culture media until required. Typically, this was the next day.

Determining protein concentration

SpyCatcher-GFP (SC-GFP) and SpyCatcher-GFP-insulin-like growth factor 1 (SC-GFP-IGF1) protein concentrations were determined by UV absorbance using a NanoDrop 2000 spectrophotometer (Thermo Fisher Scientific, UK). Molar extinction coefficients at 280 nm for each protein were determined using ExPASy (Swiss Institute of Bioinformatics, Lausanne, Switzerland).

Protein concentration was determined using the Beer-lambert equation:

$$c = \frac{A}{\varepsilon l}$$

c = concentration, A = absorbance at 280 nm, ε = molar extinction coefficient, l = pathlength

Decorating scaffolds with SpyCatcher-proteins

hSAFs required for cell studies were decorated under sterile conditions and proteins were sterile filtered prior to immobilisation.

After SpyTag attachment by CuAAC or maleimide-thiol reaction, SC-GFP or SC-GFP-IGF1 was immobilised by incubating hSAFs with two gel volumes (typically 60 µl) of 1 µM protein in Tris-HCl (25 mM Tris, 150 mM NaCl, pH 7.4) for 15 hours at 4 ºC. Protein was then removed and gels washed eight times with two gel volumes of PBS. Protein-decorated hSAFs were then stored under PBS or cell culture media, at 4 ºC until required.

SpyCatcher immobilisation assay

30 µl hSAFs were incubated with 30 µl SC-GFP or SC-GFP-IGF1 of known concentrations between 0 and 1 µM to create a calibration curve of known protein concentrations.

30 µl SC-GFP or SC-GFP-IGF1 was incubated with 30 µl SpyTag-decorated or undecorated hSAFs for 15 hours at 4 °C. Protein was then removed and gels washed eight times with 60 µl PBS, pH 7.4, at 4 °C for 30 minutes each. GFP fluorescence was quantified using a ClarioStar plate reader (BMG LabTech, Ortenberg, Germany).

SpyCatcher detachment assay

1 µM SC-GFP or SC-GFP-IGF1 were incubated with SpyTag-decorated or undecorated hSAFs for 15 hours at 4 °C, as above. Any non-specifically bound protein was removed by incubating eight times with two gel volumes PBS. Fluorescence at day 0 was then quantified using a ClarioStar plate reader (BMG LabTech, Germany).

Gels were incubated under 100 µl PBS for 1 week at 37 °C in a cell culture incubator. Supernatant was collected on day 7 and its fluorescence quantified to calculate the percentage of protein detached over the time period. Gels were then incubated for a further 3 weeks under fresh PBS. The supernatant was collected and its fluorescence quantified every 7 days, before replacing with fresh PBS.

Percentage protein detachment per week was calculated using the following equation:

$$Percentage\ protein\ detached\ per\ week = (GFP\ fluorescnece\ day\ 0 - GFP\ in\ supernatant) \times 100$$

2.4 Cell studies

Puramatrix and Matrigel formation

30 µl 0.15% (w/v) Puramatrix (Corning, Tewksbury, USA) was prepared in sterile dH_2O in wells of a 96-well plate. Gelation was triggered by gently adding 100 µl PBS and incubating at 37 °C for 1 hour. Gels were then incubated under cell culture media until required.

30 µl Matrigel (Corning, Tewksbury, USA) was prepared in wells of a 96-well plate and gelation triggered by incubation at 37 °C for 1 hour. Gels were then washed three times with PBS and incubated under cell culture media until required.

Primary neuronal cell culture

The cortex and hippocampus were dissected from E18 (18 days from mating) Wistar rat embryos, trypsin treated, mechanically dissociated and resuspended in plating media (Neurobasal medium (Gibco, UK) containing 10% horse serum, B27 (Gibco, UK), penicillin-streptomycin and 5 mM GlutaMAX (Thermo Fisher, UK)). Cells were then seeded onto hSAFs, Puramatrix or Matrigel, typically at a density of 20,000 cells per well of a 96-well plate, in plating media. After incubation at 37^{o}C in humidified air with 5% CO_2 for 2 hours the medium was changed for unsupplemented Neurobasal medium (Gibco, UK), containing only B27 (Gibco, UK) and 2 mM GlutaMAX (Thermo Fisher, UK). For IGF1 activity studies, Neurobasal medium lacking B27 was added at this point. Neurons were cultured at 37 ^{o}C until required, typically after 14 days *in vitro* (DIV).

MCF-7 cell proliferation assay and crystal violet staining

5000 MCF-7 cells were seeded into wells of a 96-well plate and cultured in MEM (10% fetal bovine serum, 1 x antibiotic-antimycotic) for 24 hours at 37 ^{o}C in humidified air with 5% CO_2. The medium was then removed, replaced with MEM without serum and cells were cultured for a further 24 hours. Cells were then treated with 0 – 30 pmoles either recombinant insulin-like growth factor 1 (rIGF1, Abcam, UK), SC-GFP-IGF1, SC-GFP, or no protein, all in serum-free MEM. Cells were cultured for a further 48 hours.

Cells were washed three times with PBS and fixed in 4% paraformaldehyde (PFA) in PBS for 20 minutes. Cells were washed a further three times in PBS before staining with crystal violet solution (0.05% (w/v) crystal violet, 20% (v/v) ethanol in dH_2O) for 30 minutes at room temperature. After a further three washes with PBS, 1% (w/v) SDS in PBS was added and cells mixed gently for 1 hour.

The absorbance of each cell suspension at 595 nm was measured using a ClarioStar plate reader (BMG LabTech, Germany). For each protein, absorbance readings were normalised to those for untreated cells (*i.e.* 0 pmoles protein).

Immunocytochemistry

Cells were washed three times with warm PBS buffer and fixed in 4% paraformaldehyde solution in PBS for 15 minutes. Cells were washed a further three times and membranes permeabilised by adding 0.1% (v/v) Triton-X-100 in PBS for 20 minutes. After washing another three times with PBS, 5% BSA in PBS was added to prevent non-specific antibody binding and cells were incubated for a further 20 minutes. Primary antibodies (anti-MAP2 polyclonal antibody, Synaptic Systems; anti-GFAP mouse monoclonal antibody, Synaptic Systems) were then added in 2.5% BSA in PBS and cells incubated for 2 hours at room temperature. Cells were then washed a further three times with PBS. Secondary antibodies (Cy3 anti-rabbit IgG, Goat, Invitrogen; Cy5 anti-mouse IgG, donkey, Jackson Immuno Research, Stratech) were added and cells incubated for a further 45 minutes at room temperature. Cells were then washed a further two times in PBS and once with H_2O before being incubated with fluoromount-G solution containing DAPI (Thermo Fisher, UK). Cells were stored at 4 ^oC until imaging.

Widefield microscopy

Images of neurons and hSAF gels were collected using a Leica DMI6000 widefield microscope fitted with a Leica DFC365FX monochrome digital camera and Leica DFC420C colour camera. Depending on the experiment, either a 5x HC PL Fluotar, 10x HC PL Fluotar, 20x N PLAN L CORR or 40x PL Fluotar L CORR objective was used. The following excitation filters were used: 360/340 nm (DAPI), 470/440 nm (Cy2), 545/526 nm (Cy3), 620/660 nm (Cy5). Typically, Z-stacks were acquired by taking 10 images through an appropriately sized sample depth. Images presented in this thesis are typically composites of these Z-stacks. Images were analysed using ImageJ.

AlamarBlue cell viability assay

AlamarBlue cell viability assay solution (Thermo Fisher Scientific, UK) was diluted 1:10 into Neurobasal medium (containing B27 and glutamax) without phenol red (Gibco, UK). The media on the cells was removed and replaced with 100 µl AlamarBlue mix. Cells were incubated for 6 hours at 37 ^oC. The medium was then transferred to a 96-well plate and fluorescence quantified using a ClarioStar plate reader (BMG LabTech, Germany)

2.5 Molecular biology

DNA transformation

All plasmids used during this project contained kanamycin-resistance genes for selecting transformed clones.

Typically, 1 µl plasmid DNA was incubated with 50 µl competent cells (either XL-10, BL21 or SHuffle *E. coli* strains) for 10 minutes on ice. Cells were heat shocked at 42 ºC for 45 seconds and incubated on ice for a further 2 minutes. 1 ml LB medium (1% (w/v) NaCl, 1% (w/v) Tryptone and 0.5% (w/v) Yeast extract) was added and the cells incubated at 37 ºC while shaking for 1 hour. Cells were then pelleted by centrifugation at 7500 x g for 1 minute and resuspended in 100 µl LB medium. Cells were then spread onto kanamycin-containing agar plates and incubated at 37 ºC overnight. Colonies were then picked and used for downstream applications.

Polymerase chain reaction (PCR)

Temperature (ºC)	**Time (seconds)**
<1000 bp inserts	
98	10
Primer Tm	30
72	30
>1000 bp vectors	
98	30
Primer Tm	30
72	360

Table 2.5.1: PCR conditions for amplifying insert and vector DNA. Primer Tm values were calculated using the online tool from NEB.

PCR was performed using a Phusion high-fidelity PCR kit (Thermo Fisher Scientific, UK). 2 µl DNA was added to 1 µl dNTP mix, 10 µl 5x Phusion HF buffer, 2.5 µl each primer, 1 µl DMSO and 0.5 µl Phusion DNA Polymerase (2 U/µl) in dH_2O. DNA fragments and vectors were then amplified using a

thermocycler (Eppendorf Limited, Stevenage, UK) and 30 cycles of the temperatures outlined in Table 2.5.1. Amplified DNA was then cleaned using a GeneJet gel extraction kit (Thermo Fisher Scientific, UK) and analysed by agarose gel electrophoresis.

Agarose gel electrophoresis

Samples of DNA for analysis were added to 6x gel loading dye (Thermo Fisher Scientific, UK) and loaded onto well of a 1% (w/v) agarose gel containing SybrSafe (Thermo Fisher Scientific, UK) for DNA visualisation. A current of 150 V was passed through the gel for 30 mins. The agarose gel was then removed and DNA visualised using a UV transilluminator.

Restriction digest and ligation

1 µl of each restriction enzyme (NEB, USA) was added to 1 µl DNA in Cutsmart buffer. The reaction was incubated for 1 hour at 37 ºC, before the addition of DpnI (NEB, USA) and a further 1 hour incubation at 37 ºC.

The digested DNA was ligated by mixing 37.5 ng insert DNA with 50 ng similarly digested vector DNA in T4 DNA ligase buffer and T4 DNA Ligase (NEB, USA). The reaction was incubated at room temperature for 30 minutes before transformation into XL10 *E. coli* cells.

Golden Gate digest and ligation

The concentration of DNA fragments to be digested and ligated by Golden Gate assembly were determined using a NanoDrop 2000 spectrophotometer (Thermo Fisher Scientific, UK). 75 ng vector DNA was added to 75 ng insert DNA in 2 µl NEB Golden Gate buffer (NEB, USA) and 1 µl Golden Gate Assembly mix (NEB, USA) in dH_2O. The reaction was incubated at 37 ºC for 1 hour and 55 ºC for 5 minutes before transforming into XL10 *E. coli* cells.

Cloning the pET28a-SC-GFP plasmid construct

A pDEST14 plasmid containing the SpyCatcher gene with an *N*-terminal His-tag was kindly gifted by Mark Howarth from Oxford University. A pET28a vector containing GFP with a 5’ flexible linker (pET28a-GFP) was gifted by James Ross, a member of the Woolfson group.

Name	Sequence	Restriction enzyme site
A	AATCCCCTGCAGGCATGTCGTACTACCATCACC	KpnI
B	GCAACTAAAGGTGACGCTCATATTGGTACC	PstI
C	GGATCTCCATGGTTGATACCTTATCAGGTTTATCAAGTGAGC	NcoI
D	CATAAGGAATTCTTAGTGGTGATGATGATGGTGGCTAGC	EcoRI

Table 2.5.2: Primers used to clone the SC-GFP construct.

The SpyCatcher gene, including the *N*-terminal His-tag, was amplified by PCR using forward and reverse primers containing 5' KpnI and PstI restriction enzyme sites, respectively (Table 2.5.2, A+B). This SpyCatcher PCR product and pET28a-GFP were digested with KpnI and PstI (NEB, USA) and the resulting products ligated using T4 DNA ligase (Takara, ClonTech, France). This product was transformed into XL-10 competent *E. coli* cells and grown on Kanamycin-containing plates overnight at 37 ºC. Bacterial colonies were picked and grown in LB medium overnight at 37 ºC. Plasmid DNA was then extracted from these cultures using a GeneJet plasmid mini-prep kit (Thermo Fisher Scientific, UK). The ligated clones were identified by PCR analysis and gel electrophoresis, and the successful ligations were sequenced (Eurofins, Bristol, UK).

The gene encoding the His-tag of SC-GFP was later moved to the protein *C* terminus using primers C and D in Table 2.5.2. The coding sequence was transferred to an empty pET28a vector through NcoI and EcoRI (NEB, USA) digestion and ligation following the above protocol.

Cloning the pET28a-SC-GFP-IGF1 plasmid construct

A gene containing the coding sequence for insulin-like growth factor-1 (IGF1) with an *N*-terminal $(GS)_6$ linker ($(GS)_6$-IGF1) – codon optimised for *E. coli* expression – was synthesised by GeneArt (Thermo Fisher, UK).

A periplasm targeting sequence was inserted into SC-GFP 5' of the coding sequence for the *N*-terminal His-tag. SC-GFP was amplified by PCR using primers C and D (Table 2.5.3). A pET28a vector was amplified using primers A and B (Table 2.5.3), which contained complementary sticky ends to D and C, respectively. These fragments were assembled by Golden Gate assembly and transformed into XL10

E. coli. Colonies were picked and inoculated in 10 ml LB medium overnight at 37 ºC while shaking (180 rpm). Plasmid DNA was extracted from these cultures using a GeneJet plasmid mini-prep kit (Thermo Fisher Scientific, UK) and the ligated clones were identified by PCR and gel electrophoresis. The successful ligations were sequenced (Eurofins, Bristol, UK).

Name	**Sequence**	**Restriction enzyme site**
A	AACGGAGGTCTCTGTAGCATGGTGAGCAAGGGCG	BsaI
B	TTTAAAGGTCTCTGTGCGCTCAGTGCCAAAATACGTGCACC GGTTTTAATCTTCATGGTATATCTCCTTCTTAAAGTTAAAC AAAATTATTTCTAGAGG	BsaI
C	AAACCCGGTCTCTGCACTCACCACCATGATGTTTAGCGCAA GCGCACTGGCAATGTCGTACTACCATCACCATCACC	BsaI
D	CCGAATGGTCTCTCTACCCGACCCCGATCCGCTC	BsaI
E	GTGACCGGTCTCTTTGCCACCACCACCACCACCAC	BsaI
F	GAATTGGGTCTCTAACCGCTAGCCTTGTACAGCTCGTCC	BsaI
G	CTAAAGGGTCTCTGGTTCTGGCTCTGGCAGC	BsaI
H	TCGTTCGGTCTCTGCAATTATGCGCTTTTTGCCGG	BsaI
I	ATCGAAGGATCCATGGTTGATACCTTATCAGGTTTATCAAG TGAGC	BamHI
J	TTCATTAAGCTTTTATGCGCTTTTTGCCGGTTTCAGC	HindIII

Table 2.5.3: Primers used to clone the SC-GFP-IGF1 construct.

The $(GS)_6$-IGF1 gene was amplified by PCR using primers G and H (Table 2.5.3). The pET28a-SC-GFP vector containing the *N*-terminal periplasmic tag was also amplified using primers with complementary sticky ends to those used to amplify $(GS)_6$-IGF1 (Table 2.5.3, E + F). These fragments were assembled by Golden Gate assembly and transformed, grown up, analysed and successful ligations selected as described above. These clones were then sequenced (Eurofins, Bristol, UK). This periplasm targeting sequence-containing construct is referred to as p-SC-GFP-IGF1.

The periplasmic targeting sequence was later removed and the SC-GFP-IGF1 coding sequence moved to a pET28a vector using primers I and J (Table 2.5.3). Both vector and insert were digested with BamHI and HindIII (NEB, USA) and ligated as described above. This construct is referred to as SC-GFP-IGF1.

Protein expression

pET28a-SC-GFP and pET28a-p-SC-GFP-IGF1 were transformed into BL21 competent *E. coli* cells, while pET28a-SC-GFP-IGF1 was transformed into SHuffle competent *E. coli* cells (NEB, US). The transformed *E. coli* were grown overnight on kanamycin-containing agar plates. Individual colonies were picked and used to inoculate a starter culture of 10 ml LB media containing 50 ng/ml kanamycin. This culture was grown at 37 ºC for 15 hours while shaking at 180 rpm. This starter culture was then used to inoculate a larger culture (typically 400 ml LB medium containing 50 ng/ml kanamycin). This was shaken (180 rpm) at 37 ºC and 30 ºC for SC-GFP and SC-GFP-IGF1, respectively, until the cell density reached A_{600} 0.6. Expression of SC-GFP and SC-GFP-IGF1 was then induced by addition of 1 mM isopropyl β-D-1-thiogalactopyranoside (IPTG) and the cultures were grown for 15 hours at 18 ºC.

Protein purification by Ni^{2+}-NTA and size exclusion chromatography (SEC)

Bacterial cultures were harvested by centrifugation at 10,000 x g for 10 minutes in a Lynx 4000 centrifuge using an F12-6x500 LEX rota (Thermo Fisher Scientific, UK) at 4 ºC. The bacterial pellets were then resuspended in 20 ml lysis buffer (25 mM Tris (pH 7.4), 150 mM NaCl, 5% glycerol, 10 mM imidazole, 1% (v/v) Triton-X-100, 1 mM phenylmethane sulfonyl fluoride (PMSF)), incubated for 10 minutes at 4 ºC, and sonicated for 5 minutes on ice. The cells were then centrifuged at 13,000 x g for 30 minutes at 4 ºC in a Lynx 4000 centrifuge using an F14-14x50cy rota (Thermo Fisher Scientific, UK).

If contained in the soluble fraction, SC-GFP and SC-GFP-IGF1 were purified without further processing. If in the insoluble fraction, the protein was refolded *in vitro* (see method below). A Ni^{2+}-NTA column was equilibrated with wash buffer (25 mM Tris (pH 7.4), 150 mM NaCl, 5% glycerol, 1% Triton-X-100 and 10 mM imidazole) before adding the soluble protein. The column was washed a further two times with wash buffer and the protein eluted by addition of elution buffer (25 mM Tris

(pH7.4), 150 mM NaCl, 400 mM imidazole). The resulting elute was collected and concentrated using an Amicon Stirred Cell concentrator (Merck Millipore, Germany).

Both proteins were further purified by size exclusion chromatography (SEC) using a SuperDex 75 size exclusion column and AKTA protein purification system (AKTAprime plus, GE Healthcare Life Sciences) using 25 mM Tris-HCl, 150 mM NaCl buffer, pH 7.4. Protein-containing fractions were analysed by SDS-PAGE and fractions deemed pure pooled, before being concentrated using an Amicon Stirred Cell concentrator (Merck Millipore, Germany). Proteins were stored at 4 ^{o}C and typically used within two days of purification.

SDS-PAGE

Proteins were resolved on a 10% (v/v) acrylamide resolving gel (4 ml H_2O, 3.3 ml 30% (v/v) acrylamide, 2.5 ml 1.5 M Tris pH 8.8, 0.1 ml 10% (w/v) SDS, 0.1 ml 10% (w/v) ammonium persulfate (APS) and 0.004 ml tetramethylethylenediamine (TEMED)), using a buffer containing 25 mM Tris, 192 mM Gly and 0.1% (w/v) SDS. Protein samples were mixed with sample buffer (50 mM Tris pH 6.8), 2% (w/v) SDS, 10% (v/v) glycerol, 1% (v/v) β-mercaptoethanol, 12.5 mM EDTA, 0.02% (w/v) bromophenol blue), boiled at 95 ^{o}C for 5 mins and loaded onto the gel. A current of 150 V was passed through the gel for 80 minutes.

The gel was removed from the tank and stained with Coomassie brilliant blue stain (0.1% (w/v) Coomassie Brilliant Blue stain, 10% (v/v) glacial acetic acid, 40% (v/v) methanol in dH_2O) for 1 hour at room temperature. The gel was then washed with dH_2O and incubated overnight in destaining solution (10% (v/v) glacial acetic acid, 40% (v/v) methanol in dH_2O). Proteins were visualised using a transilluminator.

In vitro refolding

p-SC-GFP-IGF1 was refolded *in vitro* by dialysis. The pellet was solubilised overnight by mixing at room temperature in lysis buffer containing 6 M guanidinium hydrochloride (GuHCl) (25 mM Tris, 150 mM NaCl, 5% (v/v) glycerol, 10 mM imidazole, 1% (v/v) Triton-X-100, 1 mM PMSF, 6 M GuHCl). The protein was purified by Ni^{2+}-NTA chromatography as described above, using buffers

containing 6 M GuHCl. The protein was then refolded by dialysis against 2 L refolding buffer (25 mM Tris, 150 mM NaCl, 50 mM L-Arg, 1 mM reduced glutathione and 0.3 mM oxidised glutathione) for 48 hours at room temperature. Protein was then purified by SEC as previously described.

2.6 hSAF patterning

3D printing

Moulds for microfluidic gradient generator devices and hSAFs were designed using computer aided design (CAD) software package Autodesk Inventor Professional 2014. These designs were printed using a Form 2 desktop stereolithography (SLA) 3D printer and clear photopolymer resin (FormLabs, USA). Prints were washed multiple times with isopropanol to remove any excess resin and dried overnight at room temperature.

Microfluidic device fabrication

50 g polydimethylsiloxane (PDMS) was mixed with 5 g silicon elastomer curing agent (Sigma Aldrich, UK) and mixed thoroughly. The mixture was degassed using a desiccator, poured over the 3D printed mould, and incubated at 70 ^{o}C for 4 hours. Devices were cut from the moulds using a scalpel and 50 μm inlets and outlets punched at the desired locations. The PDMS device and a glass microscope slide were cleaned using a plasma asher (Zepto, Diener electronic, Germany). The PDMS was immediately pressed feature-side down onto the slide, affixing the PDMS to the glass.

Microfluidic device testing

Two plastic syringes containing either dH_2O, rhodamine dye or food colouring were attached to the inlets of the device by 0.8 mm diameter polytetrafluoroethylene (PTFE) tubing (Cole-Parmer, USA). Syringes were affixed to two syringe pumps (NE-1000, New Era Syringe Pump Systems, USA) and solutions pumped through the device at flow rates between 0 – 200 μl/min.

Gradient patterning hSAFs by microfluidics

hSAFs were patterned by microfluidics using two methods, A and B.

A: A 30 µl p1KAz:p2 hSAF gel was formed in the patterning chamber of the microfluidic device. The gel was decorated with alk-SpyTag as previously described and washed 6 times with EDTA and 6 times with PBS. A ~10 mm x 10 mm cube of PDMS was inserted into the top of the patterning chamber and pushed down to <1 mm above the gel. The two inlets were connected to solutions of 1 µM SCGFP (in Tris-HCl, pH 7.4) and Tris-HCl buffer, pH 7.4, *via* PTFE tubing. Solutions were pumped through the device at 50 µl/min for 10 mins using two syringe pumps (New Era Syringe Pump Systems, USA). After patterning, the PDMS plug was removed and the gel washed 6 times with PBS before imaging by widefield microscopy.

B: 30 µl hSAF-p2 was dispensed into the patterning chamber and the PDMS plug inserted as above. The two inlets were connected to solutions of hSAF-p1 and hSAF-p2 in 20 mM MOPS *via* PTFE tubing. Solutions were pumped through the device at 50 µl/min for 10 mins using two syringe pumps (New Era Syringe Pump Systems, USA). After patterning, the PDMS plug was removed and gels were patterned with alk-SpyTag and SC-GFP as previously described.

Photolithographic patterning of hSAFs

Photomasks were designed in Inkscape and printed onto transparencies (JD photodata, UK).

For patterning experiments, p1KAlloc:p2 hSAFs were formed in 1 mm or 2 mm deep 3D printed plastic moulds, glued to coverslips. For cell culture experiments, these moulds were autoclaved prior to use. hSAFs were incubated under one gel volume 5 mM PEG_{2SH}, 0.1% (w/v) Irgacure 2959 in 20 mM MOPS, pH 7.4 for 30 minutes. The gel was placed into a Karl Suss MJB3 mask aligner (Suss Microtech, Germany) fitted with a 200 W mercury lamp (350-500 nm). The photomask was affixed into the mask aligner and the gel raised as close as possible to the mask without making contact. Gels were exposed to UV light (350-500 nm) through the mask for 3 minutes. Samples were then removed from the mask aligner and washed eight times with PBS before imaging by widefield microscopy.

Chapter 3

Tuning hSAFs for optimal growth of primary neurons

Introduction

As outlined in Chapter 1, hSAFs are peptide-based hydrogels developed by the Woolfson lab (12). They are formed *via* the self-assembly of two *de novo* designed α-helical peptides, hSAF-p1 and hSAF-p2 (12) which, when mixed, form a heterodimeric coiled coil with an offset interface, exposing sticky ends for longitudinal assembly into fibres (34). These fibres associate *via* weak hydrophobic interactions to form a soft (~1 kPa) hydrogel (Figure 1.3.2), which has previously been utilised for the culture of PC12 cells and neural stem cells (NSCs) (140, 141). As one of a small number of cytoscaffolds formed from designed peptides (56, 158, 229), the further development of hSAFs is of interest for the development of novel tools for cell culture and tissue engineering. In addition, such research demonstrates our relatively recently acquired ability to design peptides from first principles, which might be used to form materials with tuneable properties.

While much can be learned from the neuronal-like cell types cultured previously on hSAFs, primary neurons (PNs) are arguably a better *in vitro* model of neuronal processes *in vivo* (216). Specifically, PN cultures are heterogeneous and, thus, contain multiple neuronal cell types and, depending on the culture conditions, glia (cells that provide support to neuronal growth *in vivo*) (216, 230). In addition, owing to

their isolation from primary tissue, these cells are extremely similar to those found *in vivo*. Finally, PNs produce extensive neurite networks with mature synapses, the formation of which are essential for studying neuronal processes (231-235).

Here, I assess PN responses to the parent hSAF system in order to identify whether this material can be utilised for PN culture. I then optimise these gels as a culture substrate for neurons, by assessing PN responses to adhesion peptide modification and variations in gel stiffness.

3.1 Assessing hSAFs as a platform for primary neuronal culture

Biophysical characterisation of parent hSAFs

Initially, I wanted to assess whether hSAFs, without any additional functionality or chemical adducts, could support the growth of PN cultures. hSAF peptides (Figure 3.1.1A) were synthesised by solid phase peptide synthesis (SPPS), purified by high performance liquid chromatography (HPLC) and masses confirmed by matrix-assisted laser desorption/ionisation time of flight mass spectrometry (MALDI-TOF-MS). HPLC and MALDI-TOF-MS data for all peptides described in this thesis can be found in the Appendix (Chapter 8.1). Secondary structure and fibre formation were confirmed by circular dichroism (CD) spectroscopy and transmission electron microscopy (TEM), respectively (Figure 3.1.1 B-C). These unmodified, previously reported peptide designs (12) are hereafter referred to as the 'parent' hSAF system, or p1:p2 hSAFs.

hSAF peptides are designed to be helical in structure and, upon mixing, to form dimeric assemblies and fibres (12). CD analysis of the individual peptides confirmed that they were indeed helical and well folded, producing the classical α-helical signal with minima at 208 and 222 nm (Figure 3.1.1B). When the peptides were mixed, they remained helical, however the minima at 222 nm was red-shifted to ~225 nm and was more pronounced relative to that at 208 nm. This is indicative, though not confirmatory, of higher-order structure formation (12, 34, 236). Critically, the spectrum of the mixed

peptides did not overlay the theoretical average of the two individual peptides, suggesting they were interacting in some way. The mixtures were helical at 20 °C and 37 °C, confirming stability at the relevant temperatures for gel preparation and cell culture.

A

Heptad repeat	*gabcdef gabcdef gabcdef gabcdef*
hSAF-p1	H-KIAALKA KIAALKA EIAALEW ENAALEA-COOH
hSAF-p2	H-KIAALKA KNAALKA EIAALEW EIAALEA-COOH

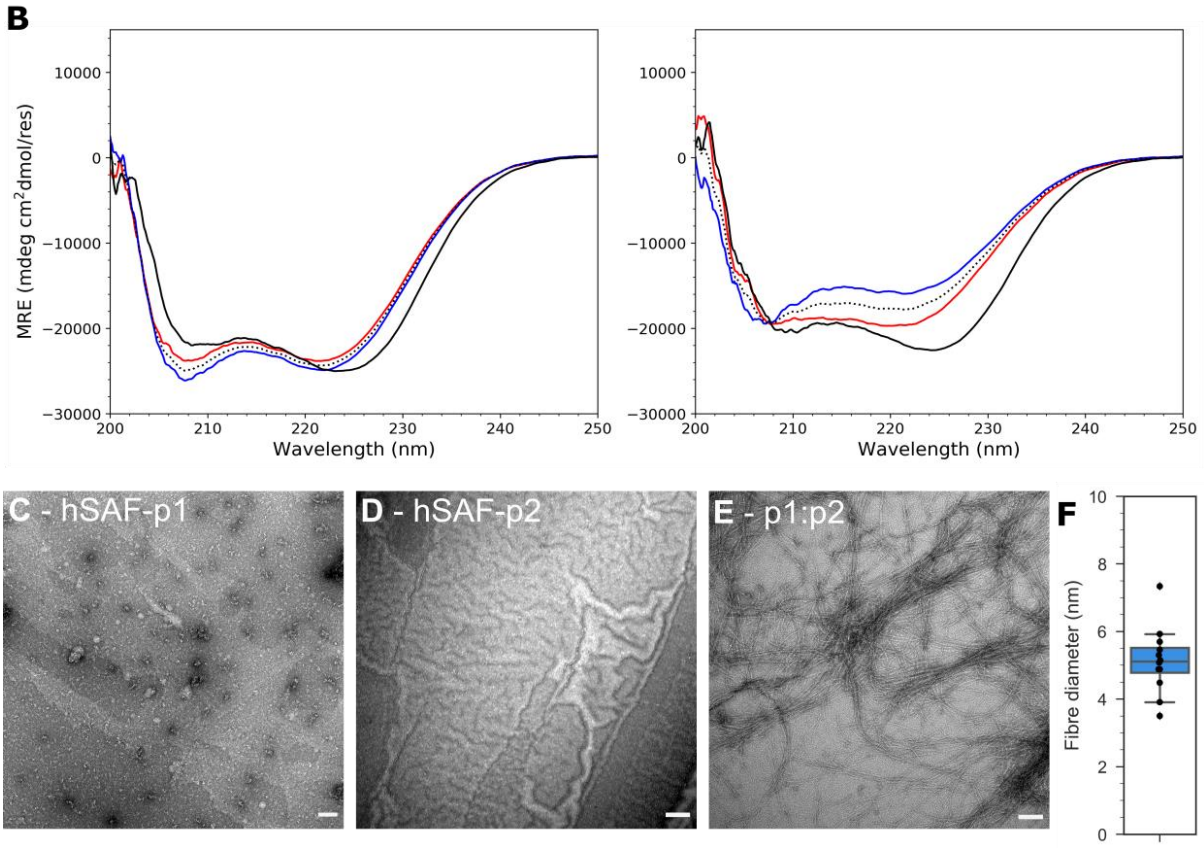

Figure 3.1.1: Solution phase characterisation of hSAF peptides and fibres. **A:** Sequences of hSAF-p1 and -p2. **B:** CD spectra of hSAF-p1 (red), hSAF-p2 (blue) and p1:p2 fibres (black). Dotted lines indicate the theoretical average spectra upon combining that of hSAF-p1 and hSAF-p2. Readings were taken at 20 °C (left panel) and 37 °C (right panel). **C-E:** TEM images of hSAF-p1 **(C)**, hSAF-p2 **(D)** and the p1:p2 mixture **(E)**. **F:** Box plot showing fibre diameters, n=10 fibres chosen at random across multiple images. Fibres were measured manually using ImageJ.

To identify whether the parent hSAF peptides formed fibres, mixed peptides were analysed by TEM (Figure 3.1.1C-E). The role of the Asn residues in hSAF-p1 and -p2 (Figure 3.1.1A) is to direct the formation of offset heterodimers rather than parallel homodimers, the former of which promotes

longitudinal assembly. TEM confirmed the individual peptides did not form fibres. When mixed, the peptides formed fibres that covered most of the EM grid. Fibres had an average diameter of 5±1 nm (Figure 3.1.1F), roughly half that previously reported (13±5 nm) (140), and extended over hundreds of nm. Fibres were prepared under identical conditions to those previously reported and, therefore, the reason for the formation of narrower fibres is unclear. Fibre diameter was consistent across all preparations and therefore this was not investigated further.

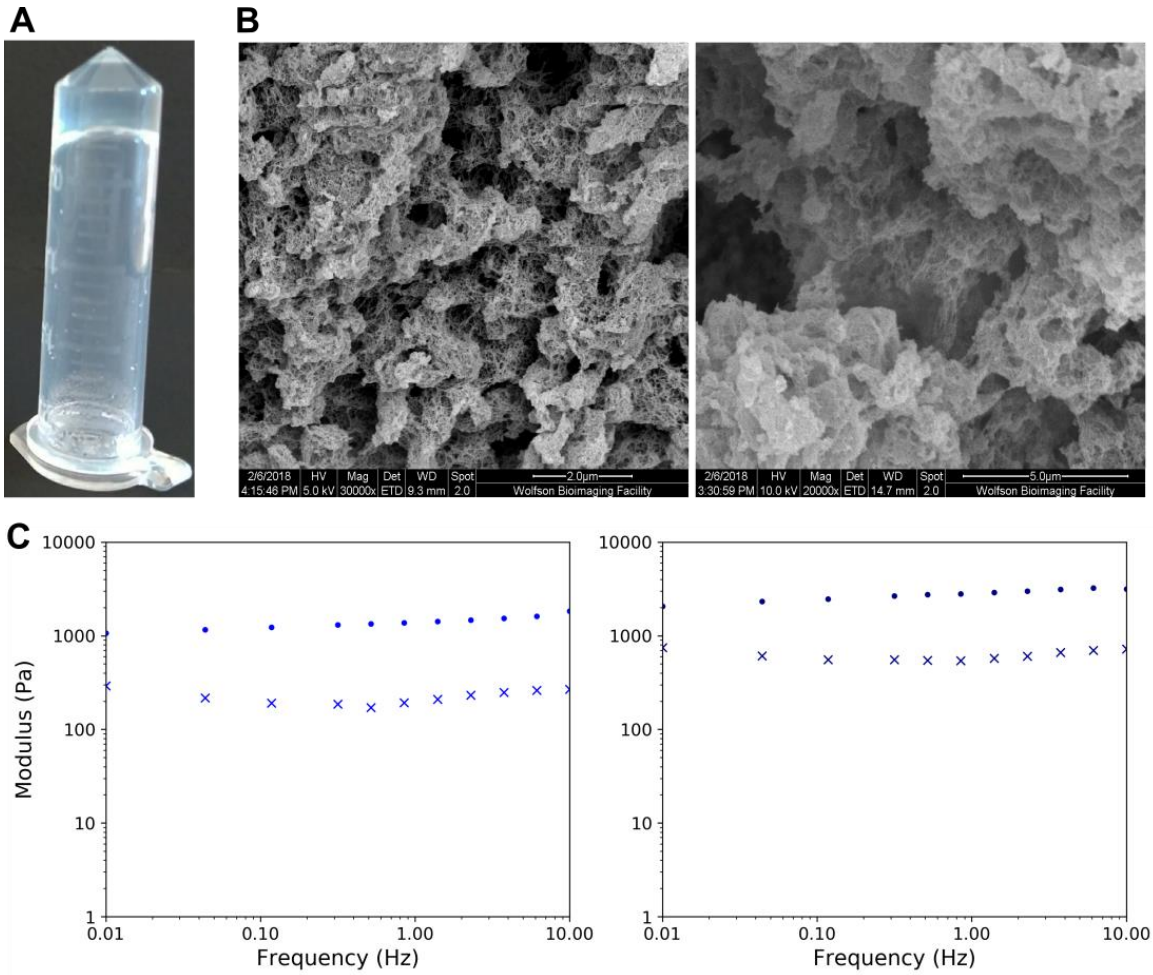

Figure 3.1.2: Biophysical analysis of the hSAF scaffold. **A:** Photograph of the resultant self-supporting gel formed upon mixing hSAF-p1 and hSAF-p2. **B:** SEM images of the p1:p2 hSAF scaffold. **C:** Frequency sweep bulk rheological analysis of p1:p2 hSAFs at 20 ºC (left panel) and 37 ºC (right panel) and 0.5% strain. G' (circles) and G'' (crosses) values are shown.

When 2 mM hSAF-p1 and 2 mM hSAF-p2 were mixed, the peptides formed a self-supporting hydrogel (Figure 3.1.2A). This gel was analysed by SEM, revealing a porous network (Figure 3.1.2B). This interconnected network resembled that reported previously (12, 140).

3.1 Assessing hSAFs as a platform for primary neuronal culture

As outlined in Chapter 1, the viscoelastic properties of a hydrogel (*i.e.* the gel stiffness) is an important consideration when designing a scaffold for cell culture. Different tissue types have different stiffnesses that make them suitable for a given cell type, and not another (63, 237) (Figure 1.2.2). Thus, a cytoscaffold of a given stiffness might support the growth of one cell type, while preventing that of another (68).

Hydrogel viscoelastic properties are typically measured by bulk rheology (238). Here, a hydrogel is exposed to small deformation forces, typically in the form of small amplitude oscillatory shear measurements, which yield values for the storage (elastic, G') and loss (viscous, G'') modulus of a material, based on its deformation upon exposure to a force (238, 239). A G' > G'' indicates the material behaves as an elastic solid, whereas a G'' > G' is indicative of viscous liquid-like behaviour. Thus, a G' > G'' for a hydrogel-forming material can be used to confirm gelation, and the elastic modulus (G') is typically stated as a measure of stiffness for such a material (239).

Bulk rheological analysis using small amplitude (0.01 – 10 Hz) oscillatory shear measurements was used to assay the elastic modulus of the parent hSAFs, previously reported to be ~1 kPa at room temperature (Figure 3.1.2C). When the peptides were mixed, a G' greater than G'' confirmed gel formation, and this remained true for all oscillation frequencies studied. Elastic moduli of 1.05 and 2.11 kPa were recorded at 20 and 37 ^{o}C, respectively, indicating that the gel stiffened slightly in response to an increase in temperature. This temperature-dependent increase in elastic modulus has been reported previously (12).

In summary, hSAF peptides prepared in this work are well folded and helical in solution, self-assemble into helical fibrous structures upon mixing, and form a soft hydrogel at room temperature, which stiffens slightly upon increasing the temperature to those relevant for cell culture. These observations are consistent with those previously reported and, thus, the parent hSAFs used herein are comparable to those used in previous studies (12, 140, 141).

hSAFs support the growth of primary neurons

hSAFs were assayed for their ability to support the growth of primary cortical neurons (PCNs), isolated from rat embryos, compared to other commercially available cell-culture materials. Two gels were chosen for comparison: Matrigel, a naturally derived gel commonly used as a cytoscaffold for many different cell types (81-83, 240); and Puramatrix, which, like hSAFs, comprises self-assembling peptides (56). These were chosen to cover the range of commercially available alternatives: Matrigel contains growth factors and other ECM components that should promote cell growth, while Puramatrix contains only the underlying structural peptides. Therefore, Matrigel is rather different to hSAFs and PCN growth was expected to be higher on Matrigel. On the other hand, Puramatrix is similar in make-up to hSAFs, and it was hoped our gel would compare favourably to it. Both have been reported to support PN growth (82-84, 86, 241, 242).

hSAFs, Puramatrix and Matrigel were compared for their ability to support the growth of PCNs by AlamarBlue assay and analysis of neurite length *via* widefield microscopy. AlamarBlue is a commonly used cell viability assay where a non-fluorescent, cell-permeable compound, resazurin, enters cells and is reduced to resorufin, a red-fluorescent compound (243). This reduction to the fluorescent form only occurs in viable cells and is, therefore, a measure of cell viability (Figure 3.1.3).

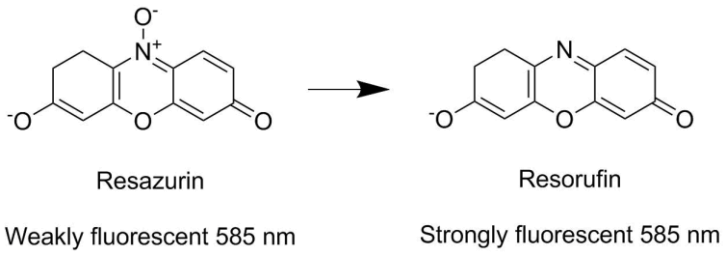

Figure 3.1.3: Chemical mechanism showing the reaction underpinning the AlamarBlue assay. The weakly fluorescent resazurin enters living cells and is reduced to resorufin, which is strongly fluorescent at 585 nm.

Like many such assays, disentangling cell viability from cell activity and number is difficult. However, as PNs are postmitotic and, therefore, do not divide, no increase in neuronal cell number should occur after seeding onto the scaffolds. Additionally, cells were co-stained for microtubule-associated protein 2 (MAP2) and glial fibrilliary associated protein (GFAP), which are specific for neuronal and glial cells, respectively. Thus, any increases in overall cell number contributed by glial cells – which do divide –

are accounted for. Neurite length was measured using the ImageJ tool NeuronJ and used as an additional indirect measure of neuronal health and growth (Figure 3.1.4).

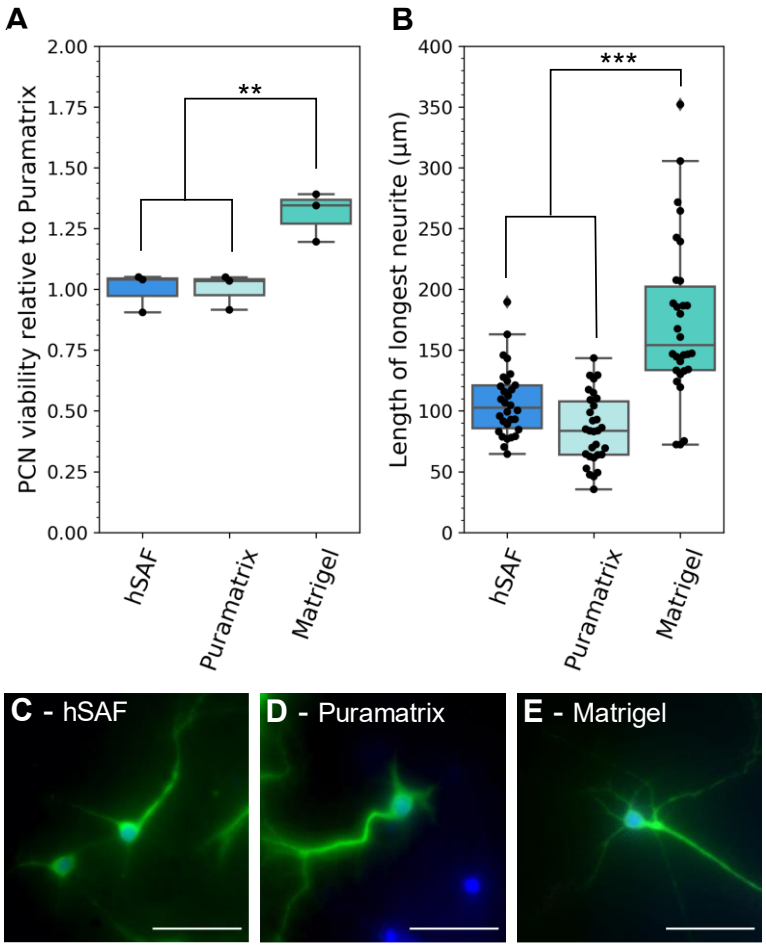

Figure 3.1.4: PCN viability and morphology on hSAFs, Puramatrix and Matrigel. **A:** Cell viability on the three gel types, determined by AlamarBlue assay, relative to Puramatrix. n = 3 measurements taken from 3 independent PCN cultures derived from 3 different rats. **B:** Length of the longest neurite for each analysed neuron on the three growth substrates. n=30 individual cells chosen randomly across the 3 different cultures. **C-E:** Representative widefield images of PN cultures on hSAFs **(C)**, Puramatrix **(D)** and Matrigel **(E)**. Scale bars are 50 µm. Cells were stained with DAPI (blue, nuclear), MAP2 (green, neuron-specific) and GFAP (magenta, glial cell-specific). Statistical analysis is by one-way ANOVA with Tukey's post-analysis. ** = P<0.01, *** = P<0.001.

PN viability and neurite outgrowth on hSAFs was comparable to that on Puramatrix: cell viability on the two gel types was very similar and median neurite length was 20 µm greater on hSAFs than on Puramatrix (Figure 3.1.4A-B). In contrast, cell viability and neurite length on Matrigel were significantly greater, with a 50% increase in median neurite length compared to hSAFs. As previously stated, the additional ECM components and growth factors in Matrigel are likely to promote neuronal growth and, therefore, these differences are to be expected. Very little glial growth was detected on any

of the scaffolds. This suggested, perhaps, that the GFAP antibody used did not bind to the target protein. However, binding was confirmed in PCN cultures grown under high-serum conditions that promote glial growth (Appendix, Figure 8.4.1). Due to the removal of serum from the medium shortly after initial cell seeding, the lack of glia in the PCN cultures (Figure 3.1.4) was unsurprising, and I was satisfied that glia were unlikely to contribute to the reduction of resazurin in the AlamarBlue assay.

These data suggest that hSAFs are a suitable culture substrate for PNs and are comparable to a commercially available peptide hydrogel (Puramatrix). However, the fact that Matrigel promotes neuronal growth to a greater extent suggests that the parent hSAFs are a suboptimal growth substrate for PNs. As outlined in Chapter 1.4, one of the major advantages of using a synthetic scaffold, such as hSAFs, is the ability to manipulate gel properties, either by introducing chemical adducts or by altering the underlying sequences of the peptides. By exploring both these avenues, I sought to optimise hSAFs for PN growth.

3.2: Assessing PCN responses to adhesion peptide-modified hSAFs

Peptides can be incorporated *via* Cu^{2+}-catalysed azide-alkyne cycloaddition (CuAAC)

The attachment, proliferation and growth of many cell types on synthetic scaffolds is improved by incorporating adhesion proteins and peptides into the gels (244). In particular, the fibronectin-derived peptide, RGDS, has been introduced into a range of cytoscaffolds and shown to have positive effects on cell growth (107, 151, 152, 157, 245). Previously, members of the Woolfson group have demonstrated increased attachment and proliferation of PC12 cells and NSCs on hSAFs when RGDS is incorporated into the scaffold *via* Cu^{2+}-catalysed azide-alkyne cycloaddition (CuAAC) (140, 141). Therefore, it was hypothesised that introducing RGDS or the laminin-derived adhesion peptide, IKVAV, into hSAFs might promote PN growth. Both of these ligands have previously been shown to do so in other systems (155, 226, 246).

CuAAC involves the reaction of an azide with a terminal alkyne, catalysed by the addition of Cu^{2+} ions, forming a covalent complex (Figure 1.4.1A). Cu^{2+} is typically provided *via* the reduction of $CuSO_4$ by a reducing agent such as sodium ascorbate (NaAsc) (144). This reaction occurs relatively quickly under ambient conditions, making it suitable for modification of hSAFs, where excessive heating or changes in pH might disassemble the gel. Cu^{2+} is cytotoxic. However previous work demonstrated effective removal of Cu^{2+} by stringent washes with EDTA, followed by PBS (140) prior to cell seeding. Therefore, CuAAC was adopted for hSAF decoration in this work.

A

Heptad repeat	*g abcdefg abcdefg abcdefg abcdef*
hSAF-p1KAz	H-KzIAALKAK IAALKAE IAALEWE NAALEA-COOH
hSAF-p2	H-K IAALKAK NAALKAE IAALEWE IAALEA-COOH

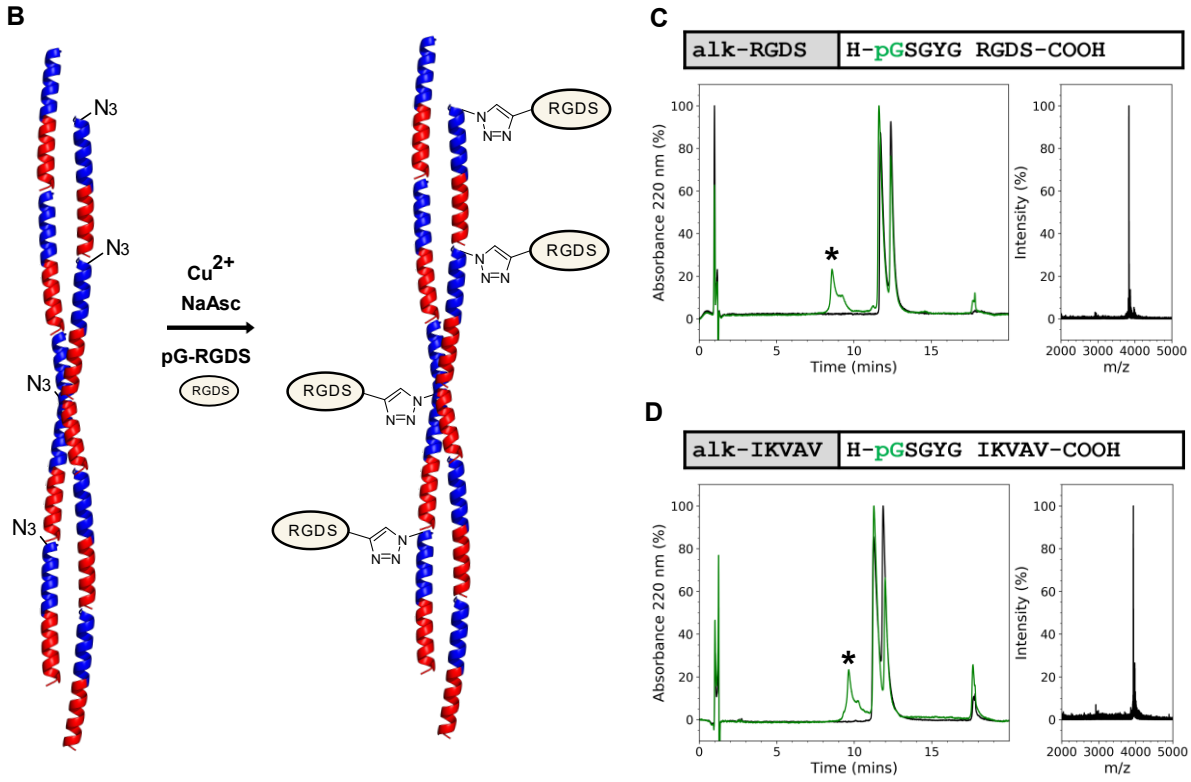

Figure 3.2.1: CuAAC-mediated decoration of hSAFs with adhesion peptides. **A:** Table showing sequences for hSAF-p1KAz and hSAF-p2, with the azidonorleucine residue highlighted in green. **B:** Schematic diagram showing CuAAC-mediated decoration of hSAFs with RGDS peptide. N_3 = azide group. **C:** Sequence of alk-RGDS, along with HPLC chromatograms for p1KAz:p2 hSAF (black) and p1KAz:p2 hSAF reacted with alk-RGDS by CuAAC (green). The mass spectrum is for the product peak labelled * (Expected mass = 3841.0 Da, recorded mass = 3840.2 Da). **D:** Sequence of alk-IKVAV along with HPLC chromatograms for p1KAz:p2 hSAF (black) and p1KAz:p2 hSAF reacted with alk-IKVAV (green). The mass spectrum is for the product peak labelled * (expected mass = 3936.3 Da, recorded mass = 3935.6 Da).

An azide-modified variant of hSAF-p1 was synthesised with an azidonorleucine (Kz) in-place of the *N*-terminal Lys residue (Figure 3.2.1A). This peptide was named hSAF-p1KAz. RGDS and IKVAV sequences were synthesised, both preceded by a flexible linker (GSGYG) to provide space between the hSAF fibres and the cell-adhesion sequence (140). These peptides contained an *N*-terminal propargylglycine (pG) residue, which possesses a side-chain alkyne (Figure 3.2.1C-D). All structures of unnatural amino acids and functional groups used in this work are listed in Chapter 2.1.

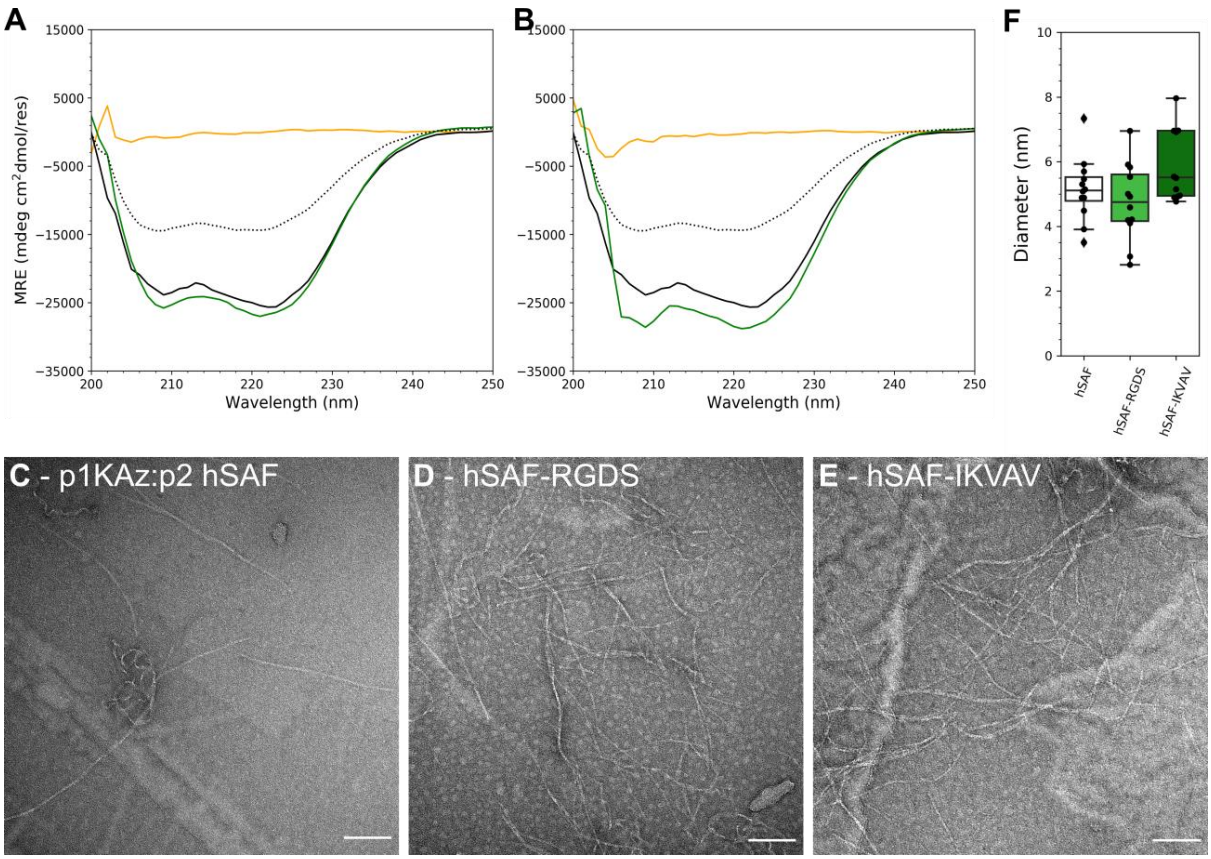

Figure 3.2.2: Biophysical characterisation of CuAAC-modified hSAFs. **A-B:** CD spectra of p1KAz:p2 hSAFs (black), alk-RGDS (**A**, yellow) or alk-IKVAV (**B**, yellow), the theoretical average of combining p1KAz:p2 hSAFs with either adhesion peptide (grey, dotted) and the recorded spectra when p1KAz:p2 hSAFs were mixed with either adhesion peptide, $CuSO_4$ and NaAsc. **C-E:** TEM images of unreacted p1KAz:p2 fibres **(C)** and those after reaction with alk-RGDS **(D)** or alk-IKVAV **(E)**. Scale bar is 100 nm. **F:** Box plot showing fibre diameters, n=10 fibres chosen at random across multiple images. Fibres were measured manually in ImageJ.

The reaction between p1KAz:p2 hSAFs and these adhesion peptides (Figure 3.2.1B) was probed by HPLC and MALDI-TOF-MS (Figure 3.2.1C-D). For both reactions, a product peak was detected by HPLC only when $CuSO_4$ and NaAsc were added to the reaction. These peaks were analysed and corresponded to the masses of the covalent complexes p1KAz-RGDS (Figure 3.2.1C) and p1KAz-

IKVAV (Figure 3.2.1D). The percentage of hSAF-p1KAz converted to these products was calculated to be ~45% based on the relative peak sizes for the reacted versus unreacted gels.

To confirm that the adhesion peptides were incorporated into hSAFs without impacting fibre stability, CD spectra and TEM images of RGDS- and IKVAV-decorated fibres were recorded. CD spectroscopy showed little change in α-helical character upon reaction of either peptide, both of which were unstructured in isolation (Figure 3.2.2A-B). In addition, TEM revealed no significant alteration in fibre morphology (Figure 3.2.2C-E). The average fibre diameter remained around 5 nm (Figure 3.2.2F), as observed in Chapter 3.1.1. These analyses confirm that CuAAC-mediated introduction of adhesive ligands does not destabilise hSAFs.

PCN growth is not promoted by the addition of adhesion peptides

PCN responses to adhesion peptide-decorated hSAFs were assessed in the same way as outlined in Chapter 3.1.1. PCNs were seeded onto undecorated, RGDS- or IKVAV-decorated hSAFs. Despite stringent washing with EDTA and PBS, I wanted to be sure that the non-peptide components of CuAAC were not influencing PCN growth. Therefore, PCNs were also seeded onto gels, treated in the same way as those decorated with RGDS or IKVAV (*i.e.* incubated with $CuSO_4$ and NaAsc), but without addition of the adhesion peptide. Puramatrix and Matrigel were used as positive controls (Figure 3.2.3).

No significant difference in cell viability or neurite length was observed on gels decorated with either RGDS or IKVAV. In fact, there was a small, though not significant, decrease in viability and neurite length when hSAFs were decorated with either adhesion peptide or incubated with $CuSO_4$ and NaAsc alone (Figure 3.2.3A-B). While this might suggest a detrimental effect of the CuAAC reaction components on PN growth, it should be noted that this reduction in viability in response to CuAAC, was not seen in similar assays described in Chapter 4. Nonetheless, I investigated an alternative, Cu^{2+}-free, mechanism for immobilising peptides on hSAFs, the details of which are outlined in Chapter 5.

Irrespective of this, the adhesion peptides assayed here had no growth-promoting effects on PNs. The comparisons with Puramatrix (Figure 3.1.4) suggest that neurons can associate with the amino acids presented by the hSAF peptides to a great enough extent that these additional adhesive ligands are not

required for cell growth. Therefore, I reasoned that their incorporation was unnecessary for downstream experiments with PNs.

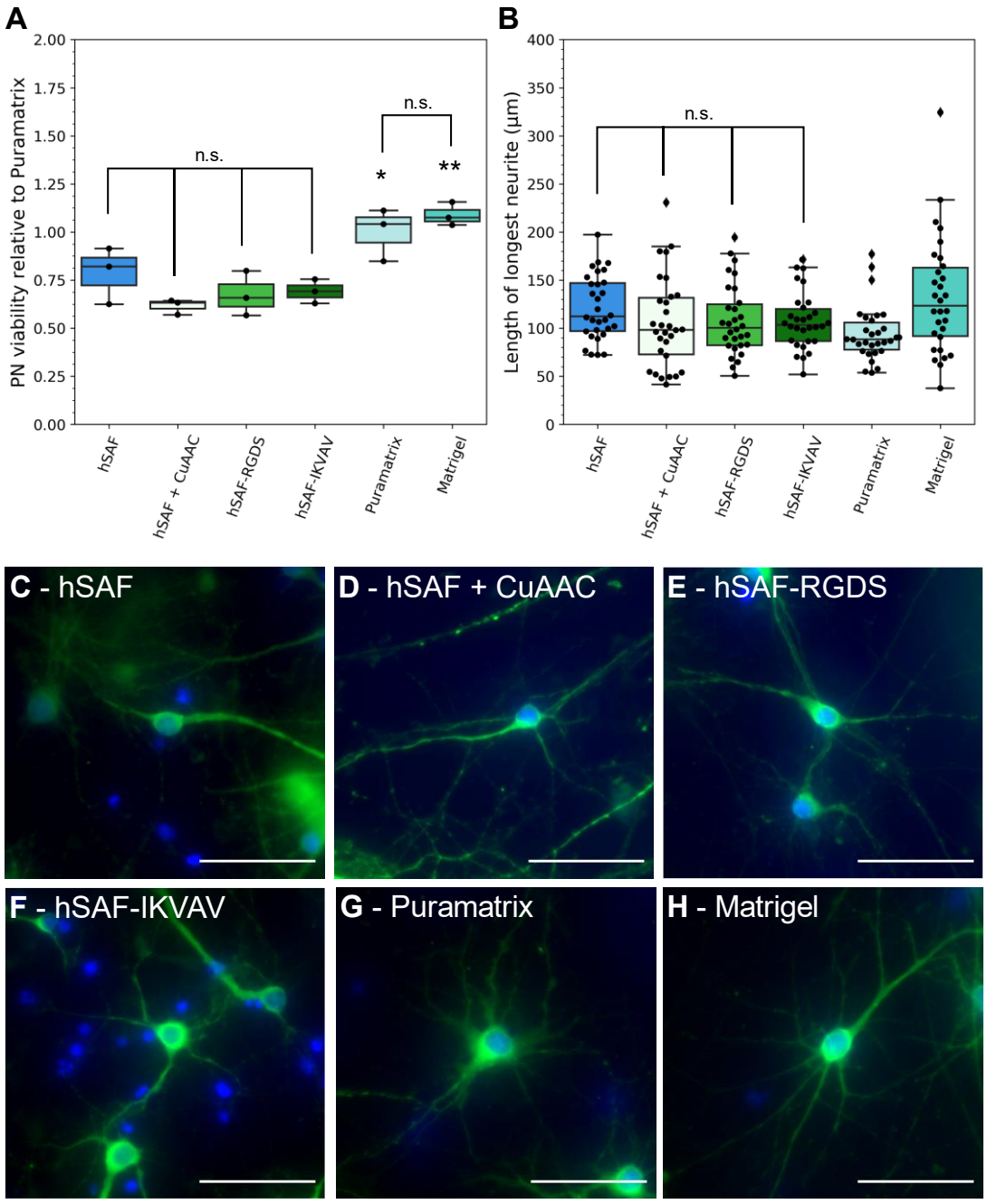

Figure 3.2.3: PCN responses to hSAFs decorated with RGDS and IKVAV peptides. **A:** Box plot showing AlamarBlue cell viability assay results for cells seeded onto the different hSAFs, Puramatrix and Matrigel. Readings were normalised to those for Puramatrix, n=3 measurements taken from 3 independent PCN cultures derived from 3 different rats. **B:** Box and volcano plots showing the length of the longest neurite measured for each analysed neuron on the different gels. Analysis was performed manually using NeuronJ, n=30 individual cells, chosen randomly across the 3 dissections. **C-H:** Representative widefield fluorescence images of neurons on the different gels. Blue = DAPI, green = MAP2 and magenta = GFAP. Scale bars are 50 µm. Statistical analysis was by one-way ANOVA with Tukey's post analysis. n.s. = not significant.

3.3: Modulating gel stiffness

Much of the work in the following section – namely the redesign of hSAFs to form stiffer gels, all rheological and SEM analyses – was conducted by Dr Alex Wasmuth, a previous member of the Woolfson group. All other biophysical characterisation and cell studies were performed by me. I am grateful for Alex's contribution to this work and thank her for beginning this project prior to my arrival in the Woolfson lab.

The stiffness of hSAFs can be altered by peptide concentration

As stated in Section 3.1.1, the elastic modulus of parent hSAFs is ~1 kPa at room temperature. This characterises hSAFs as a soft gel with viscoelastic properties analogous to brain tissue, which is widely reported to range from 0.1-1 kPa in stiffness (68-71). This value varies with age and brain region and depends upon the measurement technique used, with values as high as 16 kPa reported in particular contexts (67, 247). Many neuronal behaviours such as neurite extension, differentiation and axonal direction are reported to vary with substrate stiffness and subtle local changes thereof (102, 154, 248-250). Producing gels of varying elastic modulus would not only allow the study of neuronal responses to such changes, but also the generation of scaffolds that are best suited to different cell types, such as muscle (3-15 kPa) or bone (20 kPa – 2 GPa) (66). These stiffer scaffolds would have applications in tissue engineering and *in vitro* cell culture, similarly to the 1 kPa system. Therefore, we sought to form hSAF gels with altered elastic modulus.

It was hypothesised that varying the peptide concentration would be one way in which this might be achieved. It was reasoned that increasing hSAF peptide concentration could result in a higher density of fibres upon mixing, resulting in a greater number of interactions between adjacent fibres, and increased strength of the assembled scaffold. This method has been exploited extensively for other gel types (102, 154, 162, 249).

Parent hSAF gels contain 1 mM of each peptide. Therefore, to explore the possibility of forming softer and stiffer gels, hSAFs were formed with 0.5 and 1.5 mM each peptide. 0.5 mM appeared to be the minimum concentration required for visible gelation, while the peptides precipitated upon increasing

concentration above 1.5 mM. We compared the elastic moduli of these gels with parent hSAFs (1 mM) *via* bulk rheological analysis (Figure 3.3.1).

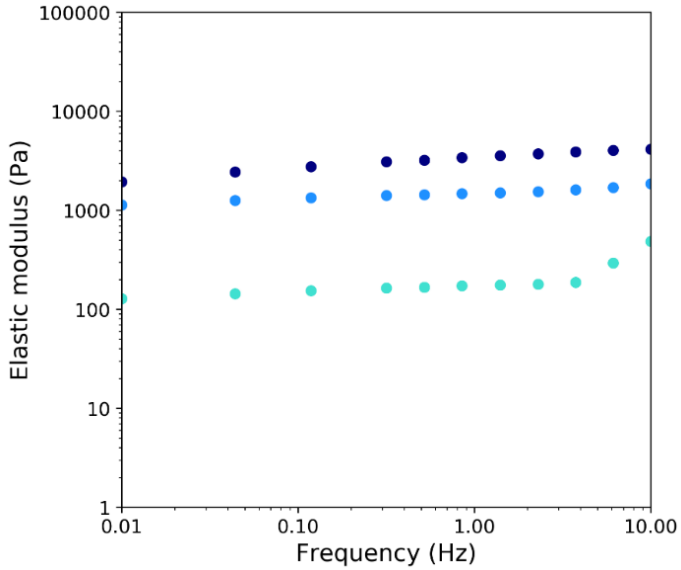

Figure 3.3.1: Frequency sweep rheological analysis showing elastic modulus (G') values for parent hSAFs at 0.5 (turquoise), 1 (light blue) and 1.5 (navy) mM. All readings were taken at 20 ºC and using 0.5% strain. This data was collected by Alex Wasmuth.

Reducing the concentration of peptide to 0.5 mM gave a gel with an elastic modulus of 0.17 kPa, while increasing the concentration to 1.5 mM yielded a 2.01 kPa gel. Relatively speaking, these gels are all soft; roughly equivalent to brain – endothelial tissue (66). hSAF-p1 and -p2 are rationally designed based on our firm understanding of coiled-coil assembly. One of the primary benefits of working with such a well-defined system is the ability to tune gel properties by further design of the underlying peptides. Therefore, it was reasoned that stiffer hSAF gels might be accessible by redesigning the α-helical peptide components.

Redesigning hSAFs for the formation of stiffer gels

As outlined in Chapter 1, the dimeric coiled-coil heptad repeat has an hpphppp pattern of hydrophobic (h) and polar (p) residues, often denoted *abcdefg* (Figure 3.3.2). In hSAFs, *a* and *d* residues provide the hydrophobic interface for dimer assembly, while *e* and *g* residues form complementary salt bridges to help specify offset dimer formation (34). Therefore, these residues are essential for coiled coil and fibre self-assembly and were left unmodified. On the other hand, the *b*, *c* and *f* residues are positioned away

from the coiled-coil interface allowing modification without impacting dimeric assembly (Figure 3.3.2).

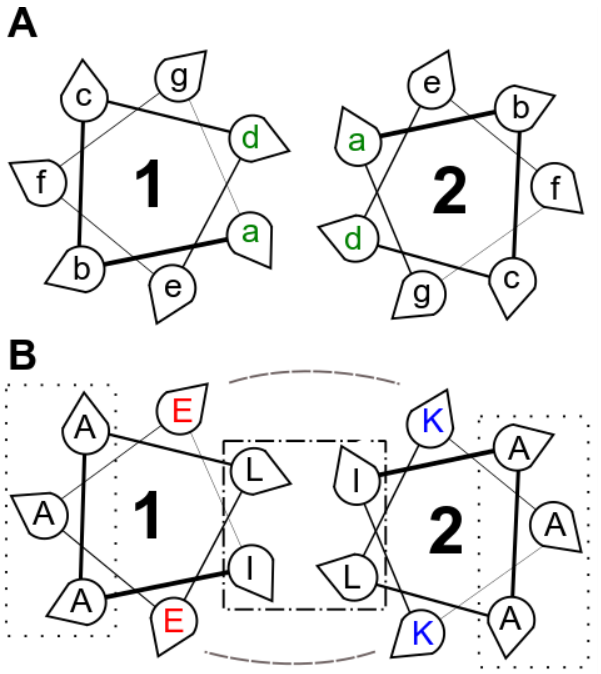

Figure 3.3.2: Helical wheel diagrams showing coiled-coil assembly. **A:** Residues are denoted *abcdefg* according to their position around the helix. Hydrophobic and polar residues are coloured green and black respectively. **B:** Position of polar and hydrophobic residues in hSAFs. The hydrophobic dimer interface is indicated by the dot-dashed line, with salt bridging residues indicated by a dashed line between Glu and Lys residues. Dotted lines indicate the *b*, *c* and *f* position residues, away from the dimer interface, which might be altered.

SAF peptides contain charged and polar residues at *b*, *c* and *f* positions that promote electrostatic interactions between fibres, leading to extensive lateral assembly and thick, crystalline fibres (34, 41). In contrast, hSAF peptides contain Ala residues at the *b*, *c* and *f* positions, with a single Trp in the third heptad *f* position. The design rationale is that these Ala/Trp surfaces promote non-specific and relatively weak hydrophobic interactions between adjacent fibres (12). This leads to little lateral assembly, narrow fibres (Figure 3.1.1) and hydrogel formation. It was reasoned that by incorporating additional Trp residues into further heptads of the hSAF peptides, hydrophobic interactions between fibres would be increased, possibly leading to stiffer gels (Figure 3.3.3).

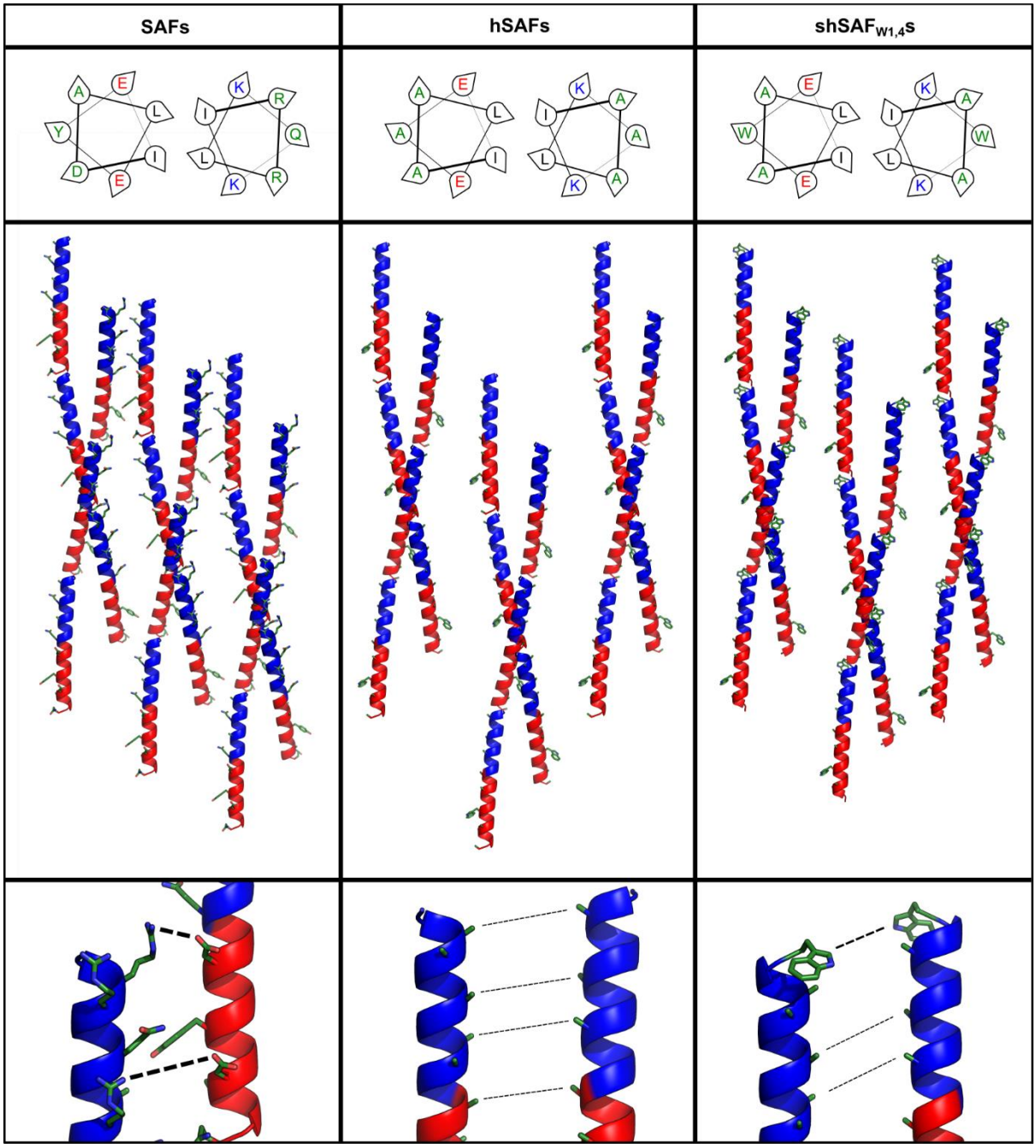

Figure 3.3.3: Lateral assembly of individual coiled-coil fibrils into fibres in SAFs, hSAFs and the newly proposed shSAF$_{W1,4}$s. Upper panels show helical wheels for the first heptad of SAFs, hSAFs and shSAF$_{W1,4}$s. Middle and lower panels depict the proposed methods of lateral assembly in each system, as described in the text. *b*, *c* and *f* position residues are shown in green and dotted lines indicate proposed electrostatic (SAFs) and hydrophobic (hSAFs and shSAF$_{W1,4}$s) interactions between residues on adjacent fibres. Models of SAF, hSAF and shSAF$_{W1,4}$ peptides were created using the web-based coiled coil modelling software CCBuilder 2.0 (251).

Previous work in the group indicated that incorporating an additional Trp residue into any of the remaining three *f* positions leads to precipitation of the peptides in solution. However, by shifting the peptide register to start at an *f* position, an additional Trp could be tolerated in the first heptad to yield

relatively water-soluble peptides. These are called shifted hydrogelating self-assembling fibres (shSAF$_{W1,4}$s) (Table 3.3.1).

Heptad repeat	*fgabcde fgabcde fgabcde fgabcde f*
hSAF-p1	H- KIAALK AKIAALK AEIAALE WENAALE A-COOH
hSAF-p2	H- KIAALK AKNAALK AEIAALE WEIAALE A-COOH
shSAF$_{W1,4}$-p1	H- WKIAALK AKIAALK AEIAALE WENAALE -COOH
shSAF$_{W1,4}$-p2	H- WKIAALK AKNAALK AEIAALE WEIAALE -COOH

Table 3.3.1: hSAF and shSAF$_{W1,4}$ peptide sequences. *f* position Trp residues are highlighted in green.

Biophysical characterisation of shSAF$_{W1,4}$ peptides and fibres

These newly designed peptides showed α-helical character by CD spectroscopy and were both well-folded (Figure 3.3.4), and shSAF$_{W1,4}$-p1 was more folded than the parent hSAF-p1 peptide (Figure 3.1.1B). However, unlike the parent system, the 222 nm minima were pronounced in both shSAF$_{W1,4}$ peptides, and red-shifted in the case of shSAF$_{W1,4}$-p2, which suggested the peptides self-assembled into higher order structure prior to their mixing. Despite this potential homomeric self-assembly, the CD spectra of the mixed peptides did not overlay closely with the theoretical average of the two individuals, indicating that the peptides interacted at 20 °C, similarly to the parent system. Thermal denaturation of the peptides confirmed this observation, with the peptide mixture appearing marginally more stable than the individual peptides (Figure 3.3.4B). Both peptides and their mixture adopted β structure upon heating above ~60 °C and, therefore, accurate melting temperatures could not be extracted (Figure 3.3.4C).

TEM analysis of the mixed peptides revealed fibre formation (Figure 3.3.4F). These were similar in diameter to hSAFs (Figure 3.3.4G). However, the new fibres appeared to bundle into larger ribbon-like structures. This is consistent with our design principle: fibres associate more readily upon insertion of the additional Trp residue. TEM analysis of the individual peptides revealed that shSAF$_{W1,4}$-p1 also formed similar fibres, though no such structures were observed in preparations of hSAF$_{W1,4}$-p2

Both CD and TEM analyses indicate that shSAF$_{W1,4}$ peptides have propensity to self-assemble into higher order structure in isolation. However, these analyses also indicate that the peptides do interact,

suggesting that complementary salt-bridges between *e* and *g* residues and hydrogen bonds between Asn residues in the core of each peptide promote heterodimeric coiled-coil assembly as designed in the parent system. It should be noted that, in preparation of samples for TEM, deposition onto a TEM grid results in a rapid increase in the effective peptide concentration on the surface, which might push the peptides towards self-assembly.

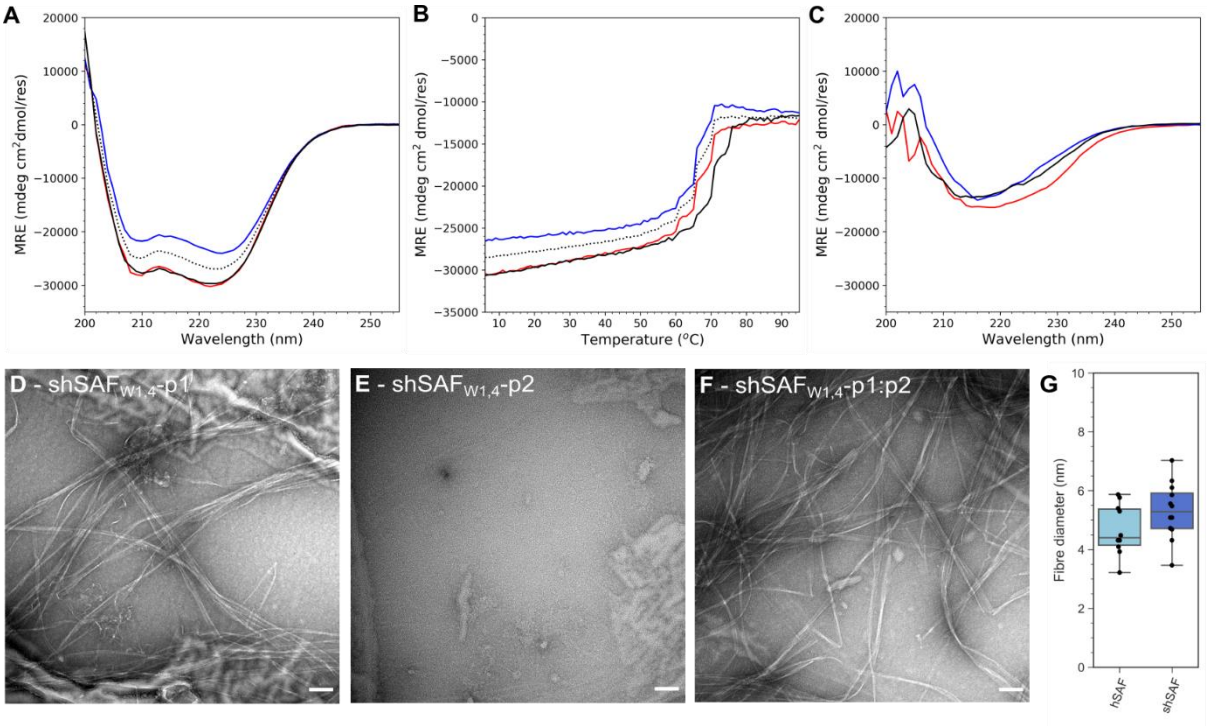

Figure 3.3.4: Solution phase characterisation of shSAF$_{W1,4}$s. **A-C:** CD spectra at 20 °C **(A)**, thermal melt curve **(B)** and CD spectra at 5 °C post-melt **(C)** for the individual shSAF$_{W1,4}$ peptides (p1 = red and p2 = blue) and mixture (black). Theoretical averages of combing the shSAF$_{W1,4}$-p1 and -p2 spectra are shown (grey, dotted). **D-F:** TEM images of shSAF$_{W1,4}$-p1 **(D)**, shSAF$_{W1,4}$-p2 **(E)** and the mixture **(F)**. Scale bar is 100 nm. **G:** Box plot showing diameter of hSAF and shSAF$_{W1,4}$ fibres, n=10 fibres chosen at random across multiple images.

While satisfying that the peptides appear to self-assemble as designed, our primary concern was the generation of hydrogels with increased elastic modulus. Therefore, I assayed the individual peptides, and the mixture, for their propensity to form a self-supporting hydrogel, *via* an inversion experiment (Figure 3.3.5). The individual peptides did not gel, whereas the mixture formed a self-supporting hydrogel when incubated overnight at 4 °C, according to the preparation protocol for parent hSAFs.

Taken together, the above experiments indicate that shSAF$_{W1,4}$ peptides are helical and well-folded in solution, similarly to the parent hSAFs. The peptides self-assemble upon mixing to form fibrous

structures (Figure 3.1.1E). These data also suggest that the individual peptides self-assemble in isolation but are nonetheless able to interact upon mixing (Figure 3.3.4). Given that these homomeric assemblies do not form a self-supporting hydrogel, I propose that fibre formation in these preparations is sufficiently rare, or the fibres formed are sufficiently unstable, to prevent gel formation. Upon mixing, heterodimer assembly should be more favoured and therefore the equilibrium will be pushed towards the fibrous state and gel formation can occur. As the aim of this work was to design hydrogels with increased elastic modulus, the mechanism of homofibre assembly was not probed further. Instead, we proceeded to characterise the elastic modulus of shSAF$_{W1,4}$ gels.

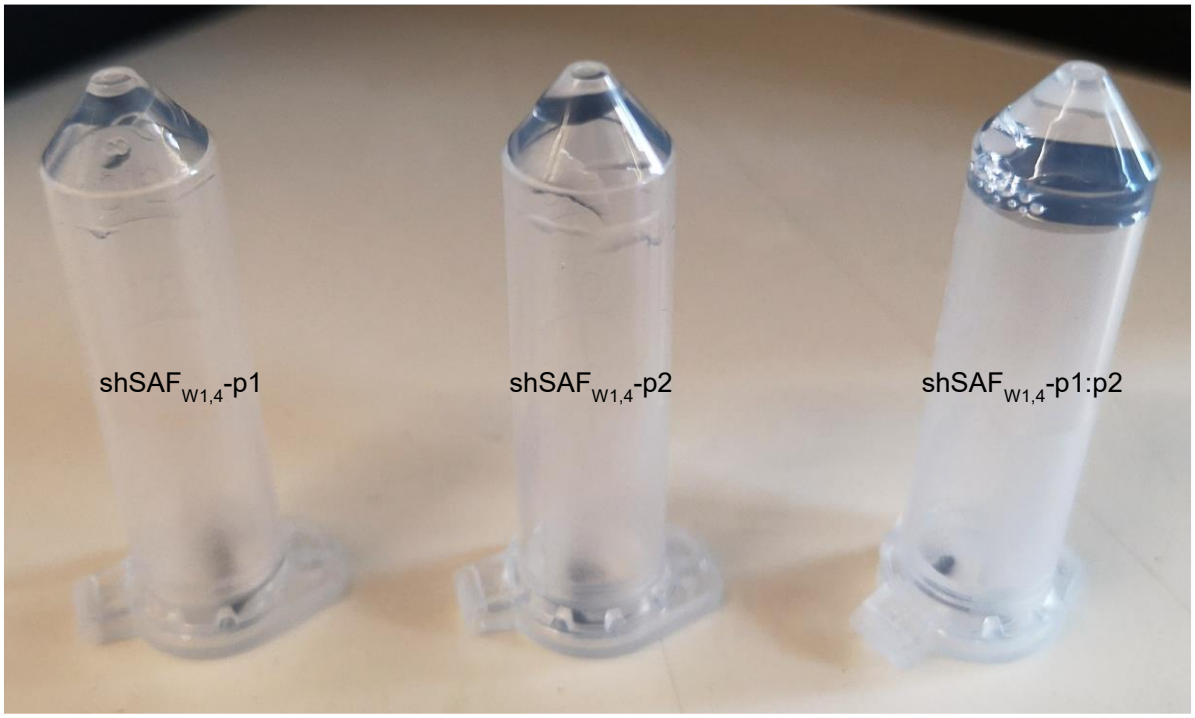

Figure 3.3.5: Photograph showing a gel-inversion assay for the individual shSAF$_{W1,4}$ peptides and the mixture.

shSAF$_{W1,4}$s can be used to form hydrogels with increased elastic modulus

Bulk rheological analysis was performed on shSAF$_{W1,4}$ samples made with 0.5, 1 and 1.5 mM each peptide (Figure 3.3.6). This demonstrated that these peptides formed gels with elastic moduli of 1.99, 3.73 and 18.32 kPa, respectively. Therefore, shSAF$_{W1,4}$s form hydrogels with increased elastic moduli compared to hSAFs, which are comparable to endothelial (1.99 kPa), fat (3.73 kPa) and muscle (18.32 kPa) tissues (63, 66).

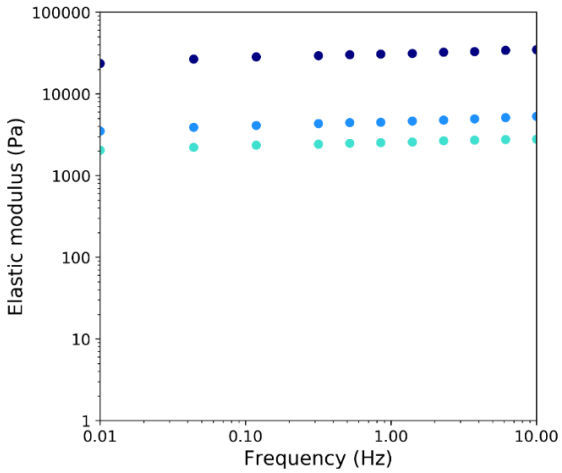

Figure 3.3.6: Bulk rheology comparing elastic moduli (G') of 0.5 mM (turquoise), 1 mM (blue) and 1.5 mM (navy) shSAF$_{W1,4}$s. All readings were taken at 20 °C and 0.5% strain. Data was collected by Alex Wasmuth.

Taking rheology data for both hSAFs and shSAF$_{W1,4}$s together, we can produce a suite of gels ranging from 0.17 – 18.32 kPa, analogous to brain – muscle tissue (Figure 3.3.7). Complete data for each gel type, showing G' and G'' values, are listed in Appendix Figure 8.4.2.

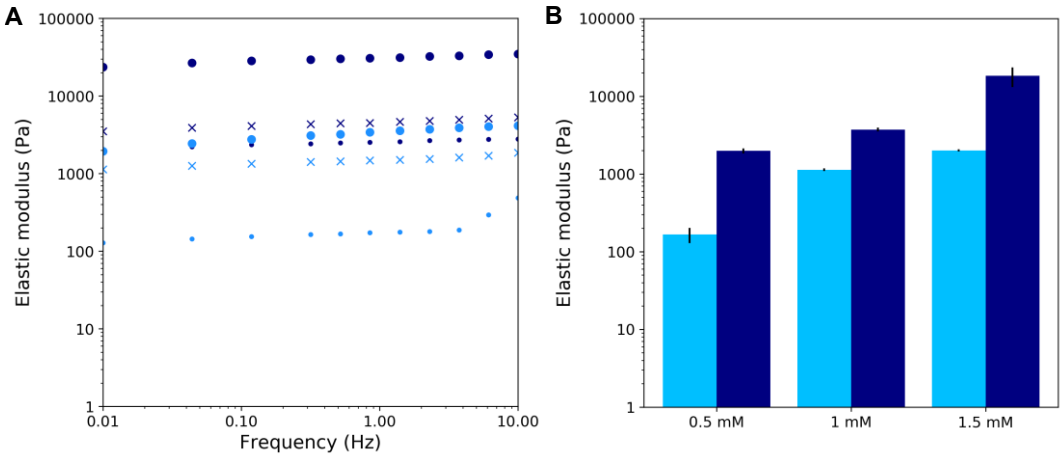

C

Gel type	Peptide concentration (mM)	Recorded mean G' (kPa)
hSAF	0.5	0.17
hSAF	1	1.13
hSAF	1.5	2.01
shSAF$_{W1,4}$	0.5	1.99
shSAF$_{W1,4}$	1	3.73
shSAF$_{W1,4}$	1.5	18.32

Figure 3.3.7: Bulk rheology data for hSAF and shSAF$_{W1,4}$ gels. **A:** Examples of frequency sweep data showing G' values for hSAFs (light blue) and shSAF$_{W1,4}$s (navy) with 0.5 (small dots), 1 (crosses) and 1.5 (large dots) mM peptide at 0.01-10 Hz. **B:** Replicate elastic moduli data recorded at 0.01 Hz, n=3, error bars show one standard deviation. Light blue = hSAFs; navy = shSAF$_{W1,4}$s. **C:** Table listing mean recorded elastic moduli at 0.01 Hz for the six different gel types. Data was collected by Alex Wasmuth.

The macrostructure of these gels was examined by SEM, which revealed the formation of porous, interconnected networks for each gel (Figure 3.3.8). Gross scaffold morphology did not appear to vary between hSAFs and shSAF$_{W1,4}$s. However, the obvious fibrous structures visible in 0.5 and 1 mM preparations were less distinct in both 1.5 mM gels. As previously mentioned, 1.5 mM is at the limit of solubility for both these peptide systems and it seems likely that a reduction of distinct fibrous structure by SEM might be a result of some aggregation of the peptides prior to or during scaffold assembly.

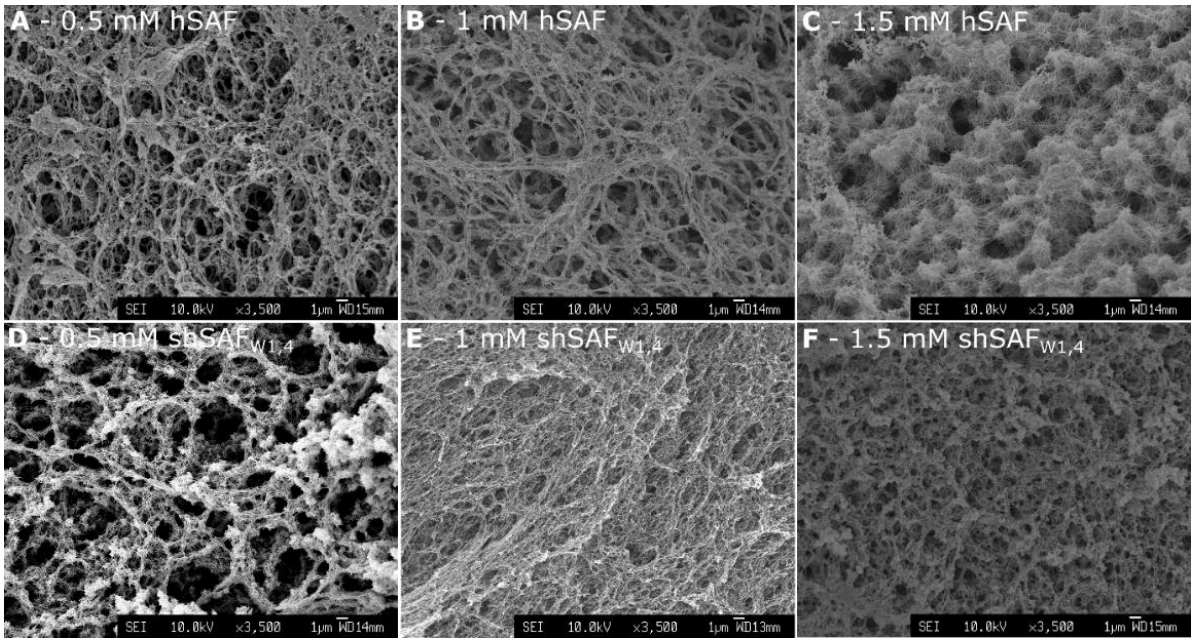

Figure 3.3.8: SEM images of 0.5 mM **(A)**, 1 mM **(B)** and 1.5 mM **(C)** hSAF and 0.5 mM **(D)**, 1.0 mM **(E)** and 1.5 mM **(F)** shSAF$_{W1,4}$ scaffolds. These data were collected by Alex Wasmuth.

Assessing primary neuronal responses to hSAF and shSAF$_{W1,4}$ gels of varying stiffness

Brain tissue typically ranges from 0.1 – 1 kPa, and neuronal development is largely reported to be promoted on growth substrates of stiffness within this range (252-254); though exceptions to this have been reported (153). Neurite outgrowth also depends on tissue elastic modulus, and it has been suggested that soft substrates (<1 kPa) promote neurite extension (102, 255). However, some reports suggest slightly stiffer growth substrates (≥1 kPa) promote neurite extension (153, 250). It seems likely then that neuronal development depends upon tissue stiffness, but the exact cellular responses observed are likely context and cell-type dependent.

3.3 Modulating gel stiffness

With the suite of hSAF and $shSAF_{W1,4}$ gels in hand, PCN responses to changes in growth substrate stiffness were analysed. As such PCNs were seeded onto 0.5 and 1.0 mM hSAF and 1.0 and 1.5 mM $shSAF_{W1,4}$ gels. These concentrations were selected to cover the range of possible elastic moduli accessible with these two gel systems; *i.e.* 0.17, 1.13, 3.73 and 18.32 kPa, respectively. Puramatrix was included as an additional control. Cell viability and neurite length after 14 days in culture were assessed by AlamarBlue assay and widefield microscopy, respectively, as outlined in Chapter 3.1 (Figure 3.3.9).

PCN viability was significantly greater on both 0.17 kPa and 1.13 kPa hSAFs compared to either $shSAF_{W1,4}$ gel, where an ~50% reduction in viability was observed. This supports literature suggesting neurons are most viable on soft gels with elastic moduli analogous to that of neuronal tissue (252-254). Neurite length was significantly increased on 1.13 kPa hSAFs when compared with 0.17 kPa hSAFs or 3.73 kPa $shSAF_{W1,4}$s (Figure 3.3.9B). This indicates that slightly stiffer gels, which possess a G' value close to the upper bound of bulk brain tissue (1 kPa), promote neurite extension, and similar findings have been reported previously (153, 250, 256).

Neurite length was also significantly greater on 18.32 kPa $shSAF_{W1,4}$s than 0.17 kPa hSAFs (Figure 3.3.9B). Promotion of neurite growth on gels that possess an elastic modulus so far from the normal range for brain tissue was unexpected, particularly as overall cell viability appeared low. However, similar small increases in neurite extension of cortical progenitors have been observed on similarly stiff growth substrates, though this was also accompanied by an increase in cell viability (153). PCN cultures are heterogeneous and will contain subpopulations of neurons that may respond differently to changes in environment. It is possible that, while most cells are unable to develop on these stiffer substrates (leading to reduced cell viability (Figure 3.3.9A)), the growth of certain neuronal subtypes is promoted. This is an interesting observation that warrants further study.

It is entirely possible that the reduction in viability on $shSAF_{W1,4}$s is simply a result of using a different peptide or gel type, rather than a result of a difference in stiffness *per se*. To investigate this, PCNs were seeded onto 1.5 mM hSAF and 0.5 mM $shSAF_{W1,4}$ gels. These possess very similar elastic moduli (2.01 and 1.99 kPa, respectively), but utilise the two different peptide systems: hSAFs and $shSAF_{W1,4}$s (Figure 3.3.9G).

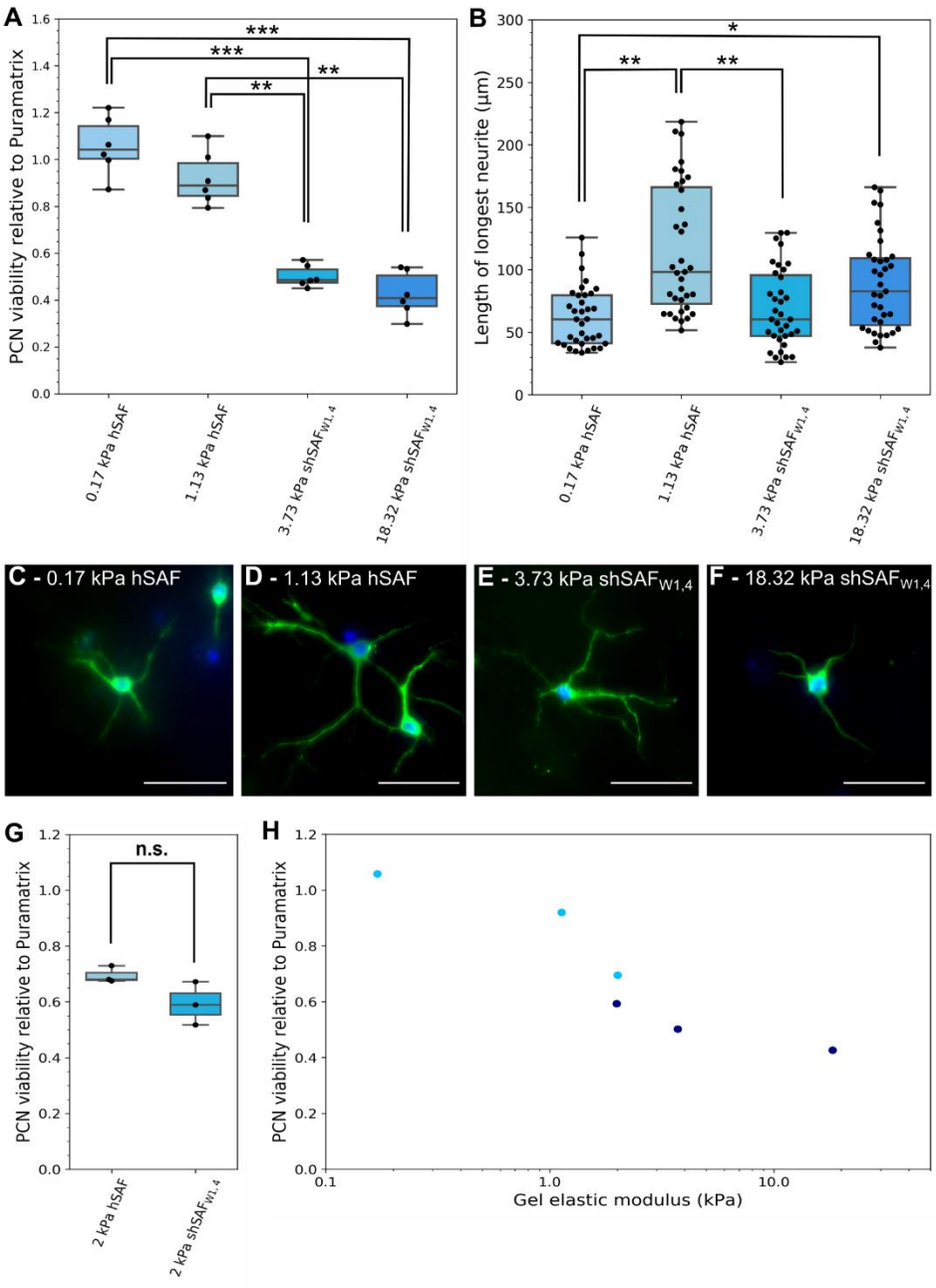

Figure 3.3.9: PCN responses to gels of varying stiffness. **A:** Box plot showing PCN viability on the four different gel types, relative to that on Puramatrix. n=6 measurements taken from 6 independent PCN cultures derived from 6 different rats. **B:** Box plot showing neurite length analysis for the longest neurite of each analysed cell. n=35 individual cells chosen at random across the 6 different dissections. **C-F:** Widefield images of PCNs on 0.17 kPa hSAFs **(C)**, 1.13 kPa hSAFs **(D)**, 3.73 kPa shSAF$_{W1,4}$s **(E)** and 18.32 kPa shSAF$_{W1,4}$s **(F)**. Scale bar = 50 µm. Blue = DAPI, green = MAP2 and magenta = GFAP. **G:** Box plot showing PCN viability on hSAF and shSAF$_{W1,4}$ gels of ~2 kPa stiffness. n=3 independent measurements. **H:** Plot of PCN viability against gel elastic modulus. All statistical analyses were by one-way ANOVA with Tukey's post analysis. * = P<0.05, ** = P<0.01, *** = P<0.001. n.s. = not significant.

There was no significant difference in PCN viability on these two gel types, with both values between those for 1.13 and 3.73 kPa gels. This suggested the changes in viability observed were responses to

gel stiffness, rather than to shSAF$_{W1,4}$s. Plotting cell viability against elastic modulus indicates that PCN viability decreases with increasing elastic modulus in a sigmoidal fashion (Figure 3.3.9H). Taken together, these data demonstrate that PCNs are most viable on growth substrates with elastic moduli that lie close to the typical range of brain tissue (0.1-1 kPa). Neurite extension by these cells is greatest on gels that are at the upper end of this stiffness range.

3.4: Conclusions

Unmodified hSAFs support the growth of PCNs to a comparable degree to Puramatrix, a commercially available and established hydrogel for neuronal culture (241, 242). The addition of adhesion peptides does not further promote cell growth, indicating that PCNs are able to adhere to hSAFs without additional ligands. These studies demonstrate the applicability of hSAFs as a culture substrate for PNs – which presents a considerable challenge – and are a step forward from previous studies with neuronal-like cell types (140, 141). It is worth reiterating that hSAFs are one of a small number of *de novo*-designed peptide cytoscaffolds (44, 48, 54, 56, 158) and one of even fewer that utilise α-helical structured peptides (142). While PNs have been cultured on other designed peptide scaffolds (136, 257, 258), to my knowledge, this is the first example of PN growth on a *de novo*-designed α-helical peptide hydrogel. As such, this work demonstrates the power of *de novo* peptide design as a method for novel cytoscaffold generation.

While these comparisons with another designed peptide gel (Puramatrix) are promising, Matrigel promotes neuronal development to a greater extent, indicating that hSAFs are a suboptimal growth substrate for PNs. Matrigel contains extracellular growth factors that promote neuronal development, and I propose that neuronal growth might be further stimulated by incorporating these growth factors into hSAFs. I investigate this possibility in Chapter 4.

Through the redesign of hSAFs to form shSAF$_{W1,4}$s, we have produced gels ranging from 0.17-18.32 kPa. Other examples of gel stiffness variation by rational redesign of peptide sequences, rather than variations in peptide cross-linking, buffer constituents or peptide concentration (135, 259-261),

exist (133, 135, 163). However, these modifications normally result in small changes to gel elastic modulus (133, 135, 163). In contrast, here we have generated peptide scaffolds that cover a large range of stiffnesses without additional non-peptide modifications or formation of a composite (260, 262, 263). Therefore, this study demonstrates that hSAFs are amenable to redesign of the underlying peptide architecture and, consequently, can be used to form gels that cover a large range of elastic moduli. By culturing PCNs on these scaffolds, I have contributed to the growing hypothesis that neurite outgrowth is promoted by relative increases in brain tissue stiffness (153, 250, 256). However, the stiffness of $shSAF_{W1,4}$ gels aligns with that of fat and muscle tissue (Figure 1.2.2) (66) and, therefore, these scaffolds are likely to be better suited to the culture of these cell types. I would like to assess muscle cell responses to scaffolds of varying stiffness. I hypothesise that growth of these cells should be stimulated on the stiffer $shSAF_{W1,4}$ gels compared with the parent hSAFs (66).

However, for further studies with neurons, I concluded that the parent 1 kPa hSAFs, without adhesion peptide modification, were best suited for PCN culture. Therefore, these gels were taken forward for the studies outlined in Chapters 4 and 5.

Chapter 4.

Incorporating full-length proteins into hSAFs

Introduction

Incorporating mimetic peptides, such as RGDS and IKVAV, into scaffolds has distinct advantages over the introduction of the whole adhesion protein, namely increased stability and ease of production (264). However, as demonstrated in Chapter 3, introducing these peptides into hSAFs has little discernible effect on PN growth. In addition, many mimetic peptides of extracellular growth factors have been developed, though with mixed results (265-268). In these cases, the introduction of whole proteins (*i.e.* adhesion proteins or neurotrophic factors) is advantageous.

Naturally derived cytoscaffolds, such as Matrigel, have the benefit of containing a cocktail of endogenous, full-length growth factors native to tissues *in vivo*, which promote cell health and growth (85). In addition, the natural ECM contains growth factor-binding molecules (such as heparin and vitronectin) that cluster these proteins at particular locations. This increases growth factor local concentration to promote their effect on cells (60-62, 269). I hypothesised that introducing whole neurotrophic factors into hSAFs might further promote PN growth. Furthermore, by having tighter control over the presence of these factors, our scaffold would have a significant advantage over Matrigel where the exact molecular make-up of constituents is not known (85). Here, I outline the development

of methods for the incorporation of whole proteins into hSAFs, the utilisation of these methods to introduce the neurotrophic factor insulin-like growth factor 1 (IGF1) into the scaffold, and assessment of PN responses to these IGF1-modified scaffolds.

4.1 Incorporating a fluorescent protein into hSAFs

Selecting an approach for protein incorporation

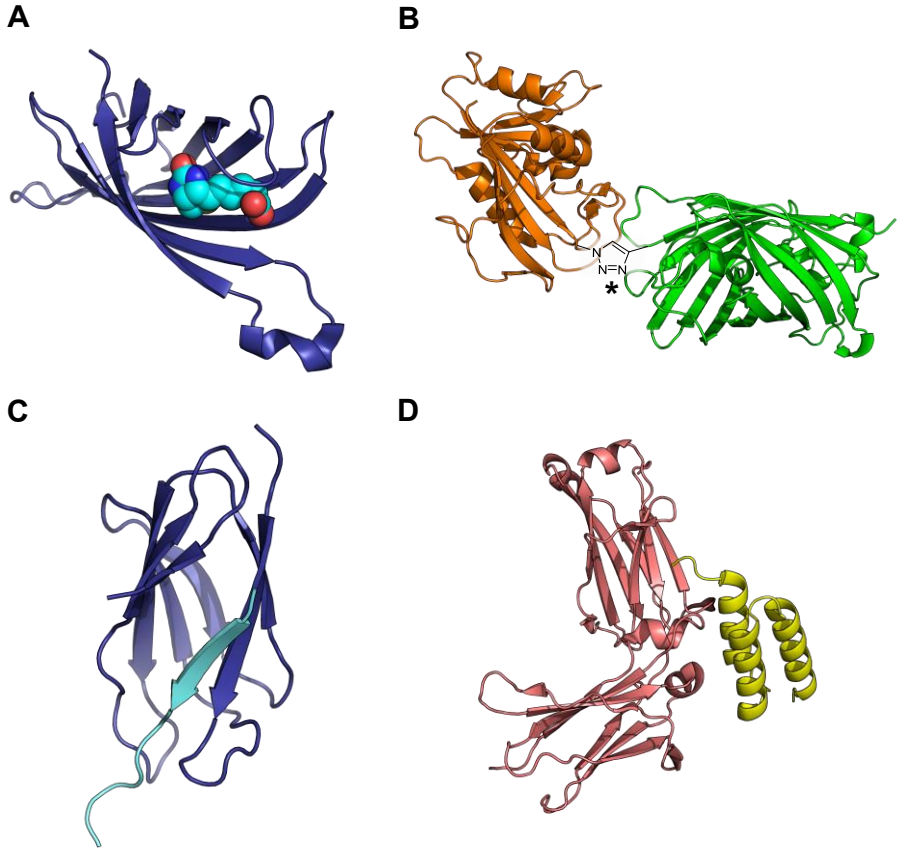

Figure 4.1.1: Common protein-based modification mechanisms. **A:** The biotin-streptavidin complex (navy = streptavidin, cyan = biotin) (270). **B:** CuAAC using proteins modified with unnatural amino acids (271), orange = dihydrofolate reductase (DHFR), green = GFP, * indicates the point at which the proteins are linked *via* CuAAC. **C:** SpyTag-SpyCatcher (cyan = SpyTag, navy = SpyCatcher) (127). **D:** The Fc-region of an IgG molecule (pink) bound to the Z-domain of protein A (yellow) (272). PDB reference codes: 3RY2 **(A)**, 1DRF and 1GFL **(B)**, 4MLI **(C)**, 4WWI **(D)**.

I postulated that modification of hSAFs with a whole protein could be achieved using one of several established methods for protein-protein or protein-peptide conjugation. These include, though are by no means limited to: affinity tag-mediated conjugation (185); enzyme-catalysed ligation (273); various

click chemistries using unnatural amino acids (274); and antibody-mediated binding (275). Examples of these are depicted in Figure 4.1.1. When selecting one of these methods, I considered the following criteria: immobilised proteins should remain bound to the scaffold over a period of weeks, a relevant amount of time for PN culture; there should be a straightforward method for quantifying protein attachment to the scaffold; and finally, the attachment method should be modular, such that any protein could be incorporated *via* a similar mechanism.

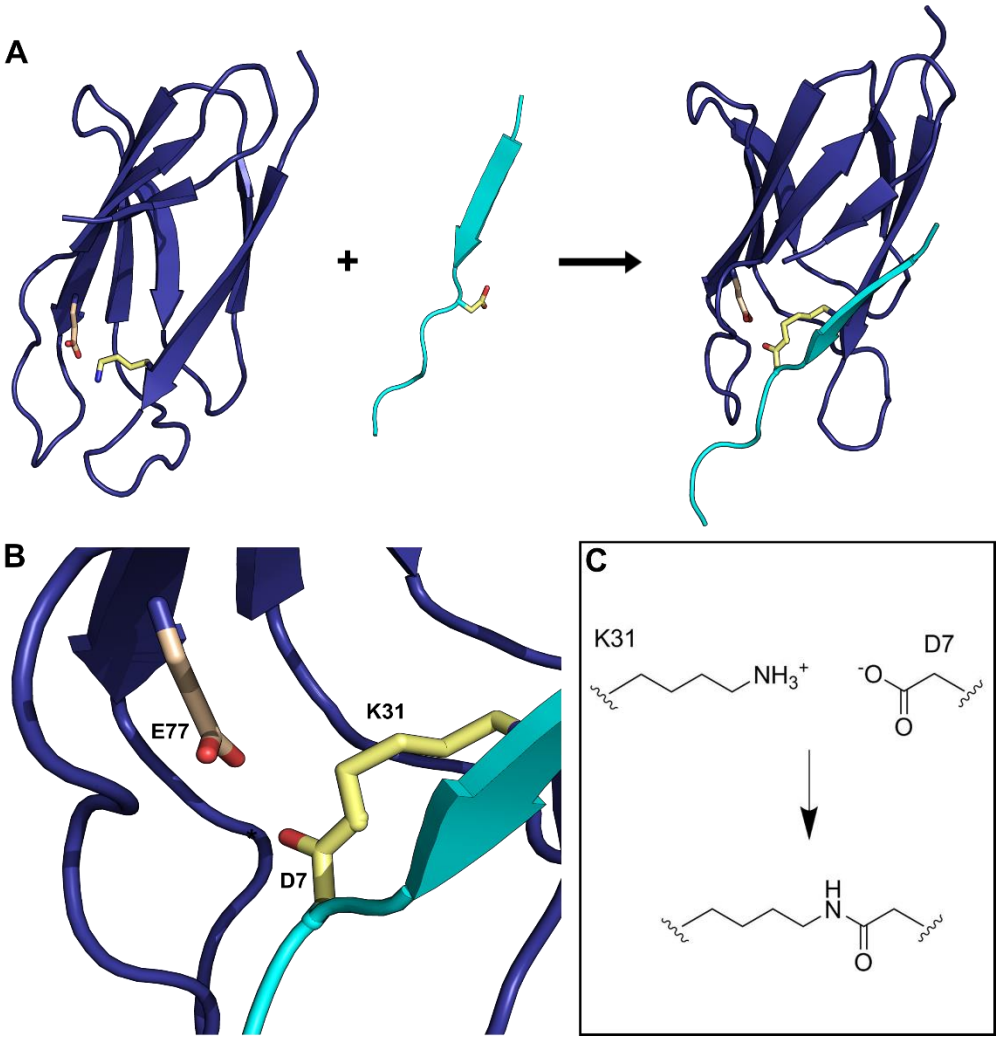

Figure 4.1.2: SpyTag-SpyCatcher. **A:** Crystal structures of SpyCatcher (navy) SpyTag (cyan) and the complex formed when the two are mixed. Asp 7 (D7) of SpyTag and Lys 31 (K31) of SpyCatcher are highlighted in yellow and Glu 77 (E77) is highlighted in wheat. **B:** Magnified image of the isopeptide bond formed between SpyTag (D7) and SpyCatcher (K31) (yellow). **C:** Chemical mechanism showing the formation of the isopeptide bond between K31 and D7. Figure and structures adapted from (127, 276). PDB code = 4MLI.

With these criteria in mind, I reasoned that proteins should be covalently linked to hSAFs. This would not only increase the stability of the protein on the scaffold – thus, maximising the length of exposure

to cells – but also allow me to control the spatial location of the protein within the gel. Therefore, affinity tag-mediated methods of immobilisation were deemed unsuitable.

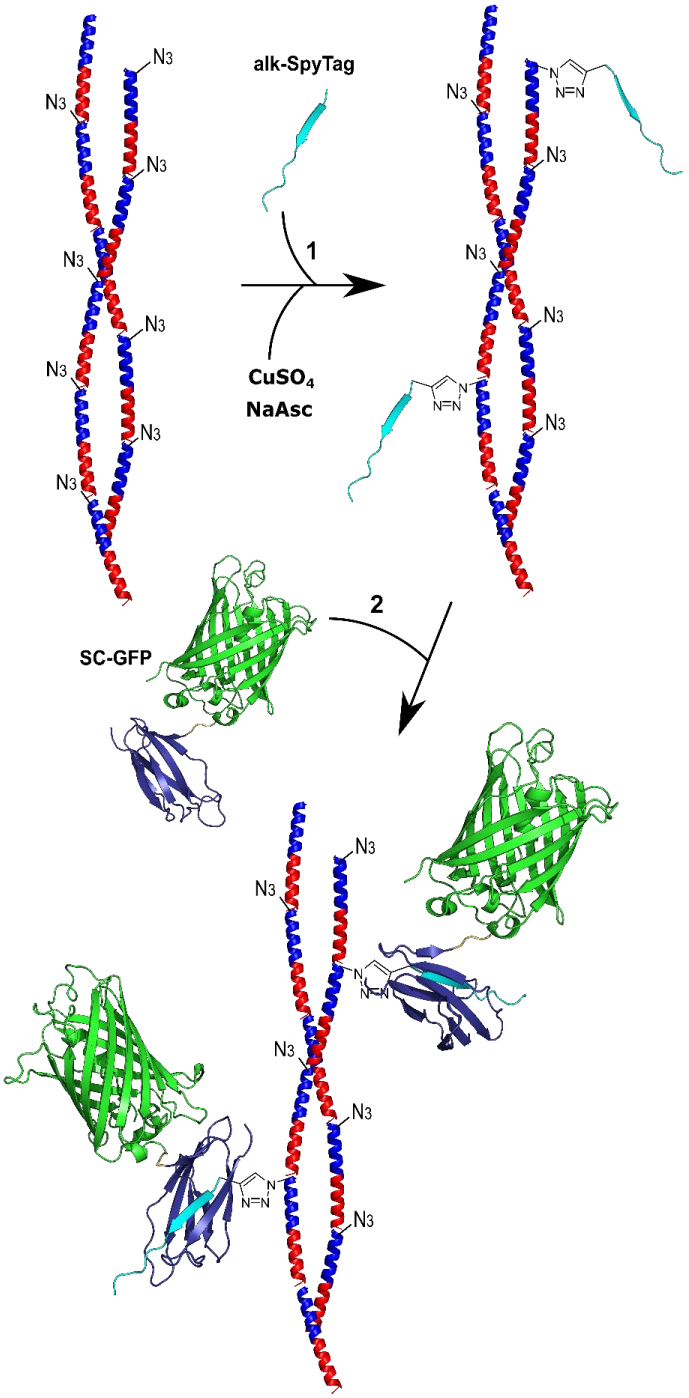

Figure 4.1.3: Schematic diagram showing SpyTag-SpyCatcher-mediated immobilisation of GFP on hSAFs. **1:** alk-SpyTag is attached to p1KAz:p2 hSAFs *via* CuAAC. **2:** fibres are then decorated with SpyCatcher-GFP (SC-GFP) *via* the formation of an isopeptide bond between SpyTag and SpyCatcher.

The Howarth group at Oxford have developed a two-component peptide-protein binding system that involves the spontaneous formation of a covalent complex, namely SpyTag-SpyCatcher (Figure 4.1.2).

The group split the CnaB2 protein from *Streptococcus pyogenes* into two binding partners: a 14 amino acid peptide (SpyTag), and a 12.4 kDa protein (SpyCatcher) (127). When mixed, Glu 77 of SpyCatcher catalyses the spontaneous formation of an isopeptide bond between Asp 7 of SpyTag and Lys 31 of SpyCatcher (Figure 4.1.2C).

This SpyTag-SpyCatcher complex is extremely thermostable and forms under ambient conditions, at neutral pH, and in minutes (127). This system has now been utilised for hydrogel formation (125), vaccine development (277) and as a research tool (278). Therefore, SpyTag-SpyCatcher was used to incorporate proteins into hSAFs *via* the method outlined in Figure 4.1.3. SpyTag peptide would first be immobilised *via* CuAAC, following the method outlined in Chapter 3. A protein-of-interest would then be fused to SpyCatcher and immobilised onto hSAFs *via* the SpyTag-SpyCatcher interaction. Initially, as a proof-of-concept, I chose to immobilise GFP on hSAFs, owing to its ease of synthesis and detectable fluorescence upon incorporation.

SpyTag can be incorporated into hSAFs *via* CuAAC

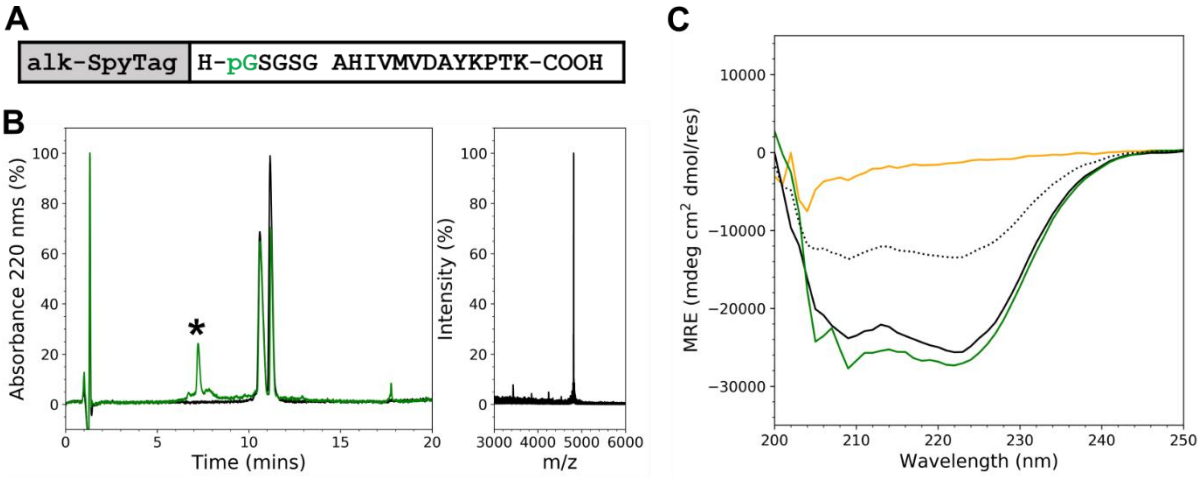

Figure 4.1.4: CuAAC-mediated immobilisation of SpyTag. **A:** alk-SpyTag peptide sequence with the *N*-terminal propargylglycine (pG) residue highlighted. **B:** HPLC chromatograms (left panel) showing p1KAz:p2 hSAFs either unreacted (black) or reacted with alk-SpyTag (green). MALDI-TOF-MS spectrum (right panel) is for the product peak labelled * (Expected mass = 4817.6 Da, recorded mass = 4816.0 Da). **C:** CD spectra of p1KAz:p2 fibres (black), alk-SpyTag (yellow), the theoretical average of mixing the two (grey, dotted) and the recorded spectra of p1KAz:p2-SpyTag fibres (green).

SpyTag peptide was synthesised with an *N*-terminal propargylglycine (pG) to allow conjugation to p1KAz:p2 hSAFs by CuAAC. This peptide was named alk-SpyTag. Its incorporation was followed by

HPLC and MALDI-TOF-MS (Figure 4.1.4) and secondary structure of SpyTag-hSAFs assessed by CD spectroscopy.

alk-SpyTag was successfully appended to hSAFs *via* CuAAC (Figure 4.1.4B). ~35% hSAF-p1KAz was converted to the reaction product, p1KAz-SpyTag (peak labelled *) (Figure 4.1.4B). Like RGDS and IKVAV, SpyTag was unstructured in isolation and interacted with p1KAz:p2 hSAFs upon mixing (Figure 4.1.4C). Fibres remained well-folded and helical upon attachment of alk-SpyTag.

Expression and purification of SpyCatcher-GFP

An expression construct encoding the SpyCatcher-GFP (SC-GFP) fusion protein, with an intervening flexible $(GS)_6$ linker and *N*-terminal His-Tag (Figure 4.1.5A-B), was produced using Golden Gate cloning methods. Briefly, the SpyCatcher sequence (kindly gifted to me by Mark Howarth), with an *N*-terminal His-Tag, was ligated into a vector containing GFP with an *N*-terminal $(GS)_6$ linker (kindly gifted by James Ross of the Woolfson group). SC-GFP was expressed in competent *E. coli* cells and subsequently purified by Ni^{2+}-affinity and size exclusion chromatography (SEC). Full experimental details are listed in Chapter 2.5. Protein purity was assessed by SDS-PAGE (Figure 4.1.5).

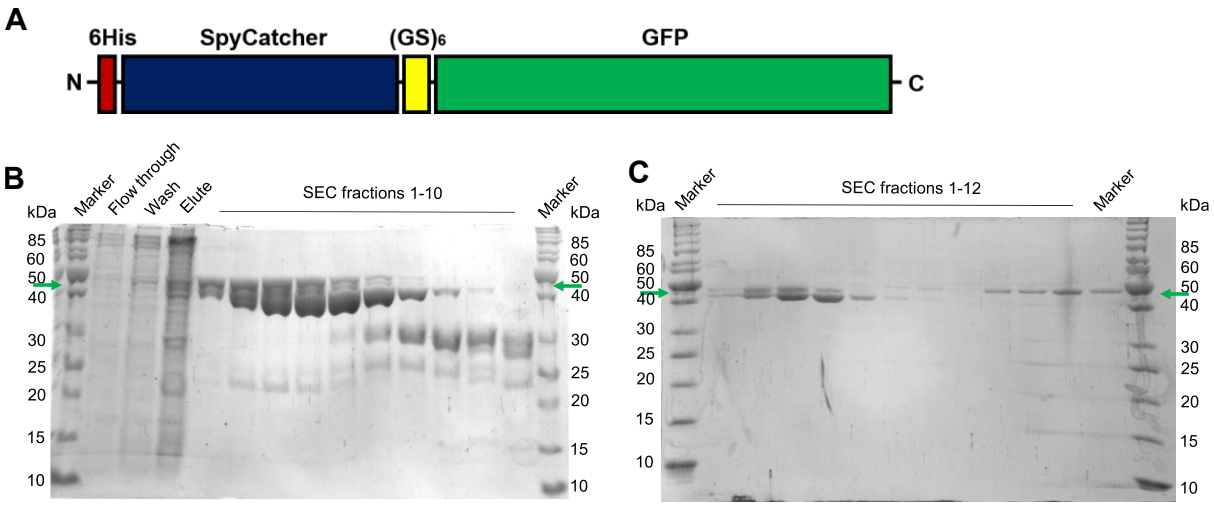

Figure 4.1.5: Expression and purification of SC-GFP with an *N*-terminal His-tag. **A:** Domain structure of SC-GFP. Full amino acid sequences for all SpyCatcher fusion proteins can be found in the Appendix (Chapter 8.3). **B:** SDS-PAGE showing Ni^{2+}-NTA- and SEC-purified SC-GFP. From left to right, lanes correspond to: Material that did not bind to the Ni^{2+}-NTA column; material removed by the wash buffer; material eluted upon addition of imidazole; and fractions resulting from SEC purification of the elute. **C:** SEC fractions 1 – 4 from B were pooled and further purified by Ni^{2+}-affinity chromatography using a gradient of imidazole. The resulting fractions were analysed by SDS-PAGE. Expected mass: 44 kDa, indicated by green arrows in B and C.

The protein obtained was roughly the expected mass for SC-GFP (44 kDa), however, multiple products were detected by SDS-PAGE (Figure 4.1.5B). Three prominent bands were present between 35 – 50 kDa, one of which was likely the 44 kDa, full length SC-GFP protein. These same three products were observed in all SC-GFP expressions. The distinct nature of the observed bands suggested these were likely not degradation products.

To separate these products, SEC fractions 1 – 4 from the initial purification (Figure 4.1.5C) were pooled and further purified using Ni^{2+}-NTA chromatography coupled with an imidazole gradient (Figure 4.1.4C). I hypothesised that the three products might have slightly different affinities for the Ni^{2+}-NTA column and, therefore, would elute at different imidazole concentrations. However, though the largest product was separated from the other two, the two smaller products could not be separated from one another using this method. Furthermore, repeated purification steps resulted in a significant reduction in protein yield.

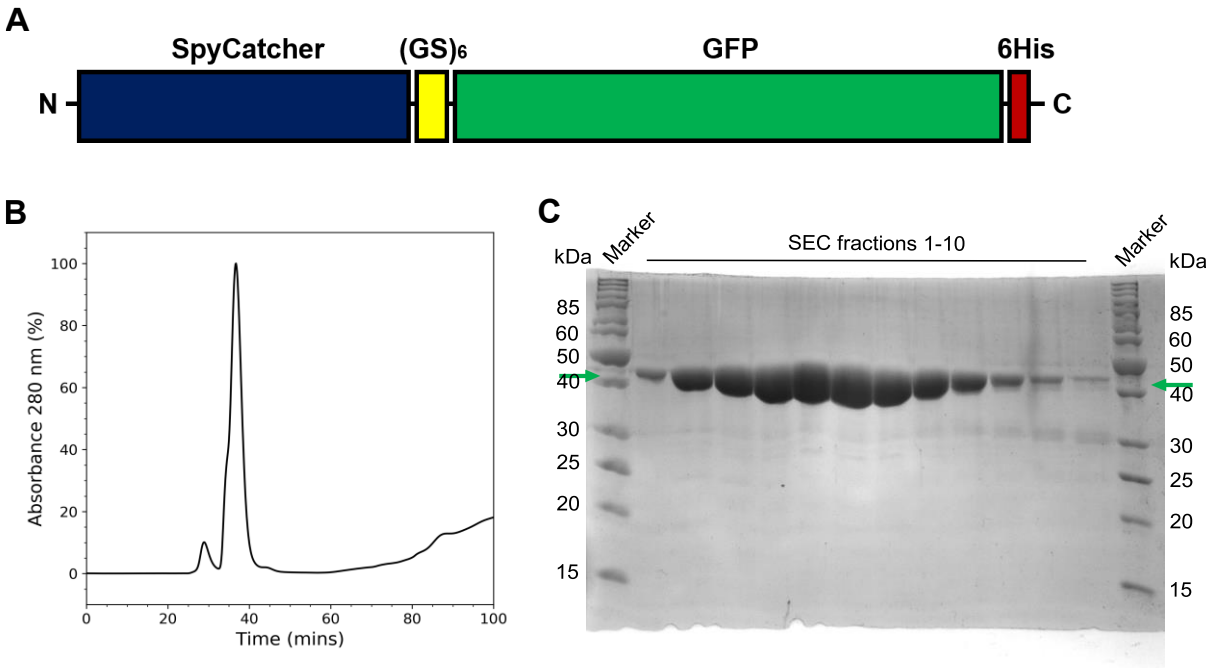

Figure 4.1.6: Expression and purification of *C*-terminal His-tagged SC-GFP. **A:** Diagram showing the domain structure of the new SC-GFP fusion protein, with a *C*-terminal His-Tag. **B:** SE chromatogram of Ni^{2+}-NTA-purified SC-GFP. **C:** SDS-PAGE gel showing the resulting fractions after SEC. Expected mass: 41 kDa, indicated by green arrows.

It was hypothesised that, if partial expression products were produced, moving the His-Tag to the *C* terminus would prevent these from co-eluting with the full-length protein. Therefore, I redesigned the expression vector by moving the His-tag to the protein *C* terminus (Figure 4.1.6A). This new construct was again expressed in *E. coli*, purified by Ni^{2+}-NTA chromatography and SEC and analysed by SDS-PAGE (Figure 4.1.6B-C). A distinct product peak was observed by SEC (Figure 4.1.6B) that corresponded to a single product by SDS-PAGE (Figure 4.1.6C), with a mass roughly that expected for the new SC-GFP protein (41 kDa – a Tobacco Etch Virus (TEV) protease site contained in the *N*-terminal His-Tag construct was also removed, resulting in the decrease in mass). The protein was obtained at high yield. This *C*-terminal His-tagged construct was used for all subsequent experiments and, henceforth, SC-GFP refers to this fusion protein.

GFP can be incorporated into hSAFs *via* SpyTag-SpyCatcher

With this SC-GFP fusion in hand, I sought to determine whether GFP could be incorporated into hSAFs *via* SpyTag-SpyCatcher. 1 μM SC-GFP was incubated with alk-SpyTag-decorated and, to determine the specificity of the SpyTag-SpyCatcher interaction, undecorated hSAFs (Figure 4.1.7). Typically, studies of neurotrophic factors *in vitro* use nM concentrations of protein (180, 279-282), and I reasoned that incubation with 1 μM protein would likely result in protein immobilisation in the nM range. However, I acknowledge that SpyTag is in a significant excess in this reaction (roughly 350 μM is immobilised on the gel (Figure 4.1.4B)) and, therefore, the concentration of SC-GFP immobilised would likely vary significantly depending on its starting concentration. Nonetheless, after extensive washes to remove non-specifically bound protein, the approximate GFP concentration on each gel was quantified *via* comparison with known concentrations of SC-GFP. Fluorescence was quantified using a ClarioStar plate reader (BMG LabTech, Germany) and widefield microscopy (Figure 4.1.7).

Very little SC-GFP bound to undecorated hSAFs, while around 5-fold more protein bound to SpyTag-decorated gels (Figure 4.1.7A-C). This indicated that SC-GFP bound with relative specificity to SpyTag-decorated hSAFs. When incubated with 1 μM SC-GFP, approximately 0.47 μM protein bound to the gel. For future studies, it is likely that individual growth factors would need to be assayed for optimum activity in order to choose a suitable starting concentration for immobilisation.

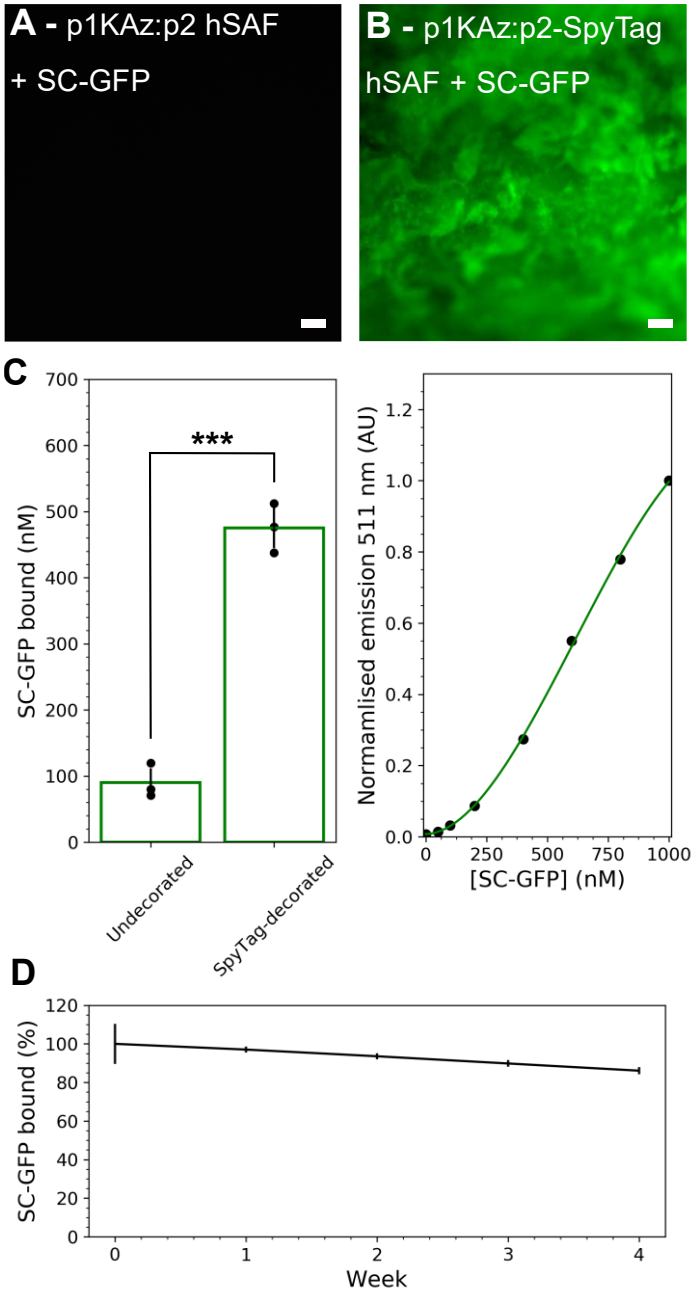

Figure 4.1.7: SC-GFP immobilisation on hSAFs. **A-B:** Widefield images showing GFP fluorescence on undecorated and SpyTag-decorated p1KAz:p2 hSAFs after incubation with SC-GFP. Scale bars = 200 μM. **C:** Quantification of protein immobilisation (left panel). Approximate bound SC-GFP concentration was calculated using a calibration curve of known SC-GFP concentrations (right panel). Calibration data was fitted to a polynomial curve. **D:** SC-GFP detachment from SpyTag-decorated hSAFs over a 4-week period. n=3 different gels. Statistical analysis was *via* t-test. *** = P<0.001. Error bars show one standard deviation from the mean.

One of the advantages of covalent immobilisation is that cells might be exposed to bioactive proteins for longer and, thus, the effect of these proteins on encapsulated cells might be maximised. Therefore, the level of SC-GFP detachment from SpyTag-decorated hSAFs over a 4-week period was assessed

(Figure 4.1.7D). Around 15% of the total SC-GFP immobilised initially was detected in the supernatant by the end of the study, leaving 85% still attached. Some detachment is expected over time, due partly to the non-specific association of some SC-GFP with the gel at the beginning of the 4-week period, despite stringent wash steps after immobilisation. In addition, as individual peptides are associated with the gel through relatively weak non-covalent interactions, some peptide, possibly that linked to GFP, is expected to dissociate from the gel over time. I was satisfied that the majority of protein remained associated with the gel over the timescale analysed. I did not perform further analysis to determine the nature of this detached component.

Protein inclusion can be tuned *via* p1KAz content

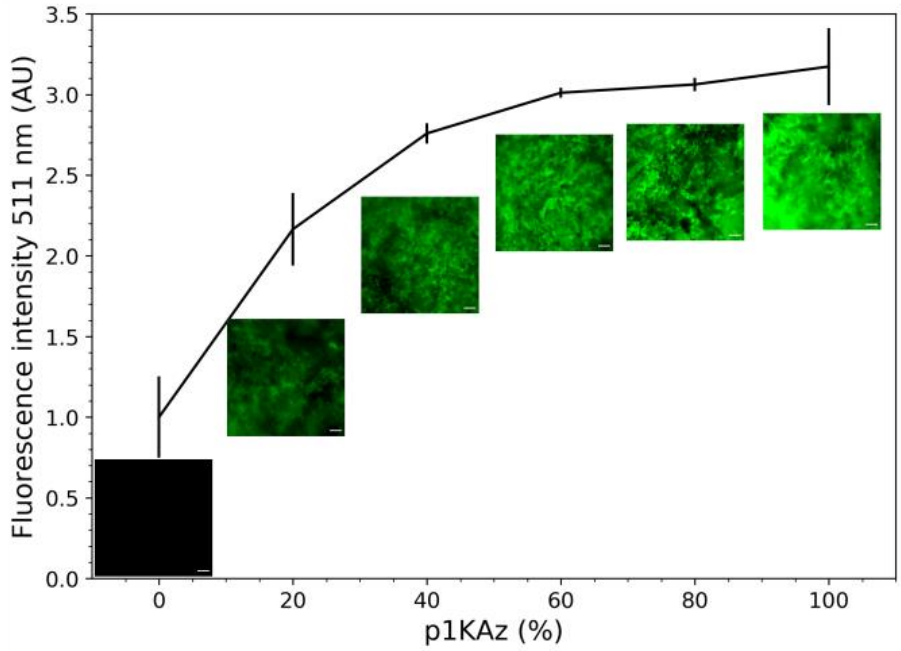

Figure 4.1.8: Controlling SC-GFP attachment by hSAF-p1KAz content. Graph showing GFP fluorescence on p1KAz:p2-SpyTag hSAFs with different hSAF-p1KAz contents, incubated with SC-GFP and washed copiously with PBS. Values are relative to 0% hSAF-p1KAz gels. n=3 different gels for each azide percentage. Error bars show one standard deviation from the mean. **Inset:** representative widefield images for each gel type, scale bars = 200 μm.

One of the main advantages of our synthetic peptide-based system is the modular way in which components can be incorporated. For example, by varying the number of azides available in the gel, it should be possible to vary the amount of SpyTag peptide and, therefore, SC-GFP protein attached to the gel. I tested this by making hSAF gels with differing hSAF-p1KAz percentages, relative to the non-

reactive hSAF-p1. These gels were decorated with alk-SpyTag and SC-GFP, and protein immobilisation quantified by widefield microscopy (Figure 4.1.8).

Little SC-GFP bound to 0% hSAF-p1KAz gels, which are unmodified with SpyTag, as no azide was present for CuAAC-mediated alk-SpyTag attachment. Inclusion of 20%, 40% and 60% hSAF-p1KAz led to roughly 2.2-, 2.75- and 3-fold increases in GFP immobilisation, respectively. This demonstrates that protein content can be tuned by varying the concentration of azide in the gel. Despite the concentration of SC-GFP (1 μM) being much lower than that of SpyTag (theoretically between 70-350 μM in 20-100% gels), protein immobilisation did not vary linearly with increasing azide content. Little further increase in protein immobilisation occurred when hSAF-p1KAz content was increased past 60%. Presumably, the low concentration of SC-GFP relative to SpyTag meant that, at high hSAF-p1KAz concentrations, azide concentration was no longer limiting to the reaction. Further incorporation would likely result from incubating with increasing SC-GFP concentrations. However, these investigations were beyond the scope of this thesis.

4.2 Incorporating insulin-like growth factor 1 (IGF1) into hSAFs *via* SpyTag-SpyCatcher

Figure 4.2.1: Crystal structure of IGF1 with its three disulphide bonds highlighted (yellow). PDB code = 1IMX.

Insulin-like growth factor 1 (IGF1, Figure 4.2.1) is a neurotrophic factor expressed throughout the brain during development. It has a range of effects on diverse neuronal cell types, including promoting neuronal survival (177, 283), neurite extension and polarity (178, 179), progenitor cell proliferation and neurogenesis (176, 180). Furthermore, it has been incorporated into similar hydrogel systems previously (186, 284) and bioactive fusions between IGF1 and additional proteins have been successfully produced in *E. coli* (186). Therefore, IGF1 was selected for immobilisation on hSAFs *via* SpyTag-SpyCatcher.

SC-GFP-IGF1 expression and purification

I chose to *N*-terminally modify IGF1 with SC-GFP as similar modifications – while maintaining IGF1 activity – had been previously reported (186, 285). The inclusion of GFP would once again allow me to easily monitor protein incorporation. The gene encoding IGF1, with an *N*-terminal $(GS)_6$ linker, optimised for expression in *E. coli*, was synthesised by GeneArt from Thermo Fisher Scientific and amplified by PCR. This was ligated into a vector containing *N*-terminal His-tagged SC-GFP (Figure 4.1.5), *C* terminal to the SC-GFP coding sequence. IGF1 contains three disulphide bonds that, in *E. coli*, need to be formed in the periplasmic space. Therefore, a periplasm-targeting sequence was introduced *via* PCR at the extreme *N* terminus. Both the His-tag and periplasm-targeting sequence were introduced away from IGF1 to reduce the likelihood of them interfering with protein folding or activity. This construct was named p-SC-GFP-IGF1 (periplasm-targeted-SpyCatcher-GFP-insulin-like growth factor, Figure 4.2.2). Full experimental details are listed in Chapter 2.5.

IGF1 expression in *E. coli* has been previously reported, but is non-trivial. The resulting protein is typically insoluble and requires *in vitro* refolding to attain the active, soluble protein (186, 286-288). As expected, upon expression in BL21 cells, p-SC-GFP-IGF1 was in the insoluble fraction. It seemed likely that this protein formed inclusion bodies before it could be transported to the periplasm for disulphide-bond formation and proper folding into its native state. p-SC-GFP-IGF1 was refolded *in vitro* by dialysis and purified by Ni^{2+}-NTA chromatography and SEC. However, SDS-PAGE analysis indicated the formation of multiple, coeluted products (Figure 4.2.2B).

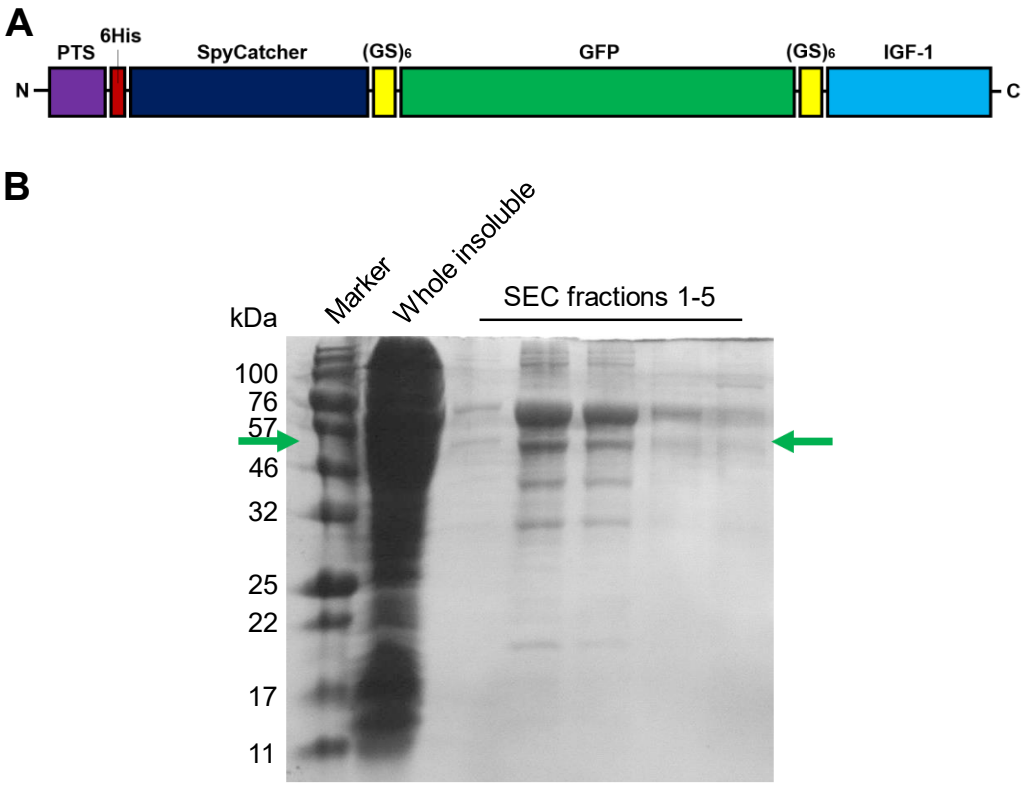

Figure 4.2.2: p-SC-GFP-IGF1. **A:** Domain structure of p-SC-GFP-IGF1. PTS = periplasm targeting sequence. **B:** SDS-PAGE analysis of Ni-NTA- and SEC-purified p-SC-GFP-IGF1 after solubilisation of the insoluble protein fraction extracted from *E. coli*. Expected mass is 51.4 kDa, assuming periplasm-tag cleavage upon exportation to the *E. coli* periplasm.

While *in vitro* refolding is an established technique for refolding aggregated protein from *E. coli*, it is also time consuming. Alternative *E. coli* strains exist that, I hypothesised, might aid expression of SC-GFP-IGF1 in its soluble form. SHuffle® T7 competent *E. coli* (SHuffle cells) are an engineered strain that allow disulphide bond formation in the *E. coli* cytoplasm (289). The periplasmic tag was removed from the p-SC-GFP-IGF1 gene by PCR, producing a new fusion, SC-GFP-IGF1, which was expressed in SHuffle cells (Figure 4.2.3). This protein was contained primarily in the soluble fraction. SEC indicated that the protein formed a discrete species and did not form large aggregates (Figure 4.2.3B). SDS-PAGE confirmed the expected mass of 52.6 kDa (Figure 4.2.3D). Therefore, this protein was used for all further studies and, hereafter, SC-GFP-IGF1 refers to this construct, expressed in SHuffle *E. coli* cells.

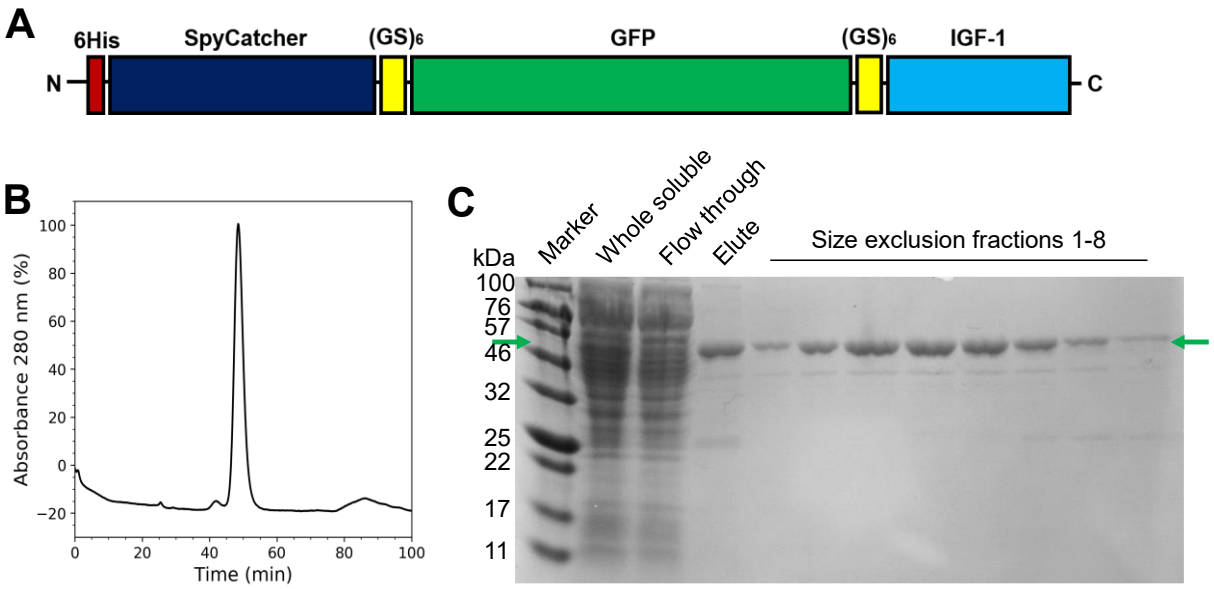

Figure 4.2.3: Expression and purification of SC-GFP-IGF1. **A:** Domain structure of SC-GFP-IGF1. **B:** SE chromatogram of SC-GFP-IGF1. **C:** SDS-PAGE gel showing SC-GFP-IGF1 after Ni^{2+}-NTA and SEC purification. Expected mass: 52.6 kDa, indicated by green arrow.

SC-GFP-IGF-1 can be incorporated into hSAFs *via* SpyTag-SpyCatcher

Immobilisation of SC-GFP-IGF1 on hSAFs was assessed as described for SC-GFP, by analysing GFP fluorescence on hSAFs compared to known SC-GFP-IGF1 concentrations (Figure 4.2.4A). SC-GFP-IGF1 immobilised on SpyTag-decorated hSAFs was around 7-fold greater than on undecorated gels. This indicated that SC-GFP-IGF1 bound specifically to SpyTag-decorated hSAFs.

In contrast to SC-GFP, SC-GFP-IGF1 detached significantly from the gel over 4 weeks, with around 60% of the total starting protein detected in the supernatant (Figure 4.2.4B). The amount of protein bound to the gel without SpyTag was similar to that observed for SC-GFP, indicating that non-specific protein binding was similar in both. However, the concentration of SC-GFP-IGF1 initially immobilised to SpyTag-decorated gels was greater for SC-GFP-IGF1 than for SC-GFP. Therefore, despite significant SC-GFP-IGF1 detachment from the gel, the concentration of immobilised protein after 4 weeks was similar in both experiments (approximately 0.36 and 0.32 μM for SC-GFP and SC-GFP-IGF1, respectively). It seems likely that – despite following an identical method for both proteins – more SC-GFP was initially removed during the wash procedure prior to measuring the immobilised protein concentration (week 0 in Figures 4.1.7D and 4.2.4B). However, this was not investigated further.

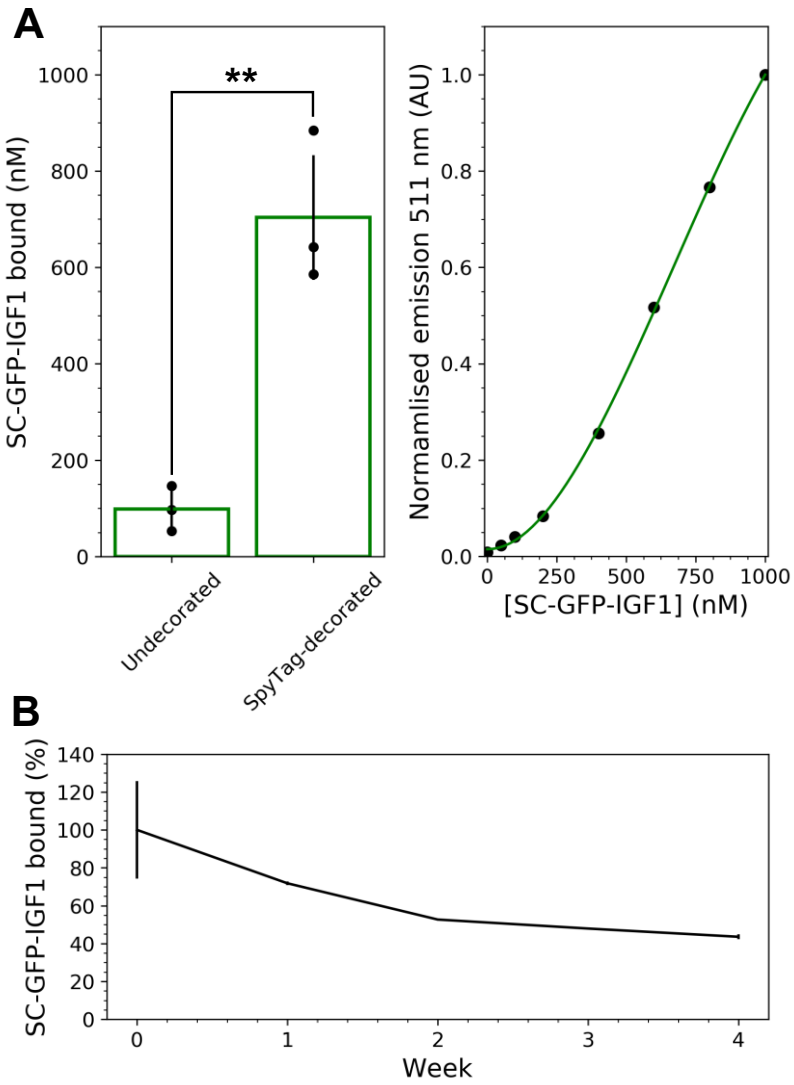

Figure 4.2.4: SC-GFP-IGF1 immobilisation on hSAFs. **A:** Quantification of protein immobilisation (left panel). Approximate bound SC-GFP-IGF1 concentration was calculated using a calibration curve of known SC-GFP-IGF1 concentrations (right panel). Calibration data was fitted to a polynomial curve. **B:** SC-GFP-IGF1 detachment from SpyTag-decorated hSAFs over a 4-week period. n=3 different gels. Statistical analysis is *via* t-test. ** = P<0.01. Error bars show one standard deviation from the mean.

Protein incorporation does not impact fibre morphology or gel viscoelastic properties

The attachment of these rather large fusion proteins to hSAFs might impact fibre stability, which might in turn impact upon the viscoelastic properties of the gel. This might inadvertently influence cell behaviour in unintended ways. Therefore, I investigated whether changes in fibre morphology or gel stiffness occurred when gels were decorated with SC-GFP or SC-GFP-IGF1. TEM images and frequency sweep rheological measurements were recorded (Figure 4.2.5).

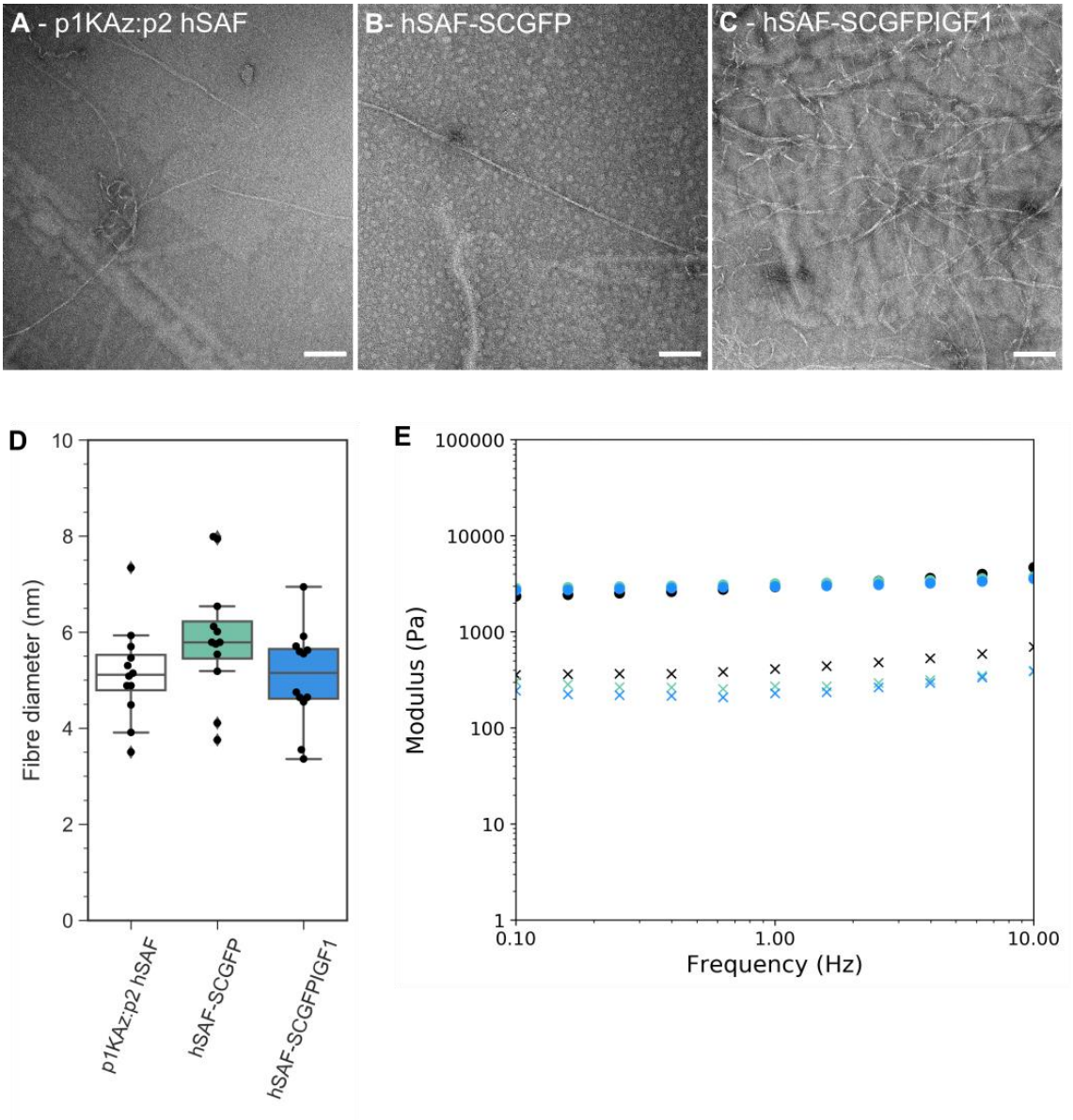

Figure 4.2.5: Biophysical characterisation of SC-GFP- and SC-GFP-IGF1-decorated hSAFs. **A-C:** TEM images of undecorated p1KAz:p2 fibres **(A)**, SC-GFP-decorated **(B)** and SC-GFP-IGF1-decorated **(C)** fibres. Scale bars = 100 nm. **D:** quantification of fibre diameter for each fibre type. n=10 fibres chosen at random across multiple images. **E:** Bulk rheological analysis of undecorated (black), SC-GFP-decorated (turquoise) and SC-GFP-IGF1-decorated (blue) hSAF gels. G' (circles) and G'' (crosses) are shown. Rheological measurements were performed at 37 ºC.

Neither incorporation of SC-GFP or SC-GFP-IGF1 impacted upon the presence or morphology of fibres (Figure 4.2.5A-D). Similarly, all gels possessed similar G' and G'' values (Figure 4.2.5E). These measurements are analogous to those recorded for the parent hSAFs at 37 ºC. Taken together, these observations suggest that introduction of proteins into hSAFs *via* SpyTag-SpyCatcher does not impact upon fibre or gel properties.

SC-GFP-IGF1 has comparable bioactivity to wildtype IGF1

Next, I determined whether SC-GFP-IGF1 retained the bioactivity of wildtype IGF1. MCF-7 cell proliferation is promoted by IGF1 and is a common read-out for IGF1 activity (186, 290). Crystal Violet is a dye that binds non-specifically to DNA and proteins and is widely used to assay cell number (291). To examine the bioactivity of my fusion proteins, MCF-7 cells, incubated with SC-GFP, SC-GFP-IGF1 or recombinant IGF1 (rIGF1, Abcam, UK), were stained with Crystal Violet (Figure 4.2.6).

When SC-GFP-IGF1 was expressed in SHuffle *E. coli* cells, most of the protein produced was contained in the soluble protein fraction. Though this suggested it had not formed large aggregates upon expression, it did not guarantee the protein had folded correctly. Therefore, this protein was refolded *in vitro* by denaturation in guanidinium hydrochloride (GuHCl) and dialysis against refolding buffer. I included this refolded protein (SC-GFP-IGF1 IVR), along with one that had not undergone refolding (SC-GFP-IGF1), in the bioactivity assay, to determine whether this was a necessary step to procure active protein (Figure 4.2.6).

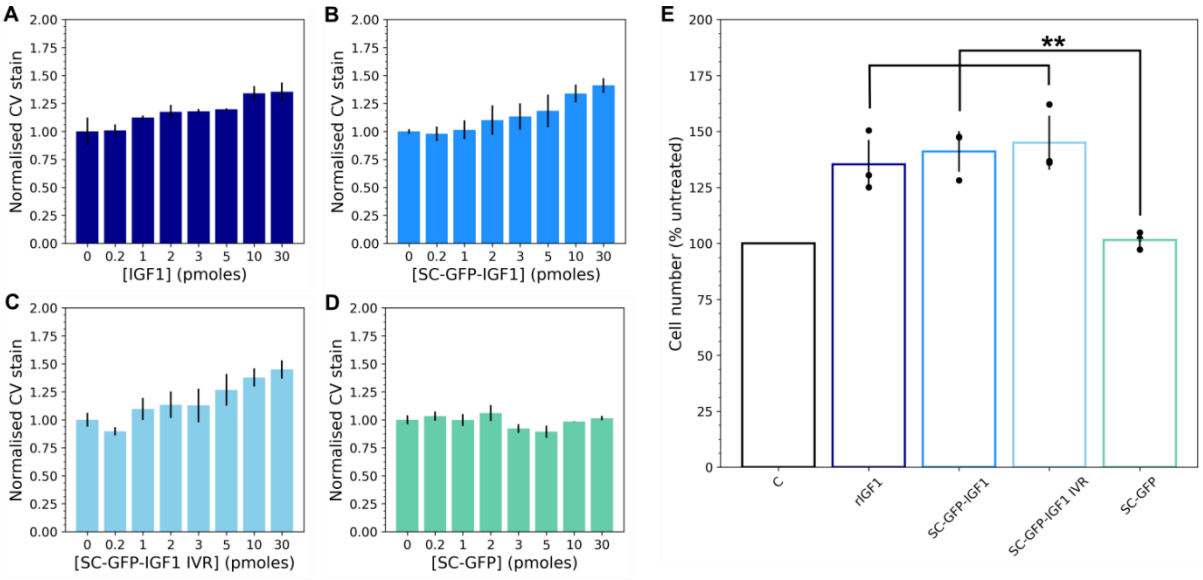

Figure 4.2.6: Assessing SC-GFP-IGF1 bioactivity. **A-D:** MCF-7 cell proliferation in response to rIGF1 **(A)**, SC-GFP-IGF1 **(B)**, SC-GFP-IGF1 IVR **(C)** and SC-GFP **(D)**, relative to untreated cells, quantified by crystal violet (CV) stain. **E:** MCF-7 cell number after treatment with 30 pmoles each protein, shown as a percentage of untreated control cells (labelled C, black). n=3. Statistical analysis was by one-way ANOVA with Tukey's post-hoc test. ** = P<0.01. Error bars show one standard deviation from the mean.

rIGF1 and the two SC-GFP-IGF1 fusions promoted MCF-7 cell proliferation in a dose-dependent manner (Figure 4.2.6A-D). All did so to a comparable level, with mean percentage increases in cell number varying from 30 – 50% compared to untreated cells (Figure 4.2.6E). SC-GFP did not induce any such increase in proliferation, indicating that the IGF1 component of the fusion was responsible for bioactivity. Thus, SC-GFP-IGF1 was determined to be active in solution regardless of whether the protein was refolded *in vitro*. Therefore, I did not refold the protein *in vitro* for downstream experiments.

IGF1-decorated hSAFs promote primary neuronal growth

With SC-GFP-IGF1 in-hand, and its bioactivity confirmed, I sought to determine PN responses to IGF1-decorated hSAFs. Given the heterogeneity of cortical cultures, and the fact that IGF1 has been widely reported to promote cell growth in the hippocampus (176-178, 292), primary hippocampal neurons (PHNs) were used for these studies. I cultured PHNs on undecorated p1KAz:p2 hSAFs, SC-GFP-hSAFs or SC-GFP-IGF1-hSAFs. PHNs were also cultured on two further unmodified p1KAz:p2 gels with rIGF1 or SC-GFP-IGF1 included in solution. Thus, I reasoned that any differences in the effect of immobilised IGF1, compared with that in solution, would be uncovered. Matrigel was included as a further control. As described in Chapter 3, AlamarBlue assay and widefield microscopy were used to measure neuronal viability and neurite length, respectively (Figure 4.2.7).

PHN viability and neurite length were significantly increased on SC-GFP-IGF1-hSAFs compared to undecorated hSAFs (Figure 4.2.7A-B). In addition, there was no significant difference in either measurement between SC-GFP-IGF1-hSAFs and Matrigel. These observations indicated that the incorporation IGF1 had the desired effect of promoting neuronal growth and survival on hSAFs to a level comparable with Matrigel.

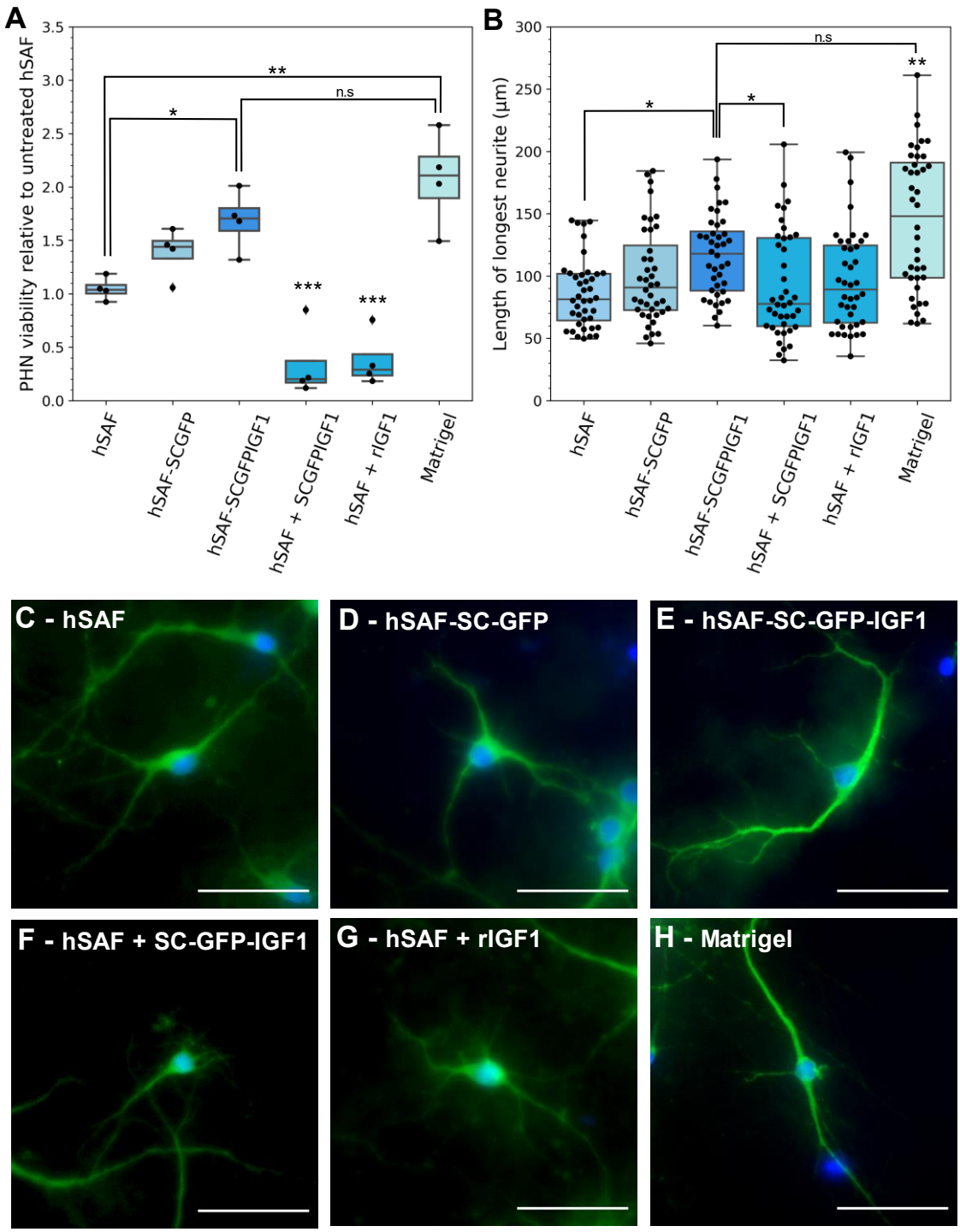

Figure 4.2.7: PHN responses to IGF1-modified hSAFs. **A:** PHN viability on the different growth substrates, relative to that on undecorated, untreated hSAFs. n=4 measurements taken from 4 independent PCN cultures derived from 4 different rats. **B:** Length of longest neurite of each analysed cell on the different growth substrates. n=40 individual cells chosen at random across the 4 dissections. **C-G:** Representative widefield images of neurons on p1KAz:p2 hSAFs **(C)**, SC-GFP **(D)** and SC-GFP-IGF1 **(E)** decorated hSAFs, p1KAz:p2 hSAFs treated with SC-GFP-IGF1 **(F)** and rIGF1 in solution **(G)**, and Matrigel **(H)**. DAPI = blue, MAP2 = green, GFAP = magenta. Scale bar = 50 µm. Images are all maximum projections of *z*-stacks. Statistical analysis was by one-way ANOVA with Tukey's post-hoc test. * = P<0.05, ** = P<0.01, *** = P<0.001. n.s. = not significant.

However, though not significant, a trend towards increases in viability and neurite length were also observed when gels were decorated with SC-GFP (Figure 4.2.7A-B). Critically, there was no significant difference in either parameter between SC-GFP- and SC-GFP-IGF1-hSAFs. This suggests that neuronal growth might be promoted by the addition of SpyCatcher or GFP, two supposedly non-neurotrophic proteins. A possible explanation for this might be the addition of positive charge to the gel surface, which would promote neuronal association (293, 294). However, both SC-GFP and SC-GFP-IGF1 are negatively charged at neutral pH and, therefore, would be expected to repel negatively charged neuronal membranes. Alternatively, SpyCatcher and GFP may contain motifs that promote neuronal adherence. SpyCatcher is derived from a bacterial adhesin (127), suggesting it may contain such cell adherence ligands, though one would assume these would have little effect on neuronal cells. I did not investigate the mechanism of neuronal growth promotion by SC-GFP further.

Addition of both SC-GFP-IGF1 and rIGF1 in solution had a significant detrimental effect on overall cell viability, without impacting neurite length (Figure 4.2.7A-B). Indeed, upon imaging, fewer cells remained after 14 days *in vitro* than in any of the other groups, suggesting significant cell death over the time studied. When delivered in solution, more IGF1 is expected to be available to cells than when the protein is immobilised. Most *in vitro* studies of IGF1 activity in neurons are performed using relatively acute IGF1 exposure times, no more than 24 hours (180, 279, 280). Some studies indicate that, with chronic exposure, IGF1 has a negative impact upon cell viability *in vitro* (295), though no such studies have been performed with PNs. IGF1 levels have also been shown to inversely correlate with lifespan and accelerate ageing in a number of animal models (296, 297). I speculate that the observed negative effect on PN viability is a potentially previously unreported effect of chronic exposure to IGF1. However, further investigation would be required to support this hypothesis.

4.3 Conclusions

I have demonstrated the incorporation of two proteins, GFP and IGF1 into hSAFs *via* the SpyTag-SpyCatcher system. Protein concentration can be tuned by varying the azide content of the gel and

4.3 Conclusions

IGF1-modified gels promote PHN viability and neurite outgrowth in culture. These findings further demonstrate the utility of hSAFs as a culture scaffold for PNs. Furthermore, they support my hypothesis that introducing a neurotrophic factor into the scaffold further promotes neuronal growth.

Modification of cytoscaffolds with proteins has been previously demonstrated (185, 187, 298, 299), as has protein decoration of self-assembling peptides (300-302), though these examples are generally limited to modifications with fluorescent proteins. Growth factors have also been passively encapsulated into designed peptide gels (187, 188). However, I believe this to be the first example of covalent modification of a *de novo* designed peptide hydrogel with a full-length protein. Thus, this work demonstrates that designed peptide cytoscaffolds can be modified with whole proteins, in a similar manner to synthetic or natural polymer derived gels.

IGF1 has previously been shown to promote neuronal growth both *in vitro* and *in vivo* (176, 177, 279), this being the primary reason for its selection in the current study . In addition, IGF1 incorporation into hydrogels has been shown to promote the growth and survival of non-neuronal cell types (186, 303-305). Therefore, my findings further demonstrate that IGF1 incorporation into biomaterials promotes the growth of a range of cell types. IGF1-decorated hSAFs promoted neurite outgrowth and neuronal viability to a similar extent to Matrigel. This confirmed my hypothesis that neuronal growth on hSAFs could be promoted to a similar extent to Matrigel upon introduction of a neurotrophic growth factor.

The protein modification strategy was chosen in such a way that it would be modular and, thus, allow the introduction of other proteins, simply by appending a different protein to the SpyCatcher module. I would have liked to explore the introduction of other growth factors, such as brain derived neurotrophic factor (BDNF) or vascular endothelial growth factor (VEGF), which might have similar growth-promoting effects on PNs. Neurotrophic factors often have synergistic effects on cell growth, and cells *in vivo* are likely to be exposed to multiple growth factors at once (306-308). Therefore, I would like to explore PN responses to tightly controlled cocktails of different growth factors. Ideally, this would involve the development of another, orthogonal, method of protein introduction, such that growth factor concentrations could be controlled independently of one another.

Another reason for adopting the chosen strategy (*i.e.* covalent modification) was that the concentration of growth factor could be temporally controlled across the gel. This might allow the direction of PN behaviour in a spatiotemporal manner. This possibility is explored in Chapter 5.

Chapter 5

Spatially patterning hSAFs

Introduction

In vivo, certain cellular behaviours are dictated by the presence of a particular bioactive molecule and its spatial and temporal presentation. Many neuronal cell behaviours rely explicitly on the spatial patterning of growth cues within the extracellular matrix (ECM). For example, developing axonal growth cones – *i.e.* structures at the tips of developing axons – respond to chemorepulsive and chemoattractive cues within the ECM (189, 309). These bind to transmembrane receptors, triggering the cytoskeletal remodelling required to turn the growth cone in a particular direction (189, 193) (Figure 5.1). This follows the chemoaffinity hypothesis outlined by Sperry in 1963 (310). Many of these growth cues have now been identified, including netrins, semaphorins, ephrins and the neurotrophins (169, 311-315). The spatial patterning of these cues within the ECM underpins this process, and the maintenance of these patterns is essential for correct patterning of the nervous system during development (193).

Directing axonal growth using biomaterials is of interest for promoting axonal regrowth and repair *in vivo* (220-222), modelling neuronal systems (*e.g.* polarised synaptic networks), and for studying the cellular mechanisms underlying axonal guidance *in vitro* (219). In addition, while spatiotemporal patterning of synthetic polymer or naturally derived gels is relatively common (97, 185, 195-197, 199, 205), there is little precedent for similarly patterning self-assembling peptide hydrogels. Therefore, the

spatiotemporal patterning of hSAFs is of interest, both due to its novelty for materials science and potential for modelling neuronal processes *in vitro*. Here, I describe the development of methods for spatially patterning hSAFs with peptides and proteins.

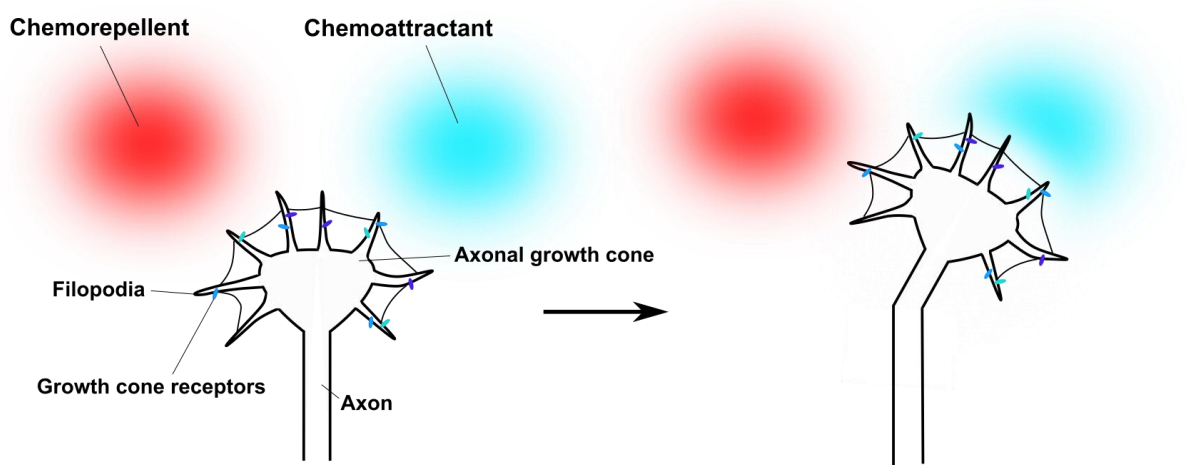

Figure 5.1: Schematic diagram showing the chemoaffinity hypothesis of axonal guidance. A developing axonal growth cone senses particular chemorepellent and chemoattractive extracellular growth cues *via* transmembrane receptors. Activation of these receptors causes cytoskeletal remodelling and turning of the growth cone either towards or away from the cue (189).

Selecting a method for spatially patterning hSAFs

Reported methods for spatially patterning hydrogels include: 3D bioprinting (201, 202, 316), photolithography (97, 185, 195, 205), microfluidics (197, 198, 317) and microcontact printing (199, 318) (Figure 5.2). Bioprinting is arguably the best explored of these and has been applied to various synthetic polymer and protein gel systems (319). However, for a gel to be suitable as a bioink for printing, it must possess the property of shear-thinning. That is, upon exposure to extrusion forces, the gel transitions to a liquid, and then back to a gel when deposited onto a print platform (319). To test whether hSAFs shear thinned, I extruded a gel through a needle. The hydrogel transitioned to a liquid state with little structural definition (data not shown), presumably due to the disruption of fibre-fibre or peptide heterodimer interactions. This rendered bioprinting unsuitable for patterning hSAFs. Microcontact printing was also disregarded, since hSAFs are relatively soft and would likely be damaged upon contact. Therefore, I tested microfluidics and photolithography as potentially suitable techniques for patterning hSAFs with growth cues.

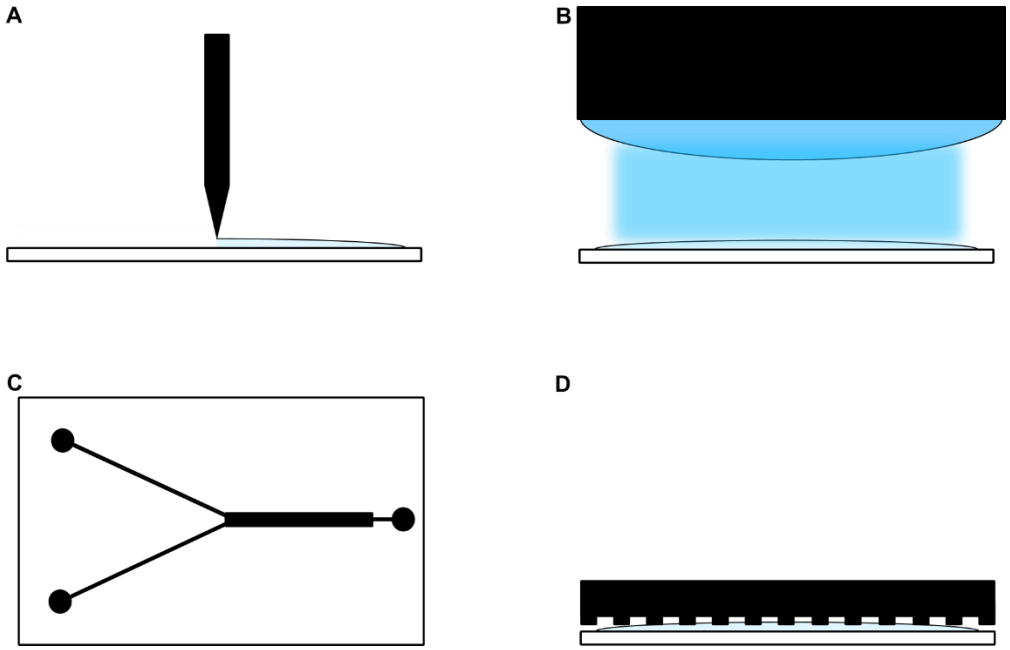

Figure 5.2: Common methods used for hydrogel micropatterning: 3D biprinting **(A)**, photolithography **(B)**, microfluidics **(C)** and microcontact printing **(D)**.

5.1: Microfluidic patterning of hSAFs

Designing a gradient-generating microfluidic device for patterning hSAFs

Developing axonal growth cones are not directed to particular locations within tissues by distinct patches of a particular neurotrophic factor, but by concentration gradients of that factor (166, 191, 320, 321). These gradients allow neuronal growth to be patterned over large distances (millimetres – centimetres) (189, 321). Therefore, I reasoned that patterning hSAFs with gradients would best model chemotaxis *in vitro*.

Microfluidics is the study and manipulation of fluid flow on the microscale, typically using devices with channels 10s or 100s of microns in diameter (322). Fluids in these channels travel by laminar flow, where minimal mixing occurs between fluids that flow parallel to one another (322). Therefore, the mixing of fluids can be manipulated using a carefully engineered series of channels. Microfluidic devices have been reported for patterning surfaces and hydrogels with gradients (323-326), of which

the diffusion mixer (327), Y-junction (317, 328) and serial dilutor (323, 329) are some of the most common (Figure 5.1.1).

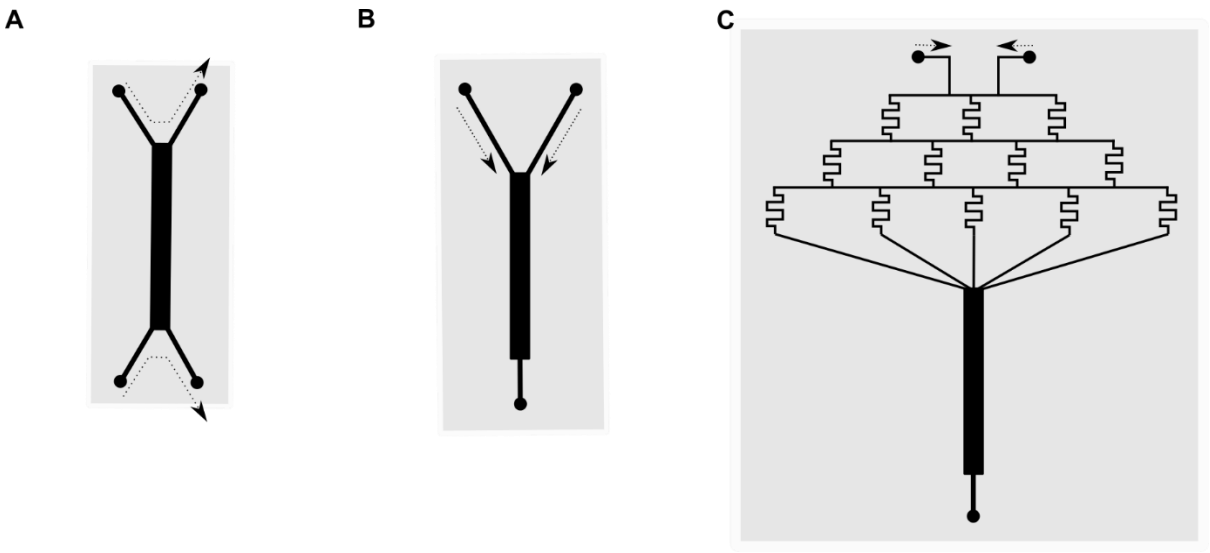

Figure 5.1.1: Common microfluidic gradient generator device designs: Diffusion mixer **(A)**, Y-junction **(B)** and serial dilutor **(C)**. Dotted arrows indicate the direction of fluid flow from the inlets to the outlets (circles).

I chose to pattern hSAFs using a serial dilutor microfluidic gradient generator (Figure 5.1.1C), largely due to the frequency with which it is reported (197, 323, 329-331). Here, two or more fluids enter the device through separate inlets. These fluids are mixed by passage through a network of channels, further mixing the solutions at every level (323). Snake channels are often included to aid further mixing (323). These channels recombine into a central chamber, forming a gradient perpendicular to the fluid flow. The solution then flows out of the device *via* an outlet. I hypothesised that a SpyTag-decorated hSAF gel, formed in the chamber, could be patterned with a gradient of SpyCatcher-GFP (SC-GFP), by flowing protein and buffer through the two inlets (Figure 5.1.2).

Typically, microfluidic device manufacture uses a master mould – usually made of silicon or 3D printed plastic – that is used to cast polydimethylsiloxane (PDMS). The moulded PDMS is then bonded to glass, forming the device. I designed master moulds using computer aided design (CAD) software, which were printed using a Form2 stereolithography (SLA) 3D printer (FormLabs, USA). These moulds were used to cast PDMS that was then bonded to a glass microscope slide. This method allows the rapid prototyping of devices at relatively low cost.

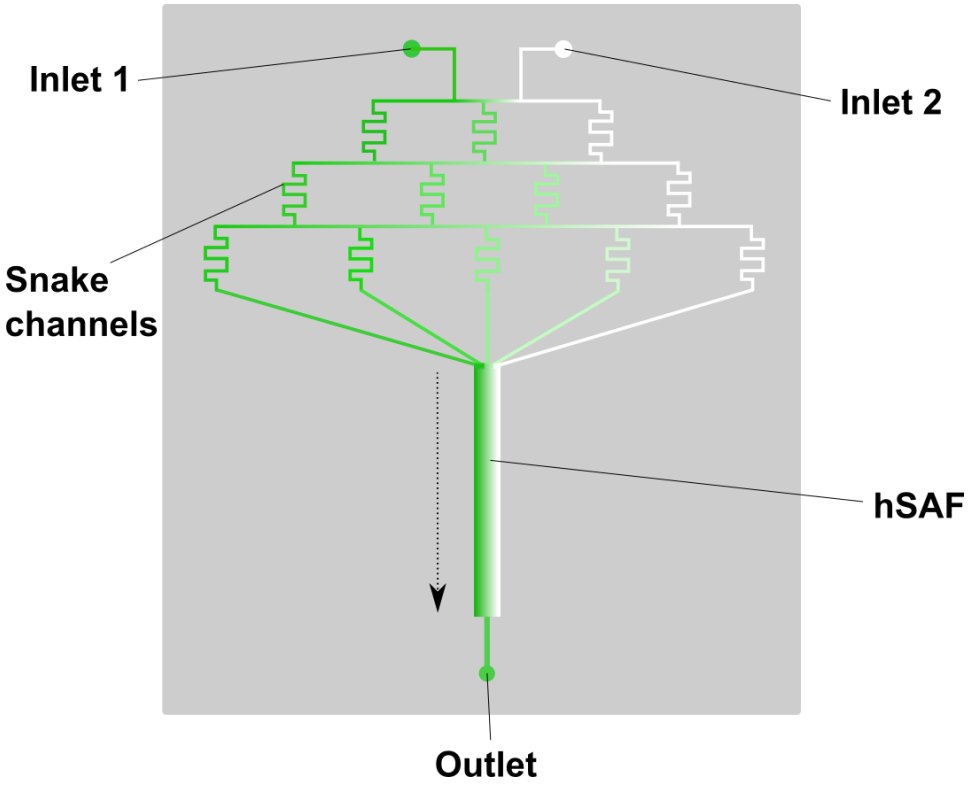

Figure 5.1.2: Schematic of the proposed design for a microfluidic gradient-generating device for patterning hSAFs. Two fluids (green and white) enter the device at inlets 1 and 2. An hSAF gel is formed in the patterning chamber and fluid exits the device *via* the outlet. The dotted arrow indicates the direction of fluid flow.

First, I chose to focus on the gradient-generating part of the device. My initial design (microfluidic gradient generator device 1 Figure 5.1.3) had 100 μm diameter channels, 5 serial dilutor levels and snake-shaped channels. Similar designs have been previously reported (197, 323) and, therefore, I proposed that this design would be suitable for gradient formation. To test whether this device could generate concentration gradients, dH_2O and rhodamine dye were pumped through inlets 1 and 2 (Figure 5.1.3B).

The device was water-tight and produced the desired pattern of rhodamine pumped alongside water, with mixing at the interface. However, several issues were evident upon operation of the device. First, the channels were not spaced far enough, meaning that the snake-channels merged, likely hampering mixing. In addition, certain channels collapsed during bonding of the PDMS to the glass. To rectify this, a second device was designed with a longer gradient generator, thus, allowing channels to be spaced further apart. This device also incorporated an open chamber for a gel to be introduced (Figure 5.1.4).

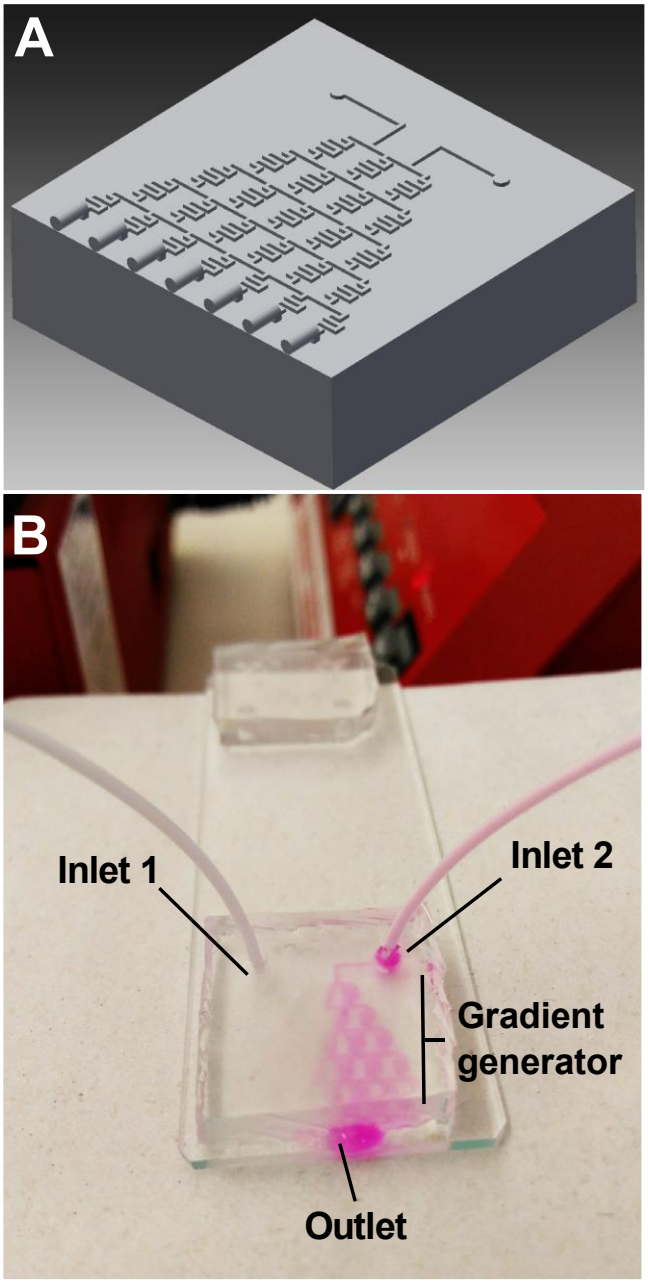

Figure 5.1.3: Microfluidic gradient generator device 1. **A:** CAD design of the device master mould, channel width =100 μm. **B:** Photograph of dH_2O and rhodamine dye pumped through inlets 1 and 2, respectively, at equal rates (50 μl/min).

Liquid flowed through the gradient generator and out into the chamber as desired. By altering the flow rate through each inlet, the dH_2O:rhodamine gradient could be shifted (Figure 5.1.4B-D). However, merging of the snake-channels persisted and any generated gradient was lost upon liquid entering the patterning chamber. I reasoned that this could be prevented by keeping the liquid under laminar flow while travelling through the chamber. However, this would require the patterning chamber to be enclosed.

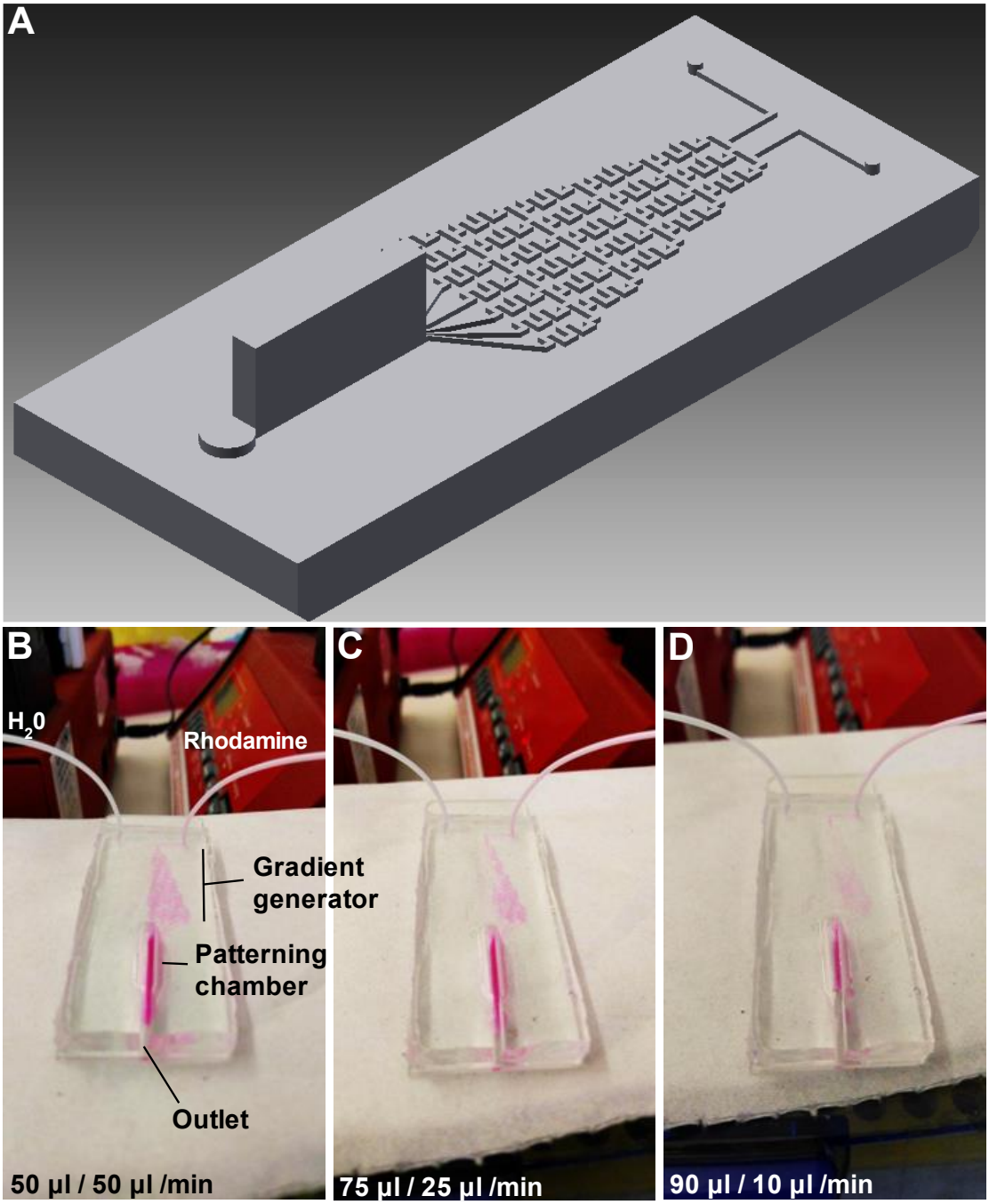

Figure 5.1.4: Microfluidic gradient generator device 2. **A:** CAD design of the mould used for the device, channel width =100 µm. **B-D:** Photographs of the device with Rhodamine and dH_2O pumped into each inlet at different rates as shown.

This poses a problem for patterning hSAFs. The gel must be formed in a closed chamber with a small total volume such that laminar flow of liquid through the chamber and, thus, the gradient, is maintained. However, the gel must then be accessible for subsequent cell culture. In addition, thorough mixing of hSAF-p1 and -p2 (required for proper gelation) in an enclosed chamber is difficult. Ideally, the gel would be formed in the patterning chamber, enclosed temporarily to allow patterning under laminar

flow, then uncovered for downstream neuronal cell culture. Approaches analogous to this have been reported previously (317), but are uncommon.

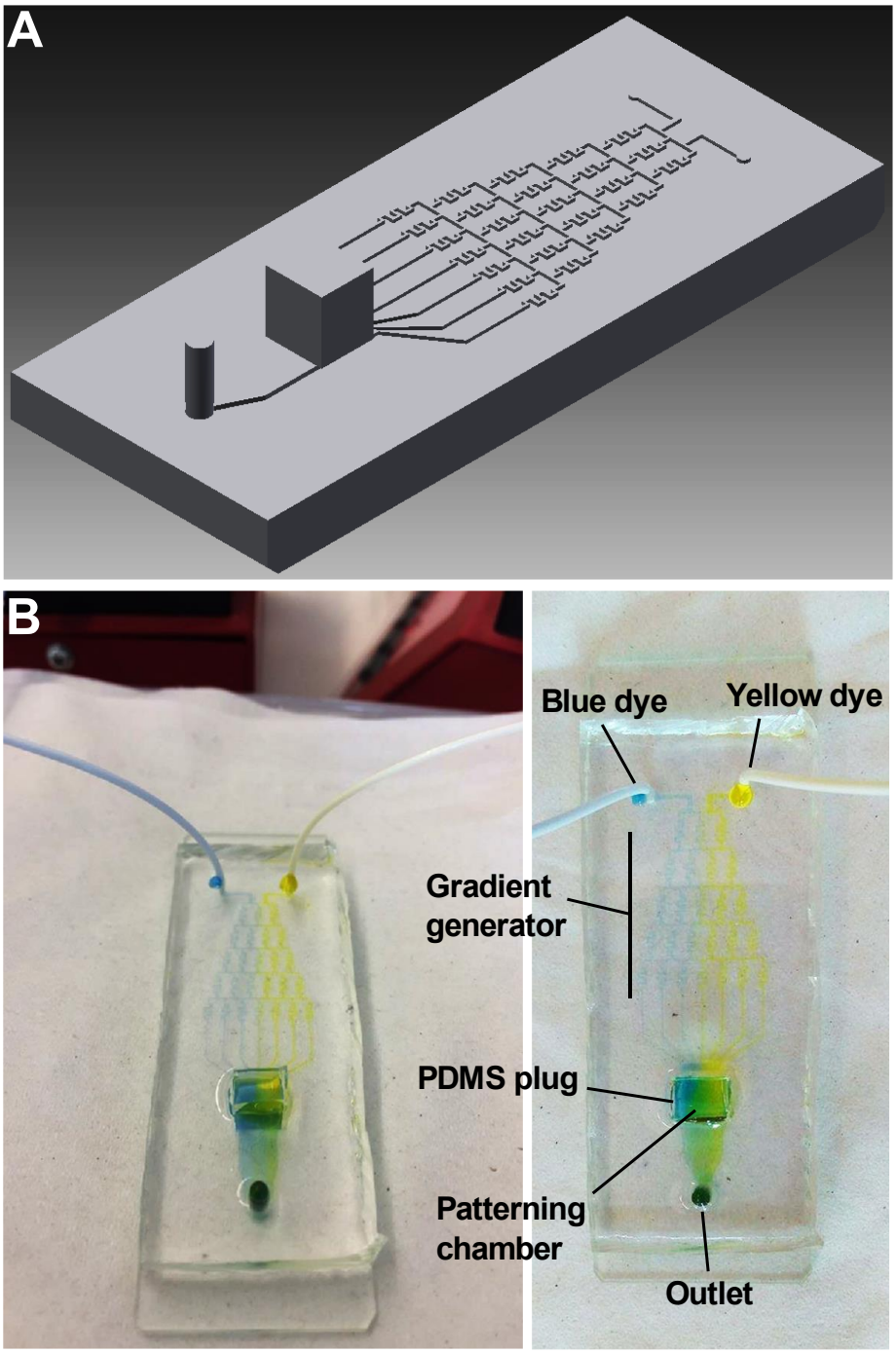

Figure 5.1.5: Microfluidic gradient generator device 3. **A:** CAD design of the mould for the device, channel width = 50 μm **B:** Photographs of the device with solutions of blue and yellow food dye pumped through either inlet at 50 μl/min. A PDMS plug was used to maintain laminar flow through the chamber while patterning.

To test this, another device was designed (microfluidic gradient generator device 3, Figure 5.1.5). Once again, this device had an open patterning chamber following the gradient generator, in which an hSAF

gel could be formed. However, this time, a PDMS plug was inserted into the chamber and positioned just above the glass slide. This was proposed to maintain laminar flow though the chamber during patterning. The plug could then be removed and the gel accessed following patterning. In addition, to prevent channel merging, narrower, further spaced channels were designed. To test this device, yellow and blue food dye solutions were flowed through the two inlets (Figure 5.1.5B).

A visible gradient of blue, through green, to yellow across the patterning chamber was observed when the PDMS plug was in place. Channels were sufficiently spaced out that liquid flowed through in the desired manner. Therefore, I used this device for initial hSAF patterning studies.

Microfluidic gradient-generating devices are unsuitable for patterning hSAFs

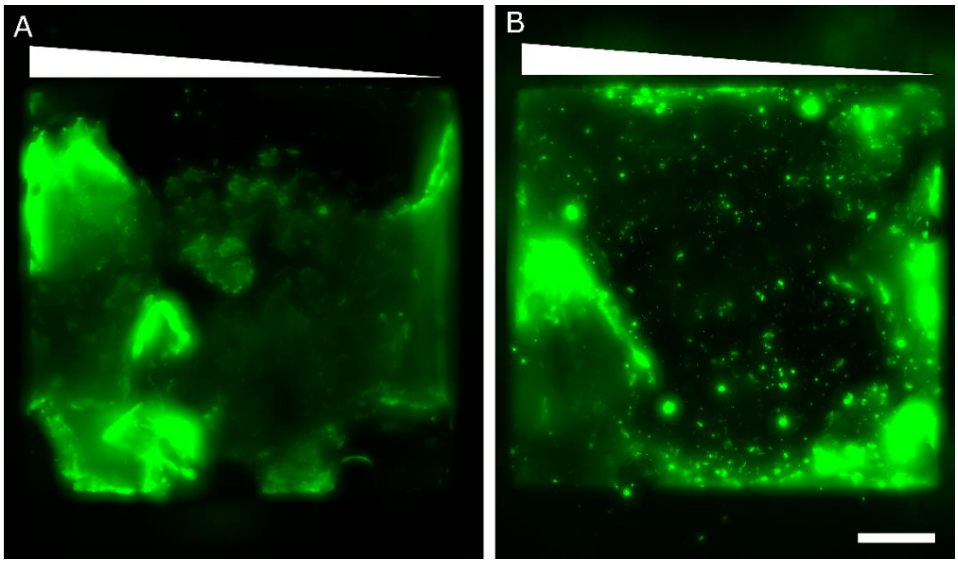

Figure 5.1.6: Widefield images of hSAFs patterned with SC-GFP using microfluidic gradient generator device 3. **A:** SpyTag-hSAFs were formed in the chamber before SC-GFP and PBS were pumped through the left and right inlet of the device, respectively. **B:** hSAF-p2 was dispensed into the chamber and the device was incubated at 4 ^{o}C while p1KAz and hSAF-p1 were pumped through the left and right inlet, respectively. alk-SpyTag and SC-GFP were subsequently patterned onto the gel as previously described. Both methods used flow rates of 50 µl/min, for each inlet, for 10 mins. The direction of flow was from top to bottom of the image. Scale bar = 1 mm.

Two methods of hSAF patterning were attempted. First, a p1KAz:p2 gel was formed in the chamber and decorated with SpyTag *via* CuAAC. PBS and SC-GFP were then flowed through the device to pattern the gel with SC-GFP. This method will be referred to as method A. In the second method, hSAF-p2 peptide was dispensed into the chamber. hSAF-p1 and hSAF-p1KAz were then flowed through the two inlets. It was hypothesised that this would form a gel in the chamber with a gradient of hSAF-p1 –

hSAF-p1KAz. SpyTag and SC-GFP were subsequently patterned onto the gel after removal of the PDMS plug. This will be referred to as method B. I patterned hSAFs using both these methods and recorded GFP fluorescence on each gel after patterning, using widefield microscopy (Figure 5.1.6).

Using both methods, very little gel remained in the chamber following patterning. For method B, this was likely due to a lack of mixing between the hSAF-p1 and hSAF-p2 peptides in the chamber. For method A, this may have resulted from disruption of the gel during patterning. In addition, placement and removal of the PDMS plug resulted in some visible damage to the gel.

These observations made me question whether microfluidics was a suitable method for patterning hSAFs. Consider method B: The protocol for hSAF gel formation (*i.e.* the mixing of two peptides) requires thorough mixing of solutions for gelation to occur. Such thorough mixing is not possible when patterning by this method without the destruction of any formed gradient. Examples of hydrogel patterning using microfluidic gradient generators typically utilise systems where gelation is triggered by photocuring (*e.g.* certain synthetic polymer hydrogels) and, thus, mixing is not required (332, 333). Therefore, hSAFs must be pre-formed, as in method A. However, gel formation within the device, and manipulation once there, is difficult. Therefore, I decided to pursue other avenues for patterning hSAFs.

5.2: Photolithographic patterning of hSAFs using thiol-ene click chemistry

Hydrogels can be patterned *via* photolithography

Photolithography is a common method for patterning 2D surfaces (334). Here, a photoreactive surface is placed under a mask with opaque and transparent regions in the desired pattern. A visible or UV light source is then shone through the mask onto the surface, triggering a light-activated reaction, either directly resulting in pattern formation, or allowing further steps to fabricate the desired pattern (334). The application of these principles to hydrogels has been pioneered by Kristie Anseth and others, using synthetic polymer gels (195, 205, 335). Manipulation of cell behaviour on these patterned scaffolds has

been reported (97, 196, 204). However, to the best of my knowledge, photolithography has not been attempted with a self-assembling peptide scaffold.

Given that hSAFs can be modified with chemical handles with relative ease, I reasoned that it should be possible to incorporate a chemical group that is sensitive to light. This should allow the photo-induced incorporation of bioactive ligands and, thus, photolithographic patterning of hSAFs (Figure 5.2.1).

Figure 5.2.1: Schematic diagram showing the proposed method for photolithographic patterning of hSAFs. An hSAF gel is covered with a photomask, through which columnated UV light is shone. This triggers a photo-activated chemical reaction only in areas of the gel exposed to UV light.

Selecting a photo-activated chemical reaction

There are two primary photo-inducible reaction types applied to surface and hydrogel patterning (336). In the first (Figure 5.2.2i), a molecule of interest is caged with a photo-cleavable group, commonly a nitrobenzyl or coumarin derivative, which are UV and visible light-labile, respectively (336). Irradiation causes this group to be removed, revealing a reactive handle that can react with a second molecule of interest. Alternatively, the reaction between the two molecules may itself be photo-activated (Figure 5.2.2ii). These methods have both been applied to hydrogels (203, 205, 224, 337) and I initially chose to pursue both.

A common photo-uncaging mechanism for peptides and proteins is the removal of a photo-labile group from a side-chain thiol on a Cys residue (224). This can then react with a maleimide or thiol on another peptide or protein (97, 338, 339). I synthesised a variant of hSAF-p1 with an *N*-terminal Cys (named

hSAF-p1Cys) and attempted to cage this peptide with a nitrobenzyl group according to (339). However, this was unsuccessful (data not shown) and, therefore, this method was abandoned.

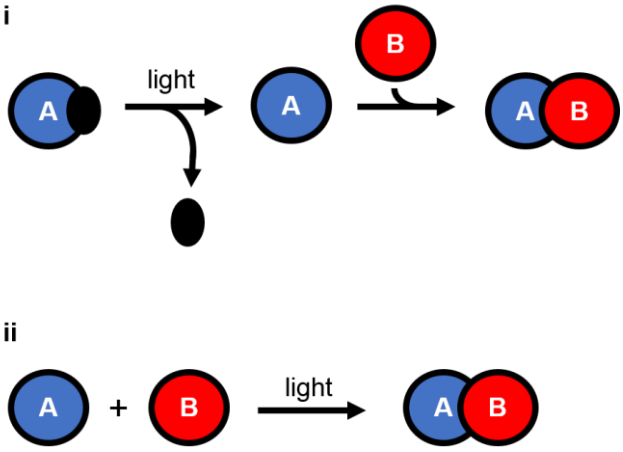

Figure 5.2.2: Schematic diagram of two common photochemical mechanisms. **i:** A photo-labile protecting group (black) is removed from molecule A by light irradiation. This allows subsequent reaction of A with B. **ii:** Molecule A reacts with molecule B directly *via* a photo-activated reaction.

Thiol-ene click chemistry (TECC)

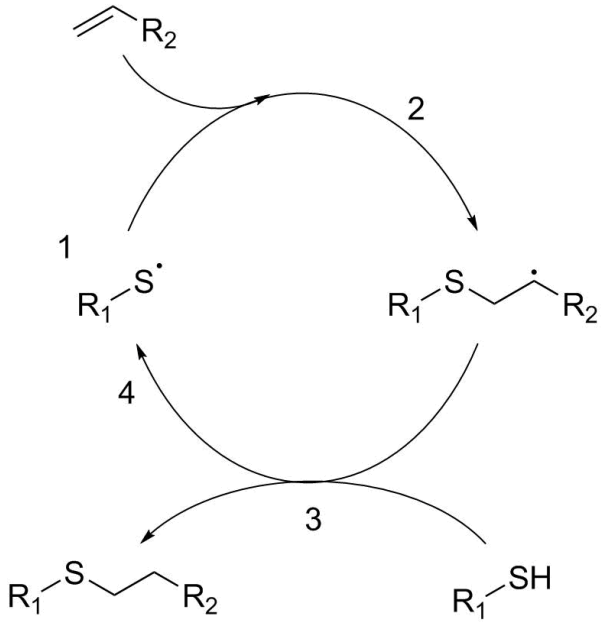

Figure 5.2.3: The thiol-ene click reaction. **1:** A thiyl radical (R_1) is generated by UV or visible light exposure in the presence of a radical photoinitiator. **2:** Propagation; thiyl radical addition to the electrophilic C of an -ene group (R_2) results in the formation of a carbon-centred radical. **3:** The carbon-centred radical species abstracts the $H^{\cdot}$ of a sulfhydryl group of another R_1 molecule, generating a further thiyl radical **(4)** and forming the covalently linked product R_1:R_2. Adapted from (146, 340).

The second method tested was the free radical-induced thiol-ene reaction (or thiol-ene click chemistry, TECC) (146, 341). Here, a thiol-containing molecule is reacted with an -ene group, following the two-step mechanism outlined in Figure 5.2.3. In the presence of a photoinitiator, irradiation with UV or visible light causes reduction of the thiol to a thiyl radical. The radical attacks the electrophilic C of an -ene group, forming a carbon-centred radical (146). This is followed by a chain transfer, where a hydrogen radical is abstracted from another thiol by the carbon-centred radical. This forms the covalently linked product and regenerates the thiyl for further propagation (146).

This reaction has been extensively utilised for patterning synthetic polymer hydrogels, often with peptides and proteins, using a variety of thiol and -ene functionalities (Figure 5.2.4) (161, 205, 337, 342-345). In addition, TECC has been utilised for the formation of peptide macrocycles *via* the reaction of Cys side chain thiols with -ene containing small molecules (346). However, examples of TECC where both the thiol and -ene groups are contained on peptides are rare. That being said, one key example is the introduction of Cys-containing peptides into SAFs *via* an allyl-Gly residue in SAF-p1, though the reaction product was attained at a very low yield (347). TECC-mediated modification of a synthetic peptide hydrogel has, to my knowledge, not been reported.

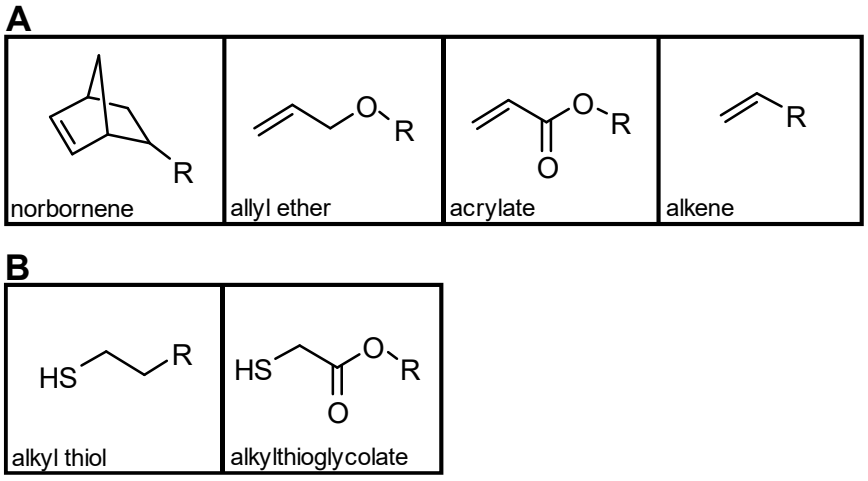

Figure 5.2.4: Common reactive -ene **(A)** and thiol **(B)** groups reported for TECC (341).

Peptides cannot be directly incorporated into hSAFs *via* TECC

As previously reported (140) and demonstrated in Chapter 3.2, the *N*-terminal Lys residue of hSAF-p1 can be replaced with azidonorleucine to enable peptide attachment *via* CuAAC. Therefore, this residue

was chosen for modification with a reactive handle for TECC. Given that this reaction is not commonly used to join two peptides, I decided to take two different approaches using two different reactive pairs of peptides, termed pair 1 and pair 2 (Figure 5.2.5). Pair 1 consisted of hSAF-p1, modified with an allyloxycarbonyl (Alloc)-Lys residue at the *N*-terminal position (hSAF-p1KAlloc) and a variant of RGDS with an *N*-terminal Cys (Cys-RGDS). I chose to use an Alloc, rather than the allyl previously used for modification of the SAFs (347), due to previous reports suggesting increased reactivity of allyl ethers compared with alkenes (348). Pair B consisted of hSAF-p1, modified with a Cys residue at the *N*-terminal position (hSAF-p1Cys), and another variant of RGDS containing an *N*-terminal norbornene group (norb-RGDS). A norbornene was chosen due to its reported increased reactivity compared to a linear alkene (341, 348). Inclusion of a norbornene in hSAF-p1 *via* modification of a Lys side chain was also intended, but synthesis of this peptide was unsuccessful.

A

Pair 1	hSAF-p1KAlloc	H-KalIAALKA KIAALKA EIAALEW ENAALEA-COOH
	Cys-RGDS	H-CGSGSG RGDS-COOH
Pair 2	hSAF-p1Cys	H-C IAALKAK IAALKAE IAALEWE NAALEA-COOH
	norb-RGDS	norb-GSGSG RGDS-COOH

B

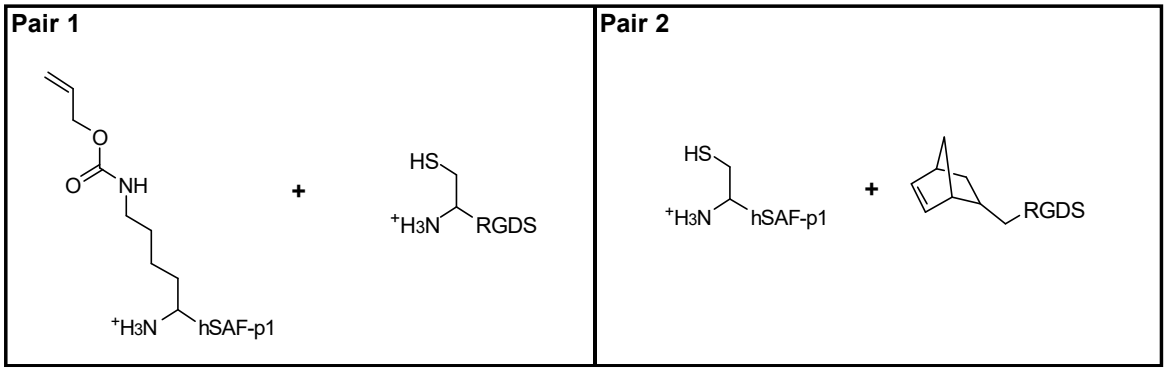

Figure 5.2.5: Peptide pairs 1 and 2 used for TECC. **A:** Sequences for each peptide. Reactive groups are highlighted in green: Alloc-Lys (Kal), Cys (C) and norbornene (norb). **B:** Structures of the thiol and -ene groups for each pair of peptides. Reactions contained 200 µM Cys-peptide, 100 µM ene-peptide and 0.1% (w/v) Irgacure 2959 in MOPS, pH 7.4.

Irgacure 2959 is one of the most commonly reported UV photoinitiators for TECC (161, 343, 347) and was chosen for these reactions. To be consistent with all other hSAF studies, all reactions were conducted at pH 7.4 in MOPS buffer. A 9W, Philips Fluo Compact UVB lamp (280 – 315 nm), placed

~1 cm above the reaction solution, was used to initiate the reaction. The individual reaction components, prior to UVB irradiation, were analysed by HPLC (Figure 5.2.6, left panels). The reaction components (200 µM Cys-peptide, 100 µM ene-peptide, 0.1% (w/v) Irgacure 2959 in MOPS, pH 7.4) were then mixed and exposed to UVB light. Product formation was monitored by HPLC (Figure 5.2.6, right panels). I hypothesised that, if the pairs of peptides formed a new conjugated product, I should observe both the disappearance of the reactants and formation of product by HPLC.

Prior to UVB irradiation, Irgacure 2959 eluted as a prominent peak with far greater absorbance at 220 nm than the peptide reactants (Figure 5.2.6A and C, grey). Furthermore, this peak overlaid exactly with that of Cys-RGDS (Figure 5.2.6A, cyan), making any disappearance of this reactant difficult to follow. Upon UVB irradiation, numerous peaks were observed, making it difficult to monitor reaction progression in either pair 1 (Figure 5.2.6B) or 2 (Figure 5.2.6D). However, all peaks were analysed by MALDI-TOF-MS and no conjugated product was observed for either pair of peptides. Due to the intensity of these peaks relative to unreacted Irgacure 2959, I suspected that these were not peptide products of the reaction, but likely formed by the photoinitiator. This was confirmed by irradiating Irgacure 2959 alone with UVB light (Figure 5.2.6E, black). A similar number of high intensity peaks were observed that closely matched those in the TECC reaction mixes. These peaks likely masked any peptide product formation, or lack thereof.

Owing to these difficulties in monitoring reactions containing Irgacure 2959, I briefly investigated a different photoinitiator, Eosin Y, which is activated by visible light (205). This did not produce any noticeable absorbance at 220 nm (Appendix Figure 8.4.3A) prior to irradiation, however, exposure to visible light resulted in the formation of multiple product peaks (Appendix Figure 8.4.3B), the masses of which did not match that of the formed product. Critically, exposure to visible light did not reduce the intensity of either reactant peak, indicating that they were not converted to product.

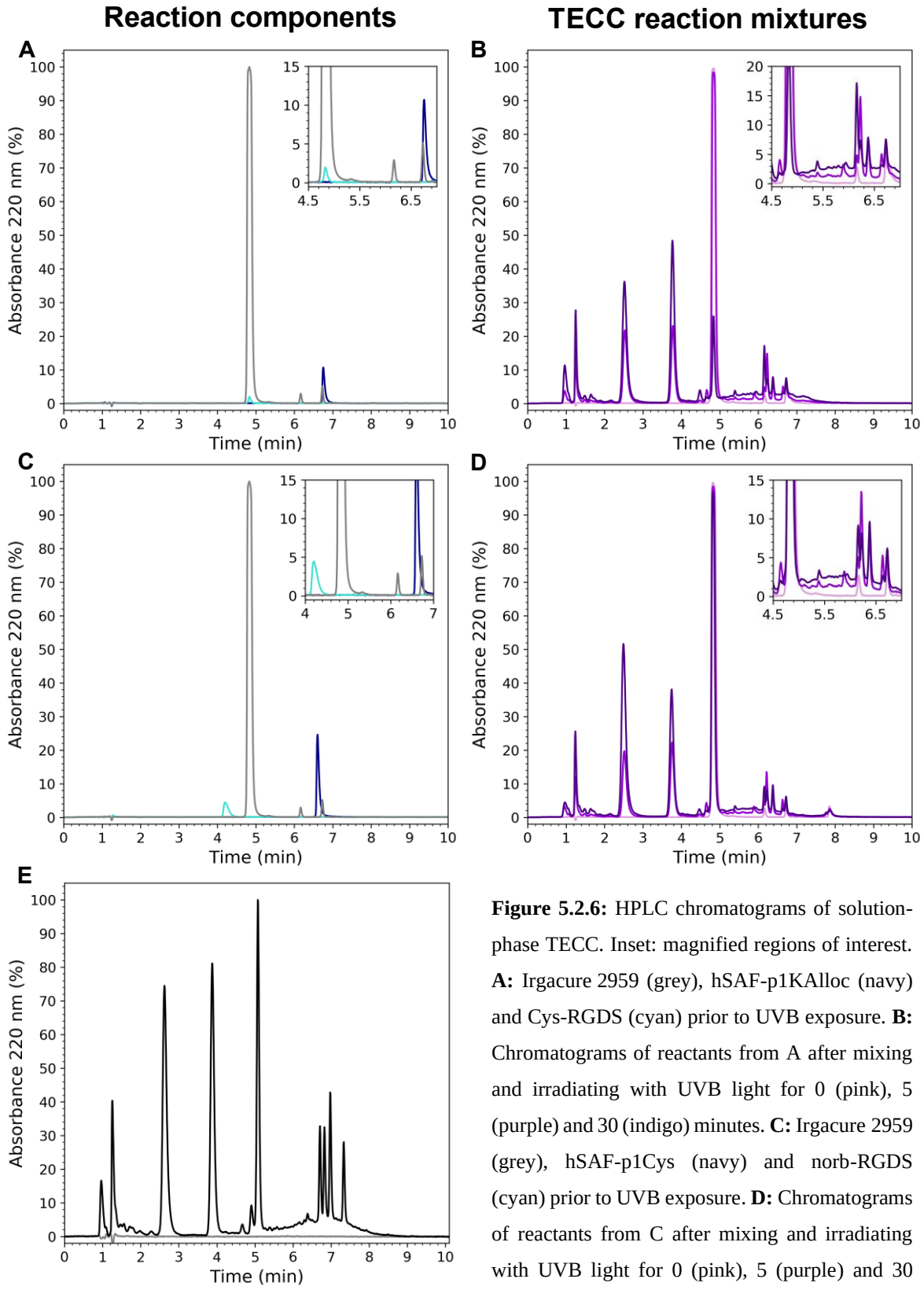

Figure 5.2.6: HPLC chromatograms of solution-phase TECC. Inset: magnified regions of interest. **A:** Irgacure 2959 (grey), hSAF-p1KAlloc (navy) and Cys-RGDS (cyan) prior to UVB exposure. **B:** Chromatograms of reactants from A after mixing and irradiating with UVB light for 0 (pink), 5 (purple) and 30 (indigo) minutes. **C:** Irgacure 2959 (grey), hSAF-p1Cys (navy) and norb-RGDS (cyan) prior to UVB exposure. **D:** Chromatograms of reactants from C after mixing and irradiating with UVB light for 0 (pink), 5 (purple) and 30 (indigo) minutes. **E:** Irgacure 2959 (black) or MOPS buffer (grey) after UVB exposure for 30 minutes. All gradients are 0 – 100% acetonitrile.

I reasoned that the reaction might be easier to follow if performed on an hSAF gel, rather than peptides in solution. This would allow any photoinitiator to be removed prior to analysis by HPLC and, thus, only peptide products of the reaction should be observed. For these studies, I returned to using Irgacure 2959. Cys inclusion in the hSAF scaffold is not desirable, as disulphide-bond formation between adjacent peptides might alter the properties of the gel (as well as render the peptides unreactive for TECC). Therefore, for all further studies, p1KAlloc:p2 hSAFs were used. These gels were prepared following the same protocol as the parent system. p1KAlloc:p2 hSAFs were incubated with 2 mM Cys-RGDS, 0.1% (w/v) Irgacure 2959 and irradiated with UVB light (Figure 5.2.7A) for 10 minutes.

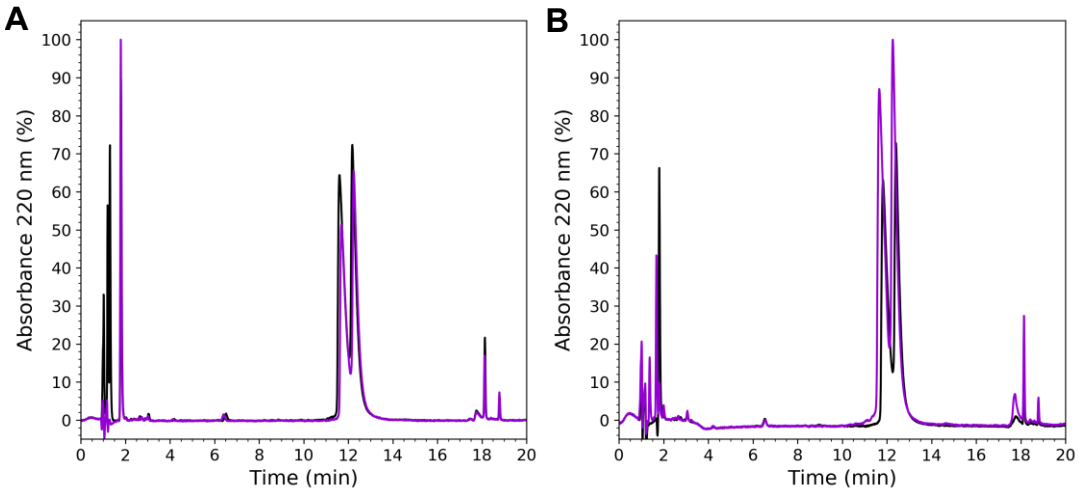

Figure 5.2.7: HPLC chromatograms showing p1KAlloc:p2 gels decorated *via* TECC. **A:** Chromatogram of p1KAlloc:p2 hSAF reacted with Cys-RGDS after 0 (black) and 10 minutes (purple) UVB irradiation. **B:** Chromatogram of p1KAlloc:p2 hSAF reacted with L-Cys *via* TECC after 0 (black) and 10 minutes (purple) UVB irradiation. The two prominent peaks common to all chromatograms correspond to hSAF-p2 (11.75 minute elution) and hSAF-p1KAlloc (12.5 minute elution). Gradients were 30 – 40% acetonitrile.

Though this new approach enabled the reaction to be followed more clearly by HPLC, no product was observed (Figure 5.2.7A). I was concerned that this was due to the formation of disulphides between adjacent Cys-RGDS peptides prior to mixing with the gel. However, addition of TCEP to the reaction mixture, to reduce these bonds, resulted in the formation of a product with a mass matching that of p1KAlloc-TCEP (Appendix Figure 8.4.4). This product was formed in a light-dependent manner, accompanied by a reduction in intensity of the hSAF-p1KAlloc reactant. As this conjugation was not desired, I did not investigate the mechanism further and omitted TCEP from all further reaction mixtures.

It is possible that, by reacting two large and sterically hindered (relative to a small-molecule or monomeric polymer building block) peptides, the thiol and -ene are unable to come into contact for long enough for the reaction to occur. Therefore, I reacted p1KAlloc:p2 hSAFs with the free amino acid L-Cys (Figure 5.2.7C). This reaction was also unsuccessful – neither formation of product, nor disappearance of reactants, was visible by HPLC. This led me to believe that either the thiol or Alloc group was unsuitable for the thiol-ene reaction to proceed under these conditions.

A small molecule PEG can be incorporated into hSAFs by TECC

TECC is not often reported between two peptides. Either the -ene or thiol is almost always contained on a synthetic polymer or small molecule (161, 337, 345). Therefore, I hypothesised that a short polymer linker, rather than a peptide, might be incorporated into p1KAlloc:p2 hSAFs by TECC. Polyethylene glycol (PEG) is one of the most commonly used synthetic polymers in materials science. As such, PEGs are commercially available with various chain lengths and terminated with a range of functional groups, including thiols.

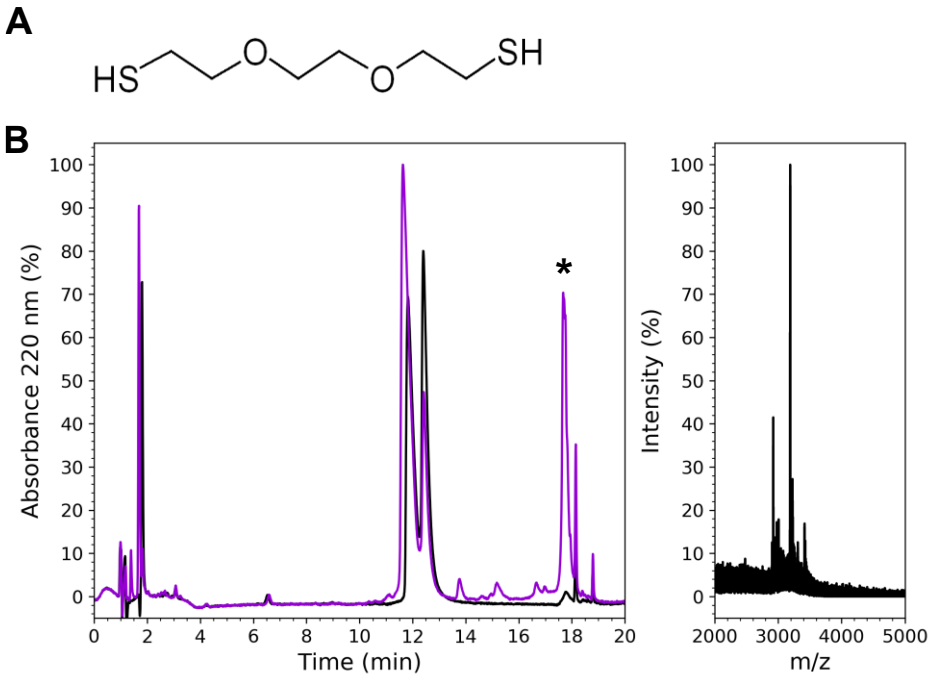

Figure 5.2.8: p1KAlloc:p2 hSAFs decorated with PEG_{2SH} by TECC. **A:** PEG_{2SH}. **B, left panel:** HPLC chromatograms of p1KAlloc:p2 hSAFs, incubated with PEG_{2SH}, and irradiated with UVB light for 0 (black) or 10 (purple) minutes. The gradient was 30 – 40% acetonitrile. **B, right panel:** MALDI-TOF-MS spectrum of the product peak labelled *. Expected mass = 3187.9, recorded mass = 3189.44 Da.

Owing to the relative lack of secondary structure of PEG chains – compared to a peptide backbone – I postulated that these thiol groups would be less sterically hindered than that of a Cys side chain and, thus, might allow TECC to proceed. Therefore, I chose to react p1KAlloc:p2 hSAFs with 2,2'-(ethylenedioxy)diethanethiol (PEG_{2SH}, Figure 5.2.8A). I reasoned that, after attachment to hSAF-p1KAlloc by TECC, the second thiol might allow conjugation with a peptide. I accepted here that, as a thiol was available at either end of PEG_{2SH}, it would be possible for both to react with two different hSAF-p1KAlloc peptides, which was not desired. To prevent this, PEG_{2SH} was provided in a 5-fold excess (5 mM). p1KAlloc:p2 hSAFs were reacted with PEG_{2SH} in the same way as for all previous studies (Figure 5.2.8B).

Upon UVB irradiation, a clear product peak was formed (Figure 5.2.8B, *) accompanied by a reduction in the intensity of the hSAF-p1KAlloc peak. MALDI-TOF-MS analysis confirmed the mass of the product to be that of the desired hSAF-p1KAlloc-PEG_{SH} complex. The approximate percentage of hSAF-p1KAlloc converted to p1KAlloc-PEG was 34%, a slightly lower yield than that achieved with CuAAC (Figure 3.2.1). No product peak corresponding to the mass of a trimeric p1KAlloc-PEG-p1KAlloc conjugate was observed. It is possible that this larger complex was undetectable by MALDI-TOF-MS, however, I was satisfied that an appreciable amount of the desired p1KAlloc-PEG_{SH} product was produced and did not probe this further.

PEG_{2SH} can act as a linker between hSAFs and RGDS *via* maleimide-thiol reaction

Given the success of TECC using p1KAlloc:p2 hSAFs and PEG_{2SH}, and the apparent lack of the p1KAlloc-PEG-p1KAlloc product, I concluded that PEG_{2SH} might act as a linker between the gel and a desired peptide. Once bound to hSAF-p1KAlloc, PEG_{2SH} would still have one thiol available for subsequent modification. I chose to target this *via* the well-characterised and commonly used maleimide-thiol reaction, which proceeds under ambient conditions without addition of catalyst (224, 349, 350). A variant of RGDS with an *N*-terminal maleimide was synthesised (mal-RGDS) and p1KAlloc:p2 hSAFs were decorated following the method outlined in Figure 5.2.9. First, PEG_{2SH} was

appended to p1KAlloc:p2 hSAFs by TECC *via* UVB light exposure. The gel was then incubated with mal-RGDS. Once again, the reaction was monitored by HPLC and MALDI-TOF-MS (Figure 5.2.10).

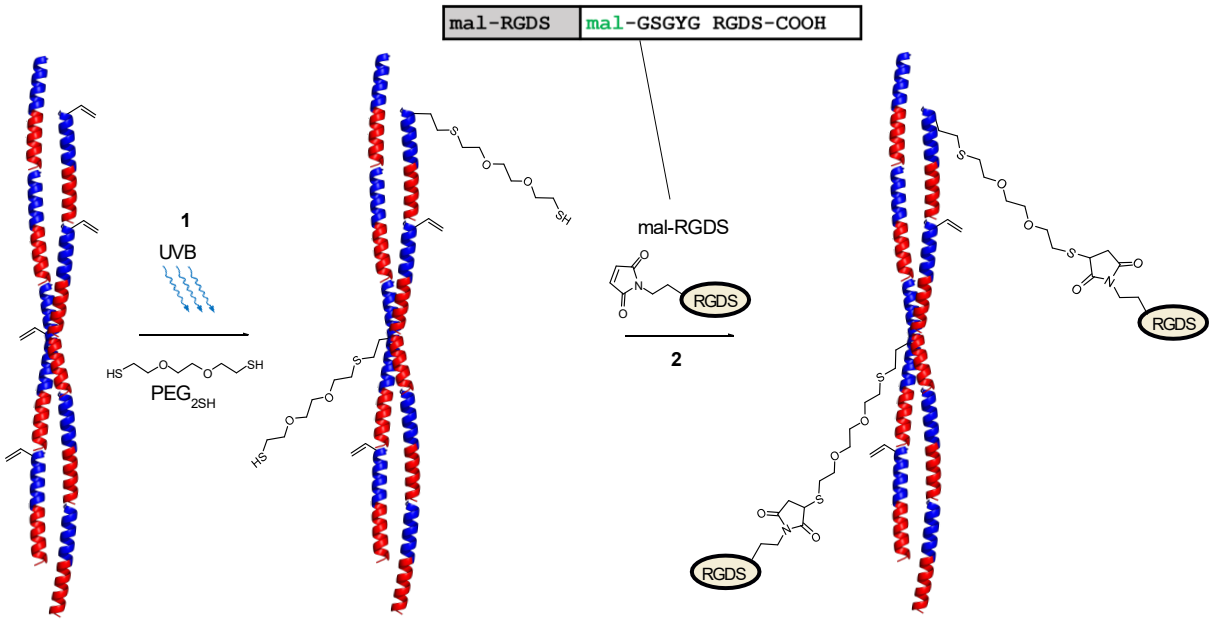

Figure 5.2.9: Schematic diagram showing photo-activated incorporation of RGDS peptide *via* TECC and thiol-maleimide chemistries. hSAF-p1KAlloc:p2 gels are formed and PEG_{2SH} incorporated *via* TECC, triggered by UVB light **(1)**. mal-RGDS can then be reacted with the second thiol of PEG_{2SH} to form the final product **(2)**, covalently modifying the gel with RGDS. The sequence of mal-RGDS is shown inset with the maleimide group highlighted in green.

Upon addition of mal-RGDS to undecorated p1KAlloc:p2 gels, no product was formed (Figure 5.2.10A, grey). However, addition of mal-RGDS to PEG_{2SH}-decorated gels (Figure 5.2.10A, navy) resulted in the formation of a product (*), which had a mass equal to the expected p1KAlloc-PEG-RGDS conjugate (Figure 5.2.10A, right panel). This led me to believe that the method outlined in Figure 5.2.9 was suitable for photo-activated attachment of peptides to hSAFs. I refer to this thiol-ene and subsequent maleimide-thiol reaction as thiol-ene, maleimide-thiol click chemistry (TE-MTCC).

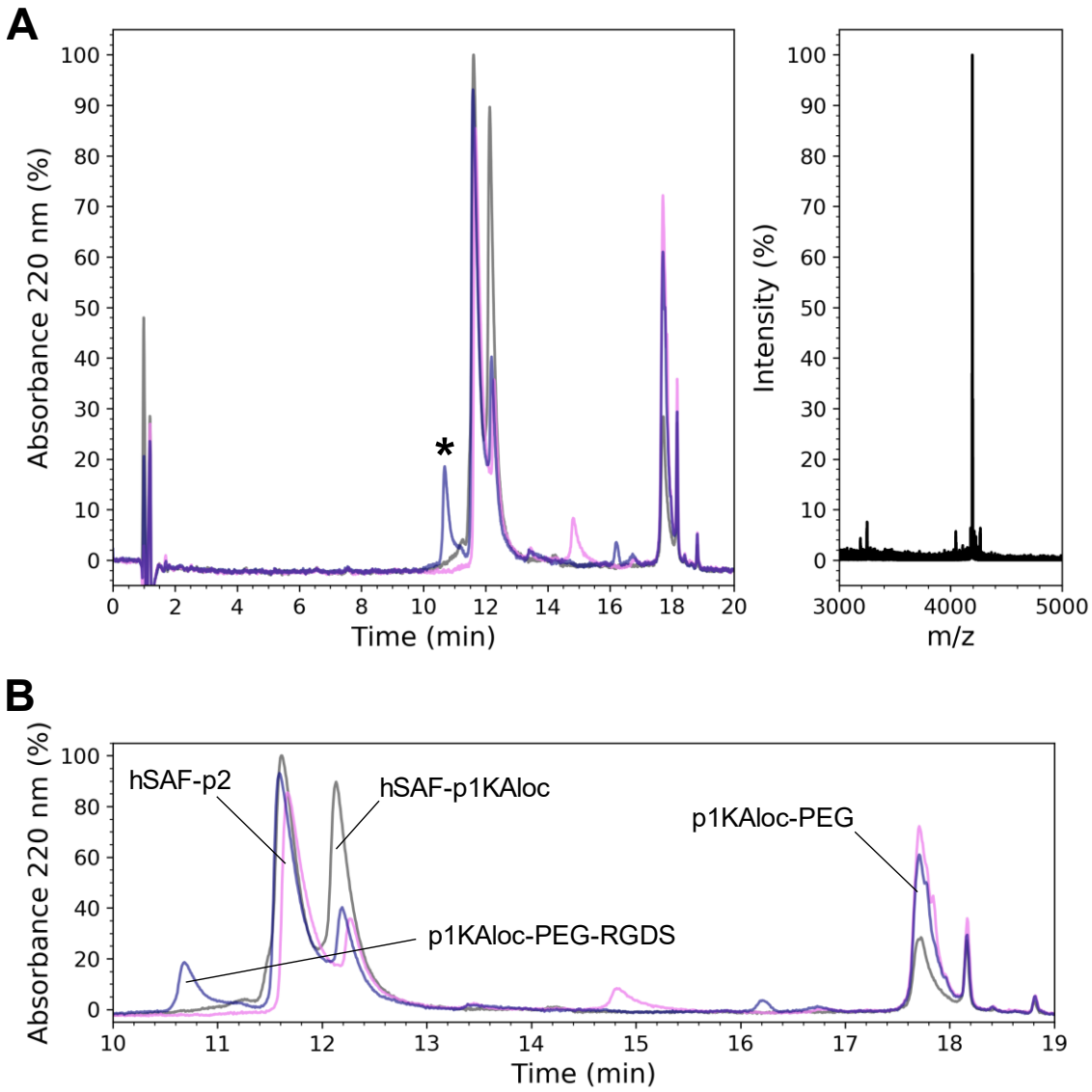

Figure 5.2.10: p1KAlloc:p2 gels reacted with PEG_{2SH} and mal-RGDS. **A, left panel:** HPLC chromatograms of p1KAlloc:p2 hSAFs: incubated with PEG_{2SH} and then mal-RGDS, but without UVB irradiation (grey); incubated with PEG_{2SH} and irradiated with UVB light for 3 minutes (pink); or incubated with PEG_{2SH}, irradiated with UVB light for 3 minutes and incubated with mal-RGDS (navy). The gradient was 30 – 40% acetonitrile. **A, right panel:** MALDI-TOF-MS spectra of the product peak labelled * in A (expected mass = 4193.8 Da, recorded mass = 4195.0 Da) that corresponds to p1KAlloc-PEG-RGDS. **B:** Expanded view of the key reactant and product peaks from A, with labels indicating each species identified by MALDI-TOF-MS.

TECC does not impact fibre stability or scaffold properties

Before proceeding further, I wanted to test if the TE-MTCC method of peptide attachment impacted the biophysical properties of hSAFs. UVB irradiation is potentially damaging to peptides (351) and might affect scaffold stability. Therefore, CD spectroscopy and TEM were performed to assess fibre stability after TE-MTCC (Figure 5.2.11A-F).

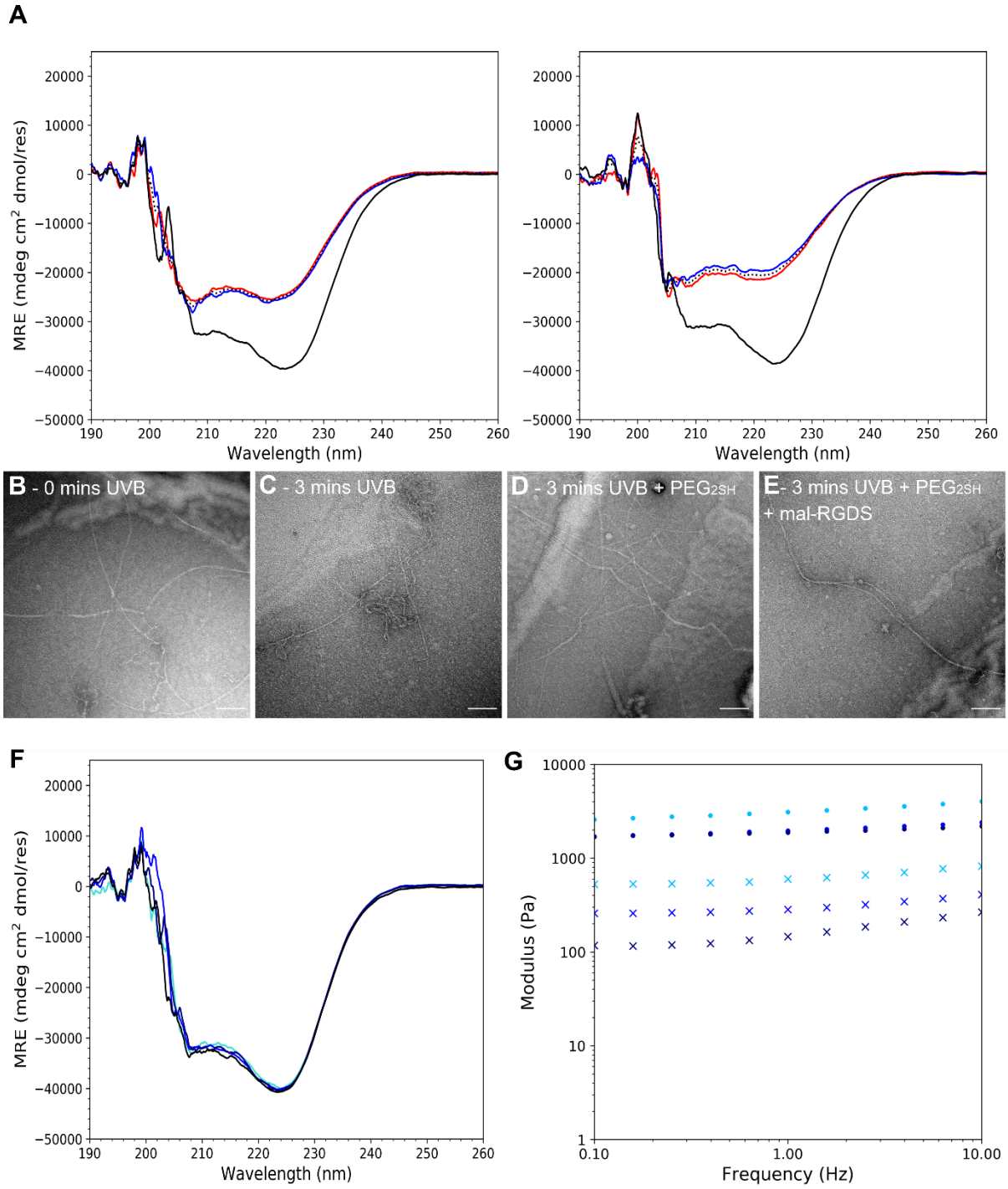

Figure 5.2.11: Biophysical characterisation of TE-MTCC-decorated hSAFs. **A:** CD spectra of hSAF-p1KAlloc (red), hSAF-p2 (blue), the theoretical average of mixing the two (grey, dotted), and the recorded spectra when the two are mixed (black). Recordings were taken at 20 (left panel) and 37 ºC (right panel). **B-E:** TEM images of: p1KAlloc:p2 fibres **(B)**; fibres after 3 minutes UVB irradiation **(C)**; after incorporation of PEG_{2SH} by UVB exposure **(D);** and after incorporation of mal-RGDS following PEG_{2SH} attachment **(E)**. **F:** CD spectra of p1KAlloc:p2 fibres after 0 (cyan) and 3 (blue) minutes UVB exposure, as well as PEG_{2SH}-decorated fibres after 3 minutes UVB exposure (navy). **G:** Frequency sweep rheological analysis of p1KAlloc:p2 hSAFs (cyan), PEG_{2SH}-decorated (blue) and mal-RGDS-decorated hSAFs (navy). G' (dots) and G'' (crosses) values are shown. Data in F and G were collected at 37 ºC.

CD indicated that hSAF-p1KAlloc and hSAF-p2 interacted and spectral red-shifting suggested they formed higher-order assemblies, with α-helical character (Figure 5.2.11A). This behaviour was similar at 20 and 37 ºC and comparable to the parent hSAFs (Figure 3.1.1). TEM revealed that the peptides formed fibres analogous to those observed for the parent and p1KAz:p2 hSAFs (Figure 5.2.11B). Similar structures were observed after 3 minutes UVB exposure (Figure 5.2.11C) and after incorporation of PEG_{2SH} (Figure 5.2.11D) and mal-RGDS (Figure 5.2.11E). In addition, CD spectroscopy of UVB-irradiated p1KAlloc:p2 hSAFs indicated that neither UVB exposure or addition of PEG_{2SH}, impacted fibre stability (Figure 5.2.11F). Taken together, these data indicate that hSAF-p1KAlloc and hSAF-p2 interact to form α-helical fibres that are stable to UVB exposure at the timescales relevant for TECC.

It is reasonable to contend that, if p1KAlloc-PEG-p1KAlloc assemblies did occur, the PEG might act as a crosslinker between fibres. This might promote fibre-fibre interactions and, therefore, increase the elastic modulus of the scaffold upon UVB irradiation. Therefore, I performed bulk rheological analysis to investigate whether TECC-mediated PEG_{2SH} introduction resulted in a change in hSAF elastic modulus (Figure 5.2.11G).

p1KAlloc:p2 hSAFs formed a gel with an elastic modulus of 2.6 kPa at 37 ºC (Figure 5.2.11G, cyan) – on the same order of magnitude as the parent system, which stiffened to 2 kPa upon heating to 37 ºC (Figure 1.1.2). Upon irradiation with UVB light, either in the absence (Figure 5.2.11G, blue) or presence (Figure 5.2.11G, navy) of PEG_{2SH}, the recorded G' fell to 1.7 kPa. This confirmed that the gel did not stiffen following TECC. The reduction in elastic modulus in response to UVB irradiation was relatively minimal and remained within the range of hSAF gels described in this thesis. I was satisfied from these observations that TE-MTCC did not markedly impact fibre stability or viscoelastic properties of the scaffold.

5.3: Patterning hSAFs with GFP *via* photolithography

GFP can be introduced into hSAFs in a light-dependent manner

By combining TE-MTCC with SpyTag-SpyCatcher, I posited that fluorescent proteins could be patterned into hSAFs. The proposed method by which this would proceed is outlined in Figure 5.3.1.

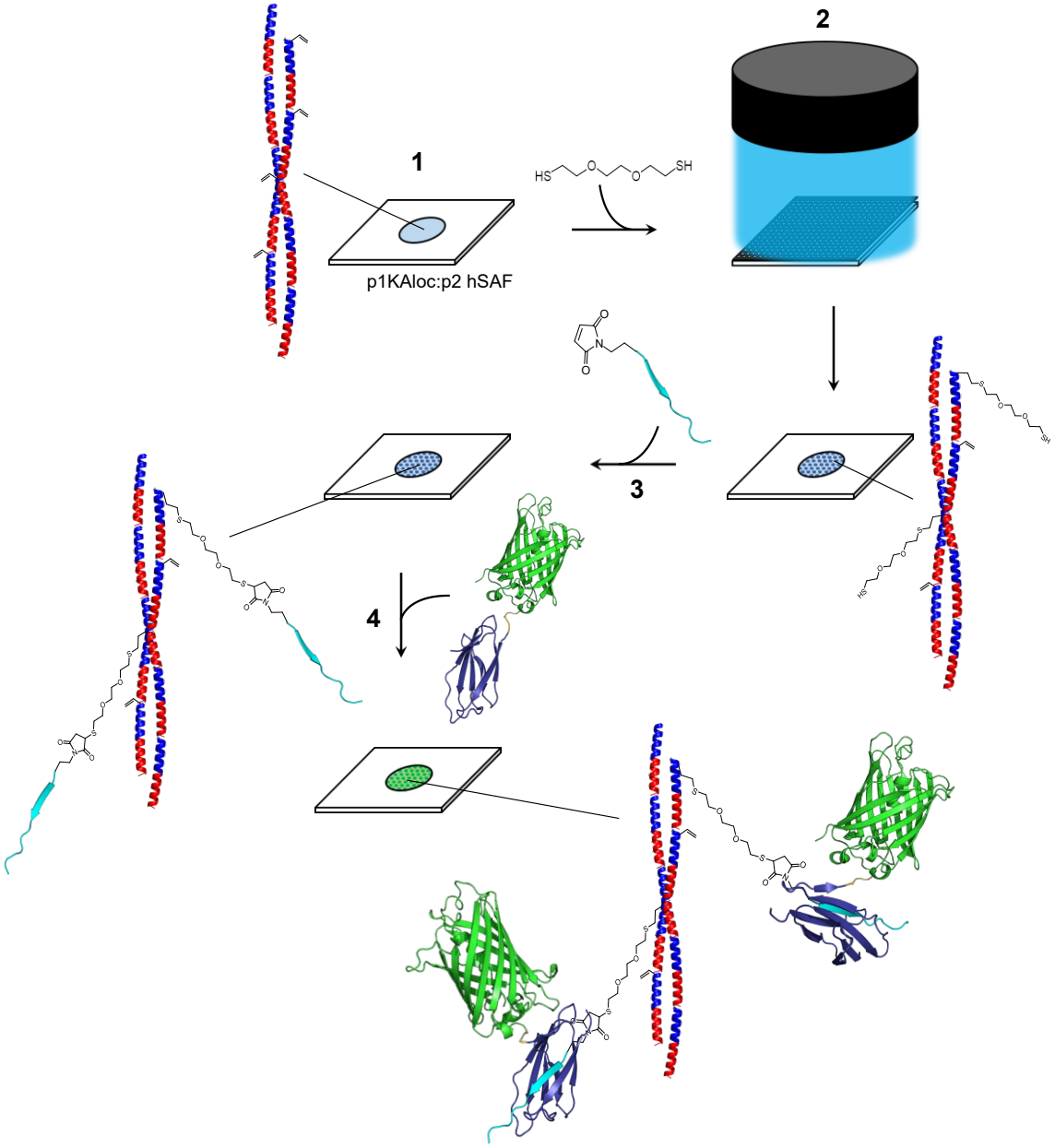

Figure 5.3.1: Schematic diagram showing TE-MTCC- and SpyTag-SpyCatcher-mediated patterning of GFP on hSAFs by photolithography. **1:** p1KAlloc:p2 hSAFs are formed on a glass slide. **2:** PEG_{2SH} and Irgacure 2959 are then added and a photomask placed over the gel. UVB light is shone through the mask onto hSAFs, creating patterns of immobilised PEG_{2SH}. **3:** mal-SpyTag is then incorporated *via* maleimide-thiol reaction. **4:** Finally, gels are incubated with SC-GFP, creating patterns of GFP immobilised on hSAFs.

First, I wanted to confirm that our method of photo-induced peptide incorporation also worked for SpyTag-SpyCatcher-mediated protein incorporation. A maleimide-modified SpyTag peptide (mal-SpyTag) was synthesised (Figure 5.3.2A). p1KAlloc:p2 hSAF gels were incubated with PEG_{2SH} and irradiated with UVB light for 0 – 5 minutes. The gels were then incubated with mal-SpyTag, and subsequently SC-GFP. GFP fluorescence on each gel was quantified using a ClarioStar plate reader (BMG LabTech, Germany) (Figure 5.3.2B).

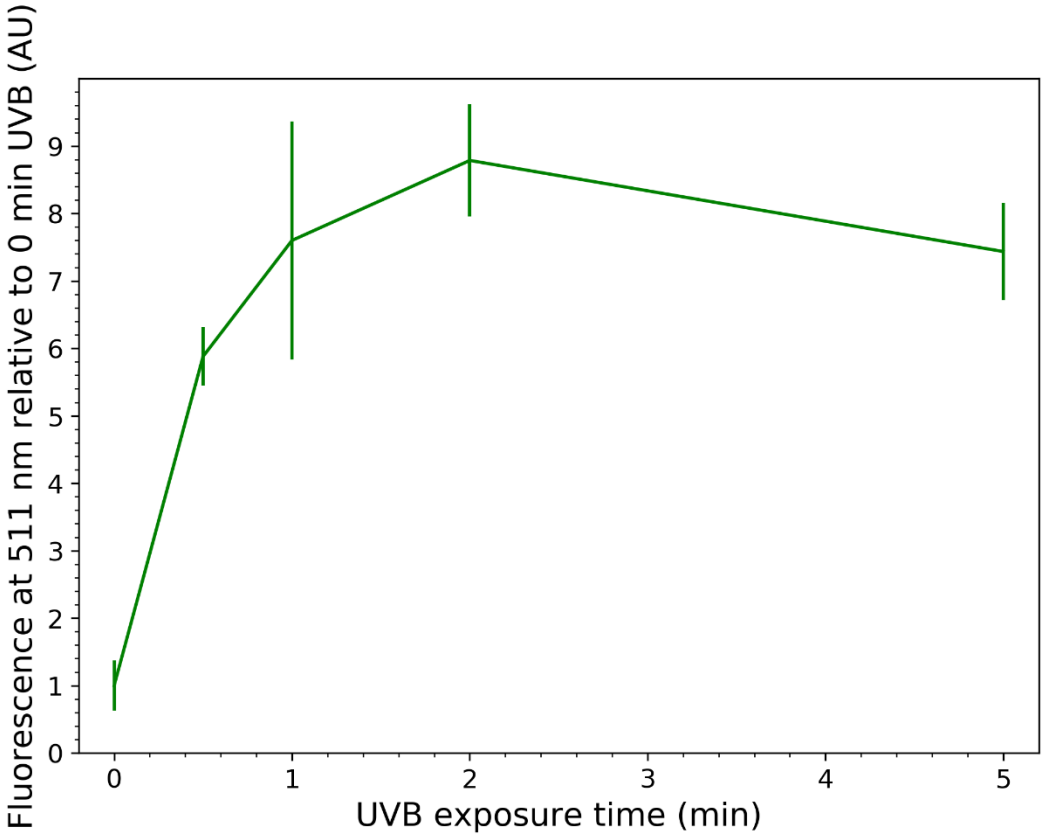

Figure 5.3.2: Photo-inducible SC-GFP incorporation. GFP fluorescence on p1KAlloc:p2 hSAFs, decorated with PEG_{2SH} *via* TECC, and subsequently mal-SpyTag and SC-GFP. Gels were irradiated with UVB light for varying lengths of time. Fluorescence values are normalised to 0 minutes UVB exposure. n=3 different gels for each condition. Error bars show one standard deviation from the mean.

GFP attachment to the scaffold increased with UVB irradiation time up to 2 minutes. This suggested that TE-MTCC and subsequent incorporation of SC-GFP proceeded as depicted in Figure 5.3.1. In addition, this suggested that 2 minutes UVB exposure was adequate for protein attachment *via* this method and, therefore, I used this time for all further photolithographic studies.

Unfortunately, attempts to monitor mal-SpyTag conjugation to p1KAlloc-PEG$_{2SH}$ by HPLC and MALDI-TOF-MS were unsuccessful. No obvious product was observed by HPLC, though a small peak very close to that of hSAF-p1KAlloc suggested that the p1KAlloc-PEG-SpyTag product coeluted with hSAF-p1KAlloc (Appendix Figure 8.4.5). However, I was unable to separate this from the higher intensity hSAF-p1KAlloc to obtain a mass. I was satisfied that, given SC-GFP attachment was promoted by UVB light exposure (Figure 5.3.2), the reaction proceeded as intended.

hSAFs can be patterned with GFP by photolithography

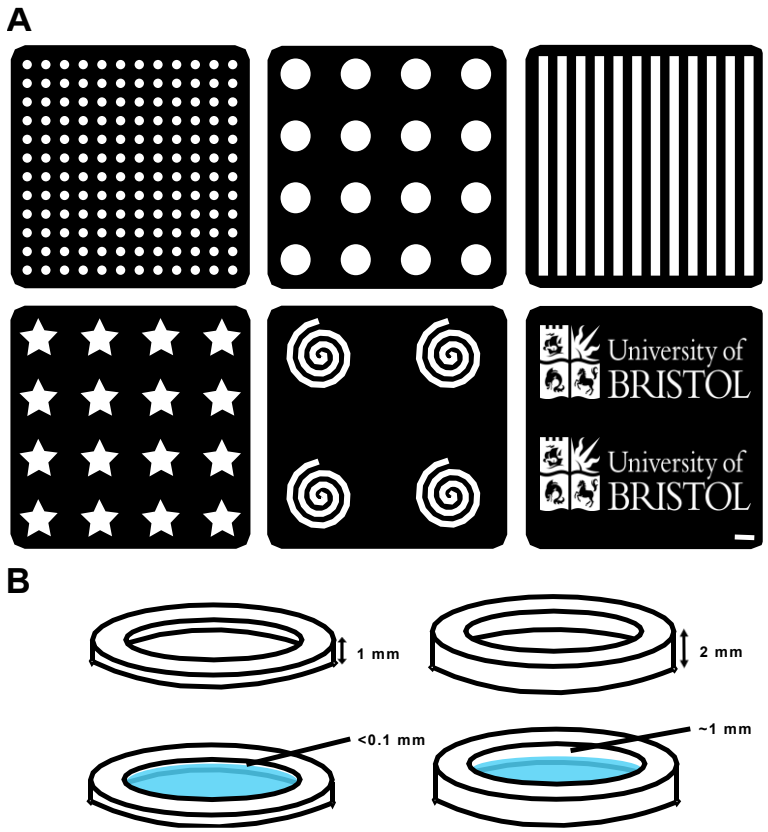

Figure 5.3.3: Design of masks and moulds for photolithography. **A:** Examples of photomask designs printed on transparent film by JD Photodata (UK) for photolithographic patterning of hSAFs. Scale bar = 200 μm. **B:** Schematic diagrams of 1 (left) and 2 mm (right) deep hSAF moulds for photolithography. These designs should result in <0.1 mm and 1 mm, respectively, between the top of the gel (blue) and the photomask, assuming the depth of a 30 μl volume gel is ~1 mm.

After determining the light exposure time required to incorporate SC-GFP, the method outlined in Figure 5.3.1 was followed to spatially pattern hSAFs with GFP. Several photomasks were printed onto transparent film (JD Photodata, UK) with feature sizes ranging from <50 – 500 μm (Figure 5.3.3A). This allowed the feature resolution achievable with this technique to be tested. The success of

photolithography depends on placing the photomask as close to the top of the hydrogel as possible, thus, minimising spreading of the light beam before it contacts the gel (352, 353). Therefore, 1 and 2 mm deep moulds were 3D printed and glued to coverslips, in which to form hSAFs (Figure 5.3.3B). These allowed the mask to be placed close to the gel surface.

Initially, a photomask with 400 μm diameter transparent spots (among the largest features designed) was used to pattern p1KAlloc:p2 hSAFs with PEG_{2SH}. Gels were subsequently incubated with mal-SpyTag, then SC-GFP, and washed copiously with PBS to remove any non-specifically associated protein. Images were collected by widefield microscopy (Figure 5.3.4).

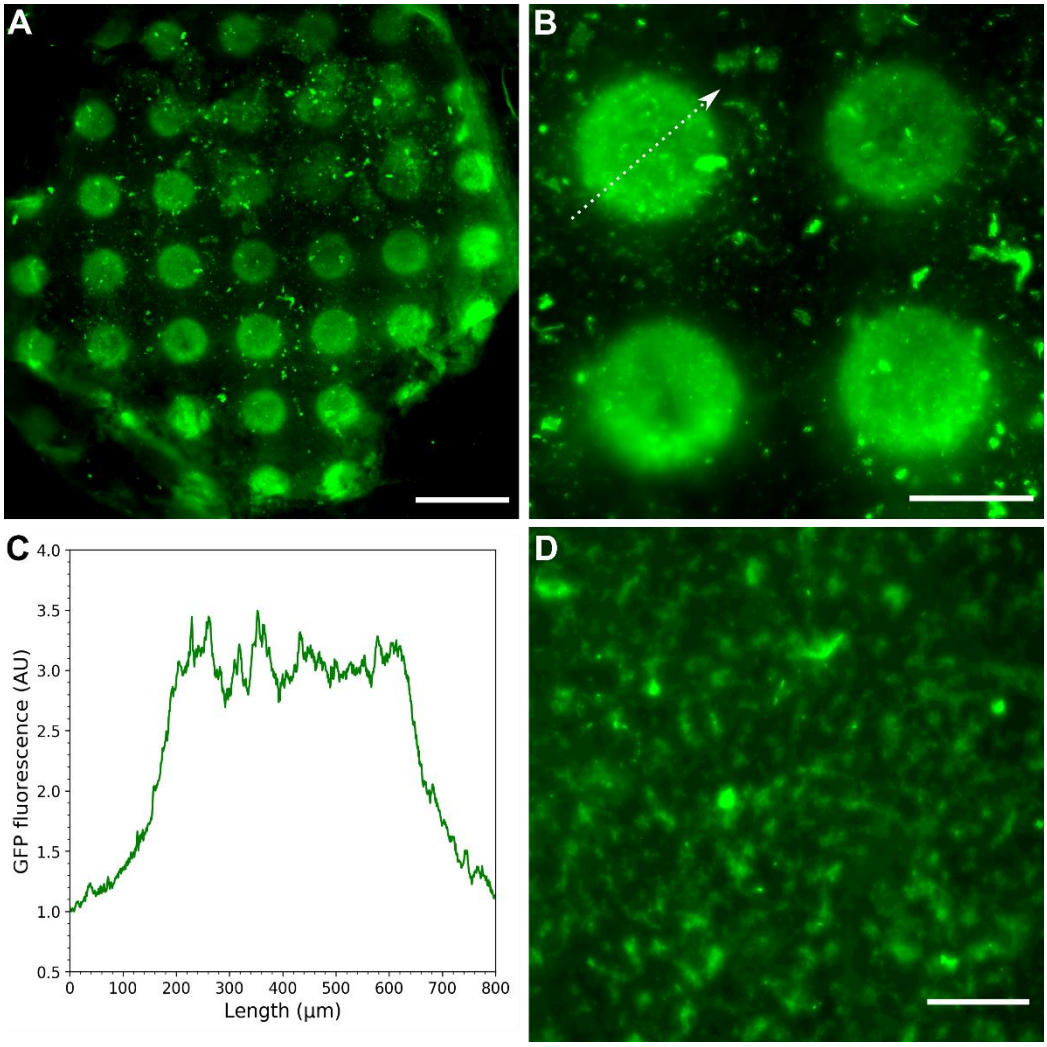

Figure 5.3.4: Photopatterning hSAFs with GFP. **A-B:** Widefield images showing spot patterns across a whole hSAF gel **(A)** and a subsection of the same gel **(B)**. Scale bars = 1000 **(A)** and 400 **(B)** μm. **C:** Fluorescence intensity plot through the dotted line in B, values are normalised to the minimum intensity recorded. **D:** Widefield image of patterned hSAFs in a 2 mm deep mould. Scale bar = 400 μm.

Spots of GFP fluorescence were clearly visible across hSAFs contained in 1 mm deep moulds (Figure 5.3.4A-B). These had an average diameter of 460 μm, despite the photomask containing 400 μm diameter spots. This indicated that some light dissipated either before contacting the gel or while travelling through it, causing some blurring at the pattern edges. Fluorescence intensity was plotted across one of these spots (Figure 5.3.4C), demonstrating that fluorescence at the spot edge increased over a length of ~100 μm. Therefore, these patterns are less sharply defined than some previously reported in other gel systems. (196, 204). This indicated that patterning hSAFs with smaller features might be challenging.

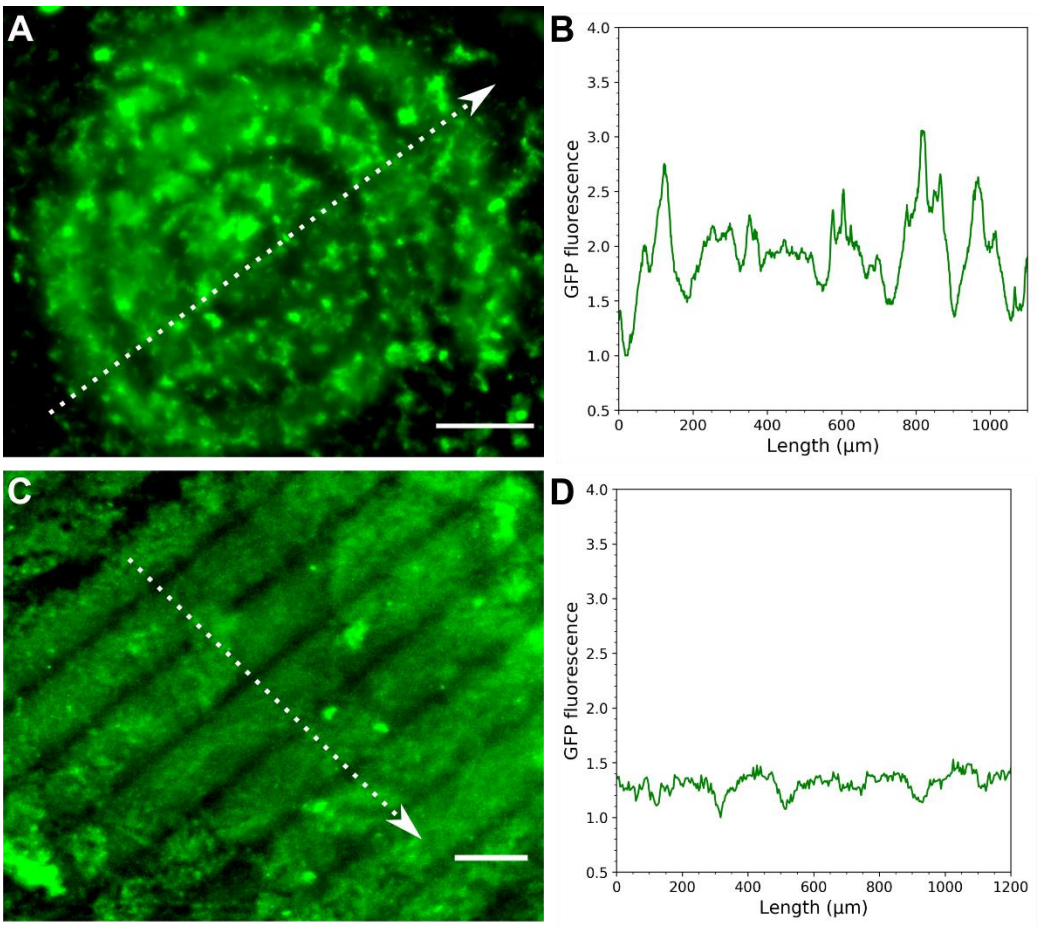

Figure 5.3.5: Patterning hSAFs with smaller features. **A-B:** Widefield image **(A)** and fluorescence intensity plot **(B)** of spiral-patterned hSAFs. Fluorescence intensity is plotted across the dotted line in A. **C-D:** Widefield image **(C)** and fluorescence intensity plot **(D)** of straight line-patterned hSAFs. Fluorescence intensity is plotted across the dotted line in C. Scale bars = 200 μm. Fluorescence values in B and C are normalised to the minimum recorded intensity

No patterns were observed when using the 2 mm moulds. As suspected, the photomask must be in very close contact with the top of the gel for patterning to be successful. Presumably, the columnated light passing through the spots dissipated before contacting the gel in the 2 mm deep moulds. This meant that the patterns of light exposure were lost and, thus, no spot patterns were visible (Figure 5.3.4D). Therefore, 1 mm deep moulds were used for all other experiments.

To understand the limitations of this photolithographic patterning method, hSAFs were patterned using two photomasks – straight lines and a spiral – both with 100 μm diameter features. Images were collected by widefield microscopy after mal-SpyTag and SC-GFP incubation (Figure 5.3.5). While both patterns were distinguishable, they were not as well defined as the 400 μm spot in Figure 5.3.4. This was demonstrated by the fluorescence intensity profiles across each pattern (Figure 5.3.5B and C). The desired pattern of alternating 100 μm-wide fluorescent and non-fluorescent regions was difficult to make out in either case, particularly for the 100 μm diameter line pattern (Figure 5.3.5C-D). Lines had an average diameter of 160 μm, meaning that the space between them was barely discernible in the fluorescence profile. I concluded from these experiments that, using the current method, feature sizes on the order of hundreds of microns are possible. However, further development would be required to achieve feature sizes of <100 μm.

5.4 Conclusions

Hydrogel micropatterning through various approaches is an established practice for synthetic and natural polymer hydrogels (97, 195, 199, 201, 202, 205, 332, 342, 354). However, while there are now many examples of synthetic peptide gels (44, 48, 54, 126, 158, 229), to the best of my knowledge, no attempts have been made to micropattern these materials. Here, through the novel application of photolithography to a designed peptide gel, I have demonstrated that hSAFs can be micropatterned with GFP. Therefore, this work demonstrates a significant step-forward for the field of synthetic peptide biomaterials – the approach taken here could be applied to other self-assembling peptide hydrogel systems with relative ease. That being said, the patterns reported here are much lower resolution and

less reproducible than some previously reported on synthetic polymer gels (196, 205). Further development of the patterning method would be required to achieve higher-resolution patterns.

A logical next step would be to pattern IGF1 into the gel and observe effects on neuronal growth. IGF1 is a reported axonal guidance factor (178, 179) and, therefore, one might expect to see patterns of neuronal growth towards regions of IGF1. However, the ephrin (166, 355), sonic hedgehog (170, 356) and semaphorin (313, 357) protein families are archetypal axonal guidance factors. The modular nature of our system, means that introduction of these proteins into hSAFs through SpyTag-SpyCatcher, should be possible.

Following the development of TE-MTCC, there are now two different methods for patterning hSAFs with peptides and proteins – CuAAC and TE-MTCC. These two reactions should be orthogonal, allowing two different peptides (or proteins) to be patterned into the gel and manipulated independently. This would allow neuronal cells to be exposed to carefully tailored cocktails of growth factors, or mixtures of adhesive ligands. I would have liked to demonstrate that CuAAC and TE-MTCC are orthogonal. For this, a second method of fluorescent protein introduction (in addition to SpyTag-SpyCatcher) would be required. The binding of biotin to streptavidin is commonly used in biotechnology (185, 270) and would likely be a suitable method to demonstrate orthogonality of these two types of click chemistry.

Though the microfluidic devices developed in this work proved unsuitable for patterning hSAFs, they might be suited to patterning neuronal growth on 2D surfaces. Microfluidic gradient generator device 3 appeared suitable for the generation of solution-phase gradients. By introducing a neurotrophic factor into one of the inlets, and maintaining flow through the device during culture, the effect of these factors on neuronal growth could be analysed in high throughput. Similar devices have been reported for such experiments (324, 358).

Chapter 6

α-helical peptides as sensors for small molecule detection

REDACTED

Chapter 7

Conclusions and future directions

Utilising *de novo* designed coiled-coil peptides as a modular scaffold for primary neurons

De novo designed peptides and proteins have huge potential as tools for basic and applied research (1). Owing to the relative infancy of the *de novo* protein design field, this potential is only beginning to be realised. Further investigation and development of designed peptide systems for specific applications is required before they can be used more broadly by the scientific community.

In Chapters 3-5, I have described the development of a *de novo* designed peptide hydrogel, hSAFs, as a novel cell culture tool for primary neurons (PNs). PN viability and neurite outgrowth on hSAFs is comparable to when cultured on the commercially available peptide hydrogel, Puramatrix, and does not require additional adhesive ligands. In addition, through the redesign of hSAFs to $shSAF_{W1,4}$, I (along with Alex Wasmuth) have demonstrated that a suite of gels ranging from 0.2 – 18 kPa can be formed. PNs are most viable on softer gels but produce longer processes on 1 kPa hSAFs. These results support previous findings (153, 250, 256) and indicate that PNs grow best on gels that closely match the elastic modulus of brain tissue (0.1 – 1 kPa). It is likely that the stiffer $shSAF_{W1,4}$ gels would be better suited to the culture of muscle cells (66). A logical next step would be to culture primary muscle cells on the different hSAF and $shSAF_{W1,4}$ gels. This would identify whether $shSAF_{W1,4}$ gels are suitable for the culture of non-neuronal mammalian cells.

Whole proteins can be incorporated into hSAFs, in a tuneable manner, *via* the SpyTag-SpyCatcher system. Modifying hSAFs with the neurotrophic factor IGF1 promotes PN survival and neurite outgrowth compared to unmodified hSAFs. IGF1-decorated hSAFs perform similarly to Matrigel in this regard. Through the adoption of thiol-ene click chemistry, I have demonstrated the incorporation of GFP in user-defined patterns. Protein incorporation and spatial patterning have been achieved using synthetic and natural polymer gels (161, 185, 196). However, to the best of my knowledge, both covalent modification with a full-length protein and spatial patterning of a designed peptide hydrogel are novel. Therefore, these studies go beyond that achieved with other designed self-assembling peptide hydrogels. An obvious initial next step would be to seed PNs onto an hSAF gel patterned with IGF1, RGDS or another neurotrophic factor, and observe effects on neuronal growth. The guidance of neuronal processes on a designed peptide hydrogel would also be a novel development.

Given its novelty, the described approach for photopatterning hSAFs warrants further investigation. Further development is required to create patterns with the resolution required to precisely direct cell behaviour *in vitro* as previously reported (223, 224). I hypothesise that the low pattern resolution reported here results from difficulties in getting the gel and photomask into close contact. This might be rectified by casting shallower gels or using bespoke glass moulds, rather than the 3D-printed ones used here. In addition, hSAFs might be patterned with multiple fluorescent proteins by using PEG linkers terminated with different functional groups.

The current study demonstrates the principle advantage of hSAFs compared with some other peptide or polymer systems: they are modular and, therefore, tuneable (Figure 7.1). hSAFs consist of two core building blocks: hSAF-p1 and hSAF-p2. Simple modification of hSAF-p1 yields hSAF-p1KAz and hSAF-p1KAlloc, which allow adhesive ligands and full-length proteins to be introduced through two different mechanisms – Cu^{2+}-catalysed azide-alkyne cycloaddition and thiol-ene, maleimide-thiol reaction. Both chemistries are tuneable, by varying hSAF-p1KAz concentration and UV light exposure, respectively. Furthermore, other simple point mutations yield shSAF-p1$_{W1,4}$ and shSAF-p2$_{W1,4}$, which can be used to form gels with increased elastic modulus. Different proteins can be incorporated *via* fusion with SpyCatcher and incubating with SpyTag-decorated gels.

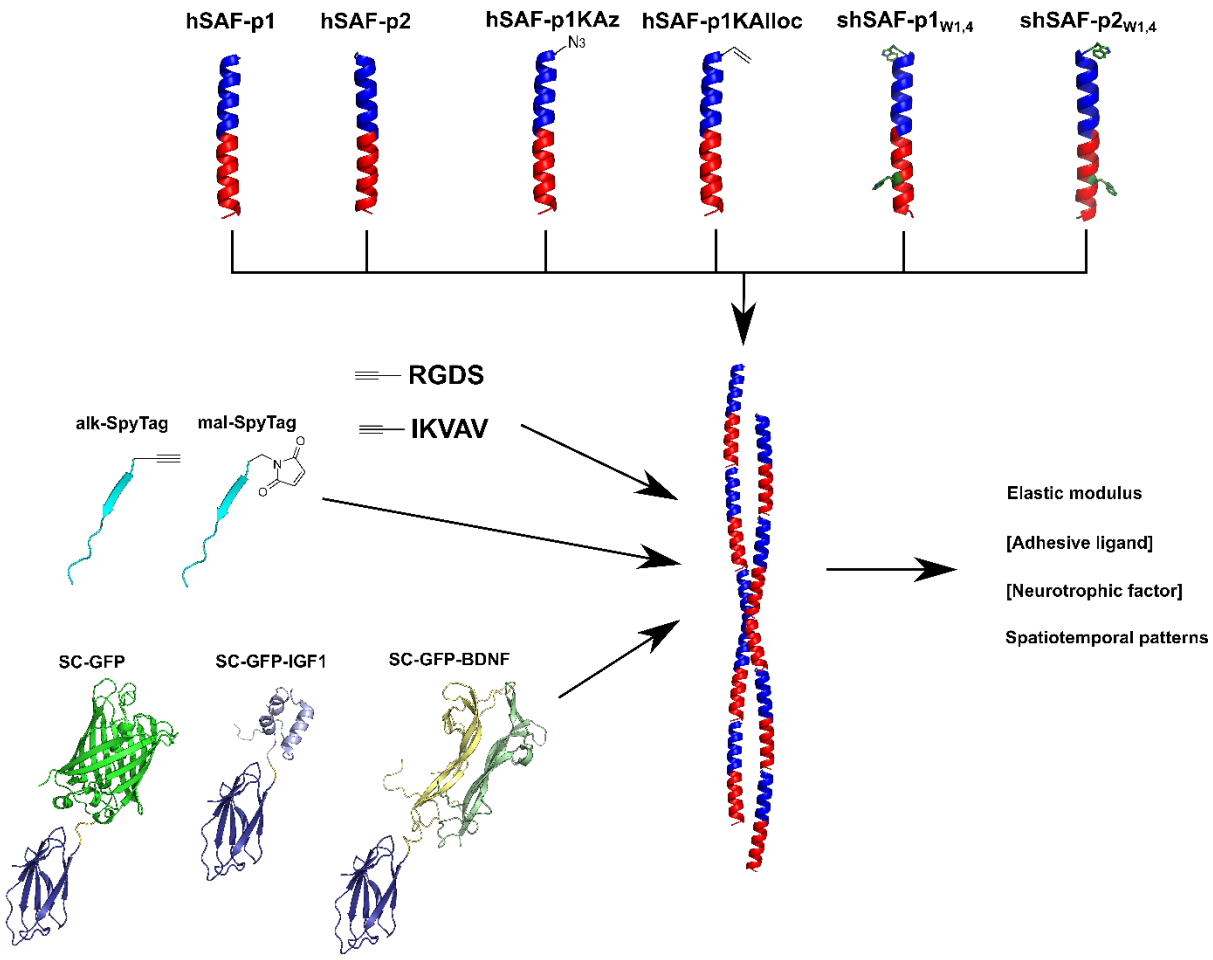

Figure 7.1: Schematic diagram showing the modular nature of hSAFs.

I envisage that these different modules could be interchanged to allow bespoke scaffolds to be formed for specific applications. Thus, hSAFs might form a customisable tool for cell culture, where components of the gel could be introduced in a plug-and-play type manner. However, before this could be achieved, each of the modules would need to be tested alongside one another to ensure they are compatible. For instance, hSAF-p1KAlloc can be used to photopattern hSAFs, while shSAF-p1$_{W1,4}$ and p2$_{W1,4}$ can be used to form stiffer gels. However, I have not yet shown that a variant of shSAF-p1$_{W1,4}$, shSAF-p1KAlloc$_{W1,4,}$ can be used to form photopatternable gels with increased elastic modulus. Demonstrating that each of the components can function orthogonally would be a logical next step. This might also involve the development of an orthogonal method for protein attachment, such as utilising the biotin-streptavidin binding system.

Despite the development of novel techniques for extensively modifying hSAFs, it must be noted that the cell biology presented here is at the proof-of-concept stage. Cell viability and neurite outgrowth are

relatively general cell health parameters. These were chosen as the focus of this work remained on developing the scaffold, however, a more in-depth study of cell behaviour would be desirable, assessing electrophysiological and molecular responses to the various hSAF modifications. The current study has provided the component building blocks (Figure 7.1), and developed the methods for directing neuronal behaviour, which a future study might be able to exploit more fully. However, the limited cell culture studies described here highlight practical difficulties with the hSAF system. The synthesis and purification of the different 28-residue peptide components requires time, reagents and expertise, all of which increase the experimental lead time. In comparison, synthesis of di-phenylalanine requires a single coupling step and minimal purification, and many synthetic polymer components are available commercially. This possibly limits the wide-spread adoption of hSAFs as a novel cytoscaffold for cell culture.

Other more explorative routes of investigation might be the application of hSAFs *in vivo*. This thesis has purposefully focused on using hSAFs for cell culture, rather than tissue engineering, as hSAFs have not yet been shown to be compatible *in vivo*. However, one might envisage that a growth factor-decorated gel, loaded with NSCs or neurons, might be used to promote neuronal regrowth *in vivo* after damage or disease (109, 222, 228, 427). Initially, immunogenicity studies would be required in order to assess whether hSAFs can be applied *in vivo*.

Finally, other discrete assemblies designed by the Woolfson group (such as trimeric, tetrameric, pentameric, hexameric and heptameric coiled coils (3, 5)) might be modified to self-assemble into biomaterials for cell culture. Burgess et al. have already demonstrated that these peptides can be modified to form nanotubes (36). It is possible that residues away from the cores of these assemblies might be modified to promote entangling of nanotubes into larger scaffolds. These scaffolds might have different properties compared with hSAFs and would increase the tool kit of peptides available for forming novel cytoscaffolds.

Utilising *de novo* designed coiled-coil peptides as a sensor for small-molecule detection

Chapter 6 outlines the development of a differential sensor for lipophilic small-molecule detection. By using an array of 15 *de novo* designed α-helical barrel peptides (αHBs) preloaded with diphenylhexatriene (DPH), molecule-specific fingerprints can be generated for 13 different fatty acids. By using machine learning methods, longer-chain, but not shorter-chain fatty acids can be correctly categorised using their fingerprints. To the best of my knowledge, this is the first example of using *de novo* designed peptides for sensing in this way.

The shorter-chain fatty acids might be correctly categorised by increasing the concentration of analyte or number of replicates used to train the SVM model. These are logical initial next steps to take. However, certain other classes of small-molecule that are less lipophilic (*e.g.* amino acids, nucleobases and sugars) are less likely to displace DPH from the αHBs and, therefore, be correctly categorised by the array. Additional αHB peptides might be included in the array, with polar residues lining the pore. These αHBs might allow the binding and, therefore, detection of polar analytes.

Ultimately though, the strength of this type of sensing lies with complex mixture detection, where the exact molecules – or combination of molecules – that one seeks to detect are not known (367). The Woolfson group is currently investigating whether the array can be used to differentiate between different complex mixtures, such as subtypes of tea, and urine samples from healthy volunteers (all unpublished work). Depending on the outcome of these proof-of-concept experiments, the array of αHBs developed here could be applied to disease diagnostics using patient whole blood, serum, urine, breath or sweat samples. Other differential sensors have been used to attempt to diagnose Alzheimer's disease (428) and cancer (376) based on subtle changes in the makeup of blood and breath samples, respectively. It is possible that our array of αHBs might be used to similarly differentiate between healthy patients and disease sufferers. In its current embodiment, the success of this would likely rely on detectable alterations in the patient lipidome or in other lipophilic compounds.

In addition, I have demonstrated that αHBs can be immobilised within an agarose hydrogel in a way that maintains their DPH-binding capacity. A logical next step would be to identify whether analyte

binding can proceed in a similar way to in solution. Following this, the solution-phase assays outlined in Chapter 6.3 would be repeated using peptides suspended in agarose. I envisage that this method of peptide immobilisation might form the basis for miniaturisation and device manufacture in the future. Attempts to immobilise the peptides by more traditional methods, *i.e.* on a glass surface, were largely unsuccessful. It remains unclear whether the peptides remain in their native conformation when immobilised. More detailed analyses to determine the secondary structure, oligomeric state and DPH binding capacity of the immobilised peptides are required before any firm conclusions can be drawn.

Concluding remarks

Both the development of hSAFs as a tuneable scaffold for neurons, and utilisation of αHBs as a differential sensor for small-molecule detection, demonstrate the application of *de novo* designed coiled-coil peptides as customisable tools for real-world applications. Both systems are modular and tuneable and, thus, demonstrate key assets of designed peptides. Therefore, this work contributes to the idea that *de novo* designed peptides are no longer simply exemplars of our firm understanding of protein folding, but tools that can be applied in diverse areas away from the field of protein design.

Chapter 8

Appendix

8.1: Peptide sequences

hSAF-p1	H-KIAALKA KIAALKA EIAALEW ENAALEA-OH
hSAF-p2	H-KIAALKA KNAALKA EIAALEW EIAALEA-OH
hSAF-p1KAz	H-KazIAALKA KIAALKA EIAALEW ENAALEA-OH
hSAF-p1KAlloc	H-KalIAALKA KIAALKA EIAALEW ENAALEA-OH
hSAF-p1Cys	H-CIAALKA KIAALKA EIAALEW ENAALEA-OH
shSAF-p1$_{W1,4}$	H-WKIAALK AKIAALK AEIAALE WENAALE-OH
shSAF-p2$_{W1,4}$	H-WKIAALK AKNAALK AEIAALE WEIAALE-OH
alk-RGDS	H-pGSGYG RGDS-NH_2
mal-RGDS	mal-GSGYG RGDS-NH_2
Cys-RGDS	H-CGSGYG RGDS-NH_2
norb-RGDS	norb-GSGYG RGDS-NH_2
alk-IKVAV	H-pGSGYG IKVAV-NH_2
alk-SpyTag	H-pGSGSG AHIVMVDAYKPTK-NH_2
Cys-SpyTag	H-CGSGSG AHIVMVDAYKPTK-NH_2
mal-SpyTag	mal-GSGSG AHIVMVDAYKPTK-NH_2
TAMRA-CC-Hept	TAMRA-GSGSGGEIAQALKEIAKALKEIAWALKEIAQALKG-NH_2

CC-Tri	Ac-GEIAAIKQEIAAIKKEIAAIKWEIEEIKQGYG-NH_2
CC-Hept-I17C	Ac-GEIAQALKEIAKALKECAWALKEIAQALKG-NH_2
AFKEIA	Ac-GEIAQAFKEIAKAFKEIAWAFKEIAQAFKG-NH_2
AIKEIA	Ac-GEIAQAIKEIAKAIKEIAWAIKEIAQAIKG-NH_2
AIKEVA	Ac-GEVAQAIKEVAKAIKEVAWAIKEVAQAIKG-NH_2
AVKEVA	Ac-GEVAQAVKEVAKAVKEVAWAVKEVAQAVKG-NH_2
AVKEIA	Ac-GEIAQAVKEIAKAVKEIAWAVKEIAQAVKG-NH_2
AMKEIA	Ac-GEIAQAMKEIAKAMKEIAWAMKEIAQAMKG-NH_2
CC-Pent	Ac-GQIEQILKQIEKILKQIEWILKQIEQILKG-NH_2
CC-Hex	Ac-GELKAIAQELKAIAKELKAIAWELKAIAQG-NH_2
CC-Hex2	Ac-GEIAKSLKEIAKSLKEIAWSLKEIAKSLKG-NH_2
CC-Hept	Ac-GEIAQALKEIAKALKEIAWALKEIAQALKG-NH_2
CC-Hept-I24D	Ac-GEIAKALREIAKALREIAWALREDAKALRG-NH_2
CC-Hept-I24E	Ac-GEIAKALREIAKALREIAWALREEAKALRG-NH_2
CC-Hept-I24K	Ac-GEIAQALREIAKALREIAWALREKAQALRG-NH_2
CC-Hept-I17K	Ac-GEIAKALREIAKALREKAWALREIAKALRG-NH_2

Table 8.1.1: Sequences for all peptides described in this thesis. Blue denotes an unnatural amino acid residue or functional group not native to proteins.

8.2 Peptide HPLC and MALDI-TOF-MS data

All peptides used in the α-helical barrel array described in Chapter 6 were synthesised and purified by other members of the Woolfson group, as described in the main text.

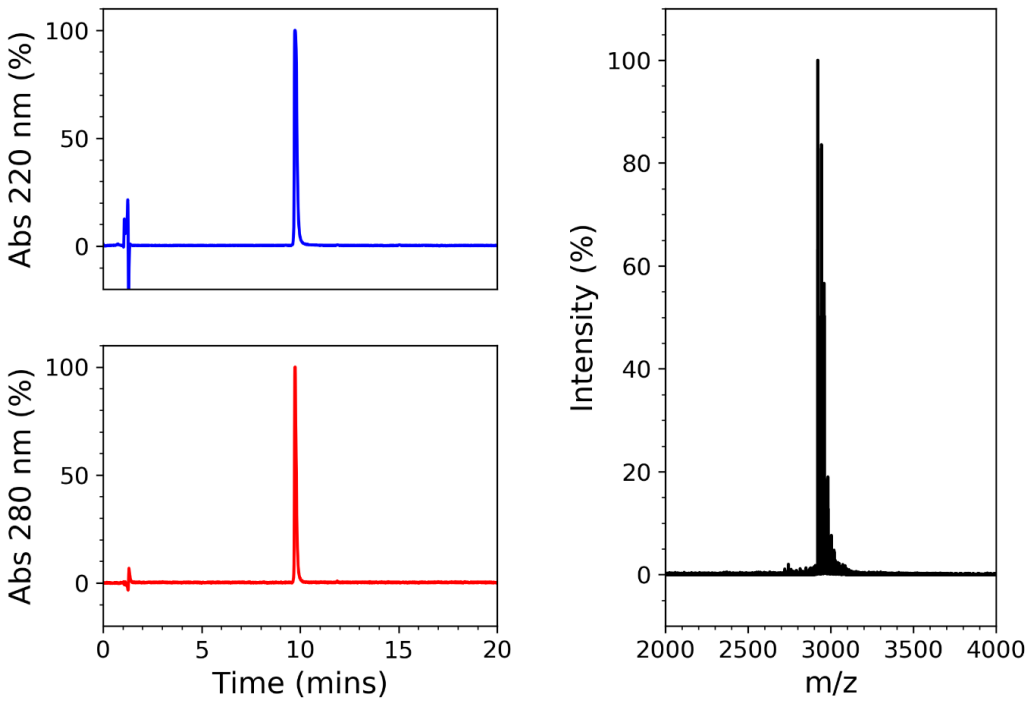

Figure 8.2.1: HPLC chromatograms (left panels) and MALDI-TOF-MS spectra (right panel) for hSAF-p1. Expected mass: 2922.0 Da. Recorded mass:2921.9 Da.

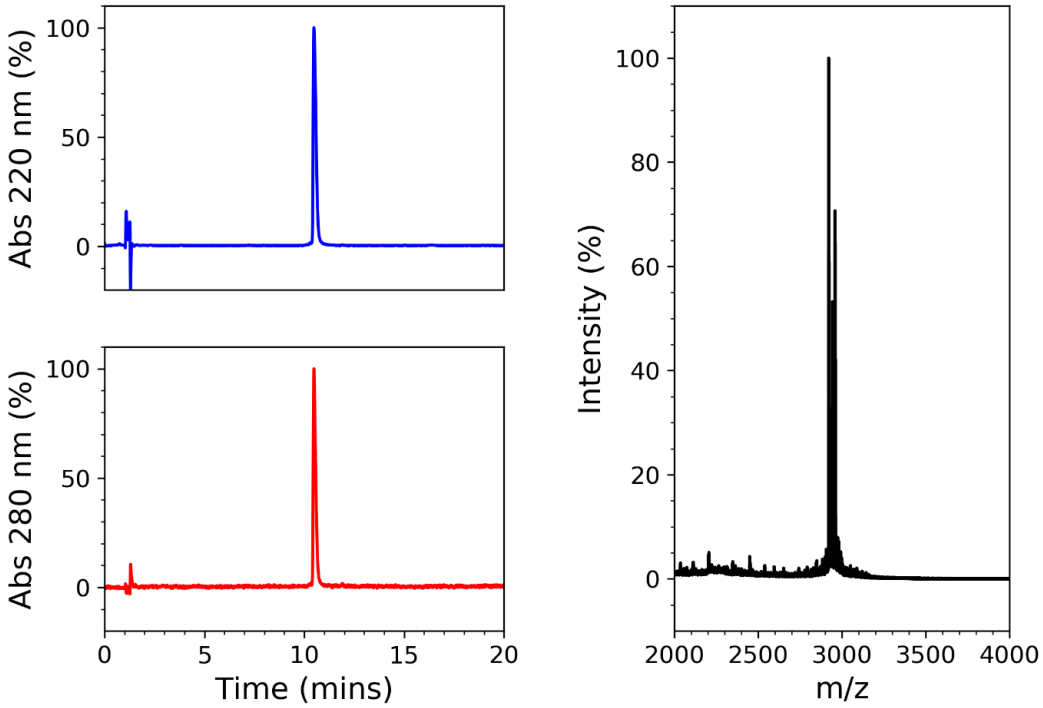

Figure 8.2.2: HPLC chromatograms (left panels) and MALDI-TOF-MS spectra (right panel) for hSAF-p2. Expected mass: 2922.0 Da. Recorded mass: 2921.0 Da.

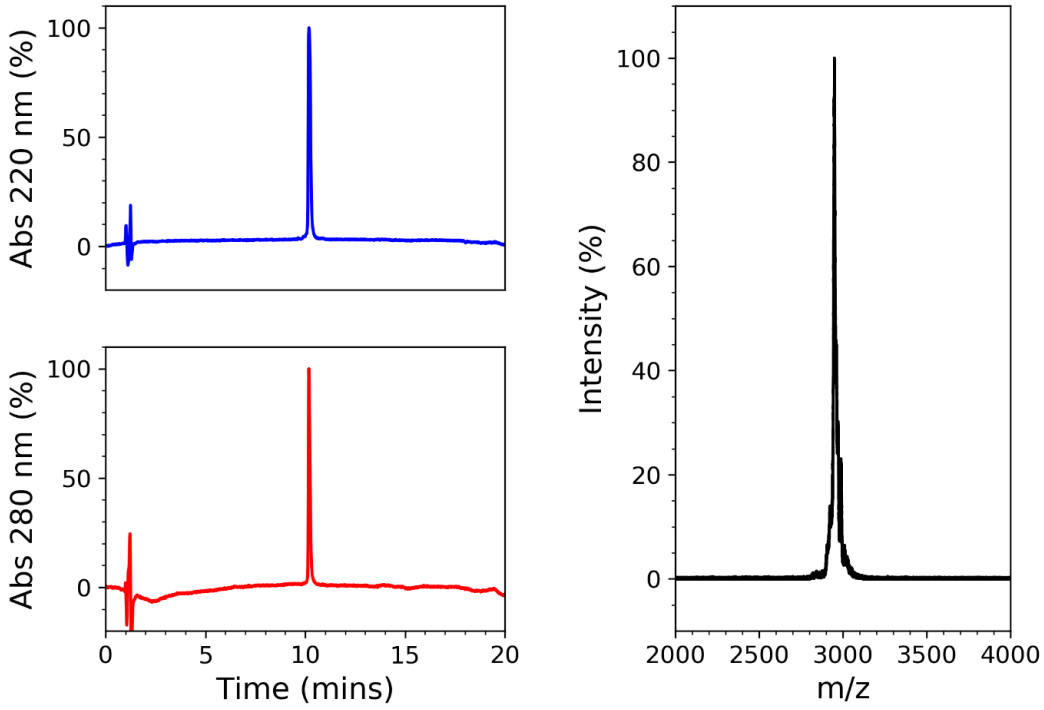

Figure 8.2.3: HPLC chromatograms (left panels) and MALDI-TOF-MS spectra (right panel) for hSAF-p1KAz. Expected mass: 2947.9 Da. Recorded mass: 2949.1 Da.

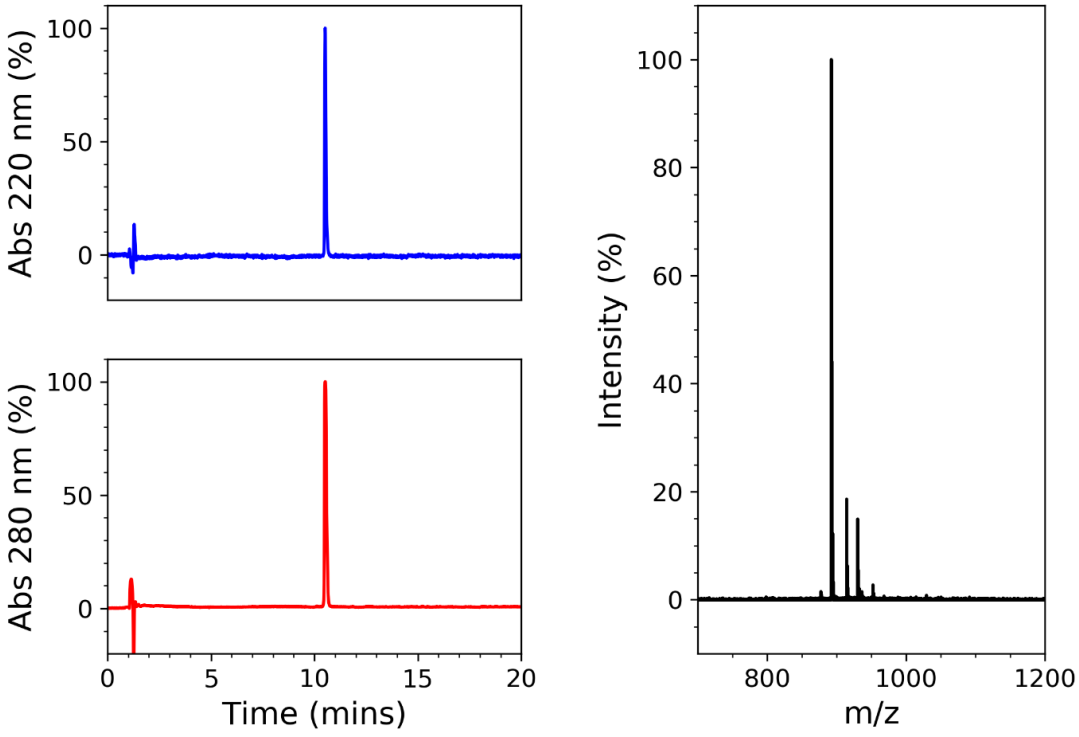

Figure 8.2.4: HPLC chromatograms (left panels) and MALDI-TOF-MS spectra (right panel) for alk-RGDS. Expected mass: 893.05 Da. Recorded mass: 892.4 Da.

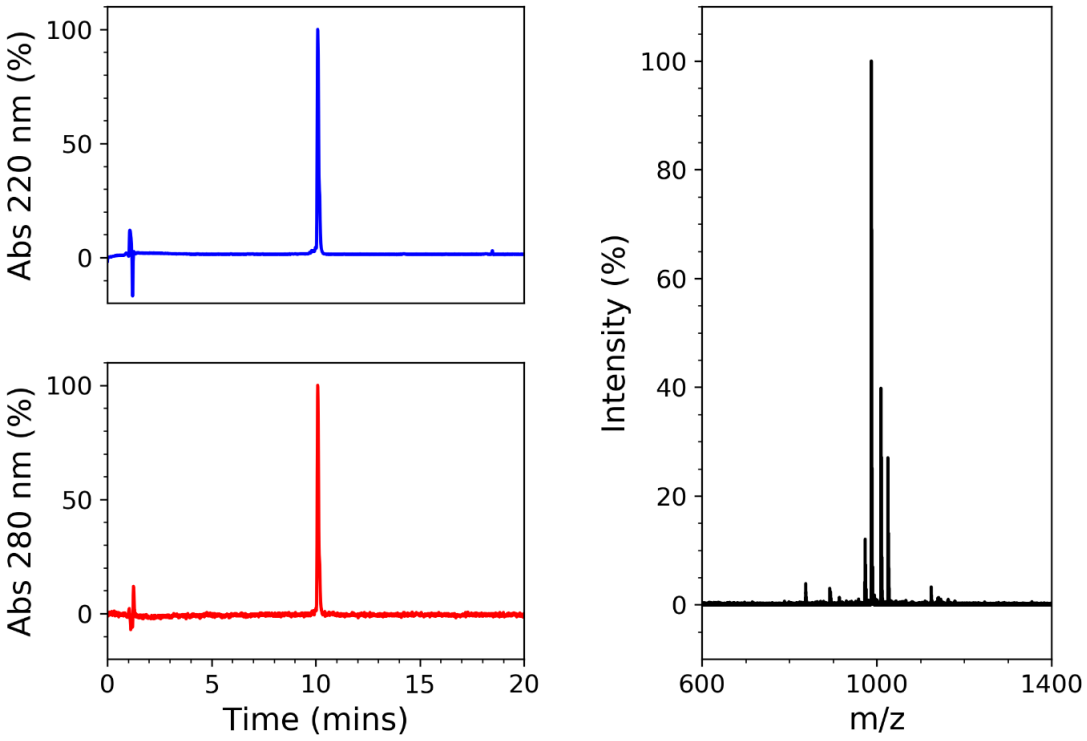

Figure 8.2.5: HPLC chromatograms (left panels) and MALDI-TOF-MS spectra (right panel) for alk-IKVAV. Expected mass: 988.25 Da. Recorded mass: 987.6 Da.

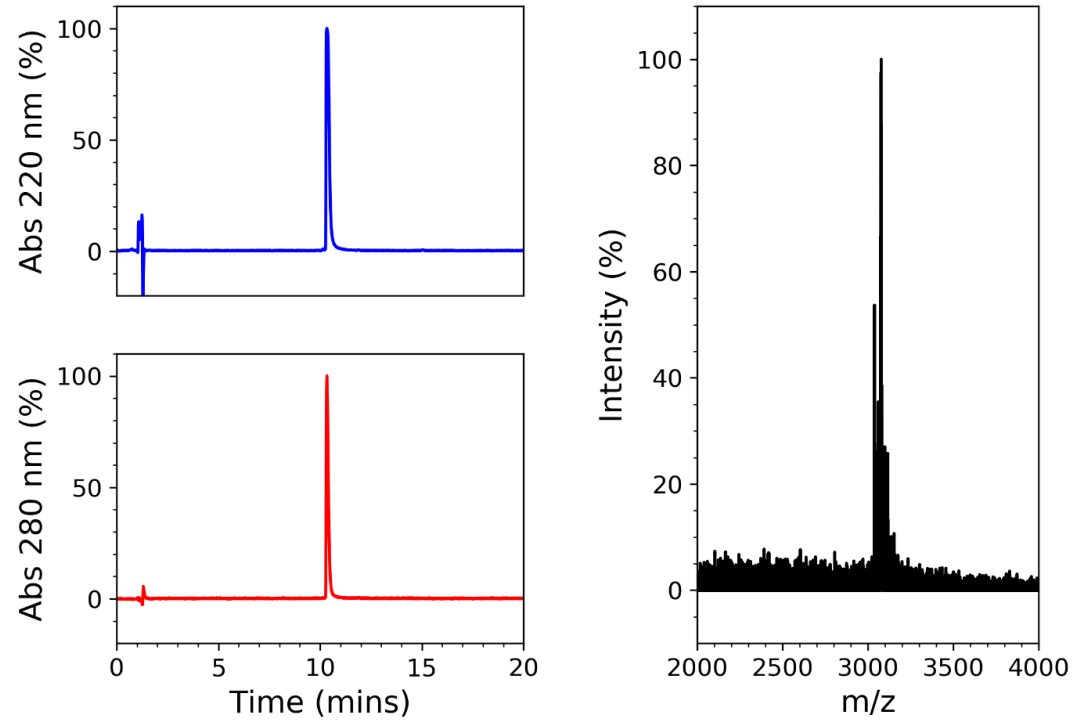

Figure 8.2.6: HPLC chromatograms (left panels) and MALDI-TOF-MS spectra (right panel) for shSAF$_{W1,4}$-p1. Expected mass: 3037.1 Da. Recorded mass: 3037.4 Da.

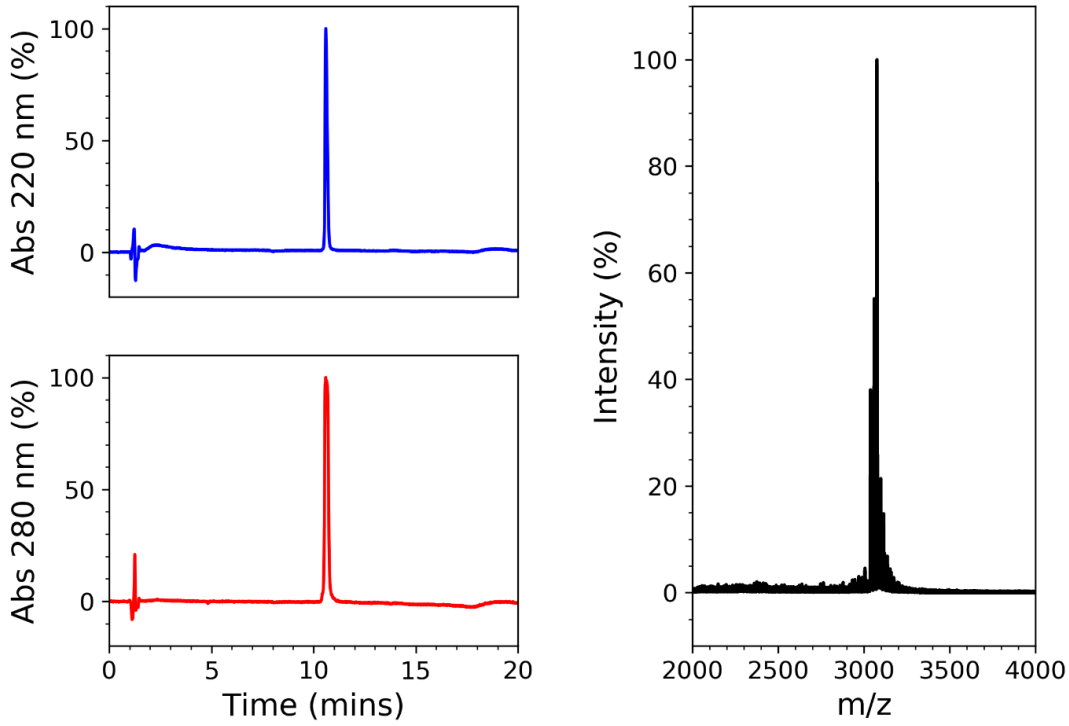

Figure 8.2.7: HPLC chromatograms (left panels) and MALDI-TOF-MS spectra (right panel) for shSAF$_{W1,4}$-p2. Expected mass: 3037.1 Da. Recorded mass: 3036.9 Da.

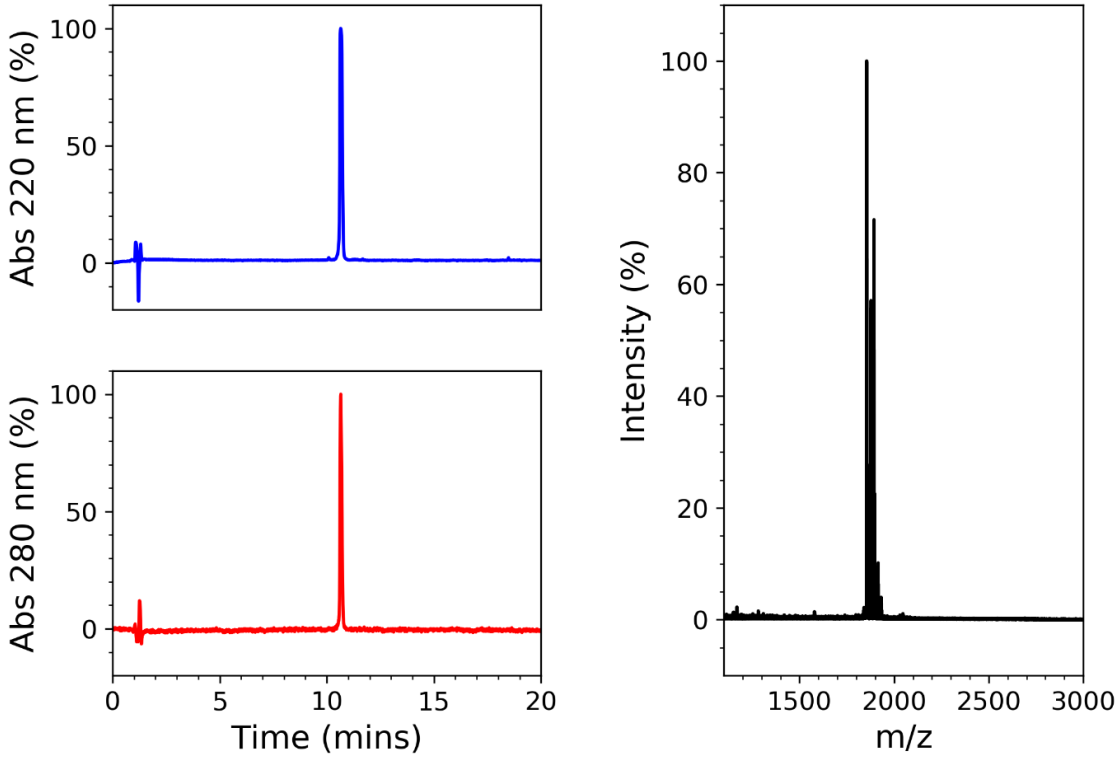

Figure 8.2.8: HPLC chromatograms (left panels) and MALDI-TOF-MS spectra (right panel) for alk-SpyTag. Expected mass: 1856.3 Da. Recorded mass: 1854.9 Da.

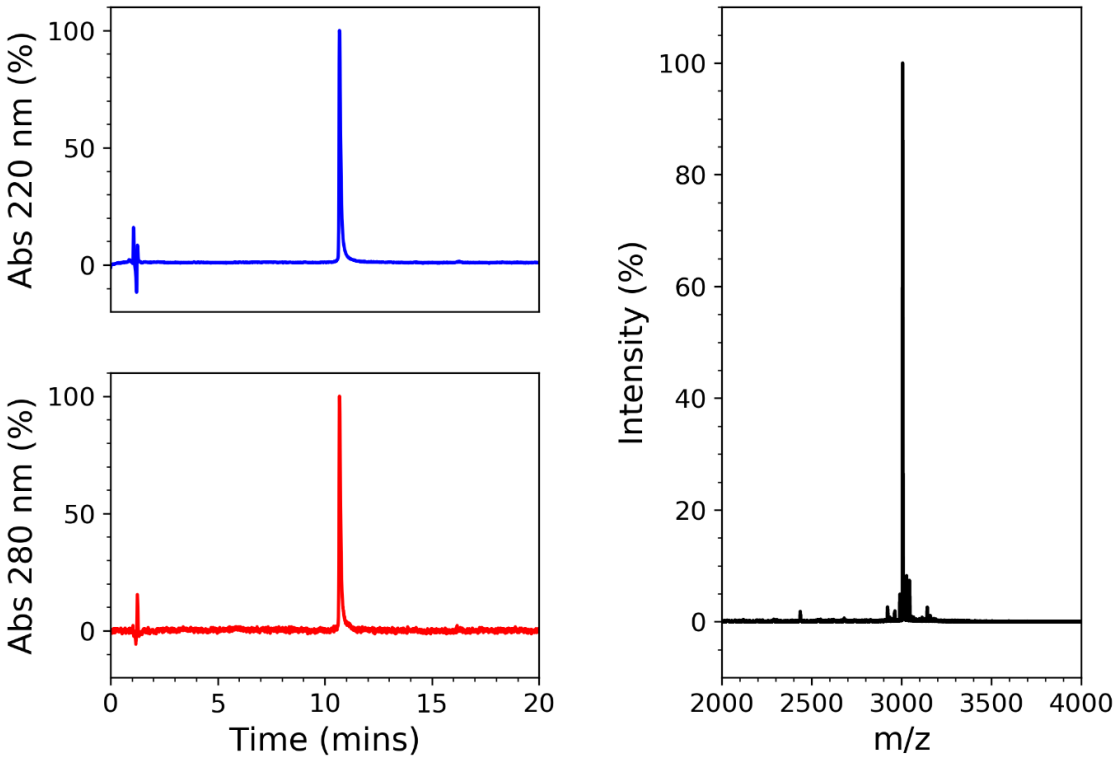

Figure 8.2.9: HPLC chromatograms (left panels) and MALDI-TOF-MS spectra (right panel) for hSAF-p1KAlloc. Recorded mass: 3005.9 Da. Expected mass: Recorded mass: 3006.1 Da.

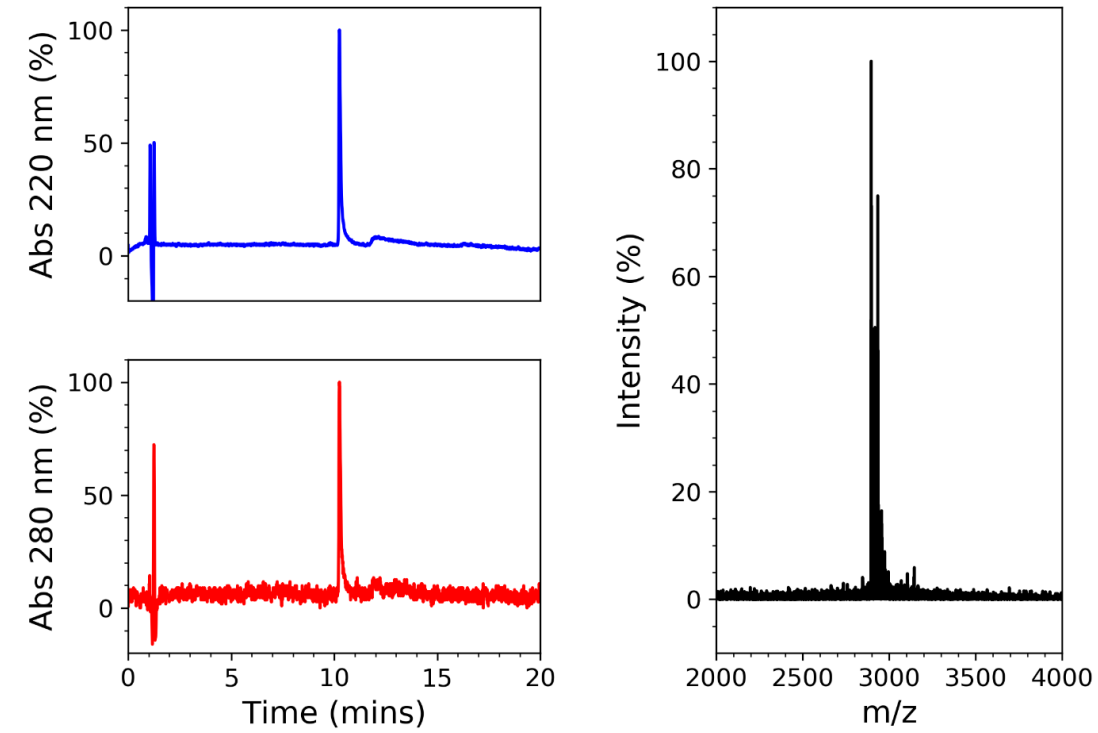

Figure 8.2.10: HPLC chromatograms (left panels) and MALDI-TOF-MS spectra (right panel) for hSAF-p1Cys. Recorded mass: 2897.0 Da. Recorded mass: 2896.3 Da.

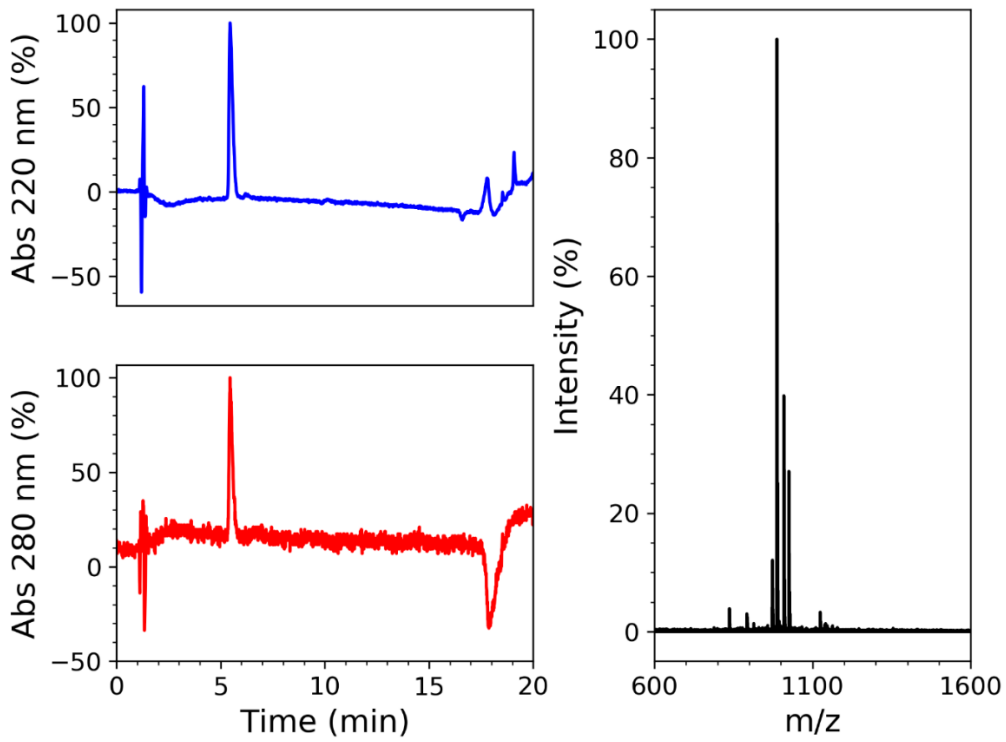

Figure 8.2.11: HPLC chromatograms (left panels) and MALDI-TOF-MS spectra (right panel) for Cys-RGDS. Expected mass: 958.3 Da. Recorded mass: 958.5 Da.

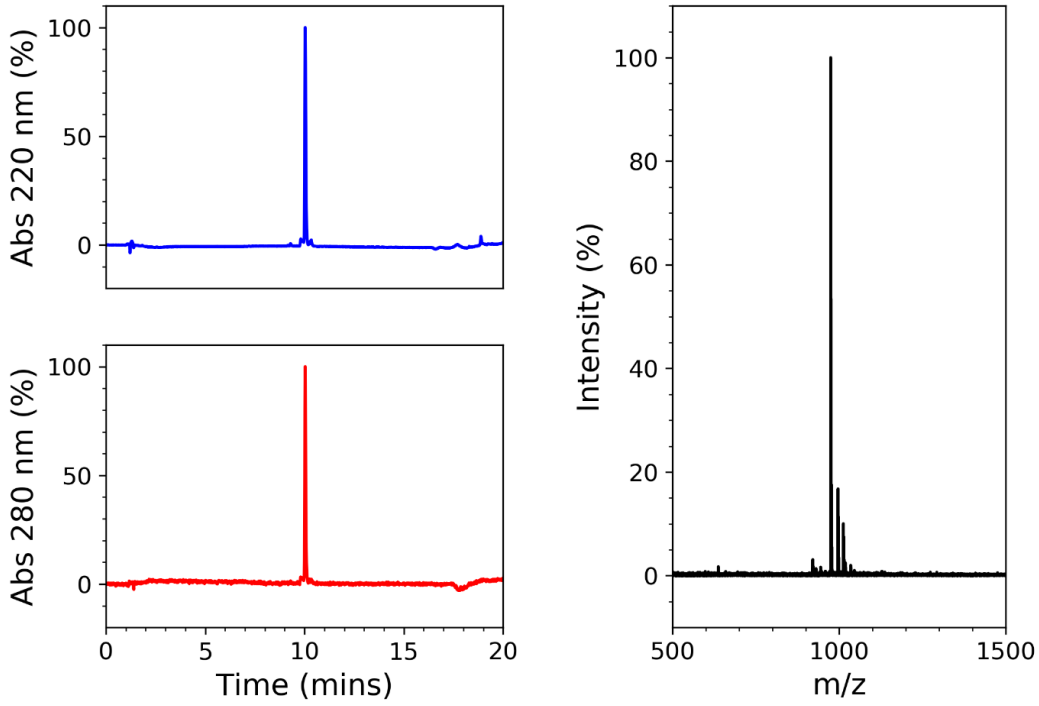

Figure 8.2.12: HPLC chromatograms (left panels) and MALDI-TOF-MS spectra (right panel) for norb-RGDS. Expected mass: 975.6 Da. Recorded mass: 976.6 Da.

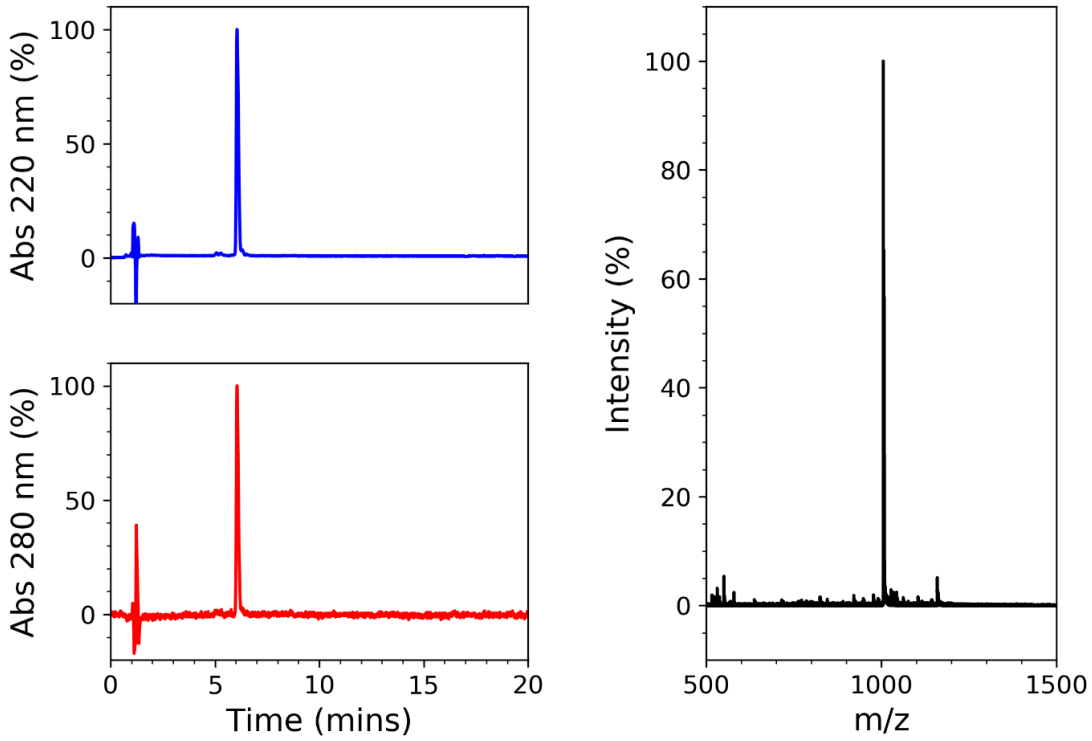

Figure 8.2.13: HPLC chromatograms (left panels) and MALDI-TOF-MS spectra (right panel) for mal-RGDS. Expected mass: 1006.1 Da. Recorded mass: 1005.6 Da

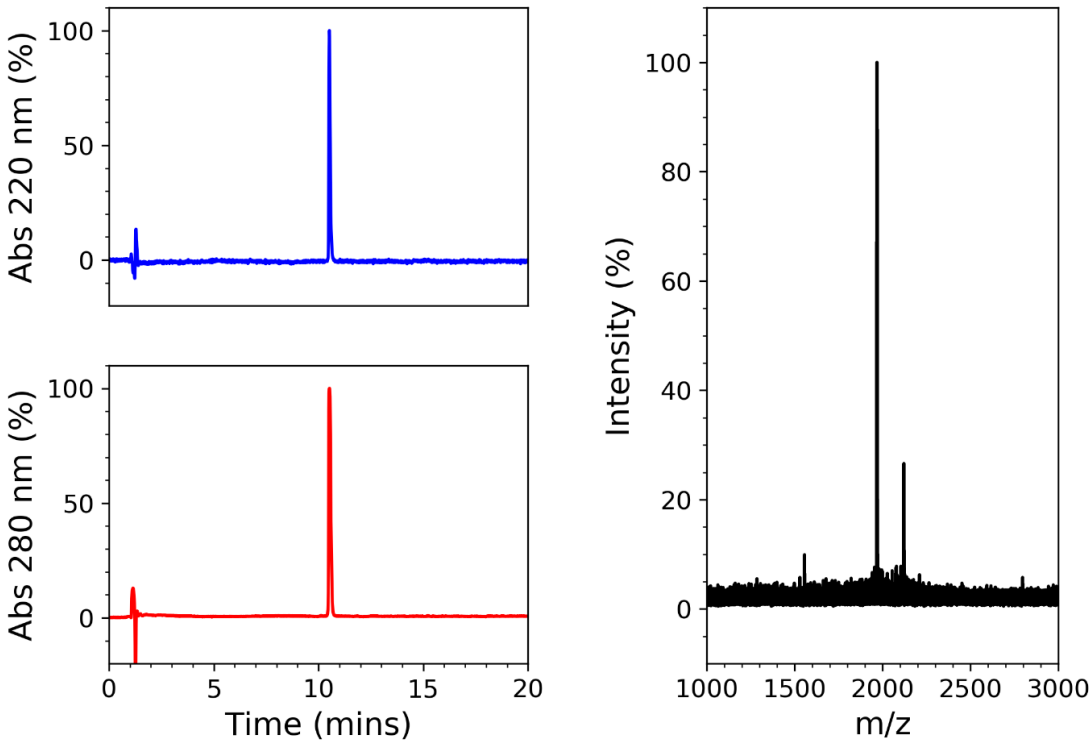

Figure 8.2.14: HPLC chromatograms (left panels) and MALDI-TOF-MS spectra (right panel) for mal-SpyTag. Expected mass: 1969.4 Da. Recorded mass: 1968.3 Da.

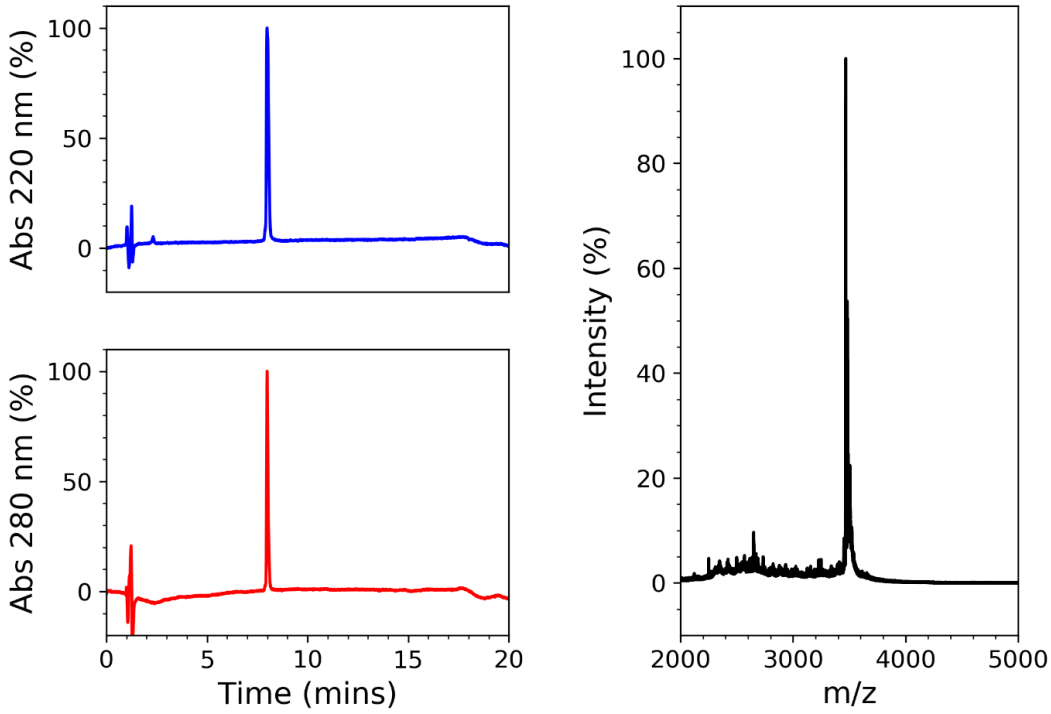

Figure 8.2.15: HPLC chromatograms (left panels) and MALDI-TOF-MS spectra (right panel) for CC-Tri. Expected mass: 3465.9 Da. Recorded mass: 3468.3 Da.

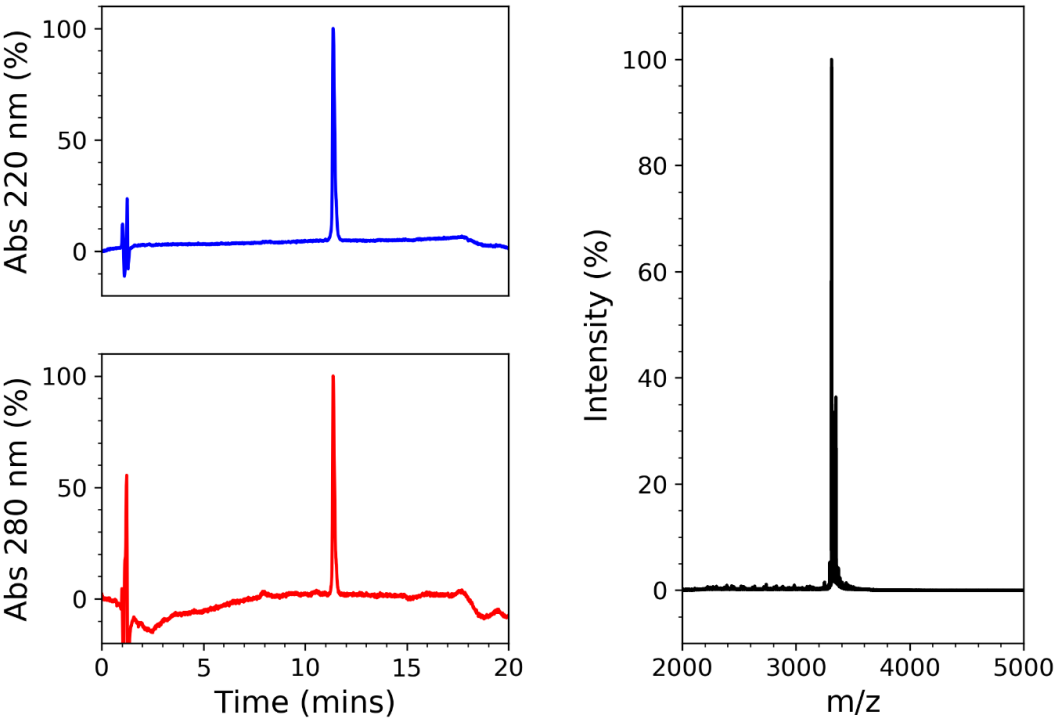

Figure 8.2.16: HPLC chromatograms (left panels) and MALDI-TOF-MS spectra (right panel) for CC-Hex2. Expected mass: 3314.6 Da. Recorded mass: 3312.1 Da.

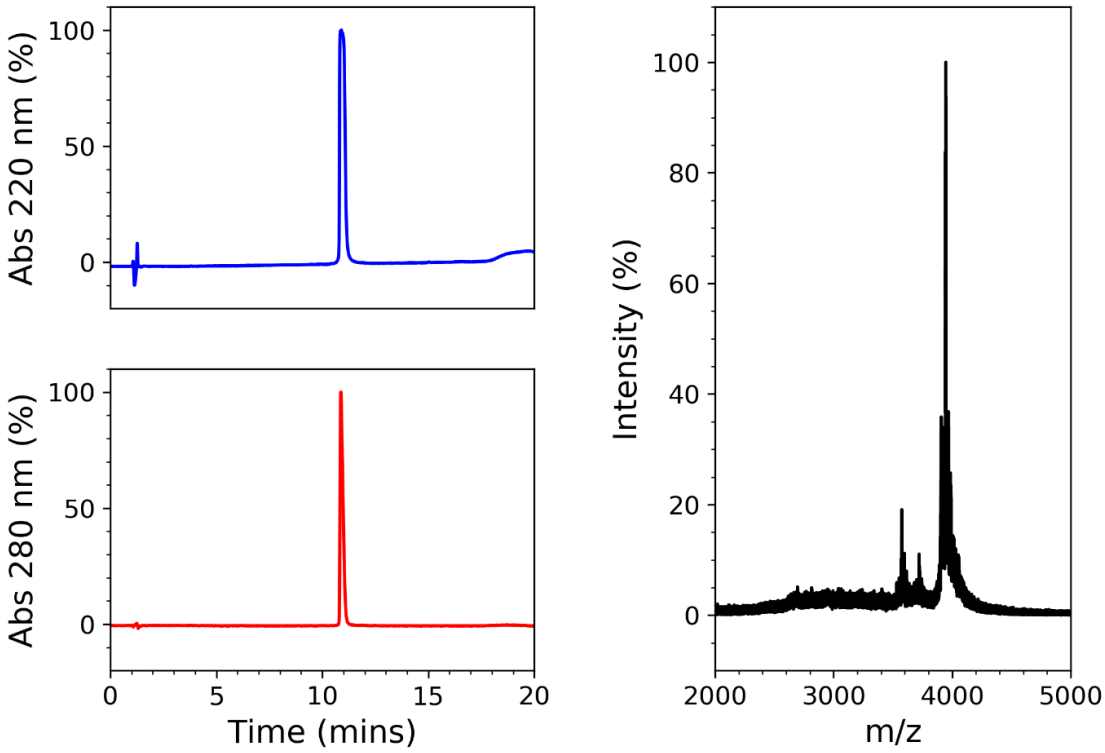

Figure 2.17: HPLC chromatograms (left panels) and MALDI-TOF-MS spectra (right panel) for CC-Hept-TAMRA. Expected mass: 3965.3 Da. Recorded mass: 3965.4 Da.

8.3 Protein sequences and plasmid maps

SpyCatcher	Dark blue
GFP	Green
Flexible linker	Yellow
His-Tag	Red
Periplasm-targeting sequence	Purple
IGF1	Light blue

MSYYHHHHHHDYDIPTTENLYFQGAMVDTLSGLSSEQGQSGDMTIEEDSATHIKFSKRDEDG
KELAGATMELRDSSGKTISTWISDGQVKDFYLYPGKYTFVETAAPDGYEVATAITFTVNEQG
QVTVNGKATKGDAHIGTGSGSGSGSGSGSTMSKGEELFTGVVPILVELDGDVNGHKFSVSGE
GEGDATYGKLTLKFISTTGKLPVPWPTLVTTLTYGVQMFARYPDHMKQHDFFKSAMPEGYVQ
ERTIFFKDDGNYKTRAEVKFEGDTLVNRIELKGIDFKEDGNILGHKLEYNYNSHNVYITADK
QKNGIKANFKIRHNIEDGGVQLADHYQQNTPIGDGPVLLPDNHYLSTQSKLSKDPNEKRDHM
VLLEFVTAAGITHGMDELYKAS*

Figure 8.3.1: Sequence of SpyCatcher-GFP (*N*-terminal His tag)

MVDTLSGLSSEQGQSGDMTIEEDSATHIKFSKRDEDGKELAGATMELRDSSGKTISTWISDG
QVKDFYLYPGKYTFVETAAPDGYEVATAITFTVNEQGQVTVNGKATKGDAHIGTGSGSGSGS
GSGSTMSKGEELFTGVVPILVELDGDVNGHKFSVSGEGEGDATYGKLTLKFISTTGKLPVPW
PTLVTTLTYGVQMFARYPDHMKQHDFFKSAMPEGYVQERTIFFKDDGNYKTRAEVKFEGDTL
VNRIELKGIDFKEDGNILGHKLEYNYNSHNVYITADKQKNGIKANFKIRHNIEDGGVQLADH
YQQNTPIGDGPVLLPDNHYLSTQSKLSKDPNEKRDHMVLLEFVTAAGITHGMDELYKASHHH
HHH*

Figure 8.3.2: Sequence of SpyCatcher-GFP (*C*-terminal His-Tag)

MKIKTGARILALSALTTMMFSASALAMSYYHHHHHHDYDIPTTENLYFQGAMVDTLSGLSSE
QGQSGDMTIEEDSATHIKFSKRDEDGKELAGATMELRDSSGKTISTWISDGQVKDFYLYPGK
YTFVETAAPDGYEVATAITFTVNEQGQVTVNGKATKGDAHIGTGSGSGSGSGSGSTMSKGEE
LFTGVVPILVELDGDVNGHKFSVSGEGEGDATYGKLTLKFISTTGKLPVPWPTLVTTLTYGV
QMFARYPDHMKQHDFFKSAMPEGYVQERTIFFKDDGNYKTRAEVKFEGDTLVNRIELKGIDF
KEDGNILGHKLEYNYNSHNVYITADKQKNGIKANFKIRHNIEDGGVQLADHYQQNTPIGDGP
VLLPDNHYLSTQSKLSKDPNEKRDHMVLLEFVTAAGITHGMDELYKASGSGSGSGSGSGSMG
PETLCGAELVDALQFVCGDRGFYFNKPTGYGSSSRRAPQTGIVDECCFRSCDLRRLEMYCAP
LKPAKSA*

Figure 8.3.3: Sequence of periplasm targeted SpyCatcher-GFP-insulin-like growth factor 1 (p-SC-GFP-IGF1)

MGSSHHHHHHSSGLVPRGSHMASMTGGQQMGRGSMVDTLSGLSSEQGQSGDMTIEEDSATHI
KFSKRDEDGKELAGATMELRDSSGKTISTWISDGQVKDFYLYPGKYTFVETAAPDGYEVATA
ITFTVNEQGQVTVNGKATKGDAHIGTGSGSGSGSGSGSTMSKGEELFTGVVPILVELDGDVN
GHKFSVSGEGEGDATYGKLTLKFISTTGKLPVPWPTLVTTLTYGVQMFARYPDHMKQHDFFK
SAMPEGYVQERTIFFKDDGNYKTRAEVKFEGDTLVNRIELKGIDFKEDGNILGHKLEYNYNS
HNVYITADKQKNGIKANFKIRHNIEDGGVQLADHYQQNTPIGDGPVLLPDNHYLSTQSKLSK
DPNEKRDHMVLLEFVTAAGITHGMDELYKASGSGSGSGSGSGSMGPETLCGAELVDALQFVC
GDRGFYFNKPTGYGSSSRRAPQTGIVDECCFRSCDLRRLEMYCAPLKPAKSA*

Figure 8.3.4: Sequence of SpyCatcher-GFP-insulin-like growth factor 1 (SC-GFP-IGF1)

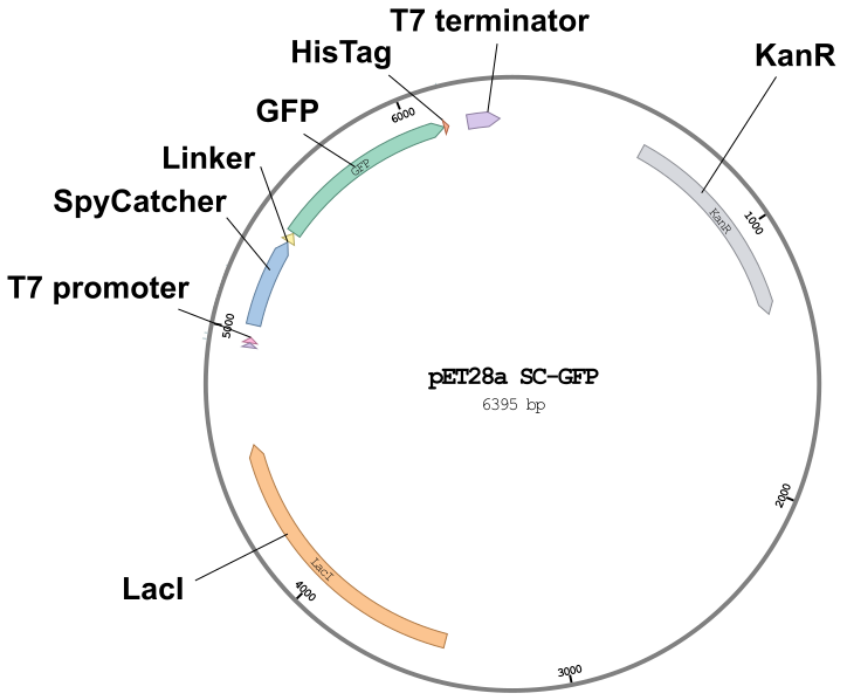

Figure 8.3.5: Map of the pET28a-SC-GFP vector used for expression of SC-GFP. The pET28a-SC-GFP-IGF1 expression vector was identical, but with the coding sequence for IGF1 inserted 3' of GFP and the HisTag gene moved to the 5' end.

8.4: Supplementary data

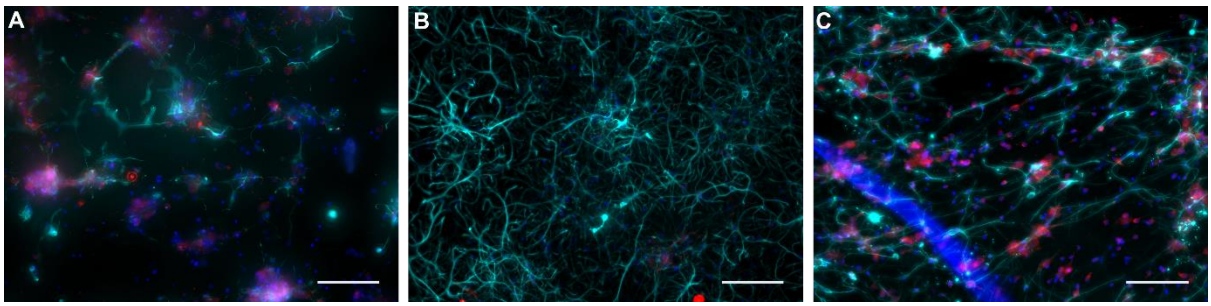

Figure 8.4.1: Widefield fluorescence images showing primary cortical neuronal cultures cultured on hSAFs (A), Puramatrix (B) and Matrigel (C). Cultures were grown in medium containing serum to 14 days *in vitro* to promote glial growth. Cultures were stained for MAP2 (red), GFAP (cyan) and DAPI (blue). Scale bars = 100 μm.

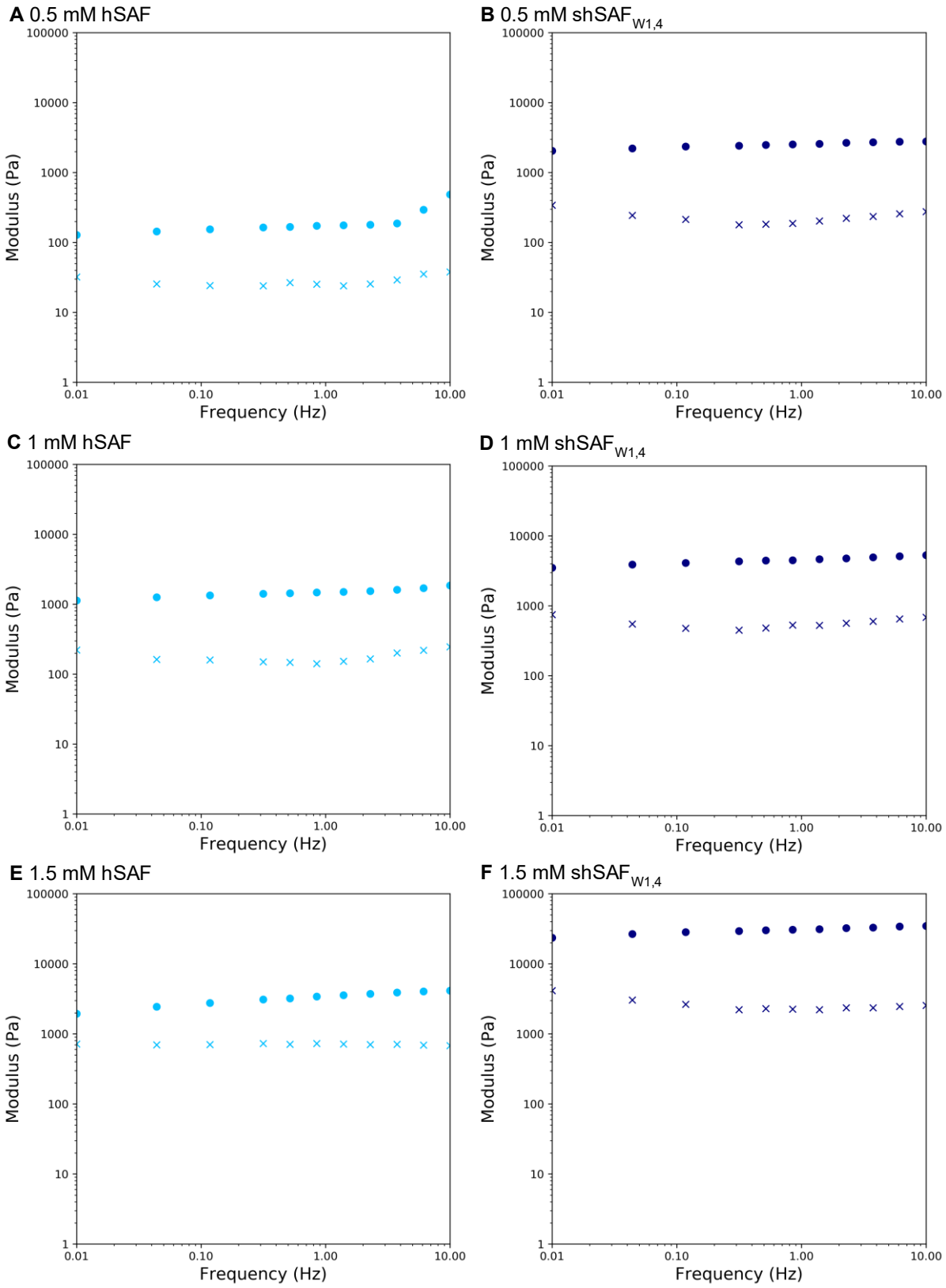

Figure 8.4.2: Bulk rheology data showing G' (circles) and G'' (crosses) for all hSAF and shSAF$_{W1,4}$ gel concentrations. Data were collected at 20 °C using a strain of 0.5%. These data were collected by Alex Wasmuth.

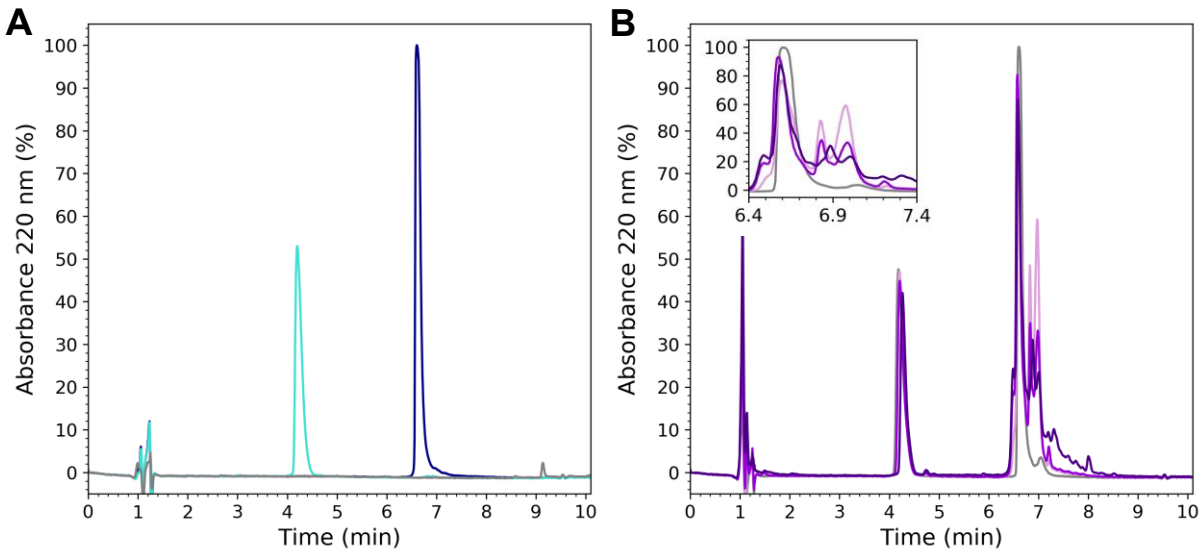

Figure 8.4.3: HPLC chromatograms of thiol-ene click reaction mixtures using Eosin Y as the photoinitiator and visible light. A: HPLC chromatograms of the individual reaction components; hSAF-p1KAz (red), C-SpyTag (green), Eosin Y (orange) and TEAO (pink). B: HPLC chromatograms of the reaction mixtures after 1 hour visible light exposure, varying Eosin Y concentration; 0 (grey), 1 (cyan), 10 (blue) and 100 (black) mg/ml.

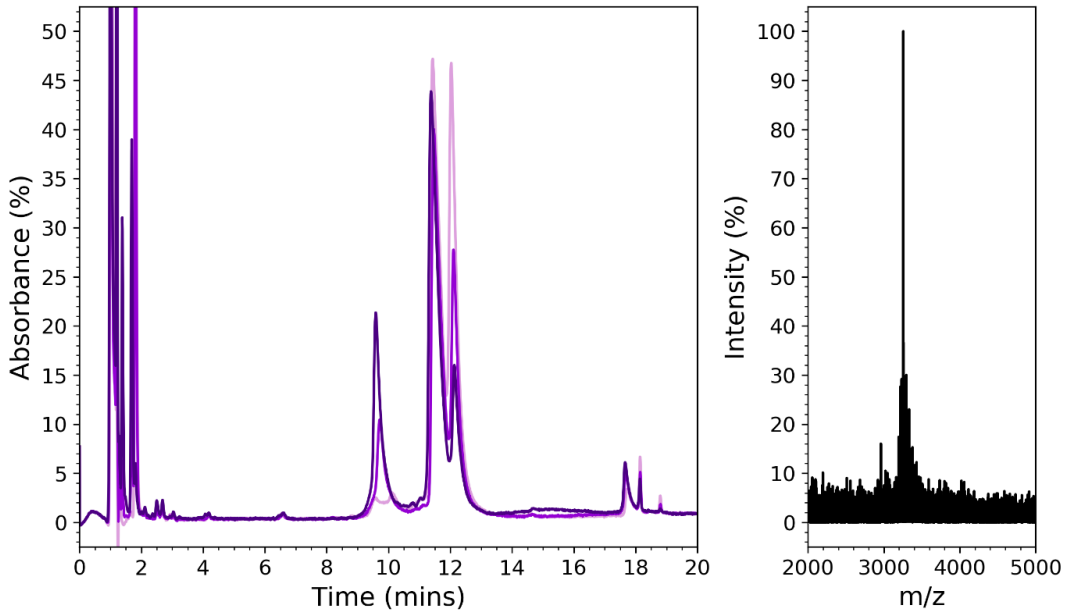

Figure 8.4.4: HPLC chromatograms and MALDI-MS spectra for p1KAlloc:p2 hSAFs reacted with 2 mM L-Cys *via* thiol-ene click chemistry in the presence of 10 equivalents (20 mM) TCEP, using Irgacure 2959 as the photoinitiator. The mass spectrum is of the peak labelled * and corresponds to the mass of hSAF-p1KAlloc + TCEP. Product mass = 3255 Da.

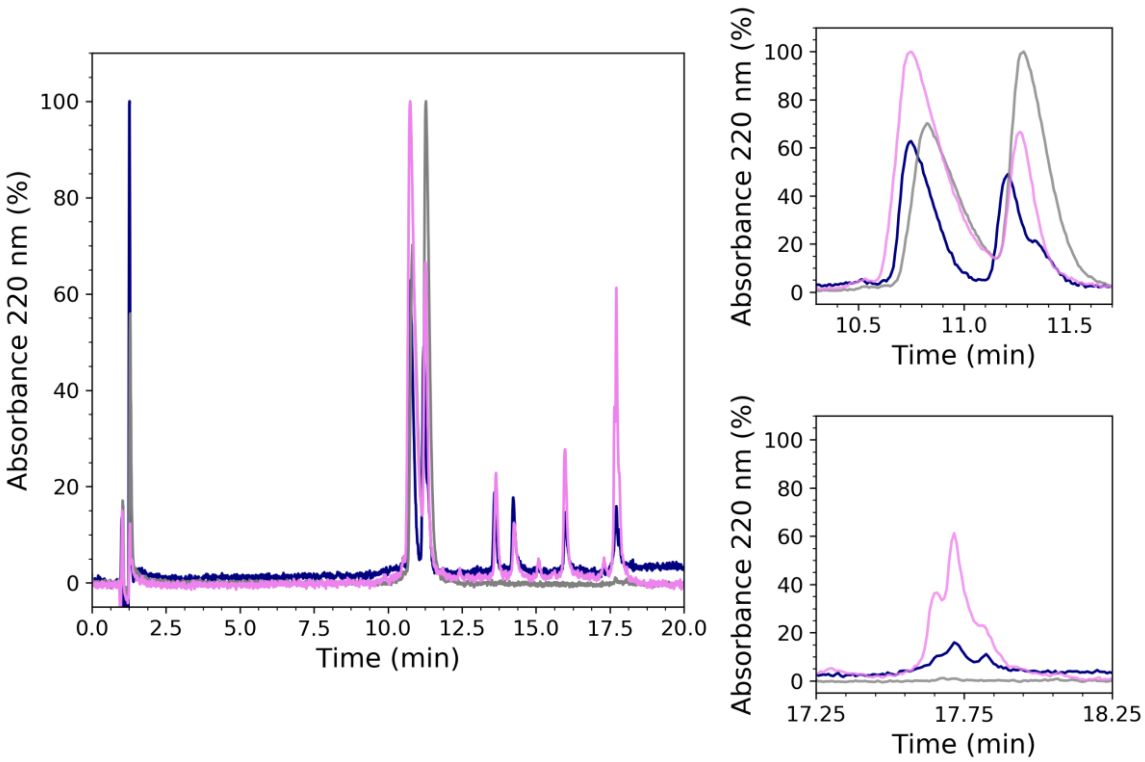

Figure 8.4.5: HPLC chromatograms showing mal-SpyTag reaction with p1KAlloc:p2-PEG_{SH} hSAFs. p1KAlloc:p2 hSAFs (grey); p1KAlloc:p2 hSAFs + PEG_{2SH} +UVB for 3 minutes (pink); p1KAlloc:p2 hSAFs + PEG_{2SH} + UVB for 3 minutes + mal-SpyTag (navy).

References

1. Huang PS, Boyken SE, Baker D. The coming of age of de novo protein design. Nature. 2016;537(7620):320-7.

2. Woolfson DN. The design of coiled-coil structures and assemblies. Advances in Protein Chemistry. 2005;70:79-112.

3. Fletcher JM, Boyle AL, Bruning M, Bartlett GJ, Vincent TL, Zaccai NR, et al. A basis set of de novo coiled-coil peptide oligomers for rational protein design and synthetic biology. ACS Synth Biol. 2012;1(6):240-50.

4. Nautiyal S, Woolfson DN, King DS, Alber T. A designed heterotrimeric coiled coil. Biochemistry. 1995;34(37):11645-51.

5. Thomson AR, Wood CW, Burton AJ, Bartlett GJ, Sessions RB, Brady RL, et al. Computational design of water-soluble alpha-helical barrels. Science. 2014;346(6208):485-8.

6. Huang PS, Oberdorfer G, Xu C, Pei XY, Nannenga BL, Rogers JM, et al. High thermodynamic stability of parametrically designed helical bundles. Science. 2014;346(6208):481-5.

7. O'Neil KT, DeGrado WF. A thermodynamic scale for the helix-forming tendencies of the commonly occurring amino acids. Science. 1990;250(4981):646-51.

8. Gradisar H, Jerala R. De novo design of orthogonal peptide pairs forming parallel coiled-coil heterodimers. J Pept Sci. 2011;17(2):100-6.

9. Thomas F, Boyle AL, Burton AJ, Woolfson DN. A set of de novo designed parallel heterodimeric coiled coils with quantified dissociation constants in the micromolar to sub-nanomolar regime. J Am Chem Soc. 2013;135(13):5161-6.

10. Zaccai NR, Chi B, Thomson AR, Boyle AL, Bartlett GJ, Bruning M, et al. A de novo peptide hexamer with a mutable channel. Nat Chem Biol. 2011;7(12):935-41.

11. Rhys GG, Wood CW, Lang EJM, Mulholland AJ, Brady RL, Thomson AR, et al. Maintaining and breaking symmetry in homomeric coiled-coil assemblies. Nat Commun. 2018;9(1):4132.

12. Banwell EF AE, Adams DJ, Birchall MA, Corrigan A, Donald AM, Kirkland M, Serpell LC, Butler MF, Woolfson DN. Rational design and application of a-helical peptide hydrogels. Nature Materials. 2009;8:596-600.

13. Burton AJ, Thomson AR, Dawson WM, Brady RL, Woolfson DN. Installing hydrolytic activity into a completely de novo protein framework. Nat Chem. 2016;8(9):837-44.

14. Thomas F, Dawson WM, Lang EJM, Burton AJ, Bartlett GJ, Rhys GG, et al. De Novo-Designed alpha-Helical Barrels as Receptors for Small Molecules. ACS Synth Biol. 2018;7(7):1808-16.

15. Smith AJ, Thomas F, Shoemark D, Woolfson DN, Savery NJ. Guiding Biomolecular Interactions in Cells Using de Novo Protein-Protein Interfaces. ACS Synth Biol. 2019;8(6):1284-93.

16. Lee MJ, Mantell J, Hodgson L, Alibhai D, Fletcher JM, Brown IR, et al. Engineered synthetic scaffolds for organizing proteins within the bacterial cytoplasm. Nat Chem Biol. 2018;14(2):142-7.

17. Fletcher JM, Harniman RL, Barnes FR, Boyle AL, Collins A, Mantell J, et al. Self-assembling cages from coiled-coil peptide modules. Science. 2013;340(6132):595-9.

18. Watkins DW, Jenkins JMX, Grayson KJ, Wood N, Steventon JW, Le Vay KK, et al. Construction and in vivo assembly of a catalytically proficient and hyperthermostable de novo enzyme. Nat Commun. 2017;8(1):358.

19. Dou J, Vorobieva AA, Sheffler W, Doyle LA, Park H, Bick MJ, et al. De novo design of a fluorescence-activating beta-barrel. Nature. 2018;561(7724):485-91.

20. Langan RA, Boyken SE, Ng AH, Samson JA, Dods G, Westbrook AM, et al. De novo design of bioactive protein switches. Nature. 2019;572(7768):205-10.

21. Doyle L, Hallinan J, Bolduc J, Parmeggiani F, Baker D, Stoddard BL, et al. Rational design of alpha-helical tandem repeat proteins with closed architectures. Nature. 2015;528(7583):585-8.

22. Brunette TJ, Parmeggiani F, Huang PS, Bhabha G, Ekiert DC, Tsutakawa SE, et al. Exploring the repeat protein universe through computational protein design. Nature. 2015;528(7583):580-4.

23. Baker EG, Williams C, Hudson KL, Bartlett GJ, Heal JW, Porter Goff KL, et al. Engineering protein stability with atomic precision in a monomeric miniprotein. Nat Chem Biol. 2017;13(7):764-70.

24. Marcos E, Chidyausiku TM, McShan AC, Evangelidis T, Nerli S, Carter L, et al. De novo design of a non-local beta-sheet protein with high stability and accuracy. Nat Struct Mol Biol. 2018;25(11):1028-34.

25. Kuhlman B, Dantas G, Ireton GC, Varani G, Stoddard BL, Baker D. Design of a novel globular protein fold with atomic-level accuracy. Science. 2003;302(5649):1364-8.

26. King NP, Bale JB, Sheffler W, McNamara DE, Gonen S, Gonen T, et al. Accurate design of co-assembling multi-component protein nanomaterials. Nature. 2014;510(7503):103-8.

27. Marcandalli J, Fiala B, Ols S, Perotti M, de van der Schueren W, Snijder J, et al. Induction of Potent Neutralizing Antibody Responses by a Designed Protein Nanoparticle Vaccine for Respiratory Syncytial Virus. Cell. 2019;176(6):1420-31 e17.

28. Lu P, Min D, DiMaio F, Wei KY, Vahey MD, Boyken SE, et al. Accurate computational design of multipass transmembrane proteins. Science. 2018;359(6379):1042-6.

29. Lalaurie CJ, Dufour V, Meletiou A, Ratcliffe S, Harland A, Wilson O, et al. The de novo design of a biocompatible and functional integral membrane protein using minimal sequence complexity. Sci Rep. 2018;8(1):14564.

30. Mravic M, Thomaston JL, Tucker M, Solomon PE, Liu L, DeGrado WF. Packing of apolar side chains enables accurate design of highly stable membrane proteins. Science. 2019;363(6434):1418-23.

31. Alberts BJ, A. Lewis, J. Raff, M. Roberts, K. Walter, P. 2008. Molecular Biology of the Cell (Fifth Edition). Garland Science, Taylor & Francis Group; 2008.

32. Chung HJ, Steplewski A, Chung KY, Uitto J, Fertala A. Collagen fibril formation. A new target to limit fibrosis. J Biol Chem. 2008;283(38):25879-86.

33. Liu Z, Qiao J, Niu Z, Wang Q. Natural supramolecular building blocks: from virus coat proteins to viral nanoparticles. Chem Soc Rev. 2012;41(18):6178-94.

34. Pandya MJ, Spooner GM, Sunde M, Thorpe JR, Rodger A, Woolfson DN. Sticky-end assembly of a designed peptide fiber provides insight into protein fibrillogenesis. Biochemistry. 2000;39(30):8728-34.

35. Shen H, Fallas JA, Lynch E, Sheffler W, Parry B, Jannetty N, et al. De novo design of self-assembling helical protein filaments. Science. 2018;362(6415):705-9.

36. Burgess NC, Sharp TH, Thomas F, Wood CW, Thomson AR, Zaccai NR, et al. Modular Design of Self-Assembling Peptide-Based Nanotubes. J Am Chem Soc. 2015;137(33):10554-62.

37. Xu C, Liu R, Mehta AK, Guerrero-Ferreira RC, Wright ER, Dunin-Horkawicz S, et al. Rational design of helical nanotubes from self-assembly of coiled-coil lock washers. J Am Chem Soc. 2013;135(41):15565-78.

38. Egelman EH, Xu C, DiMaio F, Magnotti E, Modlin C, Yu X, et al. Structural plasticity of helical nanotubes based on coiled-coil assemblies. Structure. 2015;23(2):280-9.

39. Cristie-David AS, Chen J, Nowak DB, Bondy AL, Sun K, Park SI, et al. Coiled-Coil-Mediated Assembly of an Icosahedral Protein Cage with Extremely High Thermal and Chemical Stability. J Am Chem Soc. 2019;141(23):9207-16.

40. Chen Z, Johnson MC, Chen J, Bick MJ, Boyken SE, Lin B, et al. Self-Assembling 2D Arrays with de Novo Protein Building Blocks. J Am Chem Soc. 2019;141(22):8891-5.

41. Ryadnov MG WD. Engineering the morphology of a self-assembling protein fibre. Nature Materials. 2003;2:329-32.

42. Papapostolou D SA, Atkins EDT, Oliver SJ, Ryadnov MG, Serpell LC, Woolfson DN. Engineering nanoscale order into a designed protein fiber. PNAS. 2007;104(26):10853-8.

43. Sharp TH, Bruning M, Mantell J, Sessions RB, Thomson AR, Zaccai NR, et al. Cryo-transmission electron microscopy structure of a gigadalton peptide fiber of de novo design. Proc Natl Acad Sci U S A. 2012;109(33):13266-71.

44. Potekhin SA, Melnik TN, Popov V, Lanina NF, Vazina AA, Rigler P, et al. De novo design of fibrils made of short alpha-helical coiled coil peptides. Chem Biol. 2001;8(11):1025-32.

45. Walshaw J, Woolfson DN. Open-and-shut cases in coiled-coil assembly: alpha-sheets and alpha-cylinders. Protein Sci. 2001;10(3):668-73.

46. Nagy-Smith K, Moore E, Schneider J, Tycko R. Molecular structure of monomorphic peptide fibrils within a kinetically trapped hydrogel network. Proc Natl Acad Sci U S A. 2015;112(32):9816-21.

47. Kaltofen S, Li C, Huang PS, Serpell LC, Barth A, Andre I. Computational de novo design of a self-assembling peptide with predefined structure. J Mol Biol. 2015;427(2):550-62.

48. Schneider JP, Pochan DJ, Ozbas B, Rajagopal K, Pakstis L, Kretsinger J. Responsive hydrogels from the intramolecular folding and self-assembly of a designed peptide. J Am Chem Soc. 2002;124(50):15030-7.

49. Reches M, Gazit E. Casting metal nanowires within discrete self-assembled peptide nanotubes. Science. 2003;300(5619):625-7.

50. Lopez De La Paz M, Goldie K, Zurdo J, Lacroix E, Dobson CM, Hoenger A, et al. De novo designed peptide-based amyloid fibrils. Proc Natl Acad Sci U S A. 2002;99(25):16052-7.

51. Vauthey S, Santoso S, Gong H, Watson N, Zhang S. Molecular self-assembly of surfactant-like peptides to form nanotubes and nanovesicles. Proc Natl Acad Sci U S A. 2002;99(8):5355-60.

52. Cui H, Cheetham AG, Pashuck ET, Stupp SI. Amino acid sequence in constitutionally isomeric tetrapeptide amphiphiles dictates architecture of one-dimensional nanostructures. J Am Chem Soc. 2014;136(35):12461-8.

53. Claussen RC, Rabatic BM, Stupp SI. Aqueous self-assembly of unsymmetric Peptide bolaamphiphiles into nanofibers with hydrophilic cores and surfaces. J Am Chem Soc. 2003;125(42):12680-1.

54. Zhang S, Holmes T, Lockshin C, Rich A. Spontaneous assembly of a self-complementary oligopeptide to form a stable macroscopic membrane. Proc Natl Acad Sci U S A. 1993;90(8):3334-8.

55. Dong H, Paramonov SE, Aulisa L, Bakota EL, Hartgerink JD. Self-assembly of multidomain peptides: balancing molecular frustration controls conformation and nanostructure. J Am Chem Soc. 2007;129(41):12468-72.

56. Zhang S, Holmes TC, DiPersio CM, Hynes RO, Su X, Rich A. Self-complementary oligopeptide matrices support mammalian cell attachment. Biomaterials. 1995;16(18):1385-93.

57. Frantz C SK, Weaver VM. The extracellular matrix at a glance. Journal of Cell Science. 2010;123:4195-200.

58. Albelda SM, Buck CA. Integrins and other cell adhesion molecules. FASEB J. 1990;4(11):2868-80.

59. Geiger B SJ, Bershadsky AD. Environmental sensing through focal adhesions. Nature Reviews Molecular Cell Biology. 2009;10:21-33.

60. Yayon A, Klagsbrun M, Esko JD, Leder P, Ornitz DM. Cell surface, heparin-like molecules are required for binding of basic fibroblast growth factor to its high affinity receptor. Cell. 1991;64(4):841-8.

61. Kanato Y, Ono S, Kitajima K, Sato C. Complex formation of a brain-derived neurotrophic factor and glycosaminoglycans. Biosci Biotechnol Biochem. 2009;73(12):2735-41.

62. Oyagi A, Hara H. Essential roles of heparin-binding epidermal growth factor-like growth factor in the brain. CNS Neurosci Ther. 2012;18(10):803-10.

63. Levental I GP, Janmey PA. Soft biological materials and their impact on cell function. Soft Matter. 2007(3).

64. Gillies AR, Lieber RL. Structure and function of the skeletal muscle extracellular matrix. Muscle Nerve. 2011;44(3):318-31.

65. Barros CS, Franco SJ, Muller U. Extracellular matrix: functions in the nervous system. Cold Spring Harb Perspect Biol. 2011;3(1):a005108.

66. Butcher DT, Alliston T, Weaver VM. A tense situation: forcing tumour progression. Nat Rev Cancer. 2009;9(2):108-22.

67. Tyler WJ. The mechanobiology of brain function. Nat Rev Neurosci. 2012;13(12):867-78.

68. Levental I GP. Soft biological materials and their impact on cell function. Soft MAtter. 2007(3):299-306.

69. Christ AF, Franze K, Gautier H, Moshayedi P, Fawcett J, Franklin RJ, et al. Mechanical difference between white and gray matter in the rat cerebellum measured by scanning force microscopy. J Biomech. 2010;43(15):2986-92.

70. Franze K, Janmey PA, Guck J. Mechanics in neuronal development and repair. Annu Rev Biomed Eng. 2013;15:227-51.

71. Gautier HO, Thompson AJ, Achouri S, Koser DE, Holtzmann K, Moeendarbary E, et al. Atomic force microscopy-based force measurements on animal cells and tissues. Methods Cell Biol. 2015;125:211-35.

72. Sherman LS, Matsumoto S, Su W, Srivastava T, Back SA. Hyaluronan Synthesis, Catabolism, and Signaling in Neurodegenerative Diseases. Int J Cell Biol. 2015;2015:368584.

73. Bignami A, Hosley M, Dahl D. Hyaluronic acid and hyaluronic acid-binding proteins in brain extracellular matrix. Anat Embryol (Berl). 1993;188(5):419-33.

74. Morawski M, Dityatev A, Hartlage-Rubsamen M, Blosa M, Holzer M, Flach K, et al. Tenascin-R promotes assembly of the extracellular matrix of perineuronal nets via clustering of aggrecan. Philos Trans R Soc Lond B Biol Sci. 2014;369(1654):20140046.

75. Yamaguchi Y. Lecticans: organizers of the brain extracellular matrix. Cell Mol Life Sci. 2000;57(2):276-89.

76. Baker BM CC. Deconstructing the third dimension - how 3D culture microenvironments alter cellular cues. Journal of Cell Science. 2012;125(13):3015-24.

77. Benya PD SJ. Dedifferentiated chondrocytes reexpress the differentiated collagen phenotype when cultured in agarose gels. Cell. 1982;30:215-24.

78. Rubashkin MG OG, Weaver VM. Deconstructing signalling in three dimensions. Biochemistry. 2014;53(13):2078-90.

79. Ravi M PV, Kaviya SR, Anuradha E, Solomon P. 3D cell culture systems: advantages and applications. Journal of Cellular Physiology. 2014;230(1):16-26.

80. Geckil H, Xu F, Zhang X, Moon S, Demirci U. Engineering hydrogels as extracellular matrix mimics. Nanomedicine (Lond). 2010;5(3):469-84.

81. Kleinman HK, McGarvey ML, Hassell JR, Star VL, Cannon FB, Laurie GW, et al. Basement membrane complexes with biological activity. Biochemistry. 1986;25(2):312-8.

82. Albini A, Melchiori A, Garofalo A, Noonan DM, Basolo F, Taraboletti G, et al. Matrigel promotes retinoblastoma cell growth in vitro and in vivo. Int J Cancer. 1992;52(2):234-40.

83. Xu C, Inokuma MS, Denham J, Golds K, Kundu P, Gold JD, et al. Feeder-free growth of undifferentiated human embryonic stem cells. Nat Biotechnol. 2001;19(10):971-4.

84. Ma W, Tavakoli T, Derby E, Serebryakova Y, Rao MS, Mattson MP. Cell-extracellular matrix interactions regulate neural differentiation of human embryonic stem cells. BMC Dev Biol. 2008;8:90.

85. Hughes CS, Postovit LM, Lajoie GA. Matrigel: a complex protein mixture required for optimal growth of cell culture. Proteomics. 2010;10(9):1886-90.

86. Yan W, Liu W, Qi J, Fang Q, Fan Z, Sun G, et al. A Three-Dimensional Culture System with Matrigel Promotes Purified Spiral Ganglion Neuron Survival and Function In Vitro. Mol Neurobiol. 2018;55(3):2070-84.

87. Shoulders MD, Raines RT. Collagen structure and stability. Annu Rev Biochem. 2009;78:929-58.

88. Schneider RK, Puellen A, Kramann R, Raupach K, Bornemann J, Knuechel R, et al. The osteogenic differentiation of adult bone marrow and perinatal umbilical mesenchymal stem cells and matrix remodelling in three-dimensional collagen scaffolds. Biomaterials. 2010;31(3):467-80.

89. Antoine EE, Vlachos PP, Rylander MN. Review of collagen I hydrogels for bioengineered tissue microenvironments: characterization of mechanics, structure, and transport. Tissue Eng Part B Rev. 2014;20(6):683-96.

90. Moriarty N, Pandit A, Dowd E. Encapsulation of primary dopaminergic neurons in a GDNF-loaded collagen hydrogel increases their survival, re-innervation and function after intra-striatal transplantation. Sci Rep. 2017;7(1):16033.

91. Lutolf MP, Hubbell JA. Synthetic biomaterials as instructive extracellular microenvironments for morphogenesis in tissue engineering. Nat Biotechnol. 2005;23(1):47-55.

92. Kramer RZ, Bella J, Mayville P, Brodsky B, Berman HM. Sequence dependent conformational variations of collagen triple-helical structure. Nat Struct Biol. 1999;6(5):454-7.

93. Yang Z, Pandi L, Doolittle RF. The crystal structure of fragment double-D from cross-linked lamprey fibrin reveals isopeptide linkages across an unexpected D-D interface. Biochemistry. 2002;41(52):15610-7.

94. Xu X, Jha AK, Harrington DA, Farach-Carson MC, Jia X. Hyaluronic Acid-Based Hydrogels: from a Natural Polysaccharide to Complex Networks. Soft Matter. 2012;8(12):3280-94.

95. Shu XZ, Ghosh K, Liu Y, Palumbo FS, Luo Y, Clark RA, et al. Attachment and spreading of fibroblasts on an RGD peptide-modified injectable hyaluronan hydrogel. J Biomed Mater Res A. 2004;68(2):365-75.

96. Nakaji-Hirabayashi T KK, Iwata H. Hyaluronic acid hydrogel loaded with genetically-engineered brain-derived neurotrophic factor as a neural cell carrier. Biomaterials. 2009;30(27):4581-9.

97. Rape AD, Zibinsky M, Murthy N, Kumar S. A synthetic hydrogel for the high-throughput study of cell-ECM interactions. Nat Commun. 2015;6:8129.

98. Shu XZ, Liu Y, Luo Y, Roberts MC, Prestwich GD. Disulfide cross-linked hyaluronan hydrogels. Biomacromolecules. 2002;3(6):1304-11.

99. Wu S, Xu R, Duan B, Jiang P. Three-Dimensional Hyaluronic Acid Hydrogel-Based Models for In Vitro Human iPSC-Derived NPC Culture and Differentiation. J Mater Chem B. 2017;5(21):3870-8.

100. Catelas I, Sese N, Wu BM, Dunn JC, Helgerson S, Tawil B. Human mesenchymal stem cell proliferation and osteogenic differentiation in fibrin gels in vitro. Tissue Eng. 2006;12(8):2385-96.

101. Dubey N, Letourneau PC, Tranquillo RT. Neuronal contact guidance in magnetically aligned fibrin gels: effect of variation in gel mechano-structural properties. Biomaterials. 2001;22(10):1065-75.

102. Balgude AP YX, Szymanski A, Bellamkonda RV. Agarose gel stiffness determines rate of DRG neurite extension in 3D cultures. Biomaterials. 2001;22(10):1077-84.

103. Dhoot NO, Tobias CA, Fischer I, Wheatley MA. Peptide-modified alginate surfaces as a growth permissive substrate for neurite outgrowth. J Biomed Mater Res A. 2004;71(2):191-200.

104. Ma PX. Scaffolds for Tissue Fabrication. MaterialsToday. 2004;7(5):30-40.

105. Tallawi M, Rosellini E, Barbani N, Cascone MG, Rai R, Saint-Pierre G, et al. Strategies for the chemical and biological functionalization of scaffolds for cardiac tissue engineering: a review. J R Soc Interface. 2015;12(108):20150254.

106. Sridhar BV DN, Randolph MA, Anseth KS. Covalently tethered TGF-β1 with encapsulated chondrocytes in a PEG hydrogel system enhances extracellular matrix production. Jornal of Biomedical Materials Research. 2014;102(12):4464-72.

107. Burdick JA, Anseth KS. Photoencapsulation of osteoblasts in injectable RGD-modified PEG hydrogels for bone tissue engineering. Biomaterials. 2002;23(22):4315-23.

108. A MJ, S AB, A HK, van Hest JC, Lowik DW. Soft PEG-Hydrogels with Independently Tunable Stiffness and RGDS-Content for Cell Adhesion Studies. Macromol Biosci. 2015;15(10):1338-47.

109. Freudenberg U, Hermann A, Welzel PB, Stirl K, Schwarz SC, Grimmer M, et al. A star-PEG-heparin hydrogel platform to aid cell replacement therapies for neurodegenerative diseases. Biomaterials. 2009;30(28):5049-60.

110. Zhou L, Tu J, Fang G, Deng L, Gao X, Guo K, et al. Combining PLGA Scaffold and MSCs for Brain Tissue Engineering: A Potential Tool for Treatment of Brain Injury. Stem Cells Int. 2018;2018:5024175.

111. Gregor A, Filova E, Novak M, Kronek J, Chlup H, Buzgo M, et al. Designing of PLA scaffolds for bone tissue replacement fabricated by ordinary commercial 3D printer. J Biol Eng. 2017;11:31.

112. Tuffin J, Burke M, Richardson T, Johnson T, Saleem MA, Satchell S, et al. A Composite Hydrogel Scaffold Permits Self-Organization and Matrix Deposition by Cocultured Human Glomerular Cells. Adv Healthc Mater. 2019;8(17):e1900698.

113. Jang YS, Jang CH, Cho YB, Kim M, Kim GH. Tracheal regeneration using polycaprolactone/collagen-nanofiber coated with umbilical cord serum after partial resection. Int J Pediatr Otorhinolaryngol. 2014;78(12):2237-43.

114. Nakamura H, Lee AA, Afshar AS, Watanabe S, Rho E, Razavi S, et al. Intracellular production of hydrogels and synthetic RNA granules by multivalent molecular interactions. Nat Mater. 2018;17(1):79-89.

115. Zhang L, Bailey JB, Subramanian RH, Groisman A, Tezcan FA. Hyperexpandable, self-healing macromolecular crystals with integrated polymer networks. Nature. 2018;557(7703):86-91.

116. Gilbert C, Ellis T. Biological Engineered Living Materials: Growing Functional Materials with Genetically Programmable Properties. ACS Synth Biol. 2019;8(1):1-15.

117. Nguyen PQ, Botyanszki Z, Tay PK, Joshi NS. Programmable biofilm-based materials from engineered curli nanofibres. Nat Commun. 2014;5:4945.

118. Chen AY, Deng Z, Billings AN, Seker UO, Lu MY, Citorik RJ, et al. Synthesis and patterning of tunable multiscale materials with engineered cells. Nat Mater. 2014;13(5):515-23.

119. Soliakov A, Harris JR, Watkinson A, Lakey JH. The structure of Yersinia pestis Caf1 polymer in free and adjuvant bound states. Vaccine. 2010;28(35):5746-54.

120. Du Y, Rosqvist R, Forsberg A. Role of fraction 1 antigen of Yersinia pestis in inhibition of phagocytosis. Infect Immun. 2002;70(3):1453-60.

121. Roque AI, Soliakov A, Birch MA, Philips SR, Shah DS, Lakey JH. Reversible non-stick behaviour of a bacterial protein polymer provides a tuneable molecular mimic for cell and tissue engineering. Adv Mater. 2014;26(17):2704-9, 616.

122. Peters DT, Waller H, Birch MA, Lakey JH. Engineered mosaic protein polymers; a simple route to multifunctional biomaterials. J Biol Eng. 2019;13:54.

123. Dura G, Waller H, Gentile P, Lakey JH, Fulton DA. Tuneable hydrogels of Caf1 protein fibers. Mater Sci Eng C Mater Biol Appl. 2018;93:88-95.

124. Zavialov AV, Berglund J, Pudney AF, Fooks LJ, Ibrahim TM, MacIntyre S, et al. Structure and biogenesis of the capsular F1 antigen from Yersinia pestis: preserved folding energy drives fiber formation. Cell. 2003;113(5):587-96.

125. Sun F, Zhang WB, Mahdavi A, Arnold FH, Tirrell DA. Synthesis of bioactive protein hydrogels by genetically encoded SpyTag-SpyCatcher chemistry. Proc Natl Acad Sci U S A. 2014;111(31):11269-74.

126. Wu J, Li P, Dong C, Jiang H, Bin X, Gao X, et al. Rationally designed synthetic protein hydrogels with predictable mechanical properties. Nat Commun. 2018;9(1):620.

127. Zakeri B FJ, Celik E, Chittock EC, Schwarz-Linek U, Moy VT, Howarth M. Peptide tag forming a rapid covalent bond to a protein, through engineering a bacterial adhesin. PNAS. 2012;109(12):690-7.

128. Kang MK, Colombo JS, D'Souza RN, Hartgerink JD. Sequence effects of self-assembling multidomain peptide hydrogels on encapsulated SHED cells. Biomacromolecules. 2014;15(6):2004-11.

129. Jayawarna V AM, Jowitt TA, Miller AF, Saiani A, Gough JE, Ulijn RV. Nanostructured Hydrogels for Three-Dimensional Cell Culture Through Self-Assembly of Fluorenylmethoxycarbonyl–Dipeptides. Advnaced Materials. 2006;18:611-4.

130. Frederix PW, Scott GG, Abul-Haija YM, Kalafatovic D, Pappas CG, Javid N, et al. Exploring the sequence space for (tri-)peptide self-assembly to design and discover new hydrogels. Nat Chem. 2015;7(1):30-7.

131. Nowak AP, Breedveld V, Pakstis L, Ozbas B, Pine DJ, Pochan D, et al. Rapidly recovering hydrogel scaffolds from self-assembling diblock copolypeptide amphiphiles. Nature. 2002;417(6887):424-8.

132. Hartgerink JD, Beniash E, Stupp SI. Self-assembly and mineralization of peptide-amphiphile nanofibers. Science. 2001;294(5547):1684-8.

133. Haines-Butterick L, Rajagopal K, Branco M, Salick D, Rughani R, Pilarz M, et al. Controlling hydrogelation kinetics by peptide design for three-dimensional encapsulation and injectable delivery of cells. Proc Natl Acad Sci U S A. 2007;104(19):7791-6.

134. Freeman R, Han M, Alvarez Z, Lewis JA, Wester JR, Stephanopoulos N, et al. Reversible self-assembly of superstructured networks. Science. 2018;362(6416):808-13.

135. Aulisa L, Dong H, Hartgerink JD. Self-assembly of multidomain peptides: sequence variation allows control over cross-linking and viscoelasticity. Biomacromolecules. 2009;10(9):2694-8.

136. Martin AD, Chua SW, Au CG, Stefen H, Przybyla M, Lin Y, et al. Peptide Nanofiber Substrates for Long-Term Culturing of Primary Neurons. ACS Appl Mater Interfaces. 2018;10(30):25127-34.

137. Zhang Y, Gu H, Yang Z, Xu B. Supramolecular hydrogels respond to ligand-receptor interaction. J Am Chem Soc. 2003;125(45):13680-1.

138. Zhou M, Smith AM, Das AK, Hodson NW, Collins RF, Ulijn RV, et al. Self-assembled peptide-based hydrogels as scaffolds for anchorage-dependent cells. Biomaterials. 2009;30(13):2523-30.

139. Chronopoulou L TA, Guarguaglini G, Masci G, Giammaruco F, Togna GI, Palocci C. Self-assembling peptide hydrogels promote microglial cells proliferation and NGF production. Soft Matter. 2012;8:5784-90.

140. Mehrban N AE, Wasmuth A, Hudson KL, Mullen LM, Thomson AR, Birchall MA, Woolfson DN. Assessing cellular response to functionalised a-helical peptide hydrogels. Advanced Healthcare Materials. 2014;3(9):1387-91.

141. Mehrban N ZB, Tamagnini F, Young F, Wasmuth A, Hudson K, Thomson A, Birchall M, Randall A, Song B, Woolfson D. Functionalized a-helical peptide hydrogels for neural tissue engineering. ACS Biomaterials Science and Engineering. 2015;1(6):431-9.

142. Dexter AF FN, Creasey RG, Filardo F, Boeh, MW, Jack KS. Fabrication and characterization of hydrogels formed from designer coiled-coil fibril-forming peptides. Royal Society of Chemistry Advances. 2017;7:27260-71.

143. Kolb HC, Finn MG, Sharpless KB. Click Chemistry: Diverse Chemical Function from a Few Good Reactions. Angew Chem Int Ed Engl. 2001;40(11):2004-21.

144. Rostovtsev VV, Green LG, Fokin VV, Sharpless KB. A stepwise huisgen cycloaddition process: copper(I)-catalyzed regioselective "ligation" of azides and terminal alkynes. Angew Chem Int Ed Engl. 2002;41(14):2596-9.

145. Agard NJ, Prescher JA, Bertozzi CR. A strain-promoted [3 + 2] azide-alkyne cycloaddition for covalent modification of biomolecules in living systems. J Am Chem Soc. 2004;126(46):15046-7.

146. Hoyle CE, Bowman CN. Thiol-ene click chemistry. Angew Chem Int Ed Engl. 2010;49(9):1540-73.

147. Nair DP PM, Chatani S, Gong T, Xi W, Fenoli CR, Bowman CN. The Thiol-Michael Addition Click Reaction: A Powerful and Widely Used Tool in Materials Chemistry. Chemical of Materials. 2014;26:724-44.

148. Ruoslahti E. RGD and other recognition sequences for integrins. Annu Rev Cell Dev Biol. 1996;12:697-715.

149. Giancotti FG, Ruoslahti E. Integrin signaling. Science. 1999;285(5430):1028-32.

150. Sreejalekshmi KG, Nair PD. Biomimeticity in tissue engineering scaffolds through synthetic peptide modifications-altering chemistry for enhanced biological response. J Biomed Mater Res A. 2011;96(2):477-91.

151. Cook AD, Hrkach JS, Gao NN, Johnson IM, Pajvani UB, Cannizzaro SM, et al. Characterization and development of RGD-peptide-modified poly(lactic acid-co-lysine) as an interactive, resorbable biomaterial. J Biomed Mater Res. 1997;35(4):513-23.

152. Lei Y, Gojgini S, Lam J, Segura T. The spreading, migration and proliferation of mouse mesenchymal stem cells cultured inside hyaluronic acid hydrogels. Biomaterials. 2011;32(1):39-47.

153. Farrukh A, Ortega F, Fan W, Marichal N, Paez JI, Berninger B, et al. Bifunctional Hydrogels Containing the Laminin Motif IKVAV Promote Neurogenesis. Stem Cell Reports. 2017;9(5):1432-40.

154. Hogrebe NJ, Reinhardt JW, Tram NK, Debski AC, Agarwal G, Reilly MA, et al. Independent control of matrix adhesiveness and stiffness within a 3D self-assembling peptide hydrogel. Acta Biomater. 2018;70:110-9.

155. Adams DN, Kao EY, Hypolite CL, Distefano MD, Hu WS, Letourneau PC. Growth cones turn and migrate up an immobilized gradient of the laminin IKVAV peptide. J Neurobiol. 2005;62(1):134-47.

156. Guarnieri D, De Capua A, Ventre M, Borzacchiello A, Pedone C, Marasco D, et al. Covalently immobilized RGD gradient on PEG hydrogel scaffold influences cell migration parameters. Acta Biomater. 2010;6(7):2532-9.

157. Park KH, Na K, Chung HM. Enhancement of the adhesion of fibroblasts by peptide containing an Arg-Gly-Asp sequence with poly(ethylene glycol) into a thermo-reversible hydrogel as a synthetic extracellular matrix. Biotechnol Lett. 2005;27(4):227-31.

158. Villard V, Kalyuzhniy O, Riccio O, Potekhin S, Melnik TN, Kajava AV, et al. Synthetic RGD-containing alpha-helical coiled coil peptides promote integrin-dependent cell adhesion. J Pept Sci. 2006;12(3):206-12.

159. Deforest CA, Sims EA, Anseth KS. Peptide-Functionalized Click Hydrogels with Independently Tunable Mechanics and Chemical Functionality for 3D Cell Culture. Chem Mater. 2010;22(16):4783-90.

160. Clapper JD, Pearce ME, Guymon CA, Salem AK. Biotinylated biodegradable nanotemplated hydrogel networks for cell interactive applications. Biomacromolecules. 2008;9(4):1188-94.

161. DeForest CA, Polizzotti BD, Anseth KS. Sequential click reactions for synthesizing and patterning three-dimensional cell microenvironments. Nat Mater. 2009;8(8):659-64.

162. Ahearne M, Yang Y, El Haj AJ, Then KY, Liu KK. Characterizing the viscoelastic properties of thin hydrogel-based constructs for tissue engineering applications. J R Soc Interface. 2005;2(5):455-63.

163. Anderson JM, Andukuri A, Lim DJ, Jun HW. Modulating the gelation properties of self-assembling peptide amphiphiles. ACS Nano. 2009;3(11):3447-54.

164. Hofer MM, Barde YA. Brain-derived neurotrophic factor prevents neuronal death in vivo. Nature. 1988;331(6153):261-2.

165. Ip NY, Li YP, van de Stadt I, Panayotatos N, Alderson RF, Lindsay RM. Ciliary neurotrophic factor enhances neuronal survival in embryonic rat hippocampal cultures. J Neurosci. 1991;11(10):3124-34.

166. DG W. Multiple roles of eph receptors and ephrins in neural development. Nature Reviews. 2001;2:155-64.

167. Beenken A, Mohammadi M. The FGF family: biology, pathophysiology and therapy. Nat Rev Drug Discov. 2009;8(3):235-53.

168. Nieto-Estevez V DC, Vicario-Abejon. IGF-I: A Key Growth Factor that Regulates Neurogenesis and Synaptogenesis from Embryonic to Adult Stages of the Brain. Frontiers in Neuroscience. 2016;10(52).

169. Kennedy TE, Serafini T, de la Torre JR, Tessier-Lavigne M. Netrins are diffusible chemotropic factors for commissural axons in the embryonic spinal cord. Cell. 1994;78(3):425-35.

170. Charron F, Stein E, Jeong J, McMahon AP, Tessier-Lavigne M. The morphogen sonic hedgehog is an axonal chemoattractant that collaborates with netrin-1 in midline axon guidance. Cell. 2003;113(1):11-23.

171. Jin K, Zhu Y, Sun Y, Mao XO, Xie L, Greenberg DA. Vascular endothelial growth factor (VEGF) stimulates neurogenesis in vitro and in vivo. Proc Natl Acad Sci U S A. 2002;99(18):11946-50.

172. Larpthaveesarp A, Ferriero DM, Gonzalez FF. Growth factors for the treatment of ischemic brain injury (growth factor treatment). Brain Sci. 2015;5(2):165-77.

173. Alberch J, Perez-Navarro E, Canals JM. Neuroprotection by neurotrophins and GDNF family members in the excitotoxic model of Huntington's disease. Brain Res Bull. 2002;57(6):817-22.

174. Pencea V, Bingaman KD, Wiegand SJ, Luskin MB. Infusion of brain-derived neurotrophic factor into the lateral ventricle of the adult rat leads to new neurons in the parenchyma of the striatum, septum, thalamus, and hypothalamus. J Neurosci. 2001;21(17):6706-17.

175. Huang EJ, Reichardt LF. Neurotrophins: roles in neuronal development and function. Annu Rev Neurosci. 2001;24:677-736.

176. Aberg MA, Aberg ND, Hedbacker H, Oscarsson J, Eriksson PS. Peripheral infusion of IGF-I selectively induces neurogenesis in the adult rat hippocampus. J Neurosci. 2000;20(8):2896-903.

177. Cheng CM, Cohen M, Tseng V, Bondy CA. Endogenous IGF1 enhances cell survival in the postnatal dentate gyrus. J Neurosci Res. 2001;64(4):341-7.

178. Sosa L, Dupraz S, Laurino L, Bollati F, Bisbal M, Caceres A, et al. IGF-1 receptor is essential for the establishment of hippocampal neuronal polarity. Nat Neurosci. 2006;9(8):993-5.

179. Scolnick JA, Cui K, Duggan CD, Xuan S, Yuan XB, Efstratiadis A, et al. Role of IGF signaling in olfactory sensory map formation and axon guidance. Neuron. 2008;57(6):847-57.

180. Mairet-Coello G, Tury A, DiCicco-Bloom E. Insulin-like growth factor-1 promotes G(1)/S cell cycle progression through bidirectional regulation of cyclins and cyclin-dependent kinase inhibitors via the phosphatidylinositol 3-kinase/Akt pathway in developing rat cerebral cortex. J Neurosci. 2009;29(3):775-88.

181. Liu Z, D'Amore PA, Mikati M, Gatt A, Holmes GL. Neuroprotective effect of chronic infusion of basic fibroblast growth factor on seizure-associated hippocampal damage. Brain Res. 1993;626(1-2):335-8.

182. Ham TR, Farrag M, Leipzig ND. Covalent growth factor tethering to direct neural stem cell differentiation and self-organization. Acta Biomater. 2017;53:140-51.

183. Silva AK, Richard C, Bessodes M, Scherman D, Merten OW. Growth factor delivery approaches in hydrogels. Biomacromolecules. 2009;10(1):9-18.

184. Yamaguchi N, Zhang L, Chae BS, Palla CS, Furst EM, Kiick KL. Growth factor mediated assembly of cell receptor-responsive hydrogels. J Am Chem Soc. 2007;129(11):3040-1.

185. Wylie RG, Ahsan S, Aizawa Y, Maxwell KL, Morshead CM, Shoichet MS. Spatially controlled simultaneous patterning of multiple growth factors in three-dimensional hydrogels. Nat Mater. 2011;10(10):799-806.

186. Parker J, Mitrousis N, Shoichet MS. Hydrogel for Simultaneous Tunable Growth Factor Delivery and Enhanced Viability of Encapsulated Cells in Vitro. Biomacromolecules. 2016;17(2):476-84.

187. Bruggeman KF, Rodriguez AL, Parish CL, Williams RJ, Nisbet DR. Temporally controlled release of multiple growth factors from a self-assembling peptide hydrogel. Nanotechnology. 2016;27(38):385102.

188. Galler KM, Hartgerink JD, Cavender AC, Schmalz G, D'Souza RN. A customized self-assembling peptide hydrogel for dental pulp tissue engineering. Tissue Eng Part A. 2012;18(1-2):176-84.

189. M-M SH-JP. The cell biology of neuronal navigation. Nature Cell Biology. 2001;3(3):81-8.

190. Drubin DG, Nelson WJ. Origins of cell polarity. Cell. 1996;84(3):335-44.

191. Dessaud E, McMahon AP, Briscoe J. Pattern formation in the vertebrate neural tube: a sonic hedgehog morphogen-regulated transcriptional network. Development. 2008;135(15):2489-503.

192. Xu W, Lakshman N, Morshead CM. Building a central nervous system: The neural stem cell lineage revealed. Neurogenesis (Austin). 2017;4(1):e1300037.

193. McLaughlin T OLD. Chemoaffinity hypothesis: development of topographic axonal projections. Lemke G, editor. Elesvier2009.

194. O'Leary DD, Chou SJ, Sahara S. Area patterning of the mammalian cortex. Neuron. 2007;56(2):252-69.

195. Kloxin AM, Kasko AM, Salinas CN, Anseth KS. Photodegradable hydrogels for dynamic tuning of physical and chemical properties. Science. 2009;324(5923):59-63.

196. DeForest CA, Tirrell DA. A photoreversible protein-patterning approach for guiding stem cell fate in three-dimensional gels. Nat Mater. 2015;14(5):523-31.

197. Liu Z XL, Xu B, Zhang Y, Mak A, Li Y, WY Man, Yang M. Covalently immobilized biomolecule gradient on hydrogel surface using a gradient generating microfluidic device for a quantitative mesenchymal stem cell study. Biomicrofluidics. 2012;6(2):24111-2.

198. Cosson S, Lutolf MP. Hydrogel microfluidics for the patterning of pluripotent stem cells. Sci Rep. 2014;4:4462.

199. Castano AG HV, Lagunas A, Cortina C, Montserrat N, Samiter J, Martinez E. Protein patterning on hydrogels by direct microcontact printing: application to cardiac differentiation. RSC Advances. 2014(55).

200. Murphy SV, Atala A. 3D bioprinting of tissues and organs. Nat Biotechnol. 2014;32(8):773-85.

201. Armstrong JP, Burke M, Carter BM, Davis SA, Perriman AW. 3D Bioprinting Using a Templated Porous Bioink. Adv Healthc Mater. 2016;5(14):1724-30.

202. Lozano R SL, Thompson BC, Gilmore KJ, Gorkin R, Stewart EM, Panhuis M, Romero-Ortega M, Wallace GG. 3D printing of layered brain-like structures using peptide modified gellan gum substrates. Biomaterials. 2015;67:264-73.

203. Mosiewicz KA, Kolb L, van der Vlies AJ, Martino MM, Lienemann PS, Hubbell JA, et al. In situ cell manipulation through enzymatic hydrogel photopatterning. Nat Mater. 2013;12(11):1072-8.

204. Wade RJ, Bassin EJ, Gramlich WM, Burdick JA. Nanofibrous hydrogels with spatially patterned biochemical signals to control cell behavior. Adv Mater. 2015;27(8):1356-62.

205. DeForest CA, Anseth KS. Cytocompatible click-based hydrogels with dynamically tunable properties through orthogonal photoconjugation and photocleavage reactions. Nat Chem. 2011;3(12):925-31.

206. Holmes TC, de Lacalle S, Su X, Liu G, Rich A, Zhang S. Extensive neurite outgrowth and active synapse formation on self-assembling peptide scaffolds. Proc Natl Acad Sci U S A. 2000;97(12):6728-33.

207. Cheng TY, Chen MH, Chang WH, Huang MY, Wang TW. Neural stem cells encapsulated in a functionalized self-assembling peptide hydrogel for brain tissue engineering. Biomaterials. 2013;34(8):2005-16.

208. Koutsopoulos S, Zhang S. Long-term three-dimensional neural tissue cultures in functionalized self-assembling peptide hydrogels, matrigel and collagen I. Acta Biomater. 2013;9(2):5162-9.

209. Sur S, Newcomb CJ, Webber MJ, Stupp SI. Tuning supramolecular mechanics to guide neuron development. Biomaterials. 2013;34(20):4749-57.

210. McKinnon DD, Brown TE, Kyburz KA, Kiyotake E, Anseth KS. Design and characterization of a synthetically accessible, photodegradable hydrogel for user-directed formation of neural networks. Biomacromolecules. 2014;15(7):2808-16.

211. Ju YE, Janmey PA, McCormick ME, Sawyer ES, Flanagan LA. Enhanced neurite growth from mammalian neurons in three-dimensional salmon fibrin gels. Biomaterials. 2007;28(12):2097-108.

212. Tay A, Sohrabi A, Poole K, Seidlits S, Di Carlo D. A 3D Magnetic Hyaluronic Acid Hydrogel for Magnetomechanical Neuromodulation of Primary Dorsal Root Ganglion Neurons. Adv Mater. 2018:e1800927.

213. Carballo-Molina OA VI. Hydrogels as scaffolds and delivery systems to enhance axonal regeneration after injuries. Frontiers in Cellular Neuroscience. 2015;9(13).

214. Sun Y, Li W, Wu X, Zhang N, Zhang Y, Ouyang S, et al. Functional Self-Assembling Peptide Nanofiber Hydrogels Designed for Nerve Degeneration. ACS Appl Mater Interfaces. 2016;8(3):2348-59.

215. Silva GA, Czeisler C, Niece KL, Beniash E, Harrington DA, Kessler JA, et al. Selective differentiation of neural progenitor cells by high-epitope density nanofibers. Science. 2004;303(5662):1352-5.

216. Gordan J AS, White MK. General Overview of Neuronal Cell Culture. Methods in Molecular Biology. 2013;1078:1-8.

217. Georges PC MW, Meaney DF, Sawyer ES, Janmey PA. Matrices with Compliance Comparable to that of Brain Tissue Select Neuronal over Glial Growth in Mixed Cortical Cultures. Biophysical Journal. 2006;90(8):3012-8.

218. Lindsey S, Piatt JH, Worthington P, Sonmez C, Satheye S, Schneider JP, et al. Beta Hairpin Peptide Hydrogels as an Injectable Solid Vehicle for Neurotrophic Growth Factor Delivery. Biomacromolecules. 2015;16(9):2672-83.

219. Dupin I, Dahan M, Studer V. Investigating axonal guidance with microdevice-based approaches. J Neurosci. 2013;33(45):17647-55.

220. Giger RJ, Hollis ER, 2nd, Tuszynski MH. Guidance molecules in axon regeneration. Cold Spring Harb Perspect Biol. 2010;2(7):a001867.

221. Gunther MI WN, Muller R, Blesch A. Cell-seeded alginate hydrogel scaffolds promote directed axonal regeneration in the injured rat spinal cord. Acta Biomaterialia. 2015;27(27):140-50.

222. Tsai EC, Dalton PD, Shoichet MS, Tator CH. Synthetic hydrogel guidance channels facilitate regeneration of adult rat brainstem motor axons after complete spinal cord transection. J Neurotrauma. 2004;21(6):789-804.

223. Hynd MR, Frampton JP, Dowell-Mesfin N, Turner JN, Shain W. Directed cell growth on protein-functionalized hydrogel surfaces. J Neurosci Methods. 2007;162(1-2):255-63.

224. Luo Y, Shoichet MS. A photolabile hydrogel for guided three-dimensional cell growth and migration. Nat Mater. 2004;3(4):249-53.

225. Moore K, MacSween M, Shoichet M. Immobilized concentration gradients of neurotrophic factors guide neurite outgrowth of primary neurons in macroporous scaffolds. Tissue Eng. 2006;12(2):267-78.

226. Berns EJ, Sur S, Pan L, Goldberger JE, Suresh S, Zhang S, et al. Aligned neurite outgrowth and directed cell migration in self-assembled monodomain gels. Biomaterials. 2014;35(1):185-95.

227. Xie J, MacEwan MR, Li X, Sakiyama-Elbert SE, Xia Y. Neurite outgrowth on nanofiber scaffolds with different orders, structures, and surface properties. ACS Nano. 2009;3(5):1151-9.

228. Cai Z, Gan Y, Bao C, Wu W, Wang X, Zhang Z, et al. Photosensitive Hydrogel Creates Favorable Biologic Niches to Promote Spinal Cord Injury Repair. Adv Healthc Mater. 2019;8(13):e1900013.

229. Kretsinger JK, Haines LA, Ozbas B, Pochan DJ, Schneider JP. Cytocompatibility of self-assembled beta-hairpin peptide hydrogel surfaces. Biomaterials. 2005;26(25):5177-86.

230. Banker GA, Cowan WM. Rat hippocampal neurons in dispersed cell culture. Brain Res. 1977;126(3):397-42.

231. Basarsky TA, Parpura V, Haydon PG. Hippocampal synaptogenesis in cell culture: developmental time course of synapse formation, calcium influx, and synaptic protein distribution. J Neurosci. 1994;14(11 Pt 1):6402-11.

232. Petrovic MM, Viana da Silva S, Clement JP, Vyklicky L, Mulle C, Gonzalez-Gonzalez IM, et al. Metabotropic action of postsynaptic kainate receptors triggers hippocampal long-term potentiation. Nat Neurosci. 2017;20(4):529-39.

233. Verstraelen P, Pintelon I, Nuydens R, Cornelissen F, Meert T, Timmermans JP. Pharmacological characterization of cultivated neuronal networks: relevance to synaptogenesis and synaptic connectivity. Cell Mol Neurobiol. 2014;34(5):757-76.

234. Verstraelen P, Van Dyck M, Verschuuren M, Kashikar ND, Nuydens R, Timmermans JP, et al. Image-Based Profiling of Synaptic Connectivity in Primary Neuronal Cell Culture. Front Neurosci. 2018;12:389.

235. Ho VM, Lee JA, Martin KC. The cell biology of synaptic plasticity. Science. 2011;334(6056):623-8.

236. Long MM, Urry DW, Stoeckenius W. Circular dichroism of biological membranes: purple membrane of Halobacterium halobium. Biochem Biophys Res Commun. 1977;75(3):725-31.

237. Discher DE, Janmey P, Wang YL. Tissue cells feel and respond to the stiffness of their substrate. Science. 2005;310(5751):1139-43.

238. ML O. Mechanical characterisation of hydrogel materials. International Materials Reviews. 2014;59(1):44-59.

239. Yan C, Pochan DJ. Rheological properties of peptide-based hydrogels for biomedical and other applications. Chem Soc Rev. 2010;39(9):3528-40.

240. Maria OM, Maria O, Liu Y, Komarova SV, Tran SD. Matrigel improves functional properties of human submandibular salivary gland cell line. Int J Biochem Cell Biol. 2011;43(4):622-31.

241. Kaneko A, Sankai Y. Long-term culture of rat hippocampal neurons at low density in serum-free medium: combination of the sandwich culture technique with the three-dimensional nanofibrous hydrogel PuraMatrix. PLoS One. 2014;9(7):e102703.

242. Carballo-Molina OA, Sanchez-Navarro A, Lopez-Ornelas A, Lara-Rodarte R, Salazar P, Campos-Romo A, et al. Semaphorin 3C Released from a Biocompatible Hydrogel Guides and Promotes Axonal Growth of Rodent and Human Dopaminergic Neurons. Tissue Eng Part A. 2016;22(11-12):850-61.

243. Ahmed SA, Gogal RM, Jr., Walsh JE. A new rapid and simple non-radioactive assay to monitor and determine the proliferation of lymphocytes: an alternative to [3H]thymidine incorporation assay. J Immunol Methods. 1994;170(2):211-24.

244. Weber LM, Hayda KN, Anseth KS. Cell-matrix interactions improve beta-cell survival and insulin secretion in three-dimensional culture. Tissue Eng Part A. 2008;14(12):1959-68.

245. Pierschbacher MD RE. Cell attachment activity of fibronectin can be duplicated by small synthetic fragments of the molecule. Nature. 1984;309:30-3.

246. Zou Z ZQ, Wu Y, Song Y, Wu B. Growth of rat dorsal root ganglion neurons on a novel self-assembling scaffold containing IKVAV sequence. Materials Science and Engineering. 2009;29(7):2099-103.

247. Elkin BS, Ilankovan A, Morrison B, 3rd. Age-dependent regional mechanical properties of the rat hippocampus and cortex. J Biomech Eng. 2010;132(1):011010.

248. Flanagan LA, Ju YE, Marg B, Osterfield M, Janmey PA. Neurite branching on deformable substrates. Neuroreport. 2002;13(18):2411-5.

249. Stukel JM, Willits RK. The interplay of peptide affinity and scaffold stiffness on neuronal differentiation of neural stem cells. Biomed Mater. 2018;13(2):024102.

250. Koser DE, Thompson AJ, Foster SK, Dwivedy A, Pillai EK, Sheridan GK, et al. Mechanosensing is critical for axon growth in the developing brain. Nat Neurosci. 2016;19(12):1592-8.

251. Wood CW, Woolfson DN. CCBuilder 2.0: Powerful and accessible coiled-coil modeling. Protein Sci. 2018;27(1):103-11.

252. Tanaka A, Fujii Y, Kasai N, Okajima T, Nakashima H. Regulation of neuritogenesis in hippocampal neurons using stiffness of extracellular microenvironment. PLoS One. 2018;13(2):e0191928.

253. Georges PC, Miller WJ, Meaney DF, Sawyer ES, Janmey PA. Matrices with compliance comparable to that of brain tissue select neuronal over glial growth in mixed cortical cultures. Biophys J. 2006;90(8):3012-8.

254. Leipzig ND, Shoichet MS. The effect of substrate stiffness on adult neural stem cell behavior. Biomaterials. 2009;30(36):6867-78.

255. Kostic A, Sap J, Sheetz MP. RPTPalpha is required for rigidity-dependent inhibition of extension and differentiation of hippocampal neurons. J Cell Sci. 2007;120(Pt 21):3895-904.

256. Zheng J, Lamoureux P, Santiago V, Dennerll T, Buxbaum RE, Heidemann SR. Tensile regulation of axonal elongation and initiation. J Neurosci. 1991;11(4):1117-25.

257. Okur Z, Senturk OI, Yilmaz C, Gulseren G, Mammadov B, Guler MO, et al. Promotion of neurite outgrowth by rationally designed NGF-beta binding peptide nanofibers. Biomater Sci. 2018;6(7):1777-90.

258. Semino CE, Kasahara J, Hayashi Y, Zhang S. Entrapment of migrating hippocampal neural cells in three-dimensional peptide nanofiber scaffold. Tissue Eng. 2004;10(3-4):643-55.

259. Greenfield MA, Hoffman JR, de la Cruz MO, Stupp SI. Tunable mechanics of peptide nanofiber gels. Langmuir. 2010;26(5):3641-7.

260. Koch F, Muller M, Konig F, Meyer N, Gattlen J, Pieles U, et al. Mechanical characteristics of beta sheet-forming peptide hydrogels are dependent on peptide sequence, concentration and buffer composition. R Soc Open Sci. 2018;5(3):171562.

261. Shi J, Gao Y, Zhang Y, Pan Y, Xu B. Calcium ions to cross-link supramolecular nanofibers to tune the elasticity of hydrogels over orders of magnitude. Langmuir. 2011;27(23):14425-31.

262. Wang B, Sun C, Shao Z, Yang S, Che B, Wu Q, et al. Designer self-assembling peptide nanofiber scaffolds containing link protein N-terminal peptide induce chondrogenesis of rabbit bone marrow stem cells. Biomed Res Int. 2014;2014:421954.

263. Ochbaum G, Davidovich-Pinhas M, Bitton R. Tuning the mechanical properties of alginate-peptide hydrogels. Soft Matter. 2018;14(21):4364-73.

264. Shin H, Jo S, Mikos AG. Biomimetic materials for tissue engineering. Biomaterials. 2003;24(24):4353-64.

265. Chohan MO, Li B, Blanchard J, Tung YC, Heaney AT, Rabe A, et al. Enhancement of dentate gyrus neurogenesis, dendritic and synaptic plasticity and memory by a neurotrophic peptide. Neurobiol Aging. 2011;32(8):1420-34.

266. Fletcher JM, Hughes RA. Modified low molecular weight cyclic peptides as mimetics of BDNF with improved potency, proteolytic stability and transmembrane passage in vitro. Bioorg Med Chem. 2009;17(7):2695-702.

267. Xiong S, Xu Y, Ma M, Wang H, Wei F, Gu Q, et al. Neuroprotective effects of a novel peptide, FK18, under oxygen-glucose deprivation in SH-SY5Y cells and retinal ischemia in rats via the Akt pathway. Neurochem Int. 2017.

268. Emery A. C. ELE. Signalling through the neuropeptide GPCR PAC1 induces neuritogenesis via a single linear cAMP- and ERK-dependent pathway using a novel cAMP sensor. FASEB J. 2012;26(8):3199-211.

269. Kricker JA, Towne CL, Firth SM, Herington AC, Upton Z. Structural and functional evidence for the interaction of insulin-like growth factors (IGFs) and IGF binding proteins with vitronectin. Endocrinology. 2003;144(7):2807-15.

270. Le Trong I, Wang Z, Hyre DE, Lybrand TP, Stayton PS, Stenkamp RE. Streptavidin and its biotin complex at atomic resolution. Acta Crystallogr D Biol Crystallogr. 2011;67(Pt 9):813-21.

271. Bundy BC, Swartz JR. Site-specific incorporation of p-propargyloxyphenylalanine in a cell-free environment for direct protein-protein click conjugation. Bioconjug Chem. 2010;21(2):255-63.

272. Deis LN, Wu Q, Wang Y, Qi Y, Daniels KG, Zhou P, et al. Suppression of conformational heterogeneity at a protein-protein interface. Proc Natl Acad Sci U S A. 2015;112(29):9028-33.

273. Witte MD, Theile CS, Wu T, Guimaraes CP, Blom AE, Ploegh HL. Production of unnaturally linked chimeric proteins using a combination of sortase-catalyzed transpeptidation and click chemistry. Nat Protoc. 2013;8(9):1808-19.

274. Maza JC, McKenna JR, Raliski BK, Freedman MT, Young DD. Synthesis and Incorporation of Unnatural Amino Acids To Probe and Optimize Protein Bioconjugations. Bioconjug Chem. 2015;26(9):1884-9.

275. Nilsson B, Moks T, Jansson B, Abrahmsen L, Elmblad A, Holmgren E, et al. A synthetic IgG-binding domain based on staphylococcal protein A. Protein Eng. 1987;1(2):107-13.

276. Li L, Fierer JO, Rapoport TA, Howarth M. Structural analysis and optimization of the covalent association between SpyCatcher and a peptide Tag. J Mol Biol. 2014;426(2):309-17.

277. Brune KD, Leneghan DB, Brian IJ, Ishizuka AS, Bachmann MF, Draper SJ, et al. Plug-and-Display: decoration of Virus-Like Particles via isopeptide bonds for modular immunization. Sci Rep. 2016;6:19234.

278. Khairil Anuar INA, Banerjee A, Keeble AH, Carella A, Nikov GI, Howarth M. Spy&Go purification of SpyTag-proteins using pseudo-SpyCatcher to access an oligomerization toolbox. Nat Commun. 2019;10(1):1734.

279. Chung H, Seo S, Moon M, Park S. IGF-I inhibition of apoptosis is associated with decreased expression of prostate apoptosis response-4. J Endocrinol. 2007;194(1):77-85.

280. Subramaniam S, Shahani N, Strelau J, Laliberte C, Brandt R, Kaplan D, et al. Insulin-like growth factor 1 inhibits extracellular signal-regulated kinase to promote neuronal survival via the phosphatidylinositol 3-kinase/protein kinase A/c-Raf pathway. J Neurosci. 2005;25(11):2838-52.

281. Kim JH, Roberts DS, Hu Y, Lau GC, Brooks-Kayal AR, Farb DH, et al. Brain-derived neurotrophic factor uses CREB and Egr3 to regulate NMDA receptor levels in cortical neurons. J Neurochem. 2012;120(2):210-9.

282. Matrone C, Ciotti MT, Mercanti D, Marolda R, Calissano P. NGF and BDNF signaling control amyloidogenic route and Abeta production in hippocampal neurons. Proc Natl Acad Sci U S A. 2008;105(35):13139-44.

283. Hodge RD, D'Ercole AJ, O'Kusky JR. Insulin-like growth factor-I (IGF-I) inhibits neuronal apoptosis in the developing cerebral cortex in vivo. Int J Dev Neurosci. 2007;25(4):233-41.

284. Davis ME, Hsieh PC, Takahashi T, Song Q, Zhang S, Kamm RD, et al. Local myocardial insulin-like growth factor 1 (IGF-1) delivery with biotinylated peptide nanofibers improves cell therapy for myocardial infarction. Proc Natl Acad Sci U S A. 2006;103(21):8155-60.

285. Li JA, Zhao CF, Li SJ, Zhang J, Li ZH, Zhang Q, et al. Modified insulin-like growth factor 1 containing collagen-binding domain for nerve regeneration. Neural Regen Res. 2018;13(2):298-303.

286. Chung BH CY, Yoon SH, Lee SY, Lee YI. Process development for production of recombinant human insulin-like growth factor-I in Escherichia coli. Journal of Industrial Microbiology and Biotechnology. 2000;2.

287. de Marco A. Strategies for successful recombinant expression of disulfide bond-dependent proteins in Escherichia coli. Microb Cell Fact. 2009;8:26.

288. Rattenholl A, Lilie H, Grossmann A, Stern A, Schwarz E, Rudolph R. The pro-sequence facilitates folding of human nerve growth factor from Escherichia coli inclusion bodies. Eur J Biochem. 2001;268(11):3296-303.

289. Lobstein J, Emrich CA, Jeans C, Faulkner M, Riggs P, Berkmen M. SHuffle, a novel Escherichia coli protein expression strain capable of correctly folding disulfide bonded proteins in its cytoplasm. Microb Cell Fact. 2012;11:56.

290. Dupont J, Le Roith D. Insulin-like growth factor 1 and oestradiol promote cell proliferation of MCF-7 breast cancer cells: new insights into their synergistic effects. Mol Pathol. 2001;54(3):149-54.

291. Feoktistova M, Geserick P, Leverkus M. Crystal Violet Assay for Determining Viability of Cultured Cells. Cold Spring Harb Protoc. 2016;2016(4):pdb prot087379.

292. Llorens-Martin M, Torres-Aleman I, Trejo JL. Mechanisms mediating brain plasticity: IGF1 and adult hippocampal neurogenesis. Neuroscientist. 2009;15(2):134-48.

293. Kim YH, Baek NS, Han YH, Chung MA, Jung SD. Enhancement of neuronal cell adhesion by covalent binding of poly-D-lysine. J Neurosci Methods. 2011;202(1):38-44.

294. Sun Y, Huang Z, Liu W, Yang K, Sun K, Xing S, et al. Surface coating as a key parameter in engineering neuronal network structures in vitro. Biointerphases. 2012;7(1-4):29.

295. Bitto A, Lerner C, Torres C, Roell M, Malaguti M, Perez V, et al. Long-term IGF-I exposure decreases autophagy and cell viability. PLoS One. 2010;5(9):e12592.

296. Kenyon C. A conserved regulatory system for aging. Cell. 2001;105(2):165-8.

297. Vitale G, Pellegrino G, Vollery M, Hofland LJ. ROLE of IGF-1 System in the Modulation of Longevity: Controversies and New Insights From a Centenarians' Perspective. Front Endocrinol (Lausanne). 2019;10:27.

298. Wang AY, Leong S, Liang YC, Huang RC, Chen CS, Yu SM. Immobilization of growth factors on collagen scaffolds mediated by polyanionic collagen mimetic peptides and its effect on endothelial cell morphogenesis. Biomacromolecules. 2008;9(10):2929-36.

299. Kim J, Lin B, Kim S, Choi B, Evseenko D, Lee M. TGF-beta1 conjugated chitosan collagen hydrogels induce chondrogenic differentiation of human synovium-derived stem cells. J Biol Eng. 2015;9:1.

300. DiMaio JTM, Raymond DM, Nilsson BL. Display of functional proteins on supramolecular peptide nanofibrils using a split-protein strategy. Org Biomol Chem. 2017;15(25):5279-83.

301. Hudalla GA, Sun T, Gasiorowski JZ, Han H, Tian YF, Chong AS, et al. Gradated assembly of multiple proteins into supramolecular nanomaterials. Nat Mater. 2014;13(8):829-36.

302. Wakabayashi R, Suehiro A, Goto M, Kamiya N. Designer aromatic peptide amphiphiles for self-assembly and enzymatic display of proteins with morphology control. Chem Commun (Camb). 2019;55(5):640-3.

303. Li Z Q XYY, Li H C, Guan J J. Immobilization of insulin-like growth factor-1 onto thermosensitive hydrogels to enhance cardiac progenitor cell survival and differentiation under ischemic conditions. Science China Chemistry. 2014(4):568-78.

304. Lorentz KM, Yang L, Frey P, Hubbell JA. Engineered insulin-like growth factor-1 for improved smooth muscle regeneration. Biomaterials. 2012;33(2):494-503.

305. Caliari SR, Harley BA. Composite growth factor supplementation strategies to enhance tenocyte bioactivity in aligned collagen-GAG scaffolds. Tissue Eng Part A. 2013;19(9-10):1100-12.

306. Cao X, Shoichet MS. Investigating the synergistic effect of combined neurotrophic factor concentration gradients to guide axonal growth. Neuroscience. 2003;122(2):381-9.

307. Hashimoto Y, Abiru Y, Nishio C, Hatanaka H. Synergistic effects of brain-derived neurotrophic factor and ciliary neurotrophic factor on cultured basal forebrain cholinergic neurons from postnatal 2-week-old rats. Brain Res Dev Brain Res. 1999;115(1):25-32.

308. Johnson-Farley NN, Patel K, Kim D, Cowen DS. Interaction of FGF-2 with IGF-1 and BDNF in stimulating Akt, ERK, and neuronal survival in hippocampal cultures. Brain Res. 2007;1154:40-9.

309. Mortimer D, Fothergill T, Pujic Z, Richards LJ, Goodhill GJ. Growth cone chemotaxis. Trends Neurosci. 2008;31(2):90-8.

310. Sperry RW. Chemoaffinity in the Orderly Growth of Nerve Fiber Patterns and Connections. Proc Natl Acad Sci U S A. 1963;50:703-10.

311. Kennedy TE WH, Marshall W, Tessier-Lavigne M. Axon guidance by diffusible chemoattractants: a gradient of netrin protein in the developing spinal cord. Journal of Neuroscience. 2006;26(34):8866-74.

312. Gundersen RW, Barrett JN. Neuronal chemotaxis: chick dorsal-root axons turn toward high concentrations of nerve growth factor. Science. 1979;206(4422):1079-80.

313. Koncina E RL, Gonthier B, Bagnard D. Role of Semaphorins during axon growth and guidance. Advances in Experimental Medicine and Biology. 2007;621:50-64.

314. Ming G, Song H, Berninger B, Inagaki N, Tessier-Lavigne M, Poo M. Phospholipase C-gamma and phosphoinositide 3-kinase mediate cytoplasmic signaling in nerve growth cone guidance. Neuron. 1999;23(1):139-48.

315. Luria V, Krawchuk D, Jessell TM, Laufer E, Kania A. Specification of motor axon trajectory by ephrin-B:EphB signaling: symmetrical control of axonal patterning in the developing limb. Neuron. 2008;60(6):1039-53.

316. Pati F, Jang J, Ha DH, Won Kim S, Rhie JW, Shim JH, et al. Printing three-dimensional tissue analogues with decellularized extracellular matrix bioink. Nat Commun. 2014;5:3935.

317. Allazetta S, Cosson S, Lutolf MP. Programmable microfluidic patterning of protein gradients on hydrogels. Chem Commun (Camb). 2011;47(1):191-3.

318. Lee SH, Rho WY, Park SJ, Kim J, Kwon OS, Jun BH. Multifunctional self-assembled monolayers via microcontact printing and degas-driven flow guided patterning. Sci Rep. 2018;8(1):16763.

319. Gopinathan J, Noh I. Recent trends in bioinks for 3D printing. Biomater Res. 2018;22:11.

320. Ming G, Henley J, Tessier-Lavigne M, Song H, Poo M. Electrical activity modulates growth cone guidance by diffusible factors. Neuron. 2001;29(2):441-52.

321. Tessier-Lavigne M. Axon guidance by molecular gradients. Curr Opin Neurobiol. 1992;2(1):60-5.

322. Sackmann EK, Fulton AL, Beebe DJ. The present and future role of microfluidics in biomedical research. Nature. 2014;507(7491):181-9.

323. Jeon NL DS, Chiu DT, Choi IS, Stroock AD, GM Whitesides. Generation of solution and surface gradients using microfluidic systems. Langmuir. 2000;16:8311-6.

324. Kothapalli CR, van Veen E, de Valence S, Chung S, Zervantonakis IK, Gertler FB, et al. A high-throughput microfluidic assay to study neurite response to growth factor gradients. Lab Chip. 2011;11(3):497-507.

325. Chang C-W CY-J, Tu M, Chen Y-H, Peng C-C, Liao W-H Tung Y-C. A polydimethylsiloxane–polycarbonate hybrid microfluidic device capable of generating perpendicular chemical and oxygen gradients for cell culture studies. Lab on a Chip. 2014;14:3762.

326. Xiao R-R ZW-J, Li Y-T, Zou W, Wang L, Pei X-F, Xie M, Huang W-H. Simultaneous generation of gradients with gradually changed slope in a microfluridic divice for quantifying axon response. Analytical Chemistry. 2013;85(16):7842-50.

327. Atencia J, Morrow J, Locascio LE. The microfluidic palette: a diffusive gradient generator with spatio-temporal control. Lab Chip. 2009;9(18):2707-14.

328. Holden MA KS, Castellana ET, Beskok A, Cremer PS. Generating fixed concentration arrays in a microfluidic device. Sensors and Actuators B: Chemical. 2003;92(1-2):199-207.

329. Lin F, Saadi W, Rhee SW, Wang SJ, Mittal S, Jeon NL. Generation of dynamic temporal and spatial concentration gradients using microfluidic devices. Lab Chip. 2004;4(3):164-7.

330. Englert DL, Manson MD, Jayaraman A. Flow-based microfluidic device for quantifying bacterial chemotaxis in stable, competing gradients. Appl Environ Microbiol. 2009;75(13):4557-64.

331. Campbell K, Groisman A. Generation of complex concentration profiles in microchannels in a logarithmically small number of steps. Lab Chip. 2007;7(2):264-72.

332. Burdick JA, Khademhosseini A, Langer R. Fabrication of gradient hydrogels using a microfluidics/photopolymerization process. Langmuir. 2004;20(13):5153-6.

333. Garcia S, Sunyer R, Olivares A, Noailly J, Atencia J, Trepat X. Generation of stable orthogonal gradients of chemical concentration and substrate stiffness in a microfluidic device. Lab Chip. 2015;15(12):2606-14.

334. Cirelli RA WG, Nalamasu O. Optical Lithography. Encyclopedia of Materials: Science and Technology (Second Edition)2001. p. 6441-8.

335. Gandavarapu NR, Azagarsamy MA, Anseth KS. Photo-click living strategy for controlled, reversible exchange of biochemical ligands. Adv Mater. 2014;26(16):2521-6.

336. Brown TE, Anseth KS. Spatiotemporal hydrogel biomaterials for regenerative medicine. Chem Soc Rev. 2017;46(21):6532-52.

337. Polizzotti BD, Fairbanks BD, Anseth KS. Three-dimensional biochemical patterning of click-based composite hydrogels via thiolene photopolymerization. Biomacromolecules. 2008;9(4):1084-7.

338. Musoke-Zawedde P, Shoichet MS. Anisotropic three-dimensional peptide channels guide neurite outgrowth within a biodegradable hydrogel matrix. Biomed Mater. 2006;1(3):162-9.

339. Nagarajan N, Pop M. Sequence assembly demystified. Nat Rev Genet. 2013;14(3):157-67.

340. Grim JC, Marozas IA, Anseth KS. Thiol-ene and photo-cleavage chemistry for controlled presentation of biomolecules in hydrogels. J Control Release. 2015;219:95-106.

341. Hoyle CE LT, Roper T. Thiol–enes: Chemistry of the past with promise for the future. Journal of Polymer Science Part A: Polymer Chemistry. 2004;42(21).

342. Fairbanks BD, Schwartz MP, Halevi AE, Nuttelman CR, Bowman CN, Anseth KS. A Versatile Synthetic Extracellular Matrix Mimic via Thiol-Norbornene Photopolymerization. Adv Mater. 2009;21(48):5005-10.

343. Sawicki LA, Kloxin AM. Design of thiol-ene photoclick hydrogels using facile techniques for cell culture applicationsdaggerElectronic supplementary information (ESI) available. See DOI: 10.1039/c4bm00187gClick here for additional data file. Biomater Sci. 2014;2(11):1612-26.

344. Killops KL, Campos LM, Hawker CJ. Robust, efficient, and orthogonal synthesis of dendrimers via thiol-ene "click" chemistry. J Am Chem Soc. 2008;130(15):5062-4.

345. Grim JC, Brown TE, Aguado BA, Chapnick DA, Viert AL, Liu X, et al. A Reversible and Repeatable Thiol-Ene Bioconjugation for Dynamic Patterning of Signaling Proteins in Hydrogels. ACS Cent Sci. 2018;4(7):909-16.

346. Wang Y, Bruno BJ, Cornillie S, Nogieira JM, Chen D, Cheatham TE, 3rd, et al. Application of Thiol-yne/Thiol-ene Reactions for Peptide and Protein Macrocyclizations. Chemistry. 2017;23(29):7087-92.

347. Mahmoud ZN, Gunnoo SB, Thomson AR, Fletcher JM, Woolfson DN. Bioorthogonal dual functionalization of self-assembling peptide fibers. Biomaterials. 2011;32(15):3712-20.

348. Northrop BH, Coffey RN. Thiol-ene click chemistry: computational and kinetic analysis of the influence of alkene functionality. J Am Chem Soc. 2012;134(33):13804-17.

349. Smyth DG NA, Fruton JS. Some Reactions of N-Ethylmaleimide. Journal of the American Chemical Society. 1960;82:4600-4.

350. Aizawa Y, Wylie R, Shoichet M. Endothelial cell guidance in 3D patterned scaffolds. Adv Mater. 2010;22(43):4831-5.

351. Kato Y UK, Kawakishi S. Oxidative Degradation of Collagen and Its Model Peptide by Ultraviolet Irradiation. Journal of Agriculture and Food Chemistry. 1992;40:373-9.

352. Khetan S BJ. Patterning hydrogels in three dimensions towards controlling cellular interactions. Soft Matter. 2011;3.

353. Gumuscu B, Bomer JG, van den Berg A, Eijkel JC. Photopatterning of Hydrogel Microarrays in Closed Microchips. Biomacromolecules. 2015;16(12):3802-10.

354. Tong X JJ, Zhu D, Yang F. Hydrogels with Dual Gradients of Mechanical and Biochemical Cues for Deciphering Cell-Niche Interactions. ACS Biomaterials Science and Engineering. 2016;2:845-52.

355. Knoll B, Weinl C, Nordheim A, Bonhoeffer F. Stripe assay to examine axonal guidance and cell migration. Nat Protoc. 2007;2(5):1216-24.

356. Yam PT, Langlois SD, Morin S, Charron F. Sonic hedgehog guides axons through a noncanonical, Src-family-kinase-dependent signaling pathway. Neuron. 2009;62(3):349-62.

357. Kolodkin AL. Semaphorins: mediators of repulsive growth cone guidance. Trends Cell Biol. 1996;6(1):15-22.

358. Bhattacharjee N, Folch A. Large-scale microfluidic gradient arrays reveal axon guidance behaviors in hippocampal neurons. Microsyst Nanoeng. 2017;3:17003.

359. Lavigne JJ, Anslyn EV. Sensing A Paradigm Shift in the Field of Molecular Recognition: From Selective to Differential Receptors. Angew Chem Int Ed Engl. 2001;40(17):3118-30.

360. Fleischer J, Breer H, Strotmann J. Mammalian olfactory receptors. Front Cell Neurosci. 2009;3:9.

361. Pace U, Hanski E, Salomon Y, Lancet D. Odorant-sensitive adenylate cyclase may mediate olfactory reception. Nature. 1985;316(6025):255-8.

362. Buck L, Axel R. A novel multigene family may encode odorant receptors: a molecular basis for odor recognition. Cell. 1991;65(1):175-87.

363. Bushdid C, Magnasco MO, Vosshall LB, Keller A. Humans can discriminate more than 1 trillion olfactory stimuli. Science. 2014;343(6177):1370-2.

364. Niimura Y. Olfactory receptor multigene family in vertebrates: from the viewpoint of evolutionary genomics. Curr Genomics. 2012;13(2):103-14.

365. Niimura Y, Matsui A, Touhara K. Extreme expansion of the olfactory receptor gene repertoire in African elephants and evolutionary dynamics of orthologous gene groups in 13 placental mammals. Genome Res. 2014;24(9):1485-96.

366. Askim JR, Mahmoudi M, Suslick KS. Optical sensor arrays for chemical sensing: the optoelectronic nose. Chem Soc Rev. 2013;42(22):8649-82.

367. Li Z, Askim JR, Suslick KS. The Optoelectronic Nose: Colorimetric and Fluorometric Sensor Arrays. Chem Rev. 2019;119(1):231-92.

368. Aigner D, Ungerbock B, Mayr T, Saf R, Klimant I, Borisov SM. Fluorescent materials for pH sensing and imaging based on novel 1,4-diketopyrrolo-[3,4-c]pyrrole dyesdaggerElectronic supplementary information (ESI) available: NMR and MS spectra, further sensor characteristics and sensor long-time performance. See DOI: 10.1039/c3tc31130aClick here for additional data file. J Mater Chem C Mater. 2013;1(36):5685-93.

369. Askim JR, Li Z, LaGasse MK, Rankin JM, Suslick KS. An optoelectronic nose for identification of explosives. Chem Sci. 2016;7(1):199-206.

370. Lin H, Suslick KS. A colorimetric sensor array for detection of triacetone triperoxide vapor. J Am Chem Soc. 2010;132(44):15519-21.

371. Macias G, Sperling JR, Peveler WJ, Burley GA, Neale SL, Clark AW. Whisky tasting using a bimetallic nanoplasmonic tongue. Nanoscale. 2019.

372. Rakow NA, Suslick KS. A colorimetric sensor array for odour visualization. Nature. 2000;406(6797):710-3.

373. Ghanem E, Hopfer H, Navarro A, Ritzer MS, Mahmood L, Fredell M, et al. Predicting the composition of red wine blends using an array of multicomponent Peptide-based sensors. Molecules. 2015;20(5):9170-82.

374. Adams MM, Anslyn EV. Differential sensing using proteins: exploiting the cross-reactivity of serum albumin to pattern individual terpenes and terpenes in perfume. J Am Chem Soc. 2009;131(47):17068-9.

375. Kubarych CJ, Adams MM, Anslyn EV. Serum albumins as differential receptors for the discrimination of fatty acids and oils. Org Lett. 2010;12(21):4780-3.

376. Mazzone PJ, Hammel J, Dweik R, Na J, Czich C, Laskowski D, et al. Diagnosis of lung cancer by the analysis of exhaled breath with a colorimetric sensor array. Thorax. 2007;62(7):565-8.

377. Bruce Alberts AJ, Julian Lewis, Martin Raff, Keith Roberts, Peter Walter. Molecular Biology of the Cell. 4th edition - Protein Function

New York: Garland Science; 2002.

378. Kida H, Fukutani Y, Mainland JD, de March CA, Vihani A, Li YR, et al. Vapor detection and discrimination with a panel of odorant receptors. Nat Commun. 2018;9(1):4556.

379. Rana S, Elci SG, Mout R, Singla AK, Yazdani M, Bender M, et al. Ratiometric Array of Conjugated Polymers-Fluorescent Protein Provides a Robust Mammalian Cell Sensor. J Am Chem Soc. 2016;138(13):4522-9.

380. Rana S, Le ND, Mout R, Saha K, Tonga GY, Bain RE, et al. A multichannel nanosensor for instantaneous readout of cancer drug mechanisms. Nat Nanotechnol. 2015;10(1):65-9.

381. Zhuang H, Matsunami H. Evaluating cell-surface expression and measuring activation of mammalian odorant receptors in heterologous cells. Nat Protoc. 2008;3(9):1402-13.

382. Carraher C, Nazmi AR, Newcomb RD, Kralicek A. Recombinant expression, detergent solubilisation and purification of insect odorant receptor subunits. Protein Expr Purif. 2013;90(2):160-9.

383. Song HS, Lee SH, Oh EH, Park TH. Expression, solubilization and purification of a human olfactory receptor from Escherichia coli. Curr Microbiol. 2009;59(3):309-14.

384. Testa OD, Moutevelis E, Woolfson DN. CC+: a relational database of coiled-coil structures. Nucleic Acids Res. 2009;37(Database issue):D315-22.

385. Truebestein L, Leonard TA. Coiled-coils: The long and short of it. Bioessays. 2016;38(9):903-16.

386. Fairman R, Chao HG, Lavoie TB, Villafranca JJ, Matsueda GR, Novotny J. Design of heterotetrameric coiled coils: evidence for increased stabilization by Glu(-)-Lys(+) ion pair interactions. Biochemistry. 1996;35(9):2824-9.

387. Hodges RS, Saund AK, Chong PC, St-Pierre SA, Reid RE. Synthetic model for two-stranded alpha-helical coiled-coils. Design, synthesis, and characterization of an 86-residue analog of tropomyosin. J Biol Chem. 1981;256(3):1214-24.

388. Lovejoy B, Choe S, Cascio D, McRorie DK, DeGrado WF, Eisenberg D. Crystal structure of a synthetic triple-stranded alpha-helical bundle. Science. 1993;259(5099):1288-93.

389. Dong C, Beis K, Nesper J, Brunkan-Lamontagne AL, Clarke BR, Whitfield C, et al. Wza the translocon for E. coli capsular polysaccharides defines a new class of membrane protein. Nature. 2006;444(7116):226-9.

390. Malashkevich VN, Kammerer RA, Efimov VP, Schulthess T, Engel J. The crystal structure of a five-stranded coiled coil in COMP: a prototype ion channel? Science. 1996;274(5288):761-5.

391. Burton AJ, Thomas F, Agnew C, Hudson KL, Halford SE, Brady RL, et al. Accessibility, reactivity, and selectivity of side chains within a channel of de novo peptide assembly. J Am Chem Soc. 2013;135(34):12524-7.

392. Butler LM, Yuan JM, Huang JY, Su J, Wang R, Koh WP, et al. Plasma fatty acids and risk of colon and rectal cancers in the Singapore Chinese Health Study. NPJ Precis Oncol. 2017;1(1):38.

393. Chen Y, Ma Z, Min L, Li H, Wang B, Zhong J, et al. Biomarker identification and pathway analysis by serum metabolomics of lung cancer. Biomed Res Int. 2015;2015:183624.

394. Tutino V, De Nunzio V, Caruso MG, Veronese N, Lorusso D, Di Masi M, et al. Elevated AA/EPA Ratio Represents an Inflammatory Biomarker in Tumor Tissue of Metastatic Colorectal Cancer Patients. Int J Mol Sci. 2019;20(8).

395. Xuan J, Pan G, Qiu Y, Yang L, Su M, Liu Y, et al. Metabolomic profiling to identify potential serum biomarkers for schizophrenia and risperidone action. J Proteome Res. 2011;10(12):5433-43.

396. Wang Y JL, Shen Q, Shen J, Han Y, Zhang H. Investigation on the self-assembled behaviors of C18 unsaturated fatty acids in arginine aqueous solution. RSC Advances. 2017(66).

397. Novales B, Riaublanc A, Navailles L, Houssou BH, Gaillard C, Nallet F, et al. Self-assembly and foaming properties of fatty acid-lysine aqueous dispersions. Langmuir. 2010;26(8):5329-34.

398. Stears RL, Martinsky T, Schena M. Trends in microarray analysis. Nat Med. 2003;9(1):140-5.

399. Prasad A, Hasan SMA, Grouchy S, Gartia MR. DNA microarray analysis using a smartphone to detect the BRCA-1 gene. Analyst. 2018;144(1):197-205.

400. Wang H, Ma Z, Qin J, Shen Z, Liu Q, Chen X, et al. A versatile loop-mediated isothermal amplification microchip platform for Streptococcus pneumoniae and Mycoplasma pneumoniae testing at the point of care. Biosens Bioelectron. 2019;126:373-80.

401. Brangel P, Sobarzo A, Parolo C, Miller BS, Howes PD, Gelkop S, et al. A Serological Point-of-Care Test for the Detection of IgG Antibodies against Ebola Virus in Human Survivors. ACS Nano. 2018;12(1):63-73.

402. Martinez AW, Phillips ST, Carrilho E, Thomas SW, 3rd, Sindi H, Whitesides GM. Simple telemedicine for developing regions: camera phones and paper-based microfluidic devices for real-time, off-site diagnosis. Anal Chem. 2008;80(10):3699-707.

403. Bahadir EB, Sezginturk MK. Applications of commercial biosensors in clinical, food, environmental, and biothreat/biowarfare analyses. Anal Biochem. 2015;478:107-20.

404. Engvall E PP. Enzyme-Linked Immunosorbent Assay, Elisa. The Journal of Immunology. 1972;109(1):129-35.

405. Fodor SP, Rava RP, Huang XC, Pease AC, Holmes CP, Adams CL. Multiplexed biochemical assays with biological chips. Nature. 1993;364(6437):555-6.

406. Lockhart DJ, Dong H, Byrne MC, Follettie MT, Gallo MV, Chee MS, et al. Expression monitoring by hybridization to high-density oligonucleotide arrays. Nat Biotechnol. 1996;14(13):1675-80.

407. Liu Y YJ. Oriented immobilization of proteins on solid supports for use in biosensors and biochips: a review. Microchim Acta. 2016;183:1-19.

408. Seurynck-Servoss SL, White AM, Baird CL, Rodland KD, Zangar RC. Evaluation of surface chemistries for antibody microarrays. Anal Biochem. 2007;371(1):105-15.

409. Tsukruk VV LI, Julthongpiput D. Sticky Molecular Surfaces: Epoxysilane Self-Assembled Monolayers. Langmuir. 1999;15:3029-32.

410. Welch NG, Scoble JA, Muir BW, Pigram PJ. Orientation and characterization of immobilized antibodies for improved immunoassays (Review). Biointerphases. 2017;12(2):02D301.

411. Kuzmin A PA, Wolfert MA, Popik VV. Surface Functionalization Using Catalyst-Free Azide-Alkyne Cycloaddition. Bioconjugate Chem. 2010;21:2076-85.

412. Prim D, Rebeaud F, Cosandey V, Marti R, Passeraub P, Pfeifer ME. ADIBO-based "click" chemistry for diagnostic peptide micro-array fabrication: physicochemical and assay characteristics. Molecules. 2013;18(8):9833-49.

413. Wasserberg D, Nicosia C, Tromp EE, Subramaniam V, Huskens J, Jonkheijm P. Oriented protein immobilization using covalent and noncovalent chemistry on a thiol-reactive self-reporting surface. J Am Chem Soc. 2013;135(8):3104-11.

414. Patching SG. Surface plasmon resonance spectroscopy for characterisation of membrane protein-ligand interactions and its potential for drug discovery. Biochim Biophys Acta. 2014;1838(1 Pt A):43-55.

415. Feng B, Huang S, Ge F, Luo Y, Jia D, Dai Y. 3D antibody immobilization on a planar matrix surface. Biosens Bioelectron. 2011;28(1):91-6.

416. Wang C, Feng B. [Research progress on site-oriented and three-dimensional immobilization of proteins]. Mol Biol (Mosk). 2015;49(1):3-25.

417. Carrilho E, Phillips ST, Vella SJ, Martinez AW, Whitesides GM. Paper microzone plates. Anal Chem. 2009;81(15):5990-8.

418. Olkkonen J, Lehtinen K, Erho T. Flexographically printed fluidic structures in paper. Anal Chem. 2010;82(24):10246-50.

419. Tavakoli J, Tang Y. Hydrogel Based Sensors for Biomedical Applications: An Updated Review. Polymers (Basel). 2017;9(8).

420. Abu-Rabeah K, Polyak B, Ionescu RE, Cosnier S, Marks RS. Synthesis and characterization of a pyrrole-alginate conjugate and its application in a biosensor construction. Biomacromolecules. 2005;6(6):3313-8.

421. Diehl KL, Ivy MA, Rabidoux S, Petry SM, Muller G, Anslyn EV. Differential sensing for the regio- and stereoselective identification and quantitation of glycerides. Proc Natl Acad Sci U S A. 2015;112(30):E3977-86.

422. Elci SG MD, Rana S, Tonga GY, Phillips RL, Bunz UHF, Rotello VM. Recognition of glycosaminoglycan chemical patterns using an unbiased sensor array. Chemical Science. 2013(4).

423. Wang B, Han J, Bojanowski NM, Bender M, Ma C, Seehafer K, et al. An Optimized Sensor Array Identifies All Natural Amino Acids. ACS Sens. 2018;3(8):1562-8.

424. McCleskey SC, Griffin MJ, Schneider SE, McDevitt JT, Anslyn EV. Differential receptors create patterns diagnostic for ATP and GTP. J Am Chem Soc. 2003;125(5):1114-5.

425. White SJ, Johnson SD, Sellick MA, Bronowska A, Stockley PG, Walti C. The influence of two-dimensional organization on peptide conformation. Angew Chem Int Ed Engl. 2015;54(3):974-8.

426. Taniguchi M, Lindsey JS. Database of Absorption and Fluorescence Spectra of >300 Common Compounds for use in PhotochemCAD. Photochem Photobiol. 2018;94(2):290-327.

427. Liu X PB, Wang H, Wang X-M. Self-assembling nanofiber hydrogels for central nervous system regeneration. Frontiers in Material Sciences. 2015;9(1):1-13.

428. Paraskevaidi M, Morais CLM, Lima KMG, Snowden JS, Saxon JA, Richardson AMT, et al. Differential diagnosis of Alzheimer's disease using spectrochemical analysis of blood. Proc Natl Acad Sci U S A. 2017;114(38):E7929-E38.